Simulating Past and Future Mass Balance of Place Glacier Using a Physically-Based, Distributed Glacier Mass Balance Model

by

Raju Aryal
B Sc , Tribhuvan University, Nepal, 1995
M.Sc , Tribhuvan University, Nepal, 1999
M Sc, Nagoya University, Japan, 2002

THESIS SUBMITTED IN PARTIAL FULFILLMENT OF THE REQUIREMENTS FOR
THE DEGREE OF DOCTOR OF PHILOSOPHY
IN
NATURAL RESOURCES AND ENVIRONMENTAL STUDIES

UNIVERSITY OF NORTHERN BRITISH COLUMBIA
(Prince George)
April 2015

Abstract

The objective of this study is to develop a physically-based distributed glacier mass balance (GMB) model for Place Glacier, British Columbia, Canada, and apply the model to develop the historic and the future mass balance The model is forced with climate data from Regional Atmospheric Modeling System (RAMS) mesoscale atmospheric model output from 1979-2008 for developing historic mass balance on Place Glacier The model is also run in the future (2009-2040) to develop a projection of mass balance.

The model simulated the historic glacier-wide summer and winter balance on Place Glacier satisfactorily. For all years, root mean squared error (RMSE) in simulated summer and winter balance are 0.43 m water equivalent (w e) and 0.27 m w.e., respectively. Over the period of 29 years, the model simulated a cumulative net mass balance of -33.72 m w.e. The model outperformed both empirical temperature index (TI) and enhanced TI models in simulating summer balance on Place Glacier when forced with the same RAMS variables.

A linear regression model based on Singular Value Decomposition (SVD) technique is used for downscaling future climate projections from a suite of Global Climate Models (GCMs). The cross-validation of downscaled daily air temperature showed a strong correlation with the validation dataset (r^2 =0.85, p <0.05). However, the RMSE in downscaled daily air temperature is large (=2.4°C). With spatially average correlation of 0.38 and RMSE of 7.5 mm day^{-1}, the model for daily precipitation performed less satisfactorily in downscaling large-scale precipitation. For all variables, the error statistics improved with the monthly model. Future GCM projections from CanESM2, MIROC-ESM, MPI-ESM-LR, and HadGEM2-ES, are considered for downscaling.

CanESM2 predicted a large negative glacier-wide net mass balance of -2.50 m w.e. for Place Glacier in the future. For the remaining GCMs, the average of net mass balance is -0.96 m w.e. The average of the cumulative mass loss predicted from GCMs other than CanESM2 is -31 m w.e From 2009-2040, CanESM2, MIROC, MPI and HadGEM2 predicted an area loss of 52%, 28%, 18% and 22%, respectively Overall, all downscaled GCMs, except CanESM2, performed better in predicting future mass balance for Place Glacier.

Table of Contents

List of Tables

List of Figures

List of Symbols

A'	transpose of the anomaly matrix of predictor fields
a	glacier area, initial glacier area
a_{new}	new glacier area
B	anomaly matrix of predictand fields
B_a	glacier-wide net mass balance
B_s	glacier-wide summer balance
B_w	glacier-wide winter balance
b_i	coefficient of best fit (intercept) for the i^{th} mode
b_n	net mass balance at a point on the glacier
b_s	summer mass balance at a point on the glacier
b_w	winter mass balance at a point on the glacier
b_p^k	bias (fraction) in RAMS daily precipitation at location k
b_t^k	bias (offset) in RAMS daily air temperature at location k
C	surface temperature deficit, cross-covariance matrix
C_a	specific heat capacity of dry air
C_D	turbulent transfer coefficient
C_s	specific heat capacity of ice
C_w	specific heat capacity of water
c	scaling parameter in volume-area relationship
D	diagonal of the matrix S
D_{sum}	sum of the diagonal D
d	specific mass of winter snow cover, number of days
d^*	characteristic snow depth scale for albedo modeling
d_s	winter snow depth, subsurface layer thickness
e_g	vapour pressure at measurement height
e_s	vapour pressure at the surface
F_m	modified melt factor
f	diffuse fraction of incoming shortwave radiation
g	gravitational acceleration
H	elevation referred to RAMS grid cell from where meteorological variables are retrieved.
H_{RAMS}	elevation of the RAMS grid cell nearest to the study area
H_{CDED}	elevation of the corresponding RAMS grid cell as reported by CDED DEM

H_{SRTM}	elevation of the corresponding RAMS grid cell as reported by SRTM
h	elevation of each model DEM cell
I_0	solar constant
K	total incoming shortwave radiation
K'	transpose of the anomalies of the large-scale fields
K_{dif}	diffuse shortwave radiation
K_{dir}	direct shortwave radiation
K_{DS}	downscaled large-scale field based
K_{DS}^{d}	statistically downscaled daily incoming shortwave radiation
K_{DS}^{h}	statistically downscaled hourly incoming shortwave radiation
K_H	eddy diffusivity of heat
K_{in}	RAMS hourly incoming shortwave radiation
K_{in}^{t}	daily total of K_{in}
K_M	eddy diffusivity of momentum
K_{net}	net shortwave radiation
K_{pot}	potential shortwave radiation
k	von Karman`s constant
k_s	melt factor for snow
k_i	melt factor for ice
L_f	latent heat of fusion of ice
L_{in}	RAMS incoming longwave radiation
L_{net}	net longwave radiation
L_{out}	outgoing longwave radiation
$L_{terrain}$	incoming longwave radiation from surrounding terrain
L_v	latent heat of evaporation of water
M	melt calculated from empirical models
M_m^k	monthly RAMS air temperature at location k
m_i	coefficient of best fit (slope) for the i^{th} mode
N	number of data points for SVD analysis
O_m^k	monthly observed air temperature at location k
P	RAMS adjusted hourly summer precipitation, station level pressure
P'	RAMS adjusted total winter precipitation
P_0	mean atmospheric pressure at sea level
P_g	distributed hourly summer precipitation
P_r	summer rainfall

P_s	summer accumulation
Q_E	latent heat flux
Q_G	glacier or subsurface heat flux
Q_H	sensible heat flux
Q_M	summer melt
Q_R	heat supplied by rain
$RAMS_p^k$	daily RAMS precipitation at location k
$RAMS^k$	daily RAMS air temperature at location k
R_1	mean sun-earth distance
R_2	instantaneous sun-earth distance
R_b	bulk Richardson number
r^2	squared correlation coefficient, coefficient of determination, explained variance
r_s	radiation melt factors for snow
r_i	radiation melt factors for ice
S	matrix whose diagonal contains the singular values
T_a	ambient air temperature
T_c	critical ambient air temperature required to initiate the development of KBL
T_s	glacier surface temperature
T_g	glacier air temperature at measurement height
T_0	threshold temperature for melt to occur
t	time elapsed since the last snowfall event
t^*	time scale for albedo modelling
T_x	static air temperature threshold for snow and rain
U	matrix containing the singular vectors for predictor field
u	wind speed at measurement height
V	matrix containing the singular vectors for predictand field
v	glacier volume
v_{int}	initial glacier volume
v_{new}	new glacier volume
W	orthogonally projected anomalies of the large scale variables
W_R	reconstructed field corresponding to i^{th} mode
W_i	orthogonally projected anomalies of the large-scale variables for the i^{th} mode
X	matrix containing expansion coefficients for each mode of predictor field
X_i	matrix containing expansion coefficients corresponding to i^{th} mode of predictor fields

X_P	total winter snow amount from the RAMS grid cell nearest to the study area
X_p^k	bias corrected daily RAMS precipitation for grid cell nearest to the study site
X_t^k	bias corrected daily RAMS air temperature for grid cell nearest to the study site
Y	matrix containing expansion coefficients for each mode of predictand field
Y_i	matrix containing expansion coefficients corresponding to i^{th} mode of predictand fields
v	scaling parameter in volume-area relationship
Z	local zenith angle
z	measurement height
z_0	roughness length for momentum
z_t	roughness length for temperature and vapour pressure
α	modelled surface albedo
α_f	albedo of firm
α_i	albedo of ice
α_{ns}	albedo of new snow
α_{os}	albedo of old snow
α_{snow}	modelled snow albedo
α_t	albedo of the surrounding terrain
ε_i	emissivity of ice
ε_t	emissivity of surrounding terrain
Γ_{P1}	vertical gradient of RAMS hourly summer precipitation
Γ_{P2}	vertical gradient of RAMS winter snow totals
Γ_t	lapse rate of RAMS hourly summer air temperature
γ	background potential temperature lapse rate
λ	length scale for katabatic wind modeling
μ	momentum scale
Θ	stability correction
θ	surface slope angle
ρ_a	dry air density
ρ_i	density of ice
ρ_s	density of surface layer
ρ_w	density of water
σ	Stefan-Boltzmann constant and standard deviation

Φ	sky view factor
ϕ	slope azimuth angle
ϕ_0	solar azimuth angle
φ	angle between the solar beam and the vector normal to the surface
ψ	atmospheric clear-sky transmissivity

Acknowledgements

First and foremost, this work would not have been possible without the guidance and support of my supervisor, Prof. Peter L. Jackson I want to thank you for providing me the opportunity to work on this project. I also thank my thesis committee, comprised of Dr. Dan Moore, Dr. Brian Menounos, Dr. Roger Wheate, and Dr. Stephen Déry, for their feedback and contribution.

Special thanks go to Bruce Ainslie for sharing his knowledge in numerical programming and helping in the analysis Numerical analysis would not have been possible without your assistance. I am also thankful to Joseph M. Shea for providing glacio-meteorological data from Place Glacier, Christina Tennant for assistance in using the GIS resources and Aseem Sharma for helping prepare a map of the study area. I also thank all my friends at the university and in Prince George who one way or another contributed their assistance.

Funding for this research was provided by Canadian Foundation for Climate and Atmospheric Sciences (CFCAS) grants to Prof. Peter L. Jackson through the Western Canadian Cryospheric Network (WC2N).

Last, but not the least, I owe a great deal of gratitude to my wife Manu, who has provided love and support throughout the years. Without your encouragement and patience, this project would not have been possible.

This thesis is dedicated to the memory of my father, Damodar Aryal, who always offered me encouragement and support in all my endeavors. I also dedicate this thesis to my mother Nirmala Aryal, to my wife Manu and two lovely children, Nittye and Prasidhi who are the pride and joy of my life. Any remaining errors and shortcomings in this thesis are, unfortunately, my own.

Chapter 1

Introduction

Glacier melt provides important sources of water to the rivers for water resources development and ecosystem sustenance However, mountain glaciers worldwide have shown a distinct trend of terminus retreat and mass loss since the end of the Little Ice Age (Dyurgerov and Meier 2005, Kaser et al 2006, Dyurgerov 2010). This retreat is likely caused by climate warming resulting from an increase in atmospheric concentrations of greenhouse gases caused by human activities (IPCC 2013; Marzeion et al. 2014). Continuous deglaciation and associated changes in melt-water supply can directly impact ecosystems (Morrison et al. 2002; Brown et al. 2007; Xu et al. 2009), landscape hazard and water quality (Moore et al. 2009), regional water supplies (Barnett et al. 2005; Kaser et al. 2010), hydroelectric power generation (Immerzeel et al. 2010; Viviroli et al. 2011) and global sea-level rise (Radić and Hock 2011; Gardner et al. 2013). These impacts together can have widespread social, economic and environmental implications. In some areas of the world, diminishing melt-water supply coupled with population growth will likely lead to increasing competition for water resources among the water users. As glaciers recede, melt water discharge increases due partly to earlier exposure of lower-albedo firn or ice and also due to increased energy inputs following climate warming (Braun and Escher-Vetter 1996; Singh and Kumar 1997). However, such an increase in melt water can only be transient. As the glacier continues to shrink in response to warmer climate, the effective melt area will decrease eventually reducing the melt water volume.

1.1 Statement of the Problem

Glacier monitoring is extremely important to understand their response to climate variation of all scales. In British Columbia (BC), Canada, a systematic glacier monitoring program started only during the 1960's at a few selected glaciers (Østrem 1966). Over time, the number of monitored glaciers has declined significantly with only two glaciers currently under mass balance monitoring. As a result, there is difficulty quantifying the spatial and temporal glacier variations in the region. Lack of sufficient glacier mass balance (GMB) records has not only constrained our ability to calibrate hydrologic models in glacierized catchments (Moore et al. 2009), it is also hampering efforts to predict the future state of glaciers and water resources. Although topographic maps, aerial photos and recently satellite imagery have been used for assessing glacier variation in the region (e.g., DeBeer and Sharp 2007; Bolch et al. 2010), these techniques are mainly suitable for estimating changes in glacier extent and the results they provide are less accurate than direct glaciological measurements and are of poor temporal resolution. Satellite-based radar observations have also been used for inferring GMB (Demuth and Pietroniro 1999; Gardner et al. 2011), but this technique is still considered less reliable than direct glaciological measurements. Airborne laser altimetry techniques have been used to estimate changes in glacier elevation for mass balance estimation with remarkable accuracy (Arendt et al. 2008). However, this technique of mass balance estimation is very costly for routine glacier mass balance measurements. With gridded climate data becoming increasingly available, a numerical GMB model, that has been successfully validated, can provide an alternative to both direct and indirect GMB measurements saving a substantial amount of time and resources, and can also be used to fill in gaps in the observational record of monitored glaciers. At the same

time, a numerical GMB model can be used as a tool to assess the potential impact of future climate change on glaciers, and can provide useful scientific information for formulating future water management policies.

1.2 Thesis Objectives

Previously, physically-based glacier melt modelling has been performed on an individual glacier in the southern Coast Mountains using in-situ meteorological observations (e.g., Munro and Marosz-Wantuch 2009, Shea 2010) However, these studies were mainly focused on testing the performance of different melt models at a point scale on the glacier using short-term meteorological data. There is no study in the region that used long-term historical climate data for physically-based mass balance modelling on an individual glacier with the purpose of developing GMB hindcast. Regarding the future GMB projection, there are a few studies that project future mass balance at the regional scale (e.g., Clarke et al. 2015) or at the scale of an individual glaciers (e.g., Shea and Marshall 2007; Matulla et al. 2008; Marshall et al. 2011) in western Canada, but they all used empirical or semi-empirical methods for deriving future mass balance where input variables are either used directly from large-scale climate data or downscaled using a simple statistical approach. The use of physically-based model for future GMB projection is virtually nonexistent in the region.

Here I take the first steps to applying a distributed, physically-based GMB model on one of the glaciers in the southern Coast Mountains of BC using Regional Atmospheric Modeling System (RAMS) mesoscale atmospheric model output (Cotton et al. 2003). RAMS model outputs are available from 1979-2008 (29 years) over the BC southern Coast Mountains including Vancouver Island at a spatial resolution of 8 km (Ainslie and Jackson

2010). In contrast to the method used in the previous studies, the method presented here will employ the surface energy balance approach of GMB modelling where large scale input variables for running the model are downscaled using a SVD (Singular Value Decomposition) technique of statistical downscaling. To the author's knowledge, the SVD technique for climate downscaling in conjunction with a physically-based GMB model has not been used previously in this region for climate impact studies on glaciers. This is a novel aspect of this research. The purpose of this research is outlined below.

1) Develop GMB hindcast for Place Glacier in the southern Coast Mountains of BC using a physically-based distributed GMB model forced with the output from the RAMS mesoscale model.
2) Validate the model results with the historic GMB records and compare the model performance with the results from Temperature Index (TI) and enhanced TI models.
3) Apply the model for developing mass balance projection for Place Glacier using statistically (using SVD technique) downscaled GCM future projection.

1.3 Literature Review

1.3.1 Global glacier changes

The state of a glacier is determined through mass balance measurements. On an annual basis, glacier mass balance is the difference between total accumulation (mass gain) and total ablation (mass loss). Although glacier mass balance can be measured several ways, a direct observation of mass change on the glacier surface is the most widely used method on many glaciers around the world. An extensive literature on mass balance methods can be found in Østrem and Brugman (1991). Glacier mass balance exhibits a distinct year-to-year

variation, which is largely determined by the climate of a particular year. Since glacier mass balance is a sensitive indicator of impacts of climate change on glaciers, it can help infer current climatic change in precipitation and temperature and can also assist in the analysis and modelling of climate change.

Despite its obvious importance, a maximum of only 90 glaciers worldwide have been monitored for mass balance changes in any given year (Dyurgerov 2002) perhaps due to logistical and cost constraints. Mass balance data from different glaciers around the world have been compiled and made available by the World Glacier Monitoring Service (WGMS 2011; http: www.wgms.ch access html) and its cooperative partner, the National Snow and Ice Data Center (NSIDC 2005; http: nsidc.org data nsidc-0272). A large portion of these records extend back only to the mid-20th century, and only a few mass balance data series, mainly from Europe, North America and the territory of the former Soviet Union, cover an entire period since 1960. In many of the more important mountains in the world, such as the Himalayas and Andes, among others, only a few glaciers are being monitored for mass balance measurements, and they are not continuous.

A first detailed assessment of annual glacier mass balance on global and regional scales was provided by Dyurgerov and Meier (1997a,b), and updated by Dyurgerov (2002), Dyurgerov and Meier (2005) and Dyurgerov (2010). Their analysis included all small glaciers of the world: all perennial ice masses other than the Greenland and Antarctic ice sheets, but including glaciers and ice caps that are peripheral to, and independent of, the ice sheets. Their studies categorized individual time series of mass balance records from 300 glaciers worldwide into different climatologically homogeneous samples/systems resulting in 49 mountain and sub-polar systems (primary glacier systems), 12 larger glacier regions, 6

continental-size systems, and 1 global. By extrapolating the time series of mass balance observations of all glaciers to larger areas, they computed regionally-averaged mass balance. Global averages were obtained from area-weighted specific mass balances of smaller subregions whose balances were estimated from the single-glacier observations. Dyurgerov and Meier (2005) provided a first comprehensive analysis of global glacier mass balance records from 1960-2003 Their results suggest that a majority of glaciers in the world are losing mass in the last few decades This work provided a strong platform for a similar study by Kaser et al. (2006), which combined these historical mass balance records with other independent analyses such as Cogley (2005) and Ohmura (2004) to obtain consensus estimates of global mass balance since 1960. For a period covering 1961-2004 and without including peripheral ice bodies in Greenland and Antarctica, their study estimated a global average specific balance of -283±123 mm w.e. a^{-1} (mm water equivalent per year), which is equivalent to 0.43±0.19 mm a^{-1} of sea-level rise. Including smaller peripheral ice bodies surrounding the ice sheets, the mass balance for the same period is estimated to be -231±101 mm w.e. a^{-1}, an equivalent of 0.50±0.22 mm a^{-1} of sea-level rise. Similar other studies using historic mass balance records have concluded that the glaciers in different parts of the world are showing a general tendency of mass loss, but with some regional variability (e.g., Cogley and Adams 1998; Arendt et al. 2002; Ohmura 2004; Cogley 2005).

Dyurgerov (2010), an update of Dyurgerov and Meier (2005), provided the most recent regional and global assessment of glacier mass balance, area changes, and volume changes. This analysis emphasized glacier changes over the 1960/61–2005/06 balance-years period and uses mostly data obtained by the standard glaciological method. The global glacier system considered for analysis included all mountain glaciers and sub polar ice caps

around the world. During this period, global glacier area changed from 779 $\times 10^3$ to 735$\times 10^3$ km^2 (-5.6%), with an annual rate of -0.12% a^{-1}. The average specific mass balance was -301 mm w.e. a^{-1}, which translates to a mass loss of -13 4 m w.e. for 1961-2006. On average, volume change rate was -227 km^3 a^{-1} totaling -10,400 km^3 for 1961-2006. Over this period, glaciers contributed 0.63 mm w e a^{-1} to global sea level rise This study suggested that the rate of mass loss (-473 mm w.e. a^{-1}) and volume loss (-466 km^3 a^{-1}) and sea level rise (0.97 mm w.e. a^{-1}) were particularly large for the period 1993-2006 The years 1997 and 1998 have the most negative mass balance and the greatest ice mass loss from all glaciers and icecaps considered for analysis. These results are summarized in Figure 1.1.

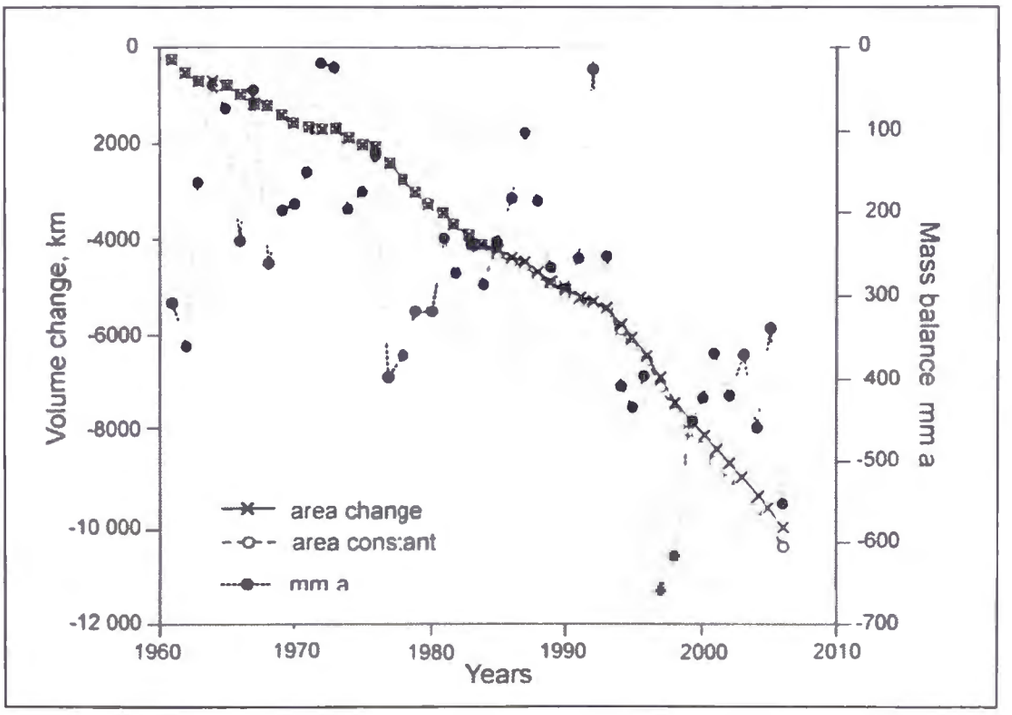

Figure 1.1 Specific glacier mass balance change from 1961 to 2006 weighted by the area of all individual glaciers (about 340 glaciers where mass balance observations were conducted) and weighted by regions/systems area (specific, mm a^{-1} water equivalent, right hand axis). Left hand axis shows globally averaged glacier volume change calculated for the area constant in time (reference area balances), and for actual glacier areas changing from year to year (conventional balances) (Dyurgerov 2010)

From 1961-2006, the assessment of glacier mass balance, area, and volume at a regional scale revealed a similar picture. Results of the analysis for major glacier systems are presented in Table 1.1.

Table 1.1 Specific mass balance, area loss, volume loss, and contribution to global sea level rise from different glacier systems around the world Values are average over the period 1961-2006. Values in the parenthesis refer to the averages for the period 1993-2006. Volume loss is based on changing glacier area Source: Dyurgerov (2010)

Glacier system	Mass balance (mm w e a^{-1})	Area change (% a^{-1})	Volume change (km^3 a^{-1})	Sea level rise (mm a^{-1})
Alaska	-764 (-1293)	-0 06	-55.4 (-93.1)	0.15 (0.26)
Conterminous North America	-582 (-900)	-0.12	-27.5 (-42)	0.076 (0.12)
Arctic	-139 (-234)	-0.08	-40 (-66)	0.11 (0.18)
Canadian Arctic Archipelagos	-102 (-202)	-0.06	-15 (-29.5)	0.042 (0.08)
Russian Arctic Archipelagos	-92 (-185)	-0.03	-5.13 (-10.2)	0.002 (0.004)
Svalbard	-372 (-440)	-0.22	-14 (-15)	0.037 (0.042)
Continental Europe	-103 (-340)	-0.21	-0.57 (-1.88)	0.0015
Circumpolar Continental Arctic	-289 (-698)	-0.12	-0.30 (-0.71)	0.008 (0.038)
Glaciers and ice caps in the periphery of Antarctic Ice Sheet	-198 (-248)	-0.07	-35.8 (-44.4)	0.101
Siberia and Far East	-135 (-191)	-0.22	-0.46 (-0.63)	0.0012
High Mountains of Asia	-404 (-569)	-0.32	-47.2 (-63.5)	0.13 (0.18)
Tropics, 23.45°N -23.45°S	-382 (-813)	-0.98	-0.92 (-1.7)	0.003
South American Cordillera, 23.45°- 45°S	-163 (-807)	-0.48	-0.39 (-1.8)	0.001
Patagonia Ice Fields and Tierra del Fuego	-874 (-1522)	0*	-17 (-30)**	0.048 (0.084)
Southern Alps in New Zealand	+198 (-440)	+0.20	+0.34 (-15)	-0.001 (0.042)

* no area change has been estimated yet, thus area has been taken constant at 19,900 km^2

** Based on constant glacier area of 19,900 km^2

Recently, as an alternative to direct mass balance measurement, the geodetic method has been widely used for monitoring mass budget of many glaciers around the world (Berthier et al. 2010; Gardner et al. 2011; Jacob et al. 2012; Gardner et al. 2013). Jacob et al. (2012) using Gravity Recovery and Climate Experiment (GRACE) satellite gravimetry from 2003 to 2010 suggested that global glacier mass loss is much less than previously thought. Gardner et al. (2013) invesigated these discrepencies by recalculating existing results from glaciological extrapolation and GRACE to a common spatial and temporal refernce and comparing the results with independent altimetric estimates from the Ice, Cloud, and Land Elevation Satellite (ICESat). Their results from different regions suggest that the local measurements are more negative than the satellite-based estimates. From 2003-2009, all regions lost mass; but the mass loss was particularly large for Arctic Canada, Alaska, coastal Greenland, the southern Andes, and high-mountain Asia. However, there was little loss from glaciers in Antarctica. Over this period, the global glacier mass budget, with Greenland and Antarctica combined, was -350 ±40 mm w.e. a^{-1}, which accounts for 29±13% of the observed sea level rise. Excluding Greenland and Antarctica, the global glacier mass budget was -420±50 mm w.e. a^{-1}. Results from this study suggests that overestimation of mass loss in the previous studies may be because of interpolation of sparse glaciological measurements that are not representative for the largest glacierized regions.

Berthier et al. (2010) used satellite imagery to estimate ice losses and sea level rise from glaciers in Alaska and northwest Canada between 1962 and 2006. Over this period, glaciers in this region have lost 41.9±8.6 km^3 a^{-1} of water, and contributed 0.12±0.02 mm a^{-1} to sea-level rise. Gardner et al. (2011) used three independent approaches: surface mass-budget modelling plus an estimate of ice discharge, altimetric analysis from ICESat, and

gravimetry analysis from GRACE to estimate mass loss of glaciers and ice caps in the Canadian Arctic Archipelago. Their results suggest that from 2004 to 2009, the Canadian Arctic Archipelago has lost 61±7 gigatonnes per year (Gt yr^{-1}) of ice, contributing 0.17 ±0.02 mm a^{-1} to sea-level rise. From 2003-2009, a similar study by Gardner et al. (2013) reported mass-budget for glaciers in western Canada and United States of -930±230 mm w.e. a^{-1}.

Next, the results of glacier fluctuation studies for conterminous North America, with a particular emphasis on glaciers in western Canada, are discussed in more detail.

1.3.2 Glacier Changes in Conterminous North America

Glaciers in the conterminous North America are mainly located in the Rocky Mountains and Interior Ranges, and along the Pacific Coast Ranges. Historic mass balance records exist for a relatively large number of glaciers in this region, but the network is still considered too sparse to represent the vast glacier covered area. Glaciers with long-term mass balance records include Peyto Glacier in the Canadian Rockies, Place Glacier in the southern Coast Mountains, South Cascade Glacier in the Cascade Mountains, and Blue Glacier in the Olympic Mountains. Mountain glaciers along the Pacific Coast Ranges have exhibited a consistently negative mass balance in the last several decades. With glacier mass balance records extending back to the past 50 years, South Cascade Glacier in Washington's North Cascade Mountains, has been in general retreat since the 19th century, and has lost more than 50% of its volume during that time (Krimmel 1999). Out of 50 years of mass balance records, more than half of the observations have negative net mass balances. This glacier has lost nearly 31 m w. e. of ice thickness during a period between 1953 and 2005 (WGMS/UNEP 2008). Most of the other glaciers in the North Cascade Mountains showed a

strong negative mass balance from 1984-1994 and a slight positive value from 1995-2000 (Pelto and Riedel 2001). Mass balance records from different glaciers in the North Cascades have suggested that regional climate patterns, not the microclimates, are the primary control of glacier annual mass balance. Mass balance of South Cascade Glacier has generally been more negative than the other glaciers in the region. Blue Glacier, a small mountain glacier in the Olympic Mountains of the Pacific Coast Range, generally had a positive mass balance until the mid-1970s and a negative mass balance ever since. From 1956-2005, the glacier lost nearly 7 m w. e. of ice thickness (WGMS UNEP 2008)

Glaciers in western Canada are mainly concentrated along the Pacific Coast and in the Rocky Mountains, which together contain nearly 30,000 km^2 of glacierized terrain (in the 1980s). This extent represents about 4% and 23% of the global and North American non-polar ice coverage, respectively (USGS 2002; Schiefer et al. 2007).

Place Glacier, on the lee-side of the southern Coast Mountains, has been experiencing a negative net mass balance since mass balance measurements started in 1965 (Moore and Demuth 2001). Between 1965 and 2005, the glacier lost a total of 34.6 m w. e. of ice thickness and its area decreased from 3.98 km^2 to 3.17 km^2 (WGMS/UNEP 2008). For a glacier with small accumulation area (little more than a third of the glacier area), this rate of mass loss is quite significant. A similar mass balance trend is seen for other glaciers in the Coast Mountains such as Bridge, Sentinel, Bench, Helm, and Tiedemann. With the current rate of mass loss, smaller glaciers such as Place and Helm are likely to disappear in the next few decades.

Similarly, Peyto Glacier, a continental glacier in the Canadian Rockies, lost a total of 21.6 m w. e. of ice between 1966 and 2005 (WGMS/UNEP 2008). During this period net

mass balance was negative for most of the years. As with the net mass balance trend for Place Glacier, mass loss for Peyto Glacier accelerated after 1976, which is also linked to the changes occurring in the adjacent Pacific Ocean via the Pacific Decadal Oscillation (PDO; Luckman 1998; Watson et al. 2006; Demuth and Keller 2006)

Because a large number of mountain glaciers in western Canada remain unmonitored, there is a difficulty assessing the overall health of glaciers in the region. Previously, remote sensing techniques have been employed to better understand the state of glaciers in western Canada (Schiefer et al. 2007, DeBeer and Sharp 2007, Koch et al. 2009; Bolch et al. 2010). Based on analysis of historic satellite imagery and aerial photographs, DeBeer and Sharp (2007) estimated changes in glacier area in the Coast Mountains, the Columbia Mountains and the Rocky Mountains of western Canada. Between 1964/65 and 2002, glacier area in the Coast Mountains decreased by 120±10 km^2 (5% of the initial ice-covered area). Similarly, from 1951 52-2001, glaciers in the Columbia and Rocky Mountains lost a total area of 20 and 6 km^2 respectively, accounting for 5 and 15% loss in initial area. Further, they estimated a total ice volume loss of 13±3 km^3 for the whole region. Koch et al. (2009) utilized a variety of remotely sensed data to determine change in length, area, and volume of glaciers in Garibaldi Provincial Park, southern Coast Mountains, BC. Their results suggest that the region has lost 49% of the early 18^{th} century ice cover area by 2005. They found that many glaciers in the region advanced between the 1960s and 1970s, but all glaciers retreated over the last 20 years. Bolch et al. (2010) developed a detailed glacier inventory using 2005 satellite imagery for British Columbia (BC) and Alberta (AB), and compared their results to 1985 extents obtained from aerial photography. They estimated an area loss for glaciers in BC and AB of 10.8±3.8% and 25.4±4.1% respectively

over the period 1985-2005. Further, they estimated a region-wide annual glacier shrinkage rate of 0.55% a^{-1}, which is comparable to rates reported for other mountain ranges in the late 20th century. Results from satellite-based glacier studies are consistent with the direct glacier mass balance records for the region, which showed a general trend of mass loss in the past few decades (WGMS/UNEP 2008).

Dyurgerov (2010) used all available mass balance records from this region to make a regional assessment of glacier mass balance from 1961-2006 (Figure 1.2). During this period, conterminous North America (excluding Alaska, Canadian Arctic Archipelagos, and Mexico) experienced an area loss of -5.7%, with an annual rate of -0.12% a^{1}. The average specific mass balance was -582 mm w.e. a^{1}, with a cumulative balance of -26.8 m w.e. Similarly average volume change rate during this period was -27.5 km^3 a^{1} totaling -1267 km^3 for 1961-2006. Over this period, glaciers in this region contributed on average 0.076 mm a^{-1} to global sea level rise. For the shorter time period of 1993-2006, the average specific mass balance was -900 mm w.e. a^{-1} whereas the volume change rate was -42 km^3 a^{-1}. During this period, glaciers contributed 0.12 mm a^{-1} on average to global sea level rise. Similarly, in western Canada, glacier area changed at the rate of -0.15% a^{-1} from 1961-2006. During this period, the average specific mass balance was -585 mm w.e. a^{-1}, which equates to a cumulative mass change of -26.9 m w.e. For the same period, glaciers experienced a volume change of -26.3 km^3 a^{-1} totaling -1260 km^3. The rate of mass change and volume change showed higher negative values for the period 1993-2006, which were -903 mm w.e. a^{-1} and -44 km^3 a^{-1}, respectively.

Although mass balance variability of some glaciers in North America has been linked to the natural climate variability in the Pacific Ocean (Mantua et al. 1997; Bitz and

Battisti 1999; Moore and Demuth 2001), part of this variability may have been caused by human-induced climate warming (IPCC 2013; Marzeion et al. 2014), which is often difficult to separate from large scale natural climate variability

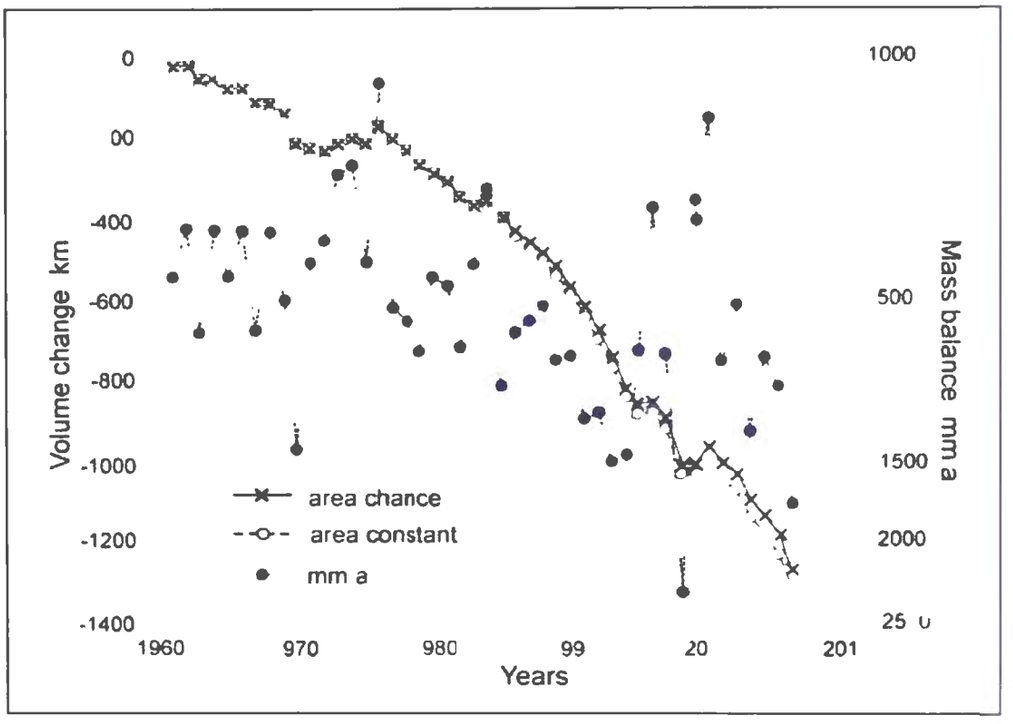

Figure 1.2 Conterminous North America region (excluding Alaska, Canadian Arctic Archipelagos, and Mexico) glacier mass balance change from 1961 until 2006 weighted by the area of all individual glaciers (specific, mm a^{-1}, right hand axis). Left hand axis shows regionally averaged glacier volume change for the constant and changing in time glacier areas, starting from 1961 (Dyurgerov 2010).

Glacier recession in BC, Canada, is associated with unusually warm air temperature and a reduction in winter snowfall since 1976 (Moore and Demuth 2001). Average annual temperature warmed by 0.6°C on the coast, 1.1°C in the interior and 1.7°C in northern BC over a period of 1895 to 1995 (BC Ministry of Water, Land and Air Protection 2002). Major rivers in the province have their headwaters in the high mountain environments. Glacier

melt provides important sources of water to these rivers for hydropower generation, agricultural, domestic and industrial uses. Although only a small percentage of the total annual runoff of these rivers comes from glacial melt, their contribution is particularly important during the summer season to maintain low flows when snowpack contribution has already diminished and rainfall is minimal (Fountain and Tangborn 1985; Hopkinson and Young 1998). Fleming and Clarke (2003) found an increasing streamflow trend in some of the glacier-fed rivers in south-western Yukon and north-western British Columbia, Canada. Long term late summer streamflow records downstream of Place Glacier suggest a negative trend in total runoff, which is attributed to a reduction in the glacier ice-covered area available for melt (Moore and Demuth 2001) Stahl and Moore (2006) went further to suggest that most glaciers in BC may already have passed the phase of increased melt runoff due to climate change. Moreover, the negative trend in streamflow discharge for some rivers in south-central BC is accompanied by a shift in the timing of low flows indicating an earlier onset of snow and glacier melt than usual (Leith and Whitefield 1998). This will potentially limit the supply of freshwater in the rivers during the dry summer season when water demand is highest. Because glacier melt water helps regulate water temperature downstream (Brown et al. 2005; Moore 2006), a decrease in melt water flux in the rivers may lead to a decline in temperature-sensitive aquatic species such as salmonids (Morrison et al. 2002). Understanding the potential impact of climate change on glaciers is one of the key issues in many glacierized regions of the world. This knowledge is crucial for formulating future water management policies in response to potential threat to freshwater availability and associated impacts on ecosystem and water resources development.

1.3.3 Glacier Mass Balance Modelling

The choice of a GMB model for regional scale glacier studies largely depends upon three factors: (a) transferability, (b) input data requirement, and (c) complexities. With increasing availability of reanalysis and mesoscale climate data together with ever-increasing computational power, (b) and (c) should no longer be a limiting factor for distributed GMB modelling at a regional scale. Ablation is one of the important components in any GMB model. Numerous melt models exist for resolving ablation within a GMB model, with varying degree of complexity Empirical temperature-index or degree-day models (hereafter TI model) (e.g., Braithwaite 1995; Hock 2003) may be preferred over surface energy balance (SEB) models mainly because of their low data requirements Although TI models are the simplest approach of GMB modelling, they are not physically-based, but rather are empirical and must have parameters calibrated using local data. Non-stationarity of model parameters in space (i.e. to glaciers other than those for which the TI model was calibrated) and time (i.e. to assess the impact of future climate on glacier mass balance) poses a serious problem for their transferability. The strong relationship between maximum air temperature and clear sky conditions during summer provided a further means to parameterize melt by combining air temperature and solar radiation together. This relationship has been utilized to develop a melt model also known as Enhanced TI models (e.g., Hock 1999; Pellicciotti et al. 2005). These models offer a better alternative to TI models as their coefficients are fairly stable between glaciers within the same mountain ranges (Carenzo et al. 2009; Wheler and Flowers 2011), but they still require local optimization when applied to glaciers in different climatic conditions (Pellicciotti et al. 2005). Empirical melt models applied at the regional scale assume that the model parameters are transferable in space and time, which is not

always true (Hock 2005; Hock et al. 2007). Sicart et al. (2008) investigated the physical basis of TI models for three glaciers in contrasting climates: Zongo in the Bolivian Tropics, St. Sorlin in the French Alps, and Storglaciären in northern Sweden. By assessing the relative contribution of each energy balance flux to the correlations between temperature and melt energy, they concluded that the relationship between air temperature and energy fluxes is highly variable from one region to another. At Zongo, net shortwave radiation controls the variability of the energy balance and is poorly correlated to temperature. At St. Sorlin, temperature correlates well with melt energy mainly through shortwave radiation. At Storglaciären, high correlations between temperature and melt energy is primarily through the sensible and latent heat fluxes. Comparison of TI melt models with physically-based melt models suggest that the TI model usually underestimates melt on the glacier surface (e.g., Hock et al. 2007; Shea 2010). In one study, an Enhanced TI melt model has been shown to yield results comparable with the results from physically-based model (Pellicciotti et al. 2008), Despite this, TI melt models have been widely used for glacier melt modelling and for estimating ablation in GMB modelling in many parts of the world (e.g., Radić and Hock 2006; Zhang et al. 2007a; Huss et al. 2008; Radić et al. 2013; Farinotti et al. 2012; Clarke et al. 2015).

At the other end of the spectrum are the GMB models based on the SEB approach. These models have been applied on glaciers in different parts of the world (Kayastha et al. 1999; Mölg and Hardy 2004; Dadic et al. 2008; Anslow et al. 2008; Mölg and Kaser 2011). In these models, ablation is calculated using a process-based approach involving surface energy fluxes. Because these models are generally transferrable in space and time (MacDougall and Flowers 2011), they can be applied to any location without need of site-

specific calibration. To better resolve spatial variation of melt on a glacier surface, distributed SEB melt models are widely used (Arnold et al. 1996; Hock and Holmgren 2005). In distributed SEB models, input variables are either extrapolated or parameterized onto the individual model grids and melt energy is calculated for each grid cell.

SEB-based GMB models have been used for climate change impact studies at the scale of individual glaciers and utilizing nearby meteorological observations (Oerlemans 1992; Klok and Oerlemans 2004) Recently, a simplified formulation of an SEB-based melt model has also been used for future runoff projections from glacierized basins in the Alps (Huss et al. 2014). However, application of SEB-based models for climate change impact studies on glaciers at a regional scale is limited (Box et al 2004; Bougamont et al. 2005; Fujita and Nuimura 2011). This is mainly due to the lack of a regional network of meteorological stations in glacierized areas. As a result, most of the studies have opted to use simple TI models for large-scale climate change impact investigation on glaciers despite the uncertainty in their transferability under different climate conditions in the future (Braithwaite and Zhang 1999; Radić and Hock 2006; Raper and Braithwaite 2006; Zhang et al. 2007a). Hock et al. (2007) investigated how mass-balance projections and sensitivities vary when using GMB models of varying complexities to compute glacier mass balance. Their finding suggests that the glacier mass loss in future glacier predictions may be under-predicted when TI or highly simplified SEB models are used instead of detailed SEB models that account for the feedback of temperature changes on each individual energy balance components separately. In the last few years, climate reanalysis products and mesoscale climate models (commonly known as Regional Climate Models, RCMs) data have offered an attractive alternative to meteorological observation for driving process-based GMB

models and melt models, both at the scale of individual glaciers and at the regional scale (e.g., Box et al. 2004; Bougamont et al. 2005, 2007; Paul and Kotlarski 2010; Ainslie and Jackson 2010; Mölg and Kaser 2011; Tennant et al. 2012; Huss et al. 2014). For the first time, Gerbaux et al. (2005) used synthetic data from the SAFRAN meteorological model to drive a physically-based distributed model on glaciers in the French Alps. The application of RCMs for cryospheric research is fairly well advanced for ice sheets. Cassano et al. (2001) and Bromwich et al. (2005) tested the performance of an RCM, which is modified for use in polar regions, over Greenland. Fettweis et al (2005) tested a coupled RCM-snow model (Modèle Atmosphérique Régional, MAR) using a detailed set of observations in western Greenland. Box and Rinke (2003) used the HIRHAM RCM, a combination of HIRLAM and ECHAM4, as a tool to evaluate simulations of historic meteorological and mass balance components over Greenland. Box et al. (2004) employed a polar version of the MM5 RCM (Polar MM5) over the Greenland Ice Sheet at 24-km spatial resolution for evaluating spatial and temporal variability of the surface mass balance and its subcomponents. The modelled accumulation and ablation rate agreed closely with the observations at the same time capturing most of the spatial and temporal variability in mass balance components fairly well. Paul and Kotlarski (2010) successfully used RCM output to run a distributed GMB model on two glaciers in the Swiss Alps. The modelled mass balance results closely agreed with the measured values while capturing differences in specific mass balance between the two glaciers and the two balance years. They further suggested that the coarse-resolution RCM can be coupled with a high resolution GMB model and applied to other regions. The spatial resolution of most RCMs is still considered too coarse to accurately represent sub-grid scale processes occurring on mountain glaciers residing in complex terrain. To address

this issue, Mölg and Kaser (2011) went further and employed the Weather Research and Forecast (WRF) model as a limited area model (LAM) at a horizontal resolution of 812 m for generating fine scale climate inputs for process-based mass balance modelling on Kersten Glacier in Mt. Kilimanjaro, East Africa Their modelling approach took into account mesoscale processes of mountain-induced atmospheric flow The mass and energy fluxes simulated using the LAM outputs were in close agreement with the fluxes calculated using on-site meteorological data. This clearly demonstrated the potential use of a LAM as a tool to downscale large-scale climate data to high-altitude meteorological conditions over a glacier and use them in forcing a process-based mass balance model. However, there are some disadvantages to this approach of GMB modelling. Modelling atmospheric processes at the scale of a glacier in complex terrain is numerically difficult and the approach is computationally intensive when used for large temporal (decade or century) and spatial (regional) scale glacier modelling.

1.3.4 Climate Downscaling

Global Climate Model (GCM) results are usually considered not optimal to be directly applied for many regional climate impact studies. GCM outputs are available at a typical grid resolution of 2°-3° latitude and longitude. At that scale, the model is unable to resolve the local sub-grid scale features and dynamics, which are essential for many regional climate impact studies. For example, GCMs cannot resolve the local topography and as a result their influence on precipitation is largely ignored. GCM projections therefore have to be spatially downscaled to the scale relevant to impact studies. Downscaling GCM climate projections has been a major challenge confronting numerical climate impact modelling.

Dynamical and statistical downscaling are two techniques widely used for downscaling coarse resolution climate fields to a particular location for impact modelling. Dynamical downscaling involves the use of mesoscale climate models driven by boundary conditions from large-scale climate fields, such as GCMs or reanalysis output, to derive small-scale information. This technique provides a dynamically consistent three-dimensional gridded dataset that represents the best estimates of the state of the atmosphere at a certain time, but they are not necessarily more accurate compared with statistical downscaling. Dynamical downscaling requires large amounts of input data and is computationally intense. As a result, the cost involved in dynamical downscaling is far higher than statistical downscaling.

On the other hand, statistical downscaling involves developing a statistical relationship linking large-scale climate variables (predictors, e.g., GCM variables) to regional or local variables (predictands, e.g., station observations). Statistical downscaling techniques range from a simple 'perturbation method' (e.g., Prudhomme et al. 2002) or 'delta change' approaches to more sophisticated regression methods (e.g., Giorgi and Hewitson 2001; Hellström et al. 2001; Hanssen-Bauer et. al 2003; Widmann et al. 2003; Huth 1999); weather typing schemes (e.g., Conway et al. 1996; Fowler et al. 2000, 2005) and weather generators (e.g., Wilks 1992; Mason 2004). There are different methods used in each group but all of them are based on the concept that regional climates are largely conditioned by the large-scale atmospheric state. There are several variants of regression methods such as the simple 'transfer function' approach that directly quantifies a relationship between the predictands and a set of predictor variables (e.g., Giorgi and Hewitson 2001) and more sophisticated methods such as artificial neural networks (ANNs)

(e.g., Zorita and von Storch 1999), canonical correlation analysis (CCA) (e.g., Bürger 1996; Huth 1999) and singular value decomposition (SVD) (e.g., Huth 1999; Widmann et al. 2003). Previously, regression methods have been used for climate downscaling in different parts of the world, but their application is mainly limited to downscaling temperature and precipitation (Huth 1999; Murphy 2000, Huth 2002; Widmann et al 2003; Kostopoulou et al. 2007). The latter study compared three statistical downscaling methods: multiple regression, CCA and ANNs, when simulating minimum and maximum temperatures over Greece using the 1000–500 hPa field as the unique predictor. Maximum temperatures were found to be better simulated than minimum temperatures and the regression methods were found to be more appropriate than the ANNs, particularly for summer. This work concluded that there is no unique solution to the downscaling issue, since different methods can offer both benefits and drawbacks.

The robustness of the results obtained from statistical downscaling depends on three factors: i) accuracy of the large-scale model in simulating the predictor variables; ii) the quality and the length of the data series used for model calibration (Wilby and Wigley 1997); and iii) the performance of the regression models in capturing the variability of the observed data (Barrow et al. 1996). The model skill largely depends upon the choice of large-scale predictor variables. Predictor variables for downscaling can be circulation based, such as large-scale sea-level pressure and geopotential heights, but can also include surface humidity, precipitation and temperature from large-scale models such as GCMs or reanalysis output. There are some key assumptions in statistical downscaling. Firstly, predictor variables are realistically simulated and are able to resolve the processes responsible for climate variability on a range of timescales. Secondly, the statistical models

are stationary in time; in other words they are valid under future climate as well. Despite the fact that the statistical relationship developed for the present day climate may not be valid for future climates, statistical downscaling techniques are still widely used mainly due to their modest data requirements and computational ease.

The statistical method of climate data downscaling has been widely used for downscaling large-scale climate variables for climate change impact studies on glaciers (e.g., Radić and Hock 2006; Raper and Braithwaite 2006; Zhang et al. 2007b; Radić et al. 2013) and hydrologic systems (e g., Prudhomme et al 2002; Salathé 2005). A few studies have even employed this technique to examine the relationship between large scale circulation fields and local glacier mass balance components for direct downscaling of future climate projections (Shea and Marshall 2007, Matulla et al. 2008; Springer et al. 2012). The popularity of statistical downscaling techniques is mainly due to their modest data requirement and computational ease. Despite this, there always remains an uncertainty whether the statistical relationships developed for the present day climate will remain valid for future climates as well. However, most of the climate impact studies on glaciers (e.g., Radić and Hock 2006; Radić et al. 2013) have used a simple statistical method for downscaling climate data, referred to as 'local scaling' (Widmann et al. 2003; Salathé 2005). For precipitation, the local scaling method simply multiplies the large-scale simulated precipitation at each local grid point by a seasonal scale factor. For temperature, the local scaling method simply applies a lapse rate correction due to elevation difference of the local grid point relative to the climate model grid. Widmann et al. (2003) suggested that the local scaling method has relatively lower skill than the SVD method for downscaling precipitation in the rain shadow of the Cascade Mountains. However, it is not possible to compare the

performance skill of the local scaling method and SVD method for air temperature downscaling due to the lack of similar study in the region.

Widmann et al. (2003) argued that the use of GCM precipitation as a predictor variable for small scale precipitation is not desirable as GCM-simulated precipitation can deviate substantially from observations, especially in complex terrain. Also, their use as a predictor for small scale precipitation was avoided earlier partly because of model fitting issues and partly because of the poor reputation of GCM precipitation (Widmann et al. 2003). Large-scale reanalysis products such as from NCEP/NCAR (National Centers for Environmental Prediction/National Center for Atmospheric Research) and ERA (European Centre for Medium-Range Weather Forecasting re-analysis), are usually considered a better choice for obtained predictor variables for climate downscaling. In the Pacific Northwest region of North America, a good agreement was found between NCEP/NCAR precipitation and observed precipitation interpolated to the NCEP/NCAR domain (e.g., Widmann and Bretherton 2000). Similar results were found elsewhere in the world (e.g., Mo and Higgins 1996; Janowiak et al. 1998). This is mainly because large-scale atmospheric states of variables such as pressure, temperature, and humidity in reanalysis output are in excellent agreement with observations, particularly in areas with a dense observational network. Furthermore, reanalyzed precipitation is derived purely from the model, without assimilation of precipitation observations (Widmann et al. 2003). The same study argued that the reanalysis can be considered as an ideal GCM, in which the time varying, synoptic-scale circulation is accurately represented. Therefore, for precipitation downscaling, large-scale reanalyzed precipitation can be a better predictor than any circulation or moisture based predictors or their combination (Widmann et al. 2003), at least for the historical period in

which reanalysis data are available. Similarly, for temperature downscaling, 500 hPa heights and 850 hPa temperature (e.g., Huth 1999) and 850 hPa temperature and 1000-500 hPa thickness (e.g., Huth 2002) have been suggested as predictors.

1.4 Thesis Outline

Chapter 2 of this thesis starts with the description of the study area and climate setting in the study domain. This chapter provides a review of the past studies on the study glacier and details the method used in measuring mass balance on this glacier.

Chapter 3 details the meteorological and geospatial data used in this research.

Chapter 4 provides a brief description of the RAMS model setup together with a detailed description of RAMS variables. This chapter details the method used in the bias correction of air temperature and reviews the work on bias correction of precipitation by Ainslie and Jackson (2010). This chapter also describes the methods used in determining the vertical gradient of air temperature and precipitation to be used for distributing these variables on the glacier surface for GMB modelling.

Chapter 5 provides a detailed description of the SEB approach and various parameterization schemes and physical equations used in the GMB model. This chapter examines the performance of the physically-based GMB model in reconstructing the historic mass balance for Place Glacier using RAMS variables. This chapter further investigates the performance of the physically-based GMB model against the performance of the less complex TI and enhanced TI based GMB models in simulating the historic mass balance for the same glacier.

Chapter 6 considers statistical downscaling of future climate projections to a finer scale. The Singular Value Decomposition (SVD) technique for large scale climate downscaling is described and implemented for downscaling ensemble GCM future projections from different GCMs.

Chapter 7 implements the SEB-based GMB model (discussed in Chapter 5) for Place Glacier in the future (2009-2040) using the downscaled GCM projections. The research performed in this chapter finally results in an ensemble projection of GMB for Place Glacier over 2009-2040.

The final chapter (Chapter 8) provides a summary of the key findings of this research. Limitations of the present research and potential areas of future research are also recommended in this chapter.

Together, this research represents an important contribution towards understanding the impact of past and future climate variation on glaciers in the southern Coast Mountains of BC. Given the significance of snow and glaciers in water resources development in the region, such information can be very important in formulating future water management policies and adaptation strategies in the region. At the same time, the GMB model developed for climate impact studies on Place Glacier can be used to obtain snow and glacier melt input for hydrologic model for operational forecasting of streamflow from alpine catchments.

Chapter 2

Study Area and Previous Studies

2.1 Introduction

The southern Coast Mountains of BC is a part of the Coast Mountains Range in northwestern North America. As of 2005, this region contained 2962 glaciers (Bolch et al. 2010). GMB observations in the southern Coast Mountains started in 1965 with Place and Sentinel glaciers as part of the International Hydrological Decade (Østrem 1966) and extended to Helm, Bridge, Bench and Tiedemann glaciers in the following years. Currently, routine monitoring is limited to only Place and Sentinel glaciers This chapter describes the location of Place Glacier and details historical mass balance and meteorological data from this glacier. A brief review of the past studies conducted on this glacier is also provided.

2.2 Study Area

Place Glacier (50°26'N, 122°36'W) is situated in the southern Coast Mountains of BC about 80 km north of Vancouver (Figure 2.2). The glacier had an area of 3.98 km^2 in 1965, when mass balance measurements first started. The glacier area decreased to 3.76 km^2 in 1981 and in 2005 it had an area of about 3.17 km^2 (WGMS 2011). For the same year, the highest and lowest elevations of this north facing glacier are ~2600 and ~1800 m above sea level (m a.s.l.), respectively. The accumulation area is little more than one third of the total glacier area, which is fairly small compared to other glaciers studied in this area (Munro and Marosz-Wantuch 2009).

Due to their proximity to the Pacific Ocean, glaciers in the southern Coast Mountains receive significant amounts of winter accumulation arising from synoptic-scale mid-latitude cyclones; this precipitation is enhanced by orographic forcing from the coastal mountain range. Winter snowpack is usually thick enough to delay the exposure of glacier ice well into the summer ablation season thus inhibiting the melt process in the ablation area. In summer, the area is usually dominated by anticyclonic systems resulting in warm and dry weather when a majority of snow and glacier melting takes place. Precipitation during the summer season is mainly convective and constitutes only a small portion of the total annual precipitation. The Coast Mountains act as a barrier to the eastward movement of moist Pacific air masses, creating a strong west–east environmental gradient across the range. Consequently, the amount of precipitation on glaciers is highest along the coast and decreases towards the interior (Hare and Hay 1974).

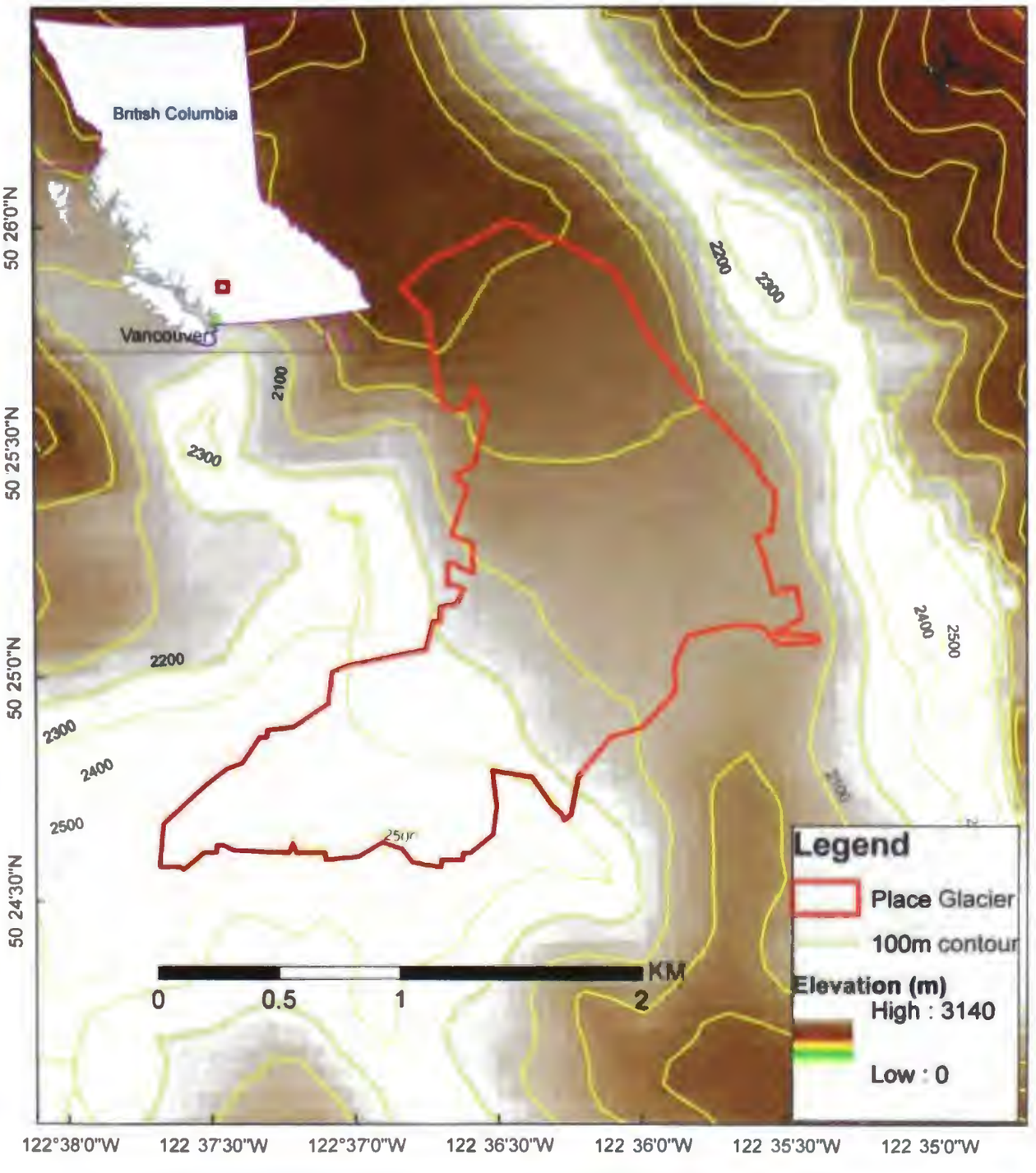

Figure 2.1 Map of Place Glacier and surrounding topography. Inset shows Place Glacier study area relative to the Province of British Columbia.

2.3 Mass Balance Measurements

Mass balance refers to a change in the mass of all or part of a glacier over some specified time period. Most mass balance studies consider changes over one year. When reporting annual or seasonal mass balances it is essential to provide information about the time system the measurement refers to. This is also important to be able to compare observations with model results. Four definitions of time system are in common use: balance year (stratigraphic) system, fixed-date (calendar date) system, floating date system, and combined system. The balance year is defined as the interval between one annual minimum of the glacier mass to the next, which, in mid and high latitudes, occurs in autumn after the end of the ablation season but before the first significant snowfall of winter. The end of this period provides a convenient end point for the balance year. This time system of mass balance measurement is also known as the stratigraphic system because in the accumulation areas annual mass balance is determined by the detection of two successive summer surfaces (annual minima) based on the stratigraphy of the snow. However, it is often difficult to be certain that a glacier has reached a minimum annual mass, especially on large glaciers where not all parts of glacier reach a minimum at the same time. The fixed-date or calendar date system, in the mid and high latitudes, is defined as the period between 1 October and 30 September, also known as hydrological (water) year. The fixed date system does not require any attention to the stratigraphy of the snow and relies only on the mass change between pre-defined dates. In practice, however, weather conditions and other factors often interfere with collecting data at fixed dates. In a floating-date system, the mass-balance year is defined by the calendar dates of the two successive surveys, which may vary from year to year and may or may not be 365 (or 366) days apart. Given the inherent problems in all three

time-systems, most glacier mass balance programs use a combination of two time-systems, usually stratigraphic time-system with either the fixed-date system or floating-date system. This time system of mass balance measurement is known as a combined system. In mid-latitudes, a seasonal time resolution of mass balance measurements corresponding to summer and winter is preferred because ablation and accumulation processes dominate in each season, respectively.

On an annual basis, net glacier mass balance (b_n) is the algebraic sum of winter balance (b_w) and summer balance (b_s) where the latter is usually negative. For a particular location on the glacier, these mass balance terms are known as specific mass balances and are reported in meters of water equivalent (m w e). Winter balance is the difference between the amount of snow that has accumulated on the glacier and the amount that is removed from the glacier surface during winter season. Surface accumulation processes include snowfall, wind drift, avalanches, deposition, and condensation. Similarly, summer balance is the difference between summer accumulation and summer ablation on the glacier surface. In the mid-latitudes, summer is usually dry and therefore the amount of snow falling on a glacier is usually small. As a result, summer balance is mainly due to ablation and is usually negative. Ablation includes melting, snow drift, calving, and sublimation.

The National Glaciology Program of the Geological Survey of Canada has been conducting a routine mass balance monitoring on Place Glacier since 1965 (Moore and Demuth 2001). Mass balance is computed using the standard glaciological method (Østrem and Brugman 1991). This method uses measurements of surface elevation change at a network of stakes, combined with end-of-winter measurements of snow depth along transects and snow density at pits. A network of ablation stakes and snowpits used for Place

Glacier mass balance measurement for 1989 is shown in Figure 2.2. The sampling network involves a primary longitudinal transect of measurement sites along the glacier's centre-line following the glacier's main direction of flow, supplemented by a number of transverse transects designed to characterize lateral variation. Along these transects, measurements are taken at the interval of 100 m Each elevation band usually contains at least one measurement point. If an elevation band does not contain measurement sites, summer and winter balances are obtained by linear interpolation of measurements from neighbouring elevation bands.

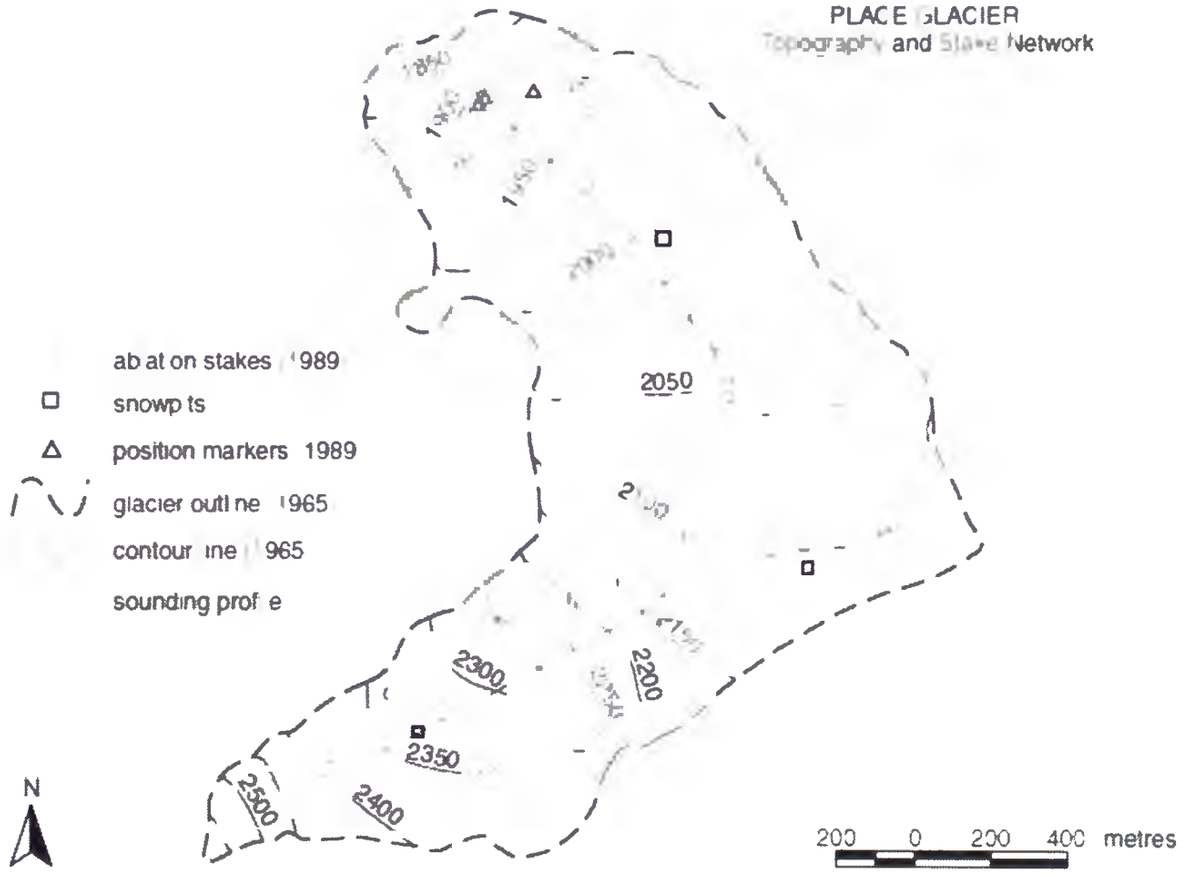

Figure 2.2 A network of ablation stakes and snowpits for mass balance measurement for 1989, Place Glacier. Glacier outline and contours are based on 1965 (Source: Moore and Demuth 2001).

2.3.1 Winter Balance

Specific winter balance (b_w) at a particular point on the glacier is determined by measuring the total snow accumulated over the winter months·

$$b_w = d_s \frac{\rho_s}{\rho_w} \qquad (2.1)$$

where d_s and ρ_s are the depth (m) and average density (kg m^{-3}) of the winter snowpack, and ρ_w is the density of water (1000 kg m^{-3}) It is assumed that the winter ablation (through melting or sublimation) is negligible For most of the years, winter accumulation is usually measured in April or May.

At each stake location, winter snowpack depth is measured from stake reading at the end of the accumulation season. In addition to this, snowpack depth is determined by digging pits or using probes. The insertion resistance of the probe increases abruptly when its tip reaches the crust that was formed the previous year. This depth is reported as winter snowpack depth. In areas where it is not possible to identify the end of the summer layer using probes, snow pit stratigraphy is used to identify the first dirt layer, which corresponds to the end of the summer surface last year. The depth above this dirt layer is reported as winter snowpack depth. Additionally, snow densities at each measurement sites are measured using both density pits and density corers. Snow density pits are constructed by excavating snow to a depth of 1.5 m below the snow surface and then sampling and weighing a known volume of snow at 10 cm intervals. To determine the snow density below 1.5 m, snow core samples of varying lengths are extracted using snow density corer. The length and weight of each core is measured in the field. The core barrel diameter and the

length of the sample are used to calculate the core volume, which is then used with the sample weight to calculate the density.

2.3.2 Summer Balance

In the mid-latitudes, where summer is characterized by a pronounced dry season with little or no snowfall, summer balance is nearly equal to summer ablation Neglecting a small amount of sublimation during summer months, summer ablation is a direct result of melting from the glacier surface. Summer ablation measurements on Place Glacier are made using aluminum stakes drilled vertically into the glacier at the end of the summer (September or October) (Figure 2.2). The height of the pole above the glacier surface is measured at the time of installation. At the end of the following summer, the height above the glacier surface is again recorded, providing a record of change in glacier surface elevation. In the accumulation area, summer ablation is usually due to melting of winter snowpack. Here, summer ablation is determined as the difference between the winter balance (m w.e.) and the residual winter snowpack amount (in m w.e.) at the end of the summer melt season. Residual winter snowpack amount is calculated from the product of the level change between readings and the late summer snow density, which is measured at each stake location. In the accumulation area where firn ablation can be expected, stakes are set and density measured prior to calculating summer ablation. In the ablation area, summer ablation is the sum of winter snow melt and ice melt. Winter snow melt is determined from winter accumulation/balance (m w.e.). Ice melt (m w. e.) is calculated from the product of the level change between readings and the glacier ice density, which is considered constant at 900 kg m^{-3}.

2.3.3 Net Balance

At each stake location on the glacier, net annual balance (m w.e.) is calculated as the sum of winter balance (m w.e.) and summer balance (m w e) However, mass balance for a particular point on a glacier is not very useful to understand the overall state of a glacier. For this, glacier-wide or area-averaged mass balance is more desirable. To determine glacier-wide net mass balance, first, the average of the mass balance terms for different stake locations within a particular elevation band is obtained This will give one summer balance and one winter balance value for each elevation band For each elevation band, these values are added together to obtain net mass balance With the knowledge of glacier area enclosed by each elevation band, glacier-wide annual net mass balance (B) is calculated using area-weighted averaging:

$$B_a = \frac{\sum_{i=1}^{i=m} A_i (b_n)_i}{\Sigma A_i} \qquad (2.2)$$

where m is the number of elevation bands considered, A_i, is the area of each elevation band, and $(b_n)_i$ is the average net mass balance for each elevation band. A similar formulation is used to calculate glacier-wide winter balance (B_w) and summer balance (B) except that net mass balance is replaced with respective winter and summer balances.

2.3.4 Sources of Uncertainty

GMB measurements have inherent uncertainty. However, uncertainties have only been quantified for a limited number of mass balance records available globally. WGMS has identified greater quantification of uncertainty in mass balance measurements as a key goal

for future research. Similar to the glacier mass balance data from other regions of the world, mass balance measurements from Place Glacier also suffer from uncertainty. The main sources of uncertainty in measured GMB data are discussed below

Spatial Averaging

The number and density of ablation stakes and snowpits for mass balance measurement is usually not sufficient to represent the entire glacier due to logistical reasons. As a result, measurements of ablation and or accumulation at individual points have to be interpolated between the measurement points and extrapolated to unmeasured regions of the glacier. Such interpolation extrapolation of the measurements contributes to uncertainty in measurements of mass balance. A good interpolation method, which addresses the processes that drive glacier mass balance distribution, should be used to minimize the uncertainty. Similarly, appropriate extrapolation methods are the key to minimize the uncertainly in glacier-wide mass balance computed from point measurements.

Measurements Errors

The field measurements are subject to errors which contribute to the uncertainty in mass balance measurements. These include errors in height determination due to measurement precision, tilt, sinking, and floating of ablation stakes; tilt of snow probes and difficulties in identifying last year's surface in the snowpack; density measurement errors and associated assumptions; superimposed ice, which is difficult to measure and for which the spatial variability is often not well captured by the stake network.

Under-sampling

The under-sampling of inaccessible or difficult glacier areas with potentially different surface balances such as those due to crevasses, debris covers, steep slopes, and avalanche zones, is another source of uncertainty in measured glacier mass balance.

Changing glacier area and elevation

Common to all mass balance series is the issue of the glacier elevation and area changing over time. Although the changing coordinates and elevation of observation points can be measured directly, glacier area of the most recent geodetic survey is typically used as a constant for the calculation of the specific glaciological balances for the years up until the next geodetic survey. This will add extra uncertainty to mass balance measurements.

Unfortunately, the mass balance data from Place Glacier does not contain any information about uncertainty. Therefore, caution should be exercised when using this mass balance record for GMB model validation and for other research purposes.

2.4 Previous Studies

Place Glacier is the most studied glacier in the region with longest available mass balance records that dates back to the 1960s. Letréguilly (1988) correlated the mass balance of three western Canadian glaciers (Peyto, Place, and Sentinel) with the meteorological records of neighbouring stations for the period 1966-1984. Place Glacier mass balance was correlated with the precipitation and temperature data. Based on this correlation, regression models were developed and mass balance was reconstructed back to 1938. Results from this study suggest that the Place Glacier's mass balance is influenced by both summer temperature and winter precipitation. The cumulative mass balance showed an overall decreasing trend. This

is perhaps the first published research on Place Glacier using mass balance records. Bitz and Battisti (1999) studied relations between Place Glacier mass balance and North Pacific atmosphere–ocean variability using data up to 1992 Bitz and Battisti (1999) found that winter and net balances at Place Glacier and other glaciers in southern British Columbia and Washington were negatively correlated with the PDO (Pacific-Decadal Oscillation). Furthermore, they found that the winter balance was positively correlated with winter precipitation, but uncorrelated with winter temperature This lack of influence of winter temperature is possibly due to the fact that Place Glacier is located at fairly high elevation and away from the coast, that most of the precipitation falls as snow, even in relatively warm winters. Summer balance was negatively correlated with summer temperature and positively correlated with winter balance. Moore and Demuth (2001) extended the work by Bitz and Battisti (1999) by considering longer time series of mass balance and large scale climate indices (up to 1999). However, unlike Bitz and Battisti (1999), which used only the PDO index for large-scale climate variability, their study included a number of other large-scale climate indices, such as SOI (Southern Oscillation Index), CT (Cold Tongue) index, and Pacific North America (PNA) index. They examined a correlation between each of these large-scale climate indices and winter balance and net balance at Place Glacier. They found that both winter and net balance is negatively correlated with the PDO, which is consistent with the result from Bitz and Battisti (1999). This result suggests that the winter accumulation on Place Glacier is greater during cold-phase winters. Similarly, net balance was negatively correlated with the PDO, and positively correlated with the SOI. Unlike the PDO and SOI, there was no significant correlation between other large-scale climate indices and winter and net balances. Also, none of the large-scale indices showed any significant

correlation with summer mass balance. The same study examined mass balance variations for Place Glacier for the period 1965 to 1999, and associated streamflow variability below Place Glacier over the period 1970 to 1984. Their analysis suggests that Place Glacier has experienced a largely negative net mass balance since mass balance measurements started in 1965. The net mass balance shifted to become more negative beginning in 1977, and the mass loss has accelerated ever since. They argued that the accelerated mass loss after 1976 is due to the shift of the PDO from cold (negative, high snowpack and cool temperature) phase to the warm (positive; low snowpack and warm temperature) phase. The continuous negative mass balance has resulted in significant terminal retreat, with the formation of a pro-glacial lake (also known as Place Lake). Summer streamflow responded to interannual variations in winter snow accumulation and summer temperatures, which control the rate of rise of the glacier snowline and melt rates. Analysis of August streamflow data suggests a negative trend in total runoff, which is attributed to reduction in ice area after 1965. Furthermore, they developed a multiple regression model to extend the mass balance time series back to the 1890s. The reconstructed series indicate that Place Glacier has experienced dominantly negative net balances over the last century.

There have been a number of studies involving modelling ablation on Place Glacier. Since most of the distributed ablation modelling on a glacier relies on meteorological measurement from off-glacier locations, Munro and Marosz-Wantuch (2009) investigated the effectiveness of off-glacier meteorological measurements in simulating ablation on Place Glacier as compared to ablation simulated using on-glacier measurements. They employed an energy balance approach for ablation simulation, but with a slightly different approach for turbulent heat fluxes estimation for on-glacier and off-glacier measurements. Turbulent

heat flux estimations using off-glacier measurements employed a heat transfer approach in which turbulent mixing due to katabatic and geostrophic flow is parameterized (e.g., Oerlemans and Grisogono 2002) Turbulent heat fluxes using on-glacier measurements are parameterized using a bulk aerodynamic approach. A comparison is made between cumulative ablation from each simulation and the total ablation measured at the glacier site during the study period. On-glacier measurements provided a reasonably good simulation of cumulative ablation. Simulation using off-glacier measurements performed best if the katabatic component of the parameterization scheme is ignored Shea (2010) compared results from melt models with a range of complexity against melt observed at four glaciers in the southern Coast Mountains that included Place Glacier. Models considered for comparison were empirical TI and enhanced TI melt models, simple SEB model, and a full SEB model. The empirical melt models used melt factors fitted to Place Glacier mass balance data from 1965-1995. Results from this study suggest that the TI model outperformed a simple SEB model and enhanced TI model, while the full SEB model without katabatic boundary layer corrections yielded the lowest error. This result is in contrast to the finding from the same study, which suggests the near surface temperature and humidity on Place Glacier are strongly affected by katabatic boundary layer development. The same study also compared the performance of these models in terms of their ability to predict the date of snow disappearance on Place Glacier. In many mountain regions, glaciers are major erosional agents and thus sources of suspended sediments (e.g., Collins 1998). Suspended sediment in glacier-fed streams not only affects hydroelectric generating facilities, it can also impact downstream ecology and water quality. Richards and Moore (2003) investigated the suspended sediment concentration from Place Glacier basin in

relation to river discharge during the ablation season of 2000 and 2001. River discharge and sediment were measured at a gauging site in Place Creek downstream of Place Glacier. Investigation was performed by separating the ablation season into nival, nival–glacial, glacial and autumn recession subseasons. They reported a variation in discharge-sediment relationship between the two study seasons, and between subseasons. Some suspended sediment released from pro-glacial Place Lake (the source of Place Creek) appeared to be lost to channel storage at low flows, especially early in the ablation season, with re-entrainment at higher flows.

Review of previous studies on Place Glacier suggests that out of a number of studies on this glacier, none have attempted the hindcasting of the mass balance of this glacier using a physically-based GMB model. The fact that this glacier has the longest mass balance record in the region perhaps makes such a study even more attractive as the mass balance data can be readily used for validating the model results. Since routine glacier mass balance measurements in the southern Coast Mountains are limited to only a few glaciers, a mass balance model validated on Place Glacier can potentially be used on other glaciers in the region for developing mass balance time series. At the same time, such a model can be used as a tool for climate change impact studies on glaciers in the region. Despite the fact that the physically-based GMB modelling is one of the promising areas of research on Place Glacier, this approach of GMB modelling has not been tested for mass balance hindcasting of this glacier in the past. Therefore, for the first time, this study aims to perform a physically-based GMB modelling on Place Glacier with the purpose of developing a mass balance hindcast and subsequently applying the model for future GMB projection. This will be a new addition to the list of research on Place Glacier.

Chapter 3

Data

Data used in this study can be divided into three categories Glacier Mass Balance (GMB) data, meteorological data and geomatic data GMB data include summer and winter balance records obtained from field-based measurements Meteorological data include variables such as air temperature, relative humidity, incoming shortwave and longwave radiation, wind speed and direction, and precipitation obtained from climate stations, mesoscale model, reanalysis model, and global climate model Geomatic data used in this study include a Digital Elevation Model (DEM) and glacier extent These data come from various sources and are discussed in more detail below.

3.1 Glacier Mass Balance Data

Long-term (1965-2005) historic MB data for Place Glacier are obtained from the World Glacier Monitoring Service (WGMS 2011), which maintains an archive of mass balance and other information collected from glaciers around the world (Table 3.1). Methods used for GMB measurement were discussed in Chapter 2. Most of the MB data are available as summer and winter balances (seasonal time scale) in elevation bands covering the entire range of glacier elevations. However, for some years, summer and winter balances are missing for a few of the higher elevation bands. Data for the missing elevation bands are linearly extrapolated. Additionally, from 1990-1993 and again from 1996-2005, summer and winter balances are missing and the record contains only glacier-wide net mass balance. However, there is no mention in the record as to how net mass balance was obtained when

summer and winter mass balances are missing. It is possible that the net mass balance for these years are based on measurements conduced at an annual time scale. GMB data from 2006-2008 is obtained from Shea (2010). GMB records from Place Glacier are used for validating GMB model results.

3.2 Meteorological Data

3.2.1 Climate Station Data

Climate station data come from the following sources

- In situ observations made on Place Glacier and in the vicinity. For more details on instruments and methods of measurement, refer to Shea (2010).
- Networks of climate stations operated by Environment Canada (EC), BC Ministry of Environment (MoE), BC Ministry of Transport and Highways (MoTH), BC Ministry of Forests, Lands, and Natural Resource Operations (MoF) and BC Hydro (BCH)

Meteorological data observed at Place Glacier are mainly used for independent model testing against observed GMB data. They are also used to validate other parameterized variables on the glacier for GMB modelling. Climate data from EC, MoE, MoTH, MoF and BCH are used to estimate bias in RAMS air temperature. These data are summarized in Table 3.1.

Table 3.1 Summary of climate station data and GMB data used in the present study. T_a = air temperature, RH = relative humidity, P = precipitation, u = wind speed, Θ = wind direction, K_{out} = reflected shortwave radiation, K_{in} = incoming shortwave radiation, L_{in} = incoming longwave radiation, Q_{net} = net radiation, SLP = sea-level pressure, b_s = summer balance, b_w= winter balance, b_n = net balance, S_d = snow depth

Data Set	Variable	Period available	Temporal resolution
*Observations at Place Glacier	T_a, RH, u, Θ, K_{out}, K_{in}, L_{in}, Q_{net}	Summer 2006, 2007 and 2008	Hourly, seasonal,
	b_s, b_w, b_n	1965-2008	annual
EC, MoE, MoTH, MoF, BCH	T_a, P, S_d	1979-2008	hourly, daily, seasonal

*Shea (2010) and WGMS (2011)

3.2.2 RAMS Mesoscale Model Data

Ainslie and Jackson (2010) used the RAMS mesoscale model v6.0 (Cotton et al. 2003) to dynamically downscale 32 km resolution North American Regional Reanalysis (NARR, Mesinger et al. 2006) data to 8 km resolution climate fields over the southern Coast Mountains of western Canada. The downscaled NARR data (hereafter RAMS variables) extend from 1979 to 2008 and cover much of southwestern BC including Vancouver Island (Figure 3.1). The data are available in hourly temporal resolution on 36 vertical levels in the atmosphere. These data have been archived at the High Performance Computing (HPC) data repository of the University of Northern British Columbia (Table 3.2). The present study takes advantage of these data to develop hindcasts of glacier mass balance in the southern Coast Mountains of BC. This is the only mesoscale climate data with the outputs necessary to drive a physically-based GMB model available for the southern Coast Mountains at a relatively fine spatial resolution of 8 km. Additionally, these gridded data are used as

predictands to develop a statistical model for downscaling a number of future GCM projections.

For GMB modelling, the following RAMS variables are used: surface (2 m) air temperature (T_a), vapour pressure (e_a), 2 m wind speed (u) and incoming shortwave radiation (K_{in}) , incoming longwave radiation (L_{in}), precipitation (P), sea-level pressure (SLP) and the vertical profile of air temperature at 13 levels in the atmosphere from the surface to 1000 m. These variables are retrieved at an hourly temporal resolution from a single RAMS grid cell nearest to the Place Glacier from 1979-2008. The topography of the inner 8 km RAMS domain and the location of Place Glacier within the domain are shown in Figure 3.2.

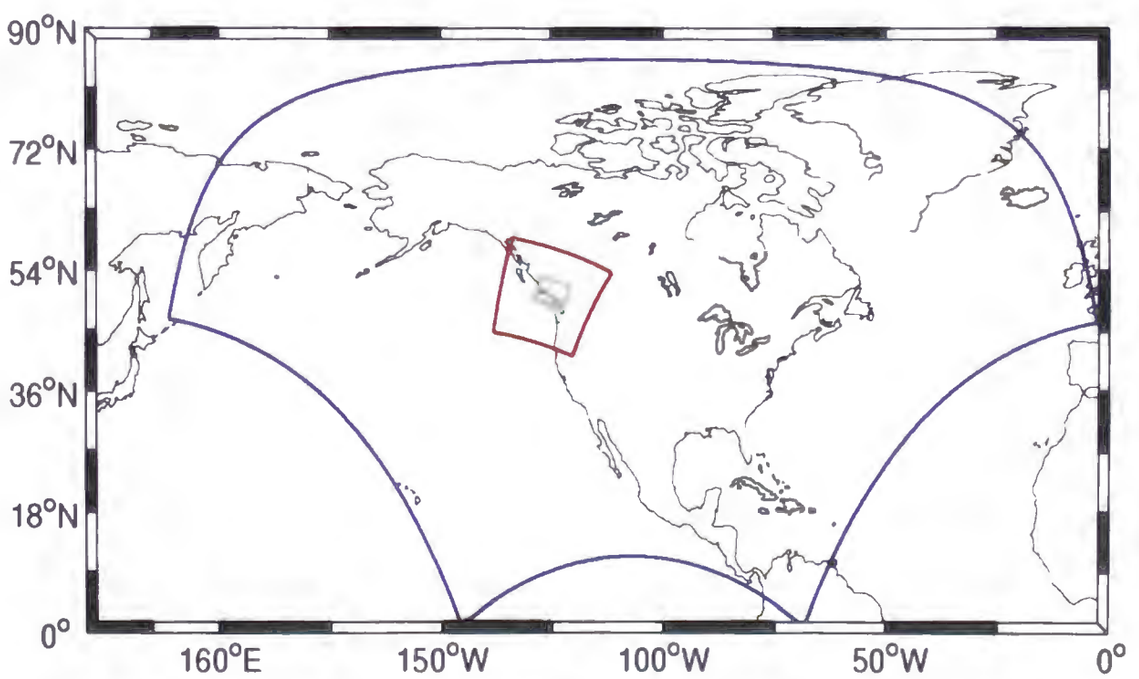

Figure 3.1 NARR (blue), RAMS outer (red) and RAMS inner (green) domain

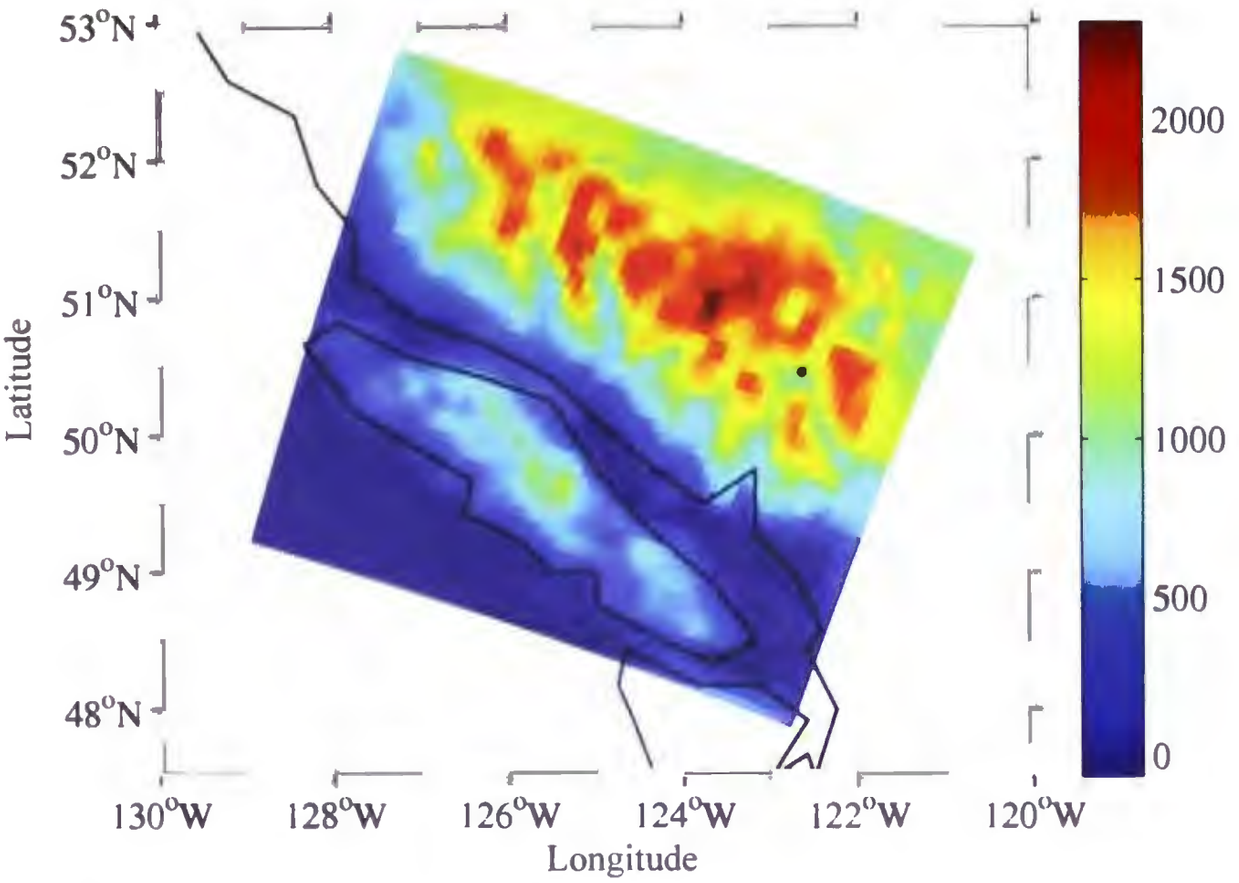

Figure 3.2 Topography of the inner 8 km RAMS domain (m) The black dot refers to the location of Place Glacier within the RAMS domain RAMS data are retrieved from the grid cell nearest to this dot.

3.2.3 NCEP/NCAR Reanalysis Data

NCEP/NCAR (National Centers for Environmental Prediction/National Center for Atmospheric Research; Kalnay et al. 1996; hereafter referred to as NCEP) reanalysis products have been widely used for glacier mass balance modelling in the past (e.g., Rasmussen and Conway 2004; Zhang et al. 2007a; Koppes et al. 2011; Andreassen et al. 2012). These reanalysis data have also been used for downscaling large-scale temperature (Huth 2002) and precipitation (Widmann et al. 2003). The NCEP reanalysis products are developed using a state-of-the-art analysis/forecast system to perform data assimilation using past data from 1948 to the present. A large subset of these data is available

(http://www.esrl.noaa.gov/psd/data) in its original 4 times daily format and as daily averages. The spatial resolution of the NCEP product (2.5 °Lat 2.5 °Lon) is similar to that of GCM products. More details on the NCEP product can be found in Kalnay et al. (1996). NCEP data are extracted from a domain that extends from 40°-60°N latitude and 110°-157°W longitude (Figure 3.3). These data include daily air temperature, vapour pressure, wind speed, incoming shortwave radiation, incoming longwave radiation, precipitation, and sea-level pressure from 1961-2008 (Table 3.2). In this study, NCEP data are used as predictors for developing a statistical model for downscaling different GCM future projections.

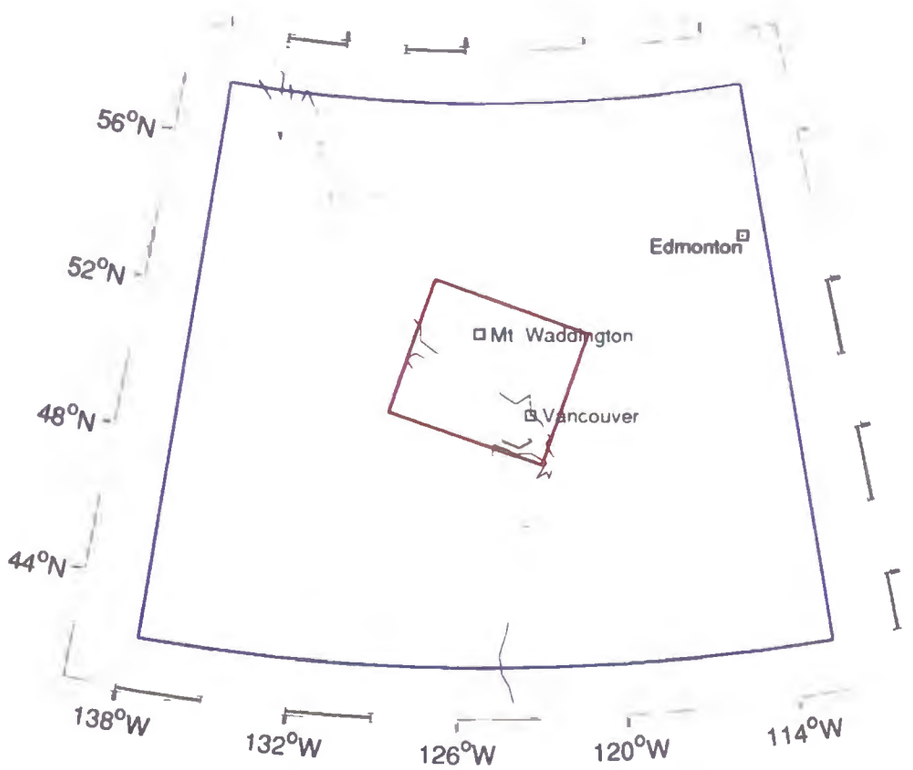

Figure 3.3 NCEP 2.5 °Lat × 2.5 °Lon resolution domain (blue) and RAMS 8 km × 8 km resolution inner domain (red) used in developing the downscaling model.

3.2.4 GCM Future Projections

Previously, a number of studies have used GCM future climates for developing future projections of glacier mass balance in different parts of the world (e.g., Radić and Hock 2006; Radić et al. 2013; Clarke et al. 2015) For the present study, future climate projections are obtained from the Coupled Model Intercomparsion Project-Phase 5 (CMIP5) multi-model experiments (http: pcmdi9.llnl.gov esgf-web-fe live) conducted for the IPCC AR5 assessment (IPCC 2013). For the CMIP5, four new emission scenarios were developed and are referred to as Representative Concentration Pathways (RCP2 6, RCP4.5, RCP6.0, and RCP8.5). The RCPs are mitigation scenarios, based on a range of projections of future population growth, technological development, and societal responses, which assume that policy actions will be taken to achieve certain emission targets (Moss et al. 2010). GCM projections are obtained from experiments that utilized an Atmosphere-Ocean Global Climate Model (AOGCM) coupled with Earth System Models (ESM). These GCMs include physical processes like those in other climate models but they can also simulate the interaction between the physical climate, the biosphere, and the chemical constituents of the atmosphere and ocean. To determine the uncertainties in model results, future climate projections are considered from four different GCMs: CanESM2 (e.g., Arora et al. 2011), MIROC-ESM (e.g., Watanabe et al. 2011), MPI-ESM-LR (e.g., Giorgetta et al. 2013), and HadGEM2-ES (e.g., Jones et al. 2011). Experimental results are considered for RCP4.5, a midrange mitigation emission scenario and for multiple runs (realizations) with different but equally realistic initial condition (e.g., Taylor et al. 2012). These GCMs are selected because they were found to perform well in simulating climatologies of several climate variables and the daily synoptic pattern in North America and its western subregion (Radić and Clarke

2011). However, it should be noted here that this evaluation was based on GCMs from CMIP3 experiments that do not include ESM, but the atmospheric-ocean component of the GCMs remains the same. For each GCM, daily results are obtained from a number of ensemble projections. Results are then averaged across the ensemble to get an ensemble-averaged daily value. As the statistical downscaling scheme used in the present study requires historic GCM fields too, they are obtained from CMIP5 historical experiments as ensembles. More details on CMIP5 historical and future experimental setups can be found in Taylor et al. (2012). Daily GCM projections considered for downscaling are air temperature, humidity, precipitation, sea-level pressure, wind speed, incoming shortwave radiation and incoming longwave radiation are used for downscaling. The historic GCM projections cover a period from 1961-2005, whereas the future projections are from 2006-2100. The domain used for extraction of GCM projections is the same as the domain used for extracting NCEP data (see Figure 3.2). More details about the GCM data sets used in the present study are given in Table 3.2.

Table 3.2 Details on gridded climate data used in the study. Variables extracted for analysis from these gridded data include air temperature, vapour pressure, wind speed, incoming shortwave radiation, incoming longwave radiation, precipitation, and sea-level pressure

Data Set	Model	Spatial Resolution (Lat · Lon)	Temporal Resolution	Source
Reanalysis fields	NCEP/NCAR[1]	2.5° · 2.5°	Daily	http: www.esrl.noaa.gov/psd/data
Mesoscale fields	RAMS 6.0	8 km · 8 km	Hourly Daily	UNBC HPC data repository (Ainslie and Jackson 2010)
GCM projections	CanESM2	2.8° · 2.8°	Daily	http pcmdi9.llnl.gov/esgf-web-fe/live
	MIROC-ESM[4]	2.8° · 2.8°	Daily	http pcmdi9.llnl.gov/esgf-web-fe/live
	MPI-ESM-LR[5]	1.9° · 1.9°	Daily	http pcmdi9.llnl.gov/esgf-web-fe/live
	HadGEM2-ES[6]	1.875° · 1.25°	Daily	http pcmdi9.llnl.gov/esgf-web-fe/live

[1] National Centers for Environmental Prediction/National Center for Atmospheric Research, Reanalysis-Forecast Model
[2] Regional Atmospheric Modelling System, version 6.0, Colorado State University
Canadian Centre for Climate Modelling and Analysis
[4] University of Tokyo, National Institute for Environmental Studies and Japan Agency for Marine-Earth Science and Technology, Japan
[5] Max-Planck-Institute for Meteorology, Germany
[6] Met. Office Hadley Centre, United Kingdom

3.3 Geomatic Data

The DEM surface for GMB modelling is obtained from the Canadian Digital Elevation Data (CDED 2013). Within the study area, the DEM has an approximate resolution of 3 arc-sec latitude and longitude, which is derived from the 1:250,000 NTS (National Topographic System) map of 1986. 1985 glacier extent information (Bolch et al. 2010) is used to extract the DEM surface for Place Glacier. The DEM is re-sampled at a uniform grid resolution of 75 m using ArcGIS (ESRI 2011). The DEM used in the GMB model is shown in Figure 3.4

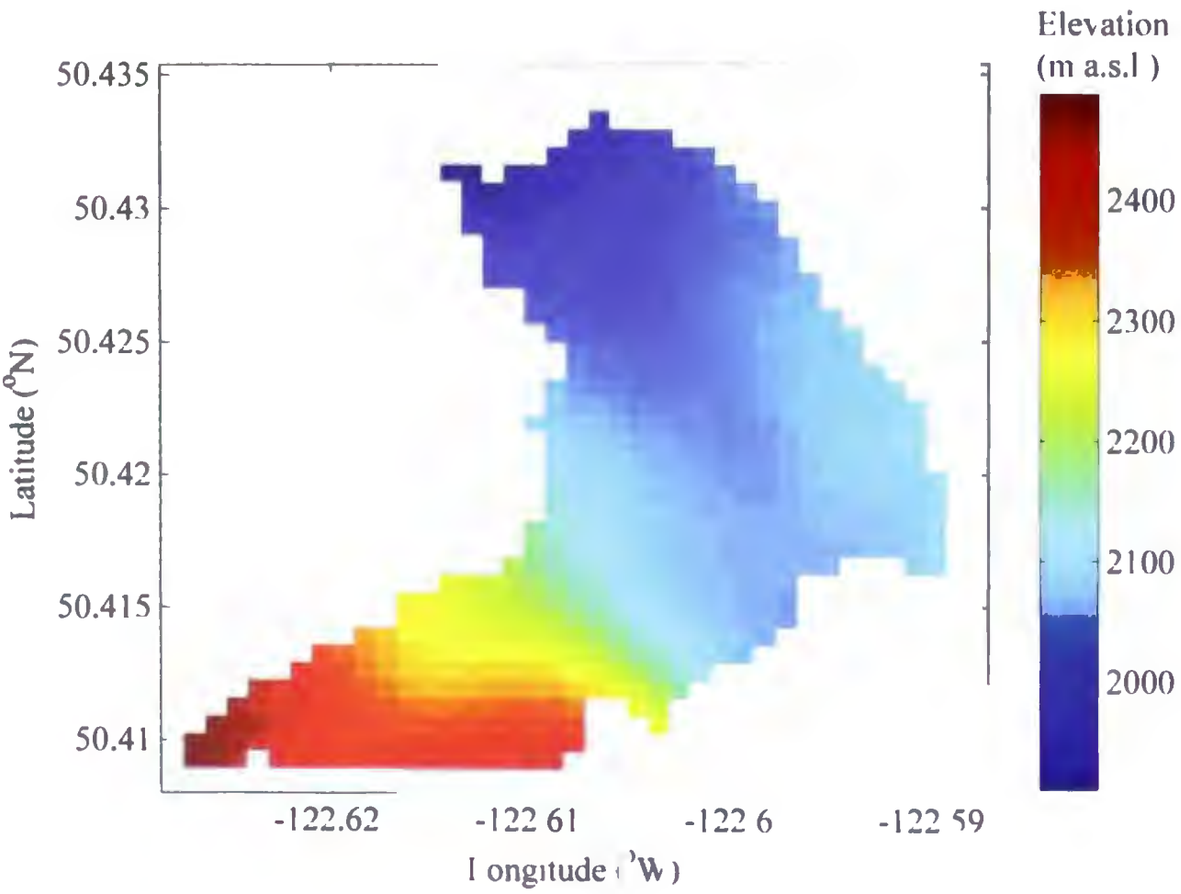

Figure 3.4 Place Glacier DEM used in the GMB model

Chapter 4

Preparation of RAMS Data for GMB Modelling

4.1 Introduction

Several regional downscaling studies have reported some amount of bias in mesoscale model outputs (e.g., Colle et al. 1999, Salathé et al 2008), especially over regions of complex terrain. Biases in mesoscale model output subsequently influence other hydrologic processes such as evapotranspiration, runoff, snow accumulation and melt. RAMS output also likely contains biases due to factors such as improper characterization of topography, incomplete model physics, and initialization errors. Therefore some form of pre-processing is necessary to remove biases present in the RAMS output before they can be used for impact assessment studies.

The 8 km resolution topography used in the RAMS mesoscale model is not able to fully resolve the real topography in the model domain and as a result there is a discrepancy between model and actual topography (Ainslie and Jackson 2010). Misrepresentation of actual topography in the mesoscale climate model is one of the major sources of bias present in model fields. Therefore, the model variables should be adjusted for this elevation difference before they are used for impact studies. This approach of climate data adjustment for the elevation difference has been applied for climate-glacier studies in the past (e.g., Radić and Hock 2006; Paul and Kotlarski 2010) and is also considered a form of downscaling.

Distributing input data on the glacier surface presents a substantial additional challenge in distributed GMB modelling. Usually, the input meteorological variables are

distributed on the glacier surface using their standard or observed gradients. When such gradients are not known, they must be parameterized using different schemes.

The objective of this chapter is to describe how RAMS mesoscale model data are prepared to be used as input variables for distributed GMB modelling on Place Glacier. This chapter details the methods used for temperature and precipitation bias correction, elevation correction for temperature and precipitation, and estimation of precipitation gradient and temperature lapse rate for their distribution in the GMB model.

4.2 RAMS Data Retrieval and Bias Correction

For the present study, RAMS hourly surface (2 m) air temperature, vapour pressure, wind speed and incoming shortwave radiation, incoming longwave radiation, precipitation, sea-level pressure, and the vertical profile of air temperature are retrieved from a single RAMS grid cell nearest to Place Glacier for the summer melt season (1 June-30 September) from 1979-2008. Additionally, precipitation is also retrieved for the winter season (1 October-31 May) from the same grid cell. Time series plots of selected RAMS variables retrieved from the grid location nearest to Place Glacier are presented in Figure 4.1.

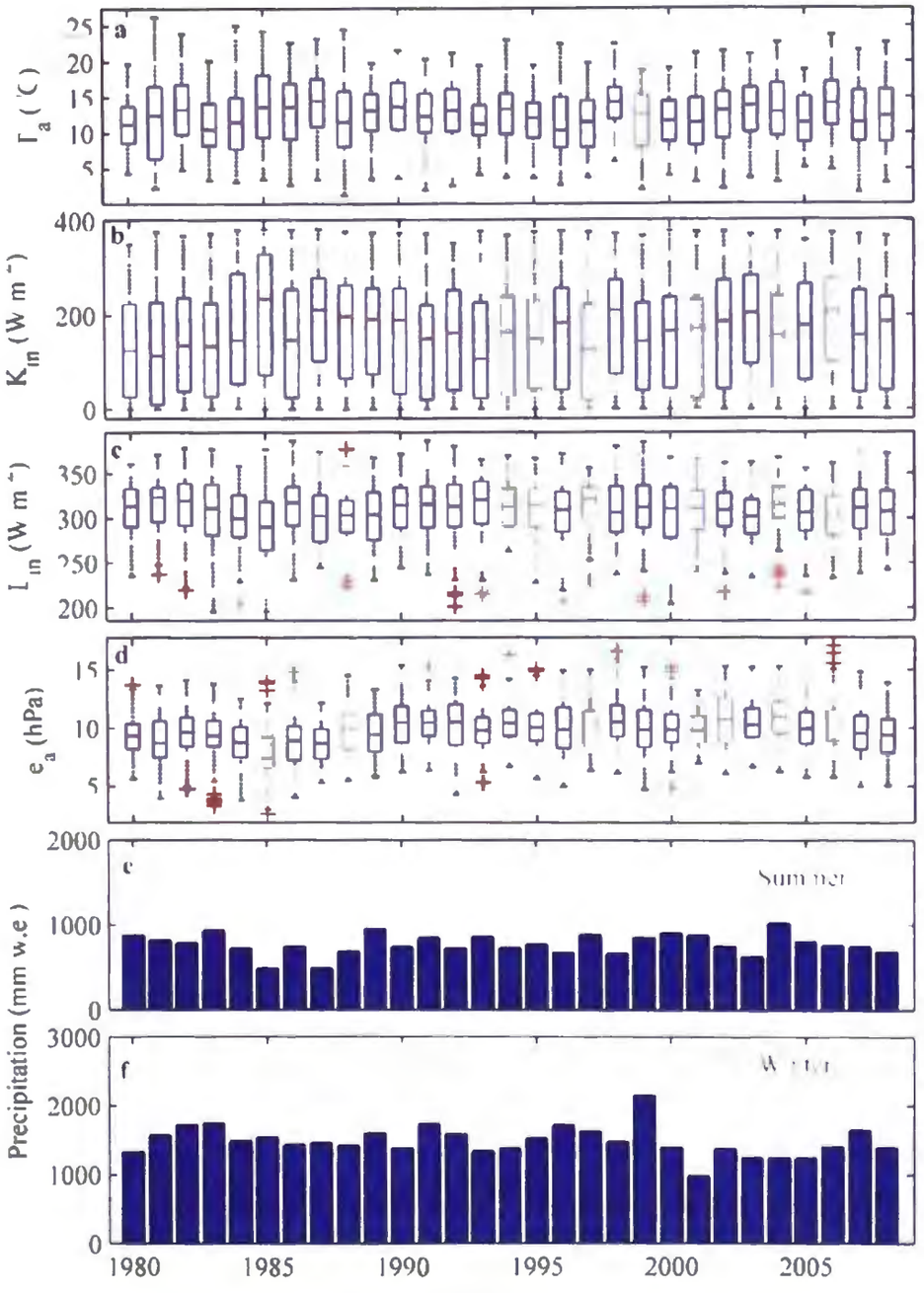

Figure 4.1 Box plot of mean daily (a) RAMS air temperature, (b) incoming shortwave radiation, (c) incoming longwave radiation, (d) vapour pressure and (e) total precipitation during the summer season (1 June- 30 September) from 1980-2008 for the RAMS grid location nearest to Place Glacier. Also shown (f) is the total winter (1 October-31 May) precipitation for the same location. The top and the bottom of the box mark the 75th and the 25th percentile of the dataset respectively. The height of the box represents the interquartile range (IQR) of the dataset and the ends of the whiskers mark the highest and lowest values of the dataset that are within 1.5 times the interquartile range of the box edges. The horizontal lines within the boxes are the median. The plus signs mark individual values outside the range of the whiskers (outliers). The values plotted are not bias-corrected.

Ainslie and Jackson (2010) estimated biases in RAMS daily precipitation for each grid cell over the southern Coast Mountains using a variety of observed precipitation data available in the region. For the present study, the bias correction factor, b_p^k, is used directly from the work by Ainslie and Jackson (2010). b_p^k is retrieved from the grid cell nearest to Place Glacier and applied to the RAMS precipitation from the same grid cell ($RAMS_p^k$) multiplicatively to get the bias-corrected RAMS precipitation, X_p^k:

$$X_p^k = RAMS_p^k . b_p^k \qquad (4.1)$$

Ainslie and Jackson (2010) compared bias-corrected precipitation with PRISM (Parameter Elevation Regression on Independent Slopes Model; Daly et al. (2002, 2008)) dataset, which is modified over BC and Yukon at a monthly time scale (Wang et al. 2006). A similar comparison is performed here, but using an original PRISM dataset in daily temporal resolution.

Following an approach similar to Ainslie and Jackson (2010), bias in RAMS air temperature is determined using daily air temperature data observed at different stations within the RAMS domain from 1979-2008. These stations included 114 EC climate stations, 4 EC Marine stations, 10 BC MoTH stations, 6 BC MoE snow pillow stations, 30 BC MoF stations, and 35 BC Hydro stations. Similar to the stations used for estimating bias in RAMS precipitation, stations chosen for bias estimation have differences between the RAMS-modelled and actual station elevations of less than 500 m. Before calculating the model bias at a particular station, RAMS daily temperature at that station is first adjusted to the station elevation by using a lapse rate of modelled RAMS daily temperature for that station. Hereinafter, the term "lapse rate" for air temperature refers to the cooling of air temperature

with height, which is normally a negative number. Methods used in determining the lapse rate will be discussed shortly. The daily modelled and observed values for each station are averaged monthly over a period from 1979-2008. This will create 12 sets of monthly temperature values from modelled and observed daily temperature data. Bias in RAMS air temperature is determined in the form of a change factor or offset by taking an arithmetic difference between the modelled and observed monthly values For station, k and for month, m RAMS air temperature offset, b^1 is determined as:

$$b_t^k = O_m^k - M_m^k \tag{4.2}$$

where the first term on the right side is the monthly observed air temperature for a location k averaged over a 1979-2008 period and the second term is the monthly RAMS air temperature for the same location averaged over the same period. For each month, b_t^k is determined for all stations and interpolated to the inner RAMS domain by means of ordinary kriging (Matheron 1963). The monthly bias values are then interpolated to each day using Cubic Spline Interpolation (Press et al. 1992). Interpolated daily bias values for all 12 months are combined together and averaged over all the months to get a single bias value for each grid cell in the RAMS domain. b_t^k is retrieved from the grid cell nearest to the Place Glacier and applied to the RAMS temperature from the same grid cell ($RAMS_t^k$) additively to get the bias-corrected daily RAMS air temperature, X_t^k:

$$X_t^k = RAMS_t^k + b_t^k \tag{4.3}$$

Validating the bias-corrected RAMS precipitation and temperature is a difficult undertaking as most of the station observations have been used for estimating the bias in these variables. In the absence of other independent data, this study used PRISM data for

validating bias-corrected RAMS precipitation and temperature. However, it should be noted here that PRISM has assimilated some of the stations used here for bias estimating in its regression model and therefore cannot be considered as entirely independent data for validation purpose. However, the purpose of this comparison is not to validate the absolute values in bias-corrected RAMS precipitation and temperature rather to compare their spatial organization relative to PRISM values Therefore, the use of PRISM data here seems to be an acceptable compromise. Due to different spatial resolution, the PRISM precipitation and temperature data are linearly interpolated to the RAMS domain before it is used for validation.

Although the RAMS variables other than air temperature and precipitation may potentially contain some amount of bias, they are not bias-corrected due to the lack of corresponding observations within the RAMS domain.

4.3 Temperature Lapse Rate

Shea (2010) demonstrated the influence of the Katabatic Boundary Layer (KBL) on glacier air temperature and vapour pressure from observations made on a few glaciers in the Coast Mountains. This study argued that the conventional way of distributing air temperature using standard or observed off-glacier lapse rate is less accurate during the summer melt season when the glacier surface is under the influence of the KBL. A well-established KBL is usually decoupled from the surrounding environment. As a consequence, this may introduce errors in the parameterization of other air temperature dependent variables including the parameterization of turbulent heat fluxes. Despite the known influence of the KBL on air temperature, most of the GMB and energy balance modelling work has used either standard

or observed (on- or off-glacier) lapse rates for distributing air temperature over the glacier surface and they appear to have provided satisfactory result (Escher-Vetter 1985; Anslow et al. 2008; Huss et al. 2008). This study follows a similar approach and distributes air temperature using fixed season air temperature lapse rate without including the influence of KBL.

The air temperature lapse rate (Γ) used for distributing air temperature across the glacier is calculated using the RAMS vertical temperature sounding data. RAMS vertical temperature sounding data were extracted for seven different locations in the southern Coast Mountains in hourly temporal resolution from 1979 to 2008 The vertical temperature sounding data extend to 13 levels in the atmosphere from the surface to 1000 m. These sounding locations were chosen close to the study site. Vertical temperature data are retrieved from the location nearest to the study glacier. The lapse rate of air temperature is calculated by linear regression of hourly air temperature with elevations from all 13 levels. Lapse rate is calculated for all hours from 1979-2008. For each year, hourly lapse rates are averaged over the period June-September to get a summer averaged temperature lapse rate. The average temperature lapse rate for a particular year is used in the GMB model for distributing air temperature on the glacier surface.

Shea (2010) detected the KBL influence on air temperature by comparing in situ air temperature measured on Place Glacier with ambient air temperature measured at an off-glacier location. However, it is not known whether a similar influence can be seen by comparing glacier air temperature with RAMS air temperature. Therefore, the KBL influence on air temperature demonstrated by Shea (2010) is further investigated here using a similar approach, but using RAMS air temperature as ambient temperature. This analysis

is important to determine whether there exists any threshold temperature, which can be used as a criterion for simulating glacier wind within the GMB modeling. For this analysis, RAMS bias-corrected air temperature data from the grid cell nearest to Place Glacier is compared with glacier air temperature data. Prior to the comparison, the RAMS air temperature data are adjusted for the elevation of the glacier observation sites using standard air temperature lapse rate.

4.4 Precipitation Gradient

Beside atmospheric conditions, topography is the single most important factor controlling the amount of precipitation falling in a region. Mountain glaciers are usually located in complex topography where significant spatial variation of precipitation exists. The physical processes that govern precipitation in complex terrain are often not modelled well by current atmospheric models. As a result, most of the GMB modelling work in the past has used a simplified approach for precipitation distribution such as assuming no vertical gradient (Escher-Vetter 1985; Arnold et al. 1996), a fixed vertical gradient (Jòhanneson et al. 1995; Oerlemans 1992), or a fixed vertical gradient determined from station measurements (Hock and Noetzli 1997; Anslow et al. 2008).

In the southern Coast Mountains, very little information is available on the vertical gradient of precipitation. The only information comes from seasonal observations of winter accumulation for a few selected glacier locations. However, winter accumulation records for most of the years are missing for higher elevations of the glacier making them less useful for estimating their vertical gradient. Furthermore, long term elevation-wise precipitation records at hourly or daily time scale is almost non-existent thus making it impossible to

determine precipitation gradients at this time scale. As an alternative, the present study will use vertical gradients of RAMS precipitation for distributing it on the glacier's surface.

To calculate the vertical gradient of RAMS hourly precipitation (Γ_{P1}) for a particular year, RAMS hourly summer precipitation for that year is first retrieved from several grid cells surrounding the study glacier covering a wide range of elevation. These precipitation values are then linearly regressed with elevations and the slope of the regression is taken as the vertical precipitation gradient. For each year, hourly vertical precipitation gradient values are averaged over the summer melt season to obtain a summer averaged value. These gradients are used in the GMB model to distribute summer hourly precipitation for different years.

Similarly, to calculate the vertical gradient of winter accumulation (Γ_{P2}), RAMS hourly winter precipitation is retrieved from the grid cells surrounding the study glacier. A static air temperature threshold of 1.0°C is applied to determine whether precipitation falls as snow. Although a wide range of air temperature thresholds have been used for discriminating liquid and solid precipitation (see Kienzle (2008) for details), this value has been most commonly used for similar studies in the past (Anslow et al. 2008; Arnold et al. 2006). Therefore, this value is retained here for the modelling. The hourly snowfall is summed over the winter season (1 October-31 May) to obtain a total winter snow amount (in w.e.). The cumulative winter snow amount from different grid cells are linearly regressed with their respective elevations and the slope of the regression is taken as a vertical gradient of winter accumulation. Γ_{P2} estimated here for different years are used in the GMB model for distributing winter total precipitation on the glacier surface.

4.5 Elevation Correction

RAMS air temperature and precipitation are adjusted for the elevation difference between RAMS topography and high resolution Digital Elevation Model (DEM) topography using an approach reported earlier by Radić and Hock (2006) and Paul and Kotlarski (2010). Although this difference in elevation can affect all model variables, the adjustment is applied only to RAMS air temperature and precipitation because they are known to have strong influence on SEB on the glacier To perform this adjustment, first the elevation difference at a number of RAMS grid cell locations within the domain is determined by comparing RAMS topography with the topography from CDED DEM (CDED 2013), which is used for GMB modeling. Only RAMS grid cells closest to specific glaciers (Place, Bridge, Helm, and Tiedemann) are chosen for this comparison. The original CDED DEM, which has an approximate resolution of 3 arc-sec latitude and longitude, is re-sampled at a uniform grid resolution of 75 m. Precipitation and temperature from the RAMS grid cell closest to the study glacier are adjusted for the elevation difference as:

$$T_a = X_t + \Gamma_t.(H_{CDED} - H_{RAMS}) \tag{4.4}$$

$$P = X_p + \Gamma_{P1}.(H_{CDED} - H_{RAMS}) \tag{4.5}$$

$$P' = X_{P'} + \Gamma_{P2}.(H_{CDED} - H_{RAMS}) \tag{4.6}$$

where, $X_{P'}$ is the total winter snow amount from the RAMS grid cell nearest to the study area, H_{RAMS} is the elevation of the RAMS grid cell nearest to the study area, and H_{CDED} is the elevation of the corresponding RAMS grid cell as reported by CDED DEM. Γ_t, Γ_{P1} and Γ_{P2} are lapse rates of RAMS hourly summer air temperature averaged over summer months,

vertical gradient of RAMS hourly summer precipitation averaged over summer months and vertical gradient of RAMS total winter precipitation, respectively.

4.6 Results and Discussion

4.6.1 Bias Correction

The present study does not attempt to perform bias correction of RAMS precipitation as this has already been done by Ainslie and Jackson (2010). Bias correction results are adopted directly from Ainslie and Jackson (2010). A summary of the key findings from Ainslie and Jackson (2010) together with the results from the present study is presented here.

The bias correction factor for RAMS precipitation within the full domain ranges from 0.2-1.76 with a mean of 0.85 and a standard deviation of 0.31 (Figure 4.2). For the Coast Mountains locations, the bias correction factors are almost as variable ranging from 0.5 to 1.2. Much of the area along the windward side of the Vancouver Island Mountains has bias correction factor greater than 1.0 implying that RAMS underpredicts precipitation there. The underprediction is particularly large at the southwestern and the northwestern edge of Vancouver Island. The isolated area of underprediction in the narrower Johnstone Strait may have been caused due to RAMS model topography not resolving the open strait at this location. Much of the interior has bias correction factors below 1.0 suggesting that the model is overpredicting precipitation there. The estimated bias correction factor for RAMS precipitation for the Place Glacier location is 0.67, which is applied to correct RAMS precipitation for the bias. The bias-corrected precipitation field over the entire domain has a maximum of 20.14 mm day^{-1} and a mean of 6.86 mm day^{-1}. These values are lower than the raw precipitation maximum of 25.31 mm day^{-1} and raw mean of 8.52 mm day^{-1}.

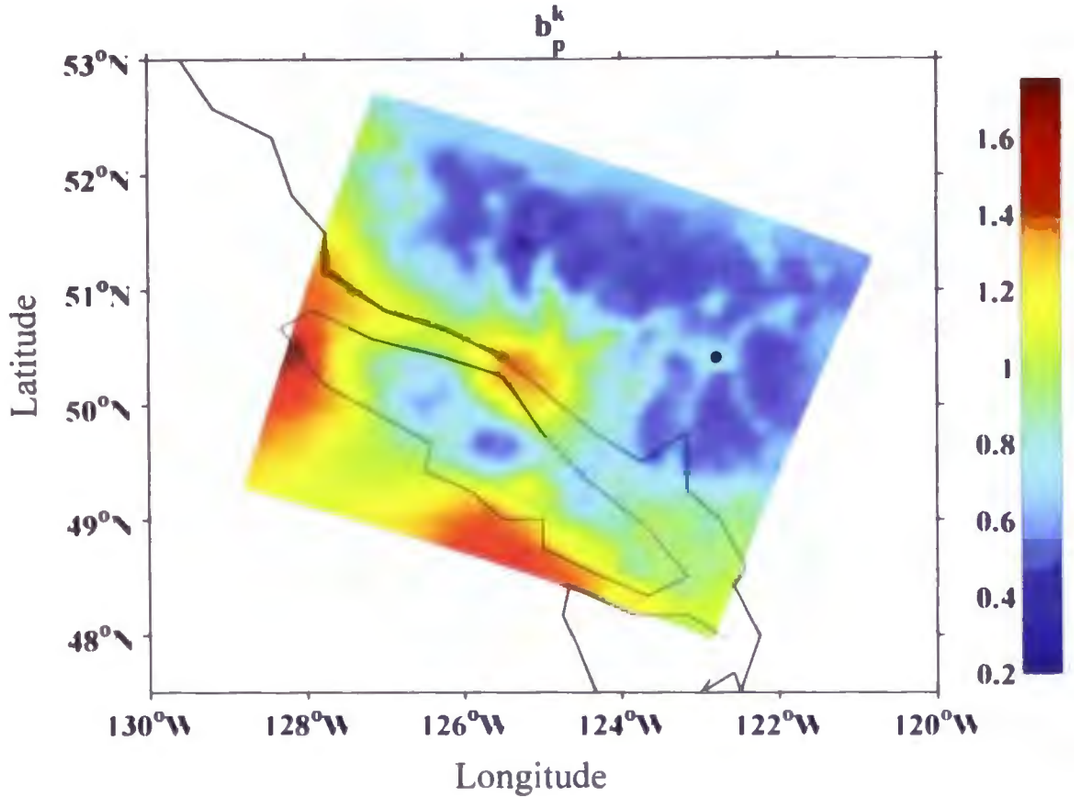

Figure 4.2 Bias correction factors (Observed/Modelled) for RAMS daily precipitation over the RAMS domain. The bias is determined using daily data from 1979-2008 (Ainslie and Jackson 2010). The black dot refers to the location of Place Glacier within the RAMS domain.

RAMS bias-corrected daily precipitation averaged over a period 1979-2008 is shown in Figure 4.3. Comparison of bias-corrected RAMS precipitation with daily PRISM precipitation gives a spatially averaged daily RMSE value of 4.6 mm day^{-1} (Figure 4.4). The difference in average daily precipitation between bias-corrected RAMS and PRISM climatologies shows a large region where they significantly differ. The difference is particularly large in the interior of Vancouver Island and along the southern Coast Mountains. With few exceptions, bias-corrected RAMS precipitation over most of Vancouver Island appears to be drier. Along most of the southern Coast Mountains, the bias-corrected RAMS precipitation tends to be wetter. The difference is significantly small along the open strait between Vancouver Island and the mainland. The maximum, minimum and

mean differences for the entire domain are 12.16, -7.08, and 1.26 mm day^{-1} respectively. The spatially averaged bias-corrected daily RAMS precipitation of 6.86 mm day^{-1} compared well with the spatially averaged PRISM precipitation of 5.90 mm day^{-1}. The two climatologies compare well in regions with low precipitation along the eastern edge of Vancouver Island and in the northeastern corner of the modelling domain. Overall, RAMS produces a wetter climatology over the southern Coast Mountains There is no significant improvement in error statistics using monthly data. Precipitation validation results from this study are slightly different from the results obtained by Ainslie and Jackson (2010). Their results show relatively better agreement between the bias-corrected RAMS precipitation and PRISM climatologies. This could be because they used a modified PRISM dataset over BC and Yukon at a monthly time scale (Wang et al. 2006) whereas the comparison performed here used original PRISM dataset in daily time scale.

Ainslie and Jackson (2010) also applied water balance to 12 drainage basins located within the RAMS domain to test the consistency of both the raw and bias-corrected precipitation fields with the streamflow. They found that the bias-corrected RAMS residual in these basins are roughly 300 mm a^{-1} lower than the PRISM residual, suggesting that the bias-corrected RAMS climatology is better in this region. Also, they validated the winter season bias-corrected RAMS precipitation (monthly values) with a number of observations within the modelling domain. The errors in bias-corrected RAMS precipitation were found to be less than the errors in raw RAMS precipitation. The estimated error values were close to the errors in PRISM precipitation. Similarly, errors were also estimated using snow course data and glacier winter balance data. The errors in bias-corrected RAMS precipitation estimated using the snow course data improved significantly compared with the error in raw

RAMS precipitation with the same data. Similar results were found with glacier winter mass balance data.

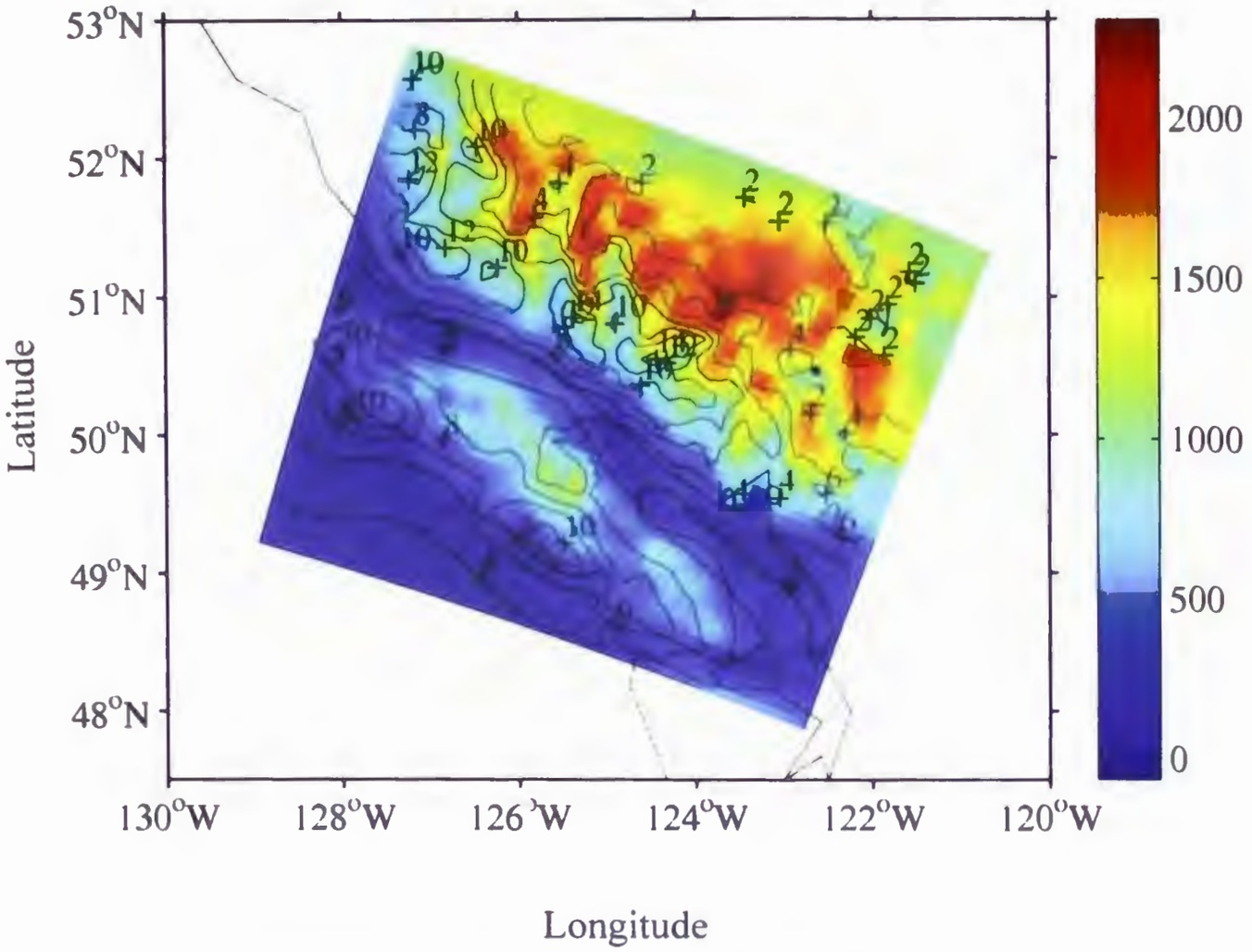

Figure 4.3 RAMS bias-corrected daily precipitation (mm day^{-1}) averaged over the period 1979-2008. The values are plotted over the topography of the inner 8 km RAMS domain (m a.s.l.). The black dot refers to the location of Place Glacier within the RAMS domain.

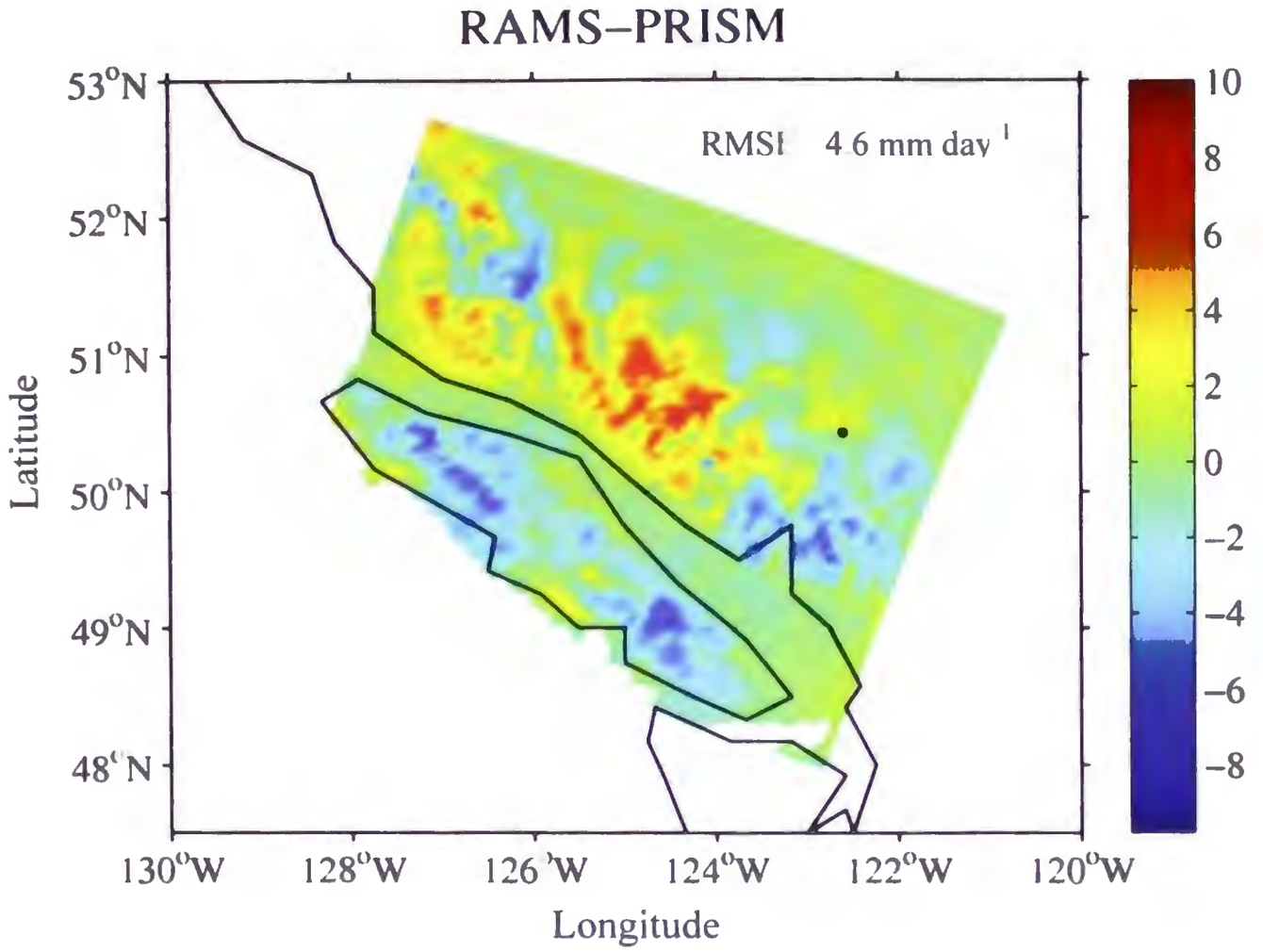

Figure 4.4 Difference between the long-term (1979-2008) averages of daily bias-corrected RAMS precipitation and PRISM precipitation (mm day^{-1}). RMSE refers to spatially averaged root mean squared error in the bias-corrected daily RAMS precipitation. The black dot refers to the location of Place Glacier within the RAMS domain.

The bias correction offsets for RAMS air temperature show a more or less uniform distribution within the domain (Figure 4.5). The estimated value within the domain ranges from 1.75 to -3.66°C with a mean of 0.75°C and a standard deviation of 0.50°C. Except for a few isolated locations, bias correction offsets for most of the locations within the domain lie between 0 and -1°C. The RAMS air temperature appears to have a cold (less than observed value) bias for most of the locations in the domain. This could be due to the RAMS model simulating snow on the ground until late in the season. There are a few isolated locations in

the southeastern part of the modelling domain where RAMS air temperature has a warm (greater than observed) bias. The estimated bias correction offset for RAMS air temperature for Place Glacier location is -0.93°C, which is applied to RAMS daily air temperature to correct for the bias. The bias-corrected RAMS air temperature over the entire domain has a maximum, minimum and a mean of 12.0, -3.8 and 4.7°C, respectively (Figure 4.6). These values are lower than the raw air temperature maximum, minimum and mean of 13.0, 3.5 and 5.4°C. Overall, the bias correction process appears to be lowering the maxima, minima and the mean in the modelled RAMS air temperature. The difference in average daily air temperature between bias-corrected RAMS and PRISM climatologies showed a highly variable result (Figure 4.7). Nearly 60% of the total grid cells within the domain reported bias-corrected RAMS air temperature cooler than PRISM air temperature while the remaining 40% reported it warmer than the PRISM air temperature. The maximum, minimum and mean differences for the entire domain are 3.30, -3.12, and -0.23°C respectively. The spatially averaged bias-corrected daily RAMS air temperature of 5.8°C compared well with the spatially averaged PRISM air temperature of 5.43°C. The spatially averaged RMSE in bias-corrected daily RAMS air temperature found by comparison with PRISM is estimated to be 1.44°C. Generally, the bias-corrected RAMS air temperature appears to be in relatively good agreement with its PRISM counterpart in the interior as compared to other locations. Jarosch et al. (2010) downscaled NARR temperature in the southern Coast Mountains using an interpolation scheme that reconstructs the vertical temperature structures to estimate surface temperatures from upper air data. They compared the downscaled results with the daily observed air temperature data from 2006-2008 for selected glacier sites in the region. For the location of Helm and Bridge glaciers, they

reported biases of 0.90°C and -0.70°C, respectively. For the same locations, the present study estimated biases of -0.90°C and -0.36°C, respectively. The temperature bias estimated here compared relatively better for the location of Bridge Glacier than for the location of Helm Glacier. However, it should be noted here that the bias estimated in this study is based on observations from a larger number of stations covering longer time period than the data used by Jarosch et al. (2010) for bias estimation.

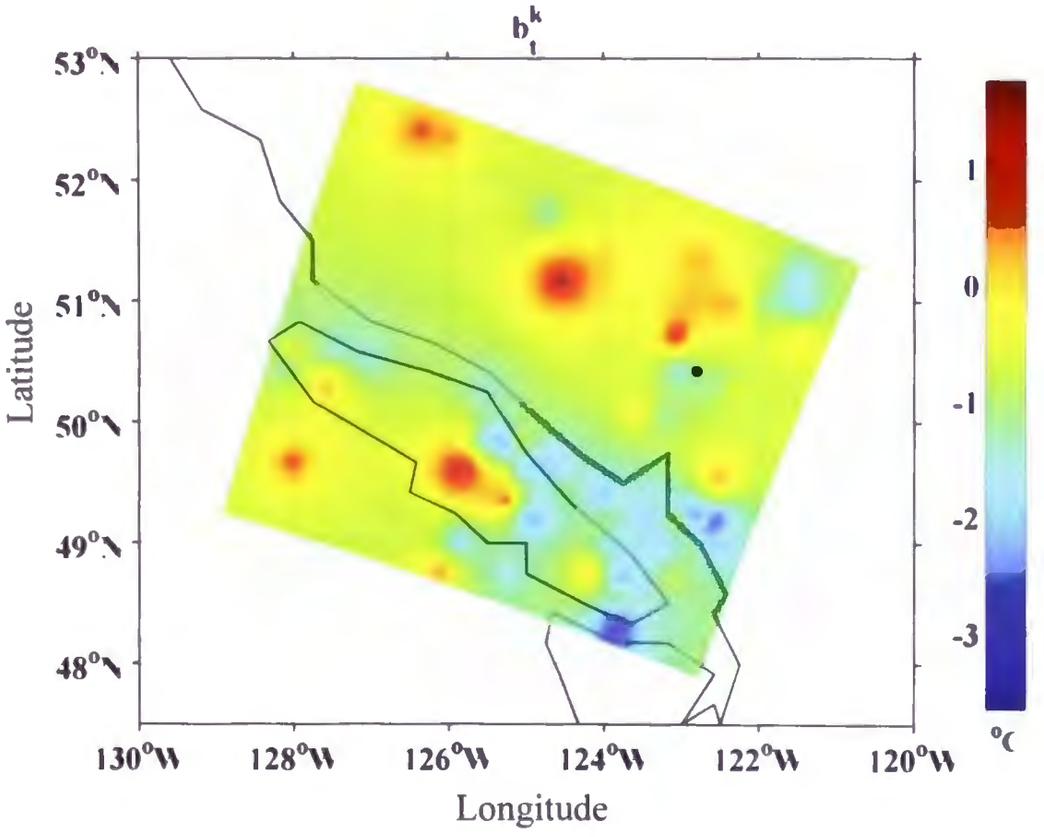

Figure 4.5 Bias correction offsets (Observed–Modelled) for RAMS daily air temperature over the RAMS domain. The bias is determined using daily data from 1979-2008. The black dot refers to the location of Place Glacier within the RAMS domain.

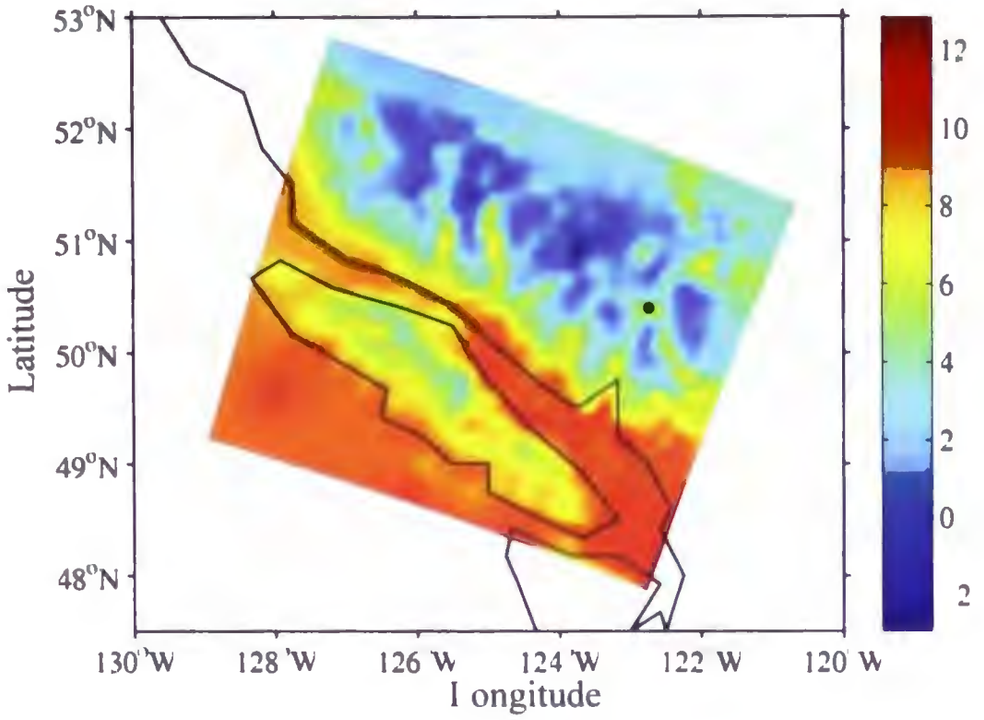

Figure 4.6 RAMS bias-corrected daily surface air temperature (°C) averaged over 1979-2008. The black dot refers to the location of Place Glacier within the RAMS domain.

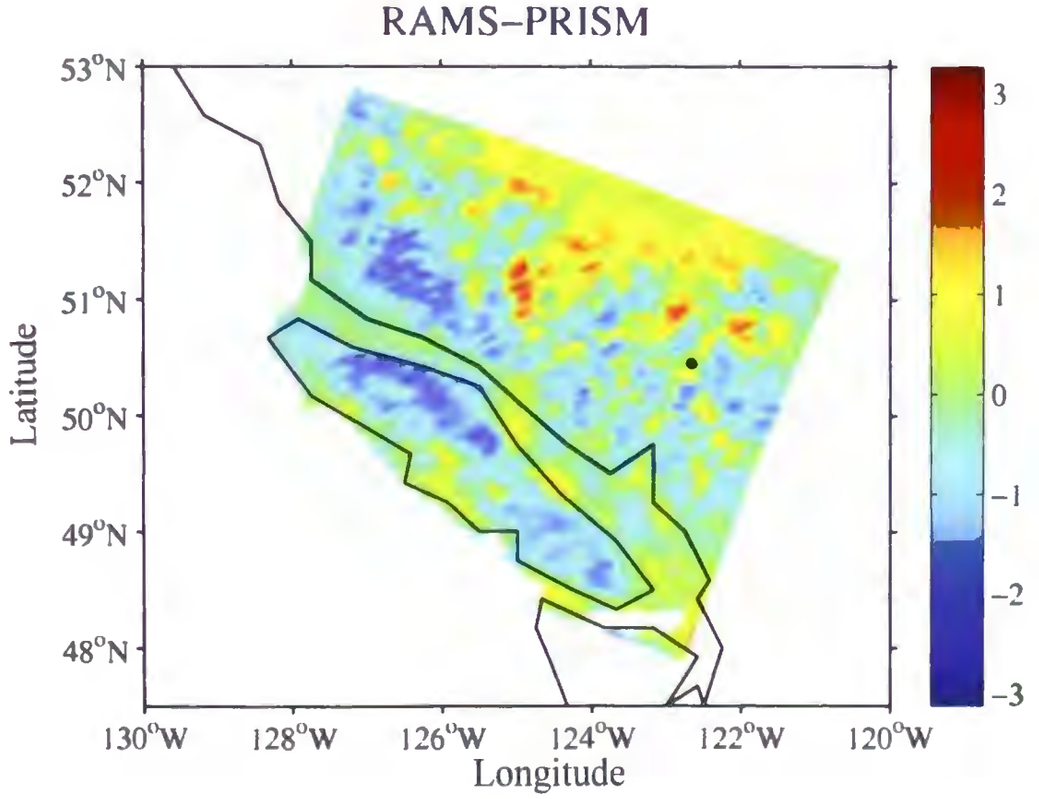

Figure 4.7 Difference between the long-term (1979-2008) averages of daily bias-corrected RAMS temperature and PRISM temperature (°C). RMSE refers to spatially averaged root mean squared error in the bias-corrected daily RAMS air temperature. The black dot refers to the location of Place Glacier within the RAMS domain.

4.6.2 Temperature Lapse Rate

For the location near Place Glacier, the calculated hourly air temperature lapse rate (Γ_t) averaged over the summer season from 1979-2008 is 7.3°C km^{-1} (Figure 4.8). The calculated lapse rate has a standard deviation of 1.7°C km^{-1}, which is nearly 25% of the mean value. The summer average temperature lapse rate determined using RAMS temperature sounding data showed similar values for different high elevation sites in the domain (Table 4.1). The rate of temperature change with height ranges from 6 9 to 7 7°C km^{-1}, which is close to the standard air temperature lapse rate of 6.5°C km^{-1} used previously at Place glacier and glaciers elsewhere in the world (e.g., Munro and Marosz-Wantuch 2009; Johanneson et al. 1995; Oerlemans 1992). Previously, Shea (2010) calculated an average summer season air temperature lapse rate of 5.0°C km^{-1} for Place Glacier Similarly, for South Cascade Glacier, which is influenced by same modes of climate as Place Glacier, an average summer season lapse rate of nearly 6.5°C km^{-1} has been reported (Anslow et al. 2008). Compared to these values, the lapse rate estimated here using RAMS vertical sounding is slightly larger. Since the RAMS reference elevation (1249 m) is lower than the minimum elevation of the glacier (1900 m), using these air temperature lapse rate values in the melt model may underestimate melt from Place Glacier.

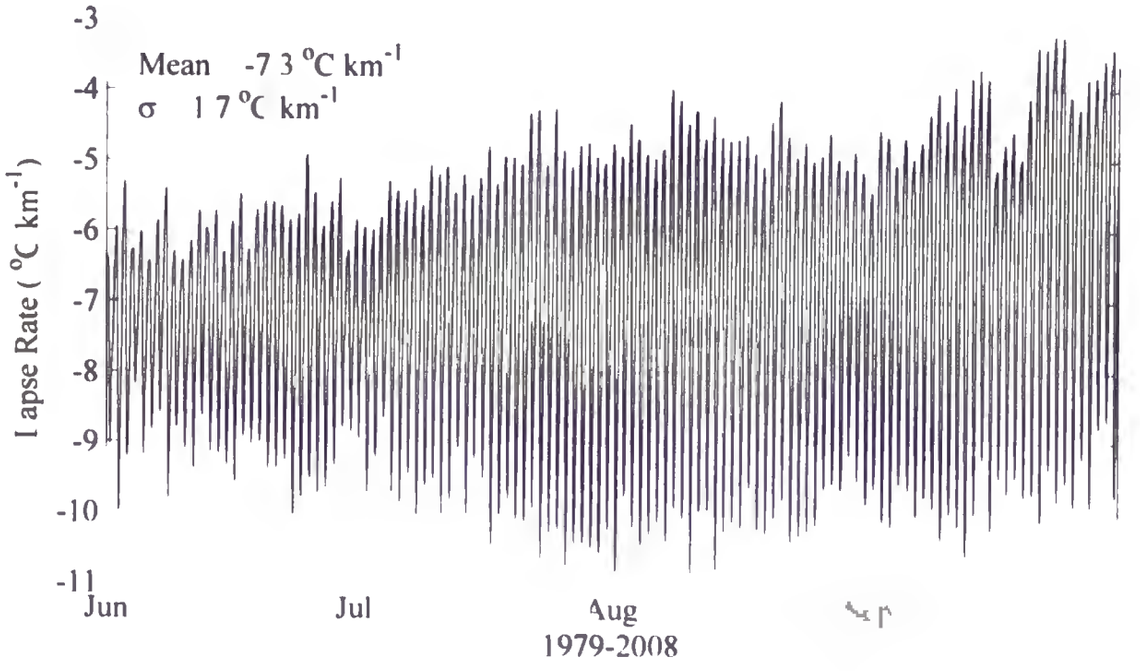

Figure 4.8 Hourly time series of calculated air temperature lapse rate (Γ) for summer months (June-September) for locations near Place Glacier. Values are averaged over the period 1979-2008. Mean and standard deviation of hourly lapse rate during this period are 7 3°C km^{-1} and 1.7°C km^{-1} respectively. Lapse rate refers to decrease in air temperature with height

The relationship between the adjusted RAMS air temperature and glacier air temperature measured at different elevations on Place Glacier is shown in Figure 4.9. For an off-glacier location, the scatter plot of RAMS bias-corrected air temperature and observed air temperature is closer to the 1:1 line indicating a lack of influence of cooling associated with katabatic winds. However, for on-glacier locations, the scatter plots appear to exhibit two different trends separated by a temperature T_c. For RAMS air temperature smaller than T_c, both temperatures approximately followed the 1:1 line suggesting a close agreement between RAMS and glacier air temperature. However, for RAMS air temperature greater than T_c, the temperatures values are significantly scattered around the 1:1 line and the slope is less than unity suggesting that RAMS temperatures overestimate glacier temperatures. A critical air temperature (T_c) values of nearly 5°C has been estimated (Figure 4.9, top right),

which represents the RAMS temperature for the development of katabatic winds. Above T_c, the glacier boundary layer will be under the influence of the KBL, which provides a cooling effect on the glacier surface layer. Below T_c, glacier air temperature should be approximately equal to the RAMS air temperature, as the KBL is either poorly developed or non-existent. Therefore, T_c can be considered as the critical ambient temperature required for the development of the KBL. A previous study on Place Glacier reported a similar result using ambient air temperatures and near-surface glacier temperatures (Shea 2010). This study reported T_c values ranging from 4.29 to 6.48°C at different locations on the glacier, which is similar to the 5°C estimated in the present study. Shea (2010) suggested an empirical method to correct for the KBL cooling effect when distributing off-glacier air temperature on the glacier surface The use of any empirical approach for air temperature distribution is avoided intentionally to facilitate generalizing the GMB model so it is transferable to other locations. Although there are some semi-empirical approaches for parameterizing sensible and latent heat fluxes within the KBL without direct correction of glacier air temperature (Oerlemans and Grisogono 2002; Munro and Marosz-Wantuch 2009), these approaches are too complex and beyond the scope of this study.

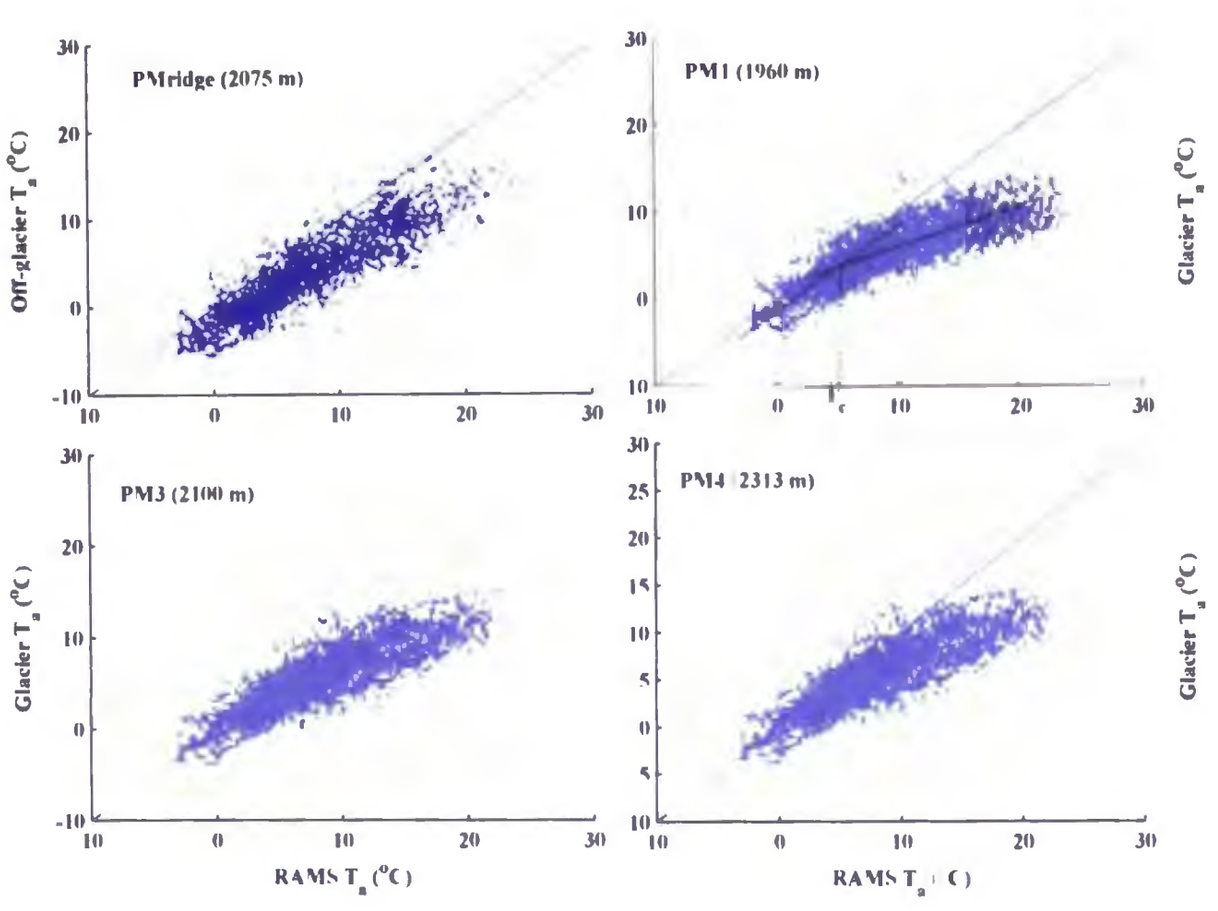

Figure 4.9 Comparison between RAMS bias-corrected air temperature and air temperature measured at an off-glacier location (top left), on glacier at 1960 m near the terminus (top right), on glacier at 2100 m a.s.l. (bottom left), and on the glacier at 2313 m (bottom right). T_c (5°C) refers to the critical RAMS temperature for the development of a KBL.

4.6.3 Precipitation Gradient

Calculated hourly summer precipitation gradient (Γ_{P1}) values averaged over a period 1979-2008 for the RAMS location closest to the Place Glacier is shown in Figure 4.10. The estimated gradient of hourly precipitation averaged over the summer season showed significant year to year variation. For Place Glacier, hourly precipitation gradient averaged over the summer season is -7.0×10^{-5} mm hr^{-1} m^{-1}. For all the selected locations (Table 4.1), the average summer season Γ_{P1} are negative suggesting that the hourly precipitation during summer decreases with elevation. Validation of this result is difficult as there have been no

studies that investigate hourly lapse rate of precipitation in the region. Most of the mass balance modeling works in the region has ignored summer accumulation (e.g., Shea 2010). For a more distant South Cascade Glacier, Anslow et al. (2008) calculated daily summer precipitation gradient values that ranged from 2.8 mm km^{-1} to 3.5 mm km^{-1} with a mean of 3.1 mm km^{-1}. The negative hourly precipitation gradient estimated here for Place Glacier and other glacier locations in the southern Coast Mountains do not agree with the results from South Cascade Glacier. The gradient of winter total precipitation ($\Gamma_{...}$) for Place Glacier exhibited significant inter-annual variation (Figure 4.11). The estimated values ranged from 0.6 to 1.5 mm m^{-1}. The average for the whole period (1980-2008) is nearly 1.0 mm m^{-1}. This value is twice as large as the long-term (1965-2005) average gradient of observed winter accumulation, which is only 0.5 mm m^{-1} (WGMS 2011). As a result, the GMB model may overestimate the winter accumulation on Place Glacier. There is a significant spatial variation in the estimated vertical gradient of winter total precipitation in the region (Table 4.1). The estimated values ranged from 0.29 mm m^{-1} for Helm Glacier to 1.47 mm m^{-1} for Bridge Glacier with a spatial average of 0.80 mm m^{-1}.

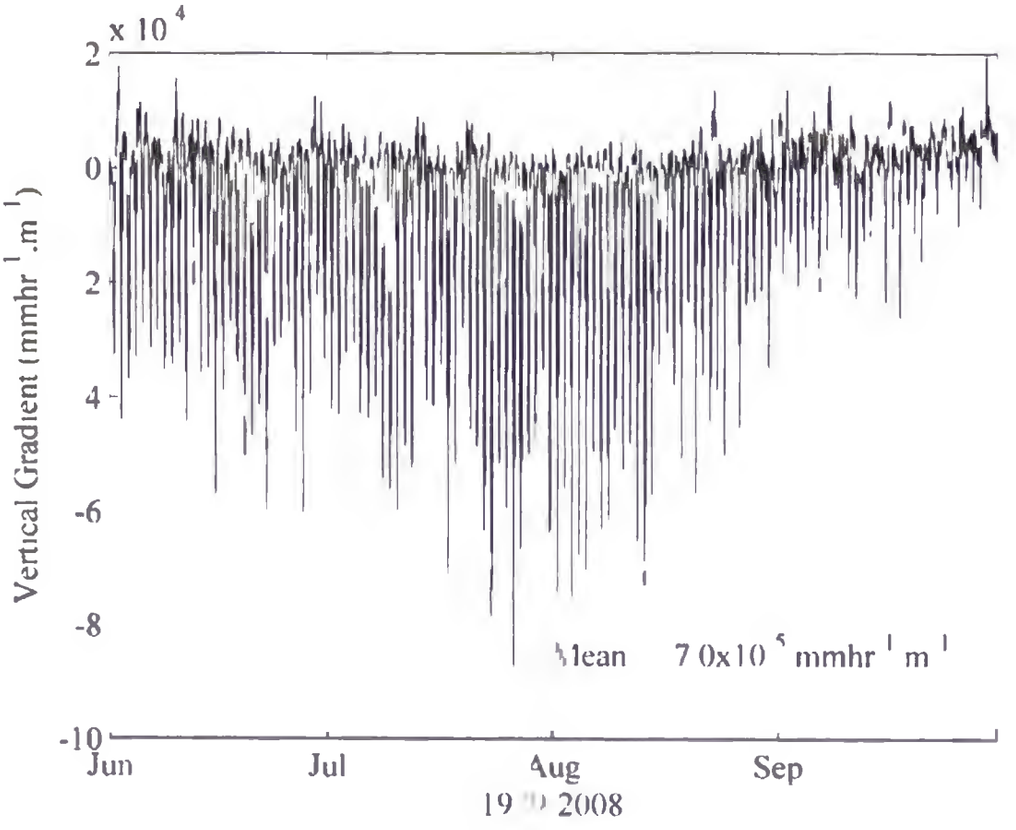

Figure 4.10 Vertical gradient of hourly summer precipitation (Γ_1) averaged over 1979-2008, Place Glacier. On average, the summer season precipitation decreased with increasing elevation.

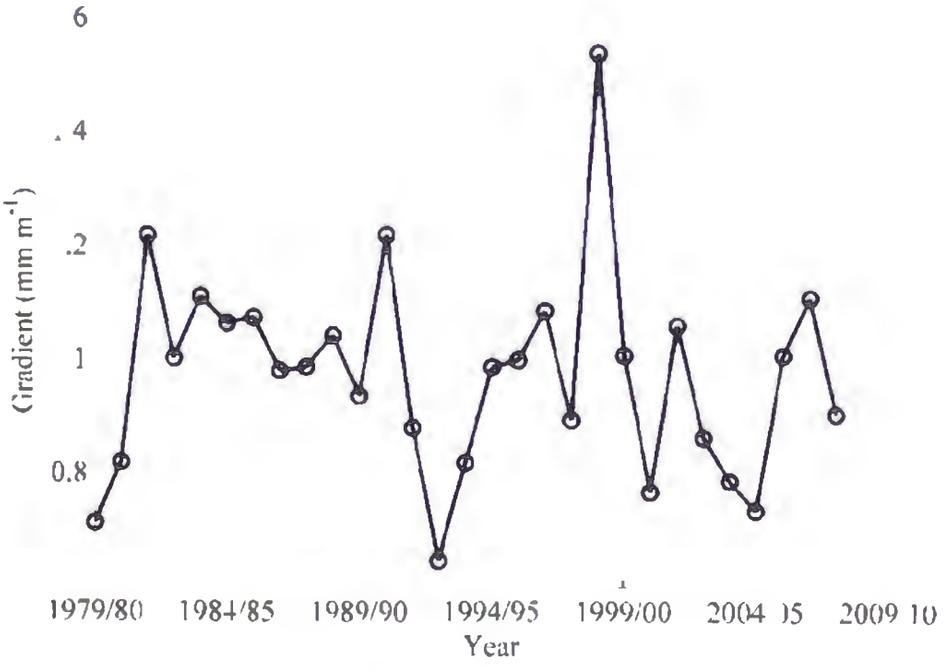

Figure 4.11 Vertical gradient of total winter season (1 October-31 May) precipitation (Γ_{P2}) estimated on Place Glacier. Average gradient for the entire period is 0.97 mm w.e.m^{-1}.

Table 4.1 Calculated lapse rate of RAMS summer air temperature, Γ_t, vertical gradient of hourly summer precipitation, Γ_{P1}, and vertical gradient of RAMS total winter precipitation, Γ_{P2}, from the grid cell nearest to selected glacier sites (Figure 4.12). All values are averages over 1979-2008.

Study glacier	Γ_t ($^{o}C.m^{-1}$)	Γ_{P1} (mm w.e.m^{-1})	Γ_{P2} (mm w.e.m^{-1})
Place	-7.7×10^{-3}	-7.0×10^{-5}	0.97
Bridge	$-6.9\cdot10^{-3}$	$-5.9\cdot10^{-5}$	1.47
Helm	$-7.3\cdot10^{-3}$	$-3.3\cdot10^{-5}$	0.29
Tiedemann	$-7.4\cdot10^{-3}$	$-2.0\cdot10^{-4}$	0.43

4.6.4 Elevation Correction

In the RAMS model, topography is averaged and smoothed over the relatively coarse RAMS horizontal resolution of 8 km. As a result, the model averages the elevation of the glacier and the surrounding mountains. Therefore, the RAMS elevation for a particular location is usually higher than the actual elevation. Elevation differences for grid cells close to a few selected glacier sites in the southern Coast Mountains (Figure 4.12) relative to CDED DEM are presented in Table 4.2. According to the RAMS model topography, the elevation of the RAMS grid cell nearest to Place Glacier is 1249 m whereas for the same location the CDED DEM gives an elevation of 998 m, a difference of -251 m. in elevation. This difference in elevation is found to vary from one location to another. RAMS grid cells nearest to the Helm and Bridge Glaciers, which are not very far from Place Glacier, have elevation differences of -574 m and -158 m, respectively. In contrast, the RAMS grid cell closest to the more northern Tiedemann Glacier shows an elevation difference of -350 m.

relative to CDED DEM. The RAMS topography is generally showing higher elevation than the CDED DEM for most of the locations.

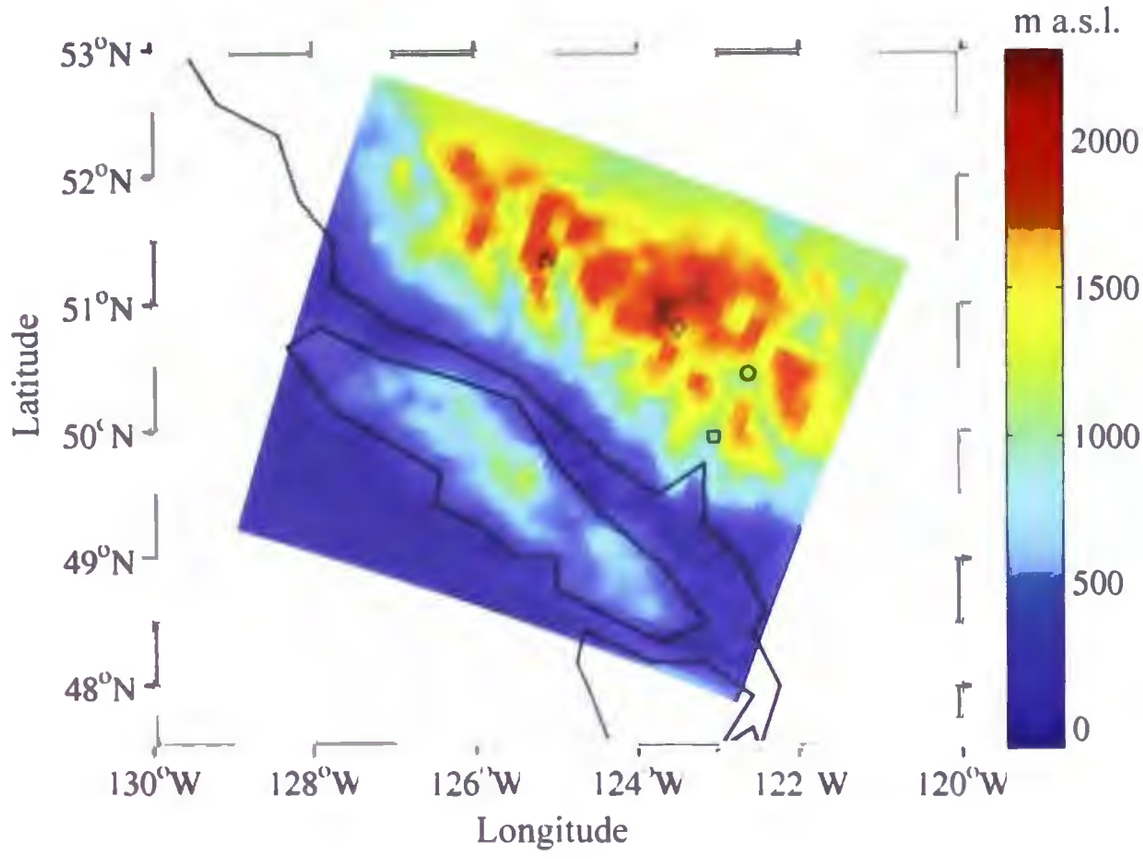

Figure 4.12 Location of Helm Glacier (□), Place Glacier ( ), Bridge Glacier (◊), and Tiedemann Glacier (Δ) in the southern Coast Mountains overlaid onto topography of the inner 8 km RAMS domain (m). These glacier sites are selected for determining elevation difference.

Table 4.2 Elevation (m a.s.l.) of RAMS grid cell nearest to selected glacier sites (Figure 3.10) as reported by CDED (H_{CDED}) and RAMS (H_{RAMS}) topography.

Glacier sites	H_{CDED}	H_{RAMS}	$H_{CDED} - H_{RAMS}$
Place	998	1249	-251
Bridge	1522	1680	-158
Helm	1688	1114	-574
Tiedemann	1482	1832	-350

Although there is a high-resolution SRTM 90 m DEM available, CDED DEM is considered for the present study because this DEM surface is derived from the topographic information of 1986, which is close to the year when historic GMB model run begins. On the contrary, the SRTM DEM is based on data collected in 2000, making it unsuitable to be used as a DEM surface for GMB modelling prior to this year. RAMS temperature and precipitation are adjusted for elevation difference relative to CDED DEM using their vertical gradients from RAMS model

4.7 Conclusion

The RAMS model overestimates precipitation in the interior and underestimates it in the Coast Mountains and Vancouver Island. There is relatively better agreement between bias-corrected RAMS precipitation and PRISM precipitation in the interior than in the Coast Mountains. Bias in RAMS air temperature is more or less uniformly distributed within the domain. Biases are relatively small in the coastal ranges and in the interior. Overall, the RAMS model seems to have a cold bias. However, validation of bias-corrected RAMS air temperature with PRISM temperature shows a mixed result in the domain. There is no distinct spatial pattern in the difference between the bias-corrected RAMS and the PRISM climatologies. Generally, the bias-corrected RAMS air temperature tends to be cooler than PRISM air temperature over the mountain range and over most of the locations on Vancouver Island. The bias-corrected air temperature agreed relatively better with the PRISM temperature over the coast than in the interior. However, it should be noted here that PRISM air temperature dataset cannot be considered as an entirely independent dataset for validation purposes. Station observations used here for estimating bias in RAMS air

temperature may also have been used in the PRISM regression model for spatial interpolation of air temperature. Therefore, the RAMS bias-corrected air temperature validation results presented here should be interpreted cautiously. Similarly, bias-corrected RAMS air temperature and precipitation results from some of the remote locations should also be interpreted cautiously as the bias for these locations are estimated based on a limited number of observations from these locations

For different sites in the southern Coast Mountains, the RAMS topography generally shows an elevation higher than the elevation relative to CDED DEM. This elevation difference is due to RAMS model averaging and smoothing the topography over its relatively coarse horizontal resolution of 8 km. RAMS air temperature and precipitation are corrected for the elevation difference between the RAMS topography and CDED DEM.

The lapse rate of hourly summer air temperature calculated for a number of sites in the southern Coast Mountains using the RAMS vertical temperature sounding data yielded results comparable to the standard air temperature lapse rate. For a location near Place Glacier, the calculated lapse rate value is slightly larger than the one estimated using in situ observations.

The comparison of bias-corrected RAMS air temperature and glacier temperature on Place Glacier shows the influence of cooling within the KBL on air temperature. Therefore, for the accurate distribution of air temperature on the glacier surface, it is important that this cooling effect be considered carefully. Although an empirical approach has been suggested previously for resolving this issue (e.g., Shea 2010), a physically-based approach is more desirable.

For selected locations in the southern Coast Mountains, the hourly summer precipitation gradient calculated from RAMS precipitation are generally negative suggesting a decrease in precipitation with elevation. The negative precipitation gradient may result in less than usual summer snowfall on Place Glacier thus overestimating melt on the glacier surface due to decreased surface albedo. This result is not consistent with the result obtained at South Cascade Glacier (Anslow et al. 2008), which reported positive gradient of daily summer precipitation. However, it should be noted here that the two results being compared here are of different temporal scales, daily results from South Cascade Glacier vs. hourly results from Place Glacier. Further research on hourly precipitation gradient in the region is recommended before making any conclusion. The gradient of RAMS winter total precipitation calculated for the Place Glacier location shows a large inter-annual variability. The long-term average gradient value is nearly twice as large as the long-term average observed values. This may potentially lead to overestimation of winter accumulation on the glacier surface.

Chapter 5

Glacier Mass Balance Modelling

5.1 Introduction

Glacier melt models of varying complexities can be used within a GMB model for determining glacier ablation, an important component of glacier mass balance. Traditionally, these melt models have been used for simulating river runoff in alpine regions for purposes such as operational forecast of streamflow, ecosystem modelling, and community water supplies. These melt models range from simple empirical temperature index (TI) models (Braithwaite 1995, Hock 2003), enhanced TI models (Hock 1999; Pellicciotti et al. 2005), to more complex physically-based Surface Energy Balance (SEB) models (Escher-Vetter 1985; Munro 1990; Oerlemans 1992; Arnold et al. 1996; Klok and Oerlemans 2002; Hock and Holmgren 2005). These models can operate at scales ranging from point melt estimates to fully distributed models. Despite the computational complexities, SEB melt models are the most physically-justified forms of melt models with a proven ability to accurately simulate snow and glacier melt (Hock 2005; Shea 2010).

The objective of this research is to develop and apply a distributed SEB-based GMB model in the southern Coast Mountains of BC. The study site is Place Glacier in the southern Coast Mountains of BC, Canada (described in Chapter 2). A hindcast of the Place Glacier GMB is developed using Regional Atmospheric Modeling System (RAMS) mesoscale atmospheric model output (Ainslie and Jackson 2010), which is available from 1979-2008 (29 years) over the BC southern Coast Mountains at a spatial resolution of 8 km. The model results are evaluated using observed mass balance. Additionally, the model is

used to examine the sensitivity of summer ablation and winter accumulation to variation in those physical parameters that govern the physics of the model. Also, the performance of the GMB model in simulating summer ablation is evaluated against the performance of two empirical melt models: (i) a TI melt model and (ii) an enhanced TI melt model. All models are forced with relevant RAMS variables retrieved from a grid cell closest to Place Glacier. Air temperature and precipitation used in the models are bias-corrected (Chapter 4).

5.2 GMB Model Formulation

At a particular model DEM cell, the annual net glacier mass balance (b_n) is the sum of winter balance (b_w) and summer balance (b_s)

$$b_n = b_w + b_s \tag{5.1}$$

where b_s is usually negative. To simplify the model, any melting during the winter season is neglected. As a result, b_w simply represents winter accumulation. The distributed GMB model developed for Place Glacier consists of two main components that separately simulate b_w and b_s on the glacier surface.

For each model grid cell, b_s is determined as a sum of the differences between summer accumulation, P_s, and summer melt, Q_M, taken over the entire summer season (1 June-30 September):

$$b_s = \sum_{1\,June}^{30\,Sept} (P_s - Q_M) \tag{5.2}$$

b_w, b_s, and b_n modelled at each cell are averaged across the DEM to obtain glacier-wide winter balance (B_w), summer balance (B_s), and annual net balance (B_a), respectively.

5.2.1 Modelling Winter Balance

For each model grid cell, winter balance is modelled by distributing RAMS winter (1 October-31 May) total precipitation using its vertical gradient

$$b_w = P' + \Gamma_{P2}.[h - H] \tag{5.3}$$

where P' is the RAMS bias-corrected winter snow total for the given year (Chapter 4), Γ_{P2} is the estimated vertical gradient of RAMS winter precipitation totals (Chapter 4), h is the elevation of each point on the glacier, and H is the elevation of the RAMS grid cell from which meteorological variables are retrieved.

5.2.2 SEB Melt Model

Q_M is calculated as a residual of the SEB equation using the following formulation (e.g., Hock and Holmgren 2005; Anslow et al. 2008),

$$Q_M = \frac{(K_{net} + L_{net} + Q_H + Q_E + Q_R - Q_G)}{L_f} \tag{5.4}$$

where K_{net} is the net shortwave radiation, L_{net} is the net longwave radiation, Q_H and Q_E are turbulent fluxes of sensible and latent heat, respectively, Q_R is heat supplied by rain falling at temperature greater than 0°C, Q_G is the heat transferred to and from the glacier

subsurface when the ice or snow of the subsurface changes temperature and L_f is the latent heat of fusion of ice (–3.34 × 10^5 J kg^{-1}). It is assumed that all rain and meltwater runs off and any surface evaporation and sublimation is neglected. Also, energy transferred due to subsurface melting and freezing is disregarded (e g., Hock and Holmgren 2005). All fluxes have units of W m^{-2}. Methods used for calculating different SEB terms in Equation (5.4) are presented next.

Solar Radiation

Solar radiation arriving at a particular location on the glacier surface is composed of both direct and diffuse components that are influenced by the amount of cloud, terrain slope and aspect, and surrounding topographic shading. The model estimates solar radiation on the glacier surface by first partitioning the RAMS solar radiation into direct and diffuse components. Partitioning is done using the diffuse fraction, f, which is determined based on the ratio of RAMS solar radiation, K_{in}, to potential radiation, K_{pot} values. Potential radiation is calculated following Iqbal (1983):

$$K_{pot} = I_0 \left(\frac{R_1}{R_2} \right)^2 \psi^{\frac{P}{P_0 \cos Z}} \qquad (5.5)$$

where I_0 is the solar constant (=1368 W m^{-2}), R_1 and R_2 are the mean sun–earth and instantaneous distances respectively, P is station level pressure, P_0 is mean atmospheric pressure at sea level (=1013.25 hPa), ψ is the atmospheric clear-sky transmissivity, which is kept constant at 0.75 (Oke 1987) and Z is the local zenith angle, which is calculated using the algorithm of Walraven (1978).

f is calculated using the empirical relationship developed for an alpine site in western Canada (Huo 1991):

$$f = \begin{cases} 0.12 & \frac{K_{in}}{K_{pot}} \geq 0.8 \\ 0.166 + 9.57.K_n - 36.71.K_n^2 + 48.50.K_n^3 - 22.03.K_n^4 & 0.22 < \frac{K}{K_{pot}} < 0.8 \\ 1.015 - 0.208.K_{in} & \frac{K_{in}}{K_{pot}} \leq 0.22 \end{cases} \quad (5.6)$$

The diffuse (K_{dif}) and direct (K_{dir}) radiation components are calculated using f from equation (5.6):

$$K_{dif} = K_{in}.f \quad (5.7)$$

$$K_{dir} = K_{in}.(1-f) \quad (5.8)$$

In a mountainous area, radiation arriving on the valley floor is controlled by the surrounding terrain. Direct radiation from the atmosphere is greatly reduced by the surrounding valley walls and therefore most of the shortwave radiation is comprised of diffuse radiation received from the surrounding slope. The effect of terrain on radiation arriving at the glacier surface is incorporated by considering the hemispheric fraction of sky viewable at a given grid cell. This fraction, also known as sky-view factor, Φ, is determined from the elevation of the surrounding grid cells using the algorithm proposed by Dozier and Frew (1990). Total shortwave radiation arriving at a particular grid cell on the glacier surface is calculated using the following equation:

$$K = [K_{dir}.\cos\varphi + K_{dif}.\Phi + K_{in}.\alpha_t(1-\Phi)] \quad (5.9)$$

φ is the angle between the solar beam and the vector normal to the grid cell in question and α_t is the albedo of the surrounding terrain, which is fixed at 0.21 (MacDougall and Flowers 2011). φ is calculated using the equation proposed by Garnier and Ohmura (1968):

$$\cos\varphi = \cos\theta\cos Z + \sin\theta\sin Z\cos(\phi_0 - \phi) \qquad (5.10)$$

where θ is the slope angle of the surface and ϕ_0 and ϕ are the solar azimuth and the slope azimuth angles, respectively. The effect of shadows cast by terrain on direct solar radiation is not considered.

The net shortwave radiation absorbed on the glacier surface is calculated by adjusting K for surface albedo, α:

$$K_{net} = K(1-\alpha) \qquad (5.11)$$

Albedo Submodel

A number of albedo parameterization models have been developed for different alpine glaciers around the world (Oerlemans and Knap 1998; Klok and Oerlemans 2004; Brook et al. 2000) and have been used within a SEB model on glaciers in alpine locations (Hock and Holmgren 2005; Anslow et al. 2008; Munro and Marosz-Wantuch 2009). The present study follows the work by Munro and Marosz-Wantuch (2009) and used the albedo model of Oerlemans and Knap (1998):

$$\alpha_{snow} = \alpha_{os} + (\alpha_{ns} - \alpha_{os})\exp(\frac{-t}{t^*}) \qquad (5.12)$$

where α_{ns} and α_{os} are the albedo of new snow (0.84) and old snow (0.65), respectively (Cuffey and Paterson 2010), t is the time elapsed since the last snowfall event and t^* is a time scale (21.9 days). Albedo decay is performed by taking t 31 days, which allows for aging of snow cover prior to when a model run begins (Munro and Marosz-Wantuch 2009). t value is set at the beginning of the model run and remain unchanged assuming that the summer snowfall has no influence on snow aging process Next, surface albedo, α, is modelled by including the effects of snow depth

$$\alpha = \alpha_{snow} + (\alpha_{\ f} - \alpha_{snow}) \exp(\frac{-d}{d^*}) \qquad (5\ 13)$$

where α_{snow} is the albedo of snow, α . the albedo of underlying surface, which can take the albedo value for either ice or firn, d is the specific mass of winter snow cover, and d^* is a characteristic snow depth scale. A d^* value of 25 mm w.e used by Anslow et al. (2008) is adopted here. The albedo of firn and ice are fixed at 0.53 and 0.29, respectively (Cuffey and Paterson 2010). Here ice albedo of that for dirty ice is used because the ablation area of most of the glaciers in the southern Coast Mountains is covered with some amount of dust during the summer melt season. According to Equation (5.12), the albedo of new snow decays exponentially with time. Similarly, according to Equation (5.13), the albedo decay process finally ceases once the winter snow cover has disappeared (i.e. d = 0) in which situation the surface albedo takes the value of that for the underlying surface.

Longwave Radiation

Similar to shortwave radiation flux, longwave radiation arriving on the glacier surface is greatly changed by the surrounding terrain. While part of the incoming longwave sky

radiation is obstructed by the surrounding valley wall, the glacier surface receives some additional longwave radiation emitted by the valley walls Net longwave radiation, L_{net}, at each model grid is estimated using the sky-view factor, Φ.

$$L_{net} = [L_{in}(\Phi) + L_{terrain}(1-\Phi)] - L_{out} \quad (5.14)$$

where L_{in} is the RAMS incoming longwave radiation and $L_{terrain}$ is the radiation received from surrounding terrain. $L_{terrain}$ is calculated as

$$L_{terrain} = \varepsilon_t \sigma T^4 \quad (5.15)$$

where ε_t is the emissivity of the surrounding terrain taken as 0 95 (Anslow et al. 2008), σ is the Stefan-Boltzmann constant (- 5 67 × 10 ⁻ W m⁻² K⁻⁴) and T is the surface temperature of the terrain, which is assumed to be the same as near surface air temperature. This parameterization has shown to work well despite being oversimplified (Greuell et al. 1997).

L_{out} is calculated from the glacier surface temperature, T_s, using the Stefan-Boltzmann relationship with emissivity of that for ice, ε_i=0.98 (Anslow et al. 2008):

$$L_{out} = \varepsilon_i \sigma T_s^4 \quad (5.16)$$

L_{out} reflected from the surface $(L_{out}[1-\varepsilon_i])$ is neglected.

Turbulent Heat Fluxes

Sensible (Q_H) and latent (Q_E) heat fluxes at the glacier surface are calculated employing a bulk transfer approach following recent SEB modelling work (Anslow et al. 2008; Hock and Holmgren 2005):

$$Q_H = \rho_a C_a C_D u(T_g - T_s) \quad (5.17)$$

$$Q_E = \rho_a L_v C_D u(0.622/P)(e_g - e_s) \quad (5.18)$$

where ρ_a is the dry air density that is calculated on each model grid using the ideal gas equation, C_a is the specific heat of dry air (=1004 J kg^{-1} K^{-1}), L_v is the latent heat of vapourization for water (=2.45 × 10^6 J kg^{-1}). P, u, T_z, and e_g are station pressure (hPa), wind speed (m s^{-1}), air temperature (°C), and vapour pressure (hPa) at the reference height of 2 m above the glacier surface, respectively T_s and e_s are temperature and vapour pressure at the surface, respectively. e_s is calculated from the saturation vapor pressure over a plane surface of pure water at temperature T_s using a standard formulation C_D is the turbulent transfer coefficient for heat and water vapour that is calculated as.

$$C_D = \frac{k^2}{[\log(z/z_0).\log(z/z_t)]}.\Theta \qquad (5.19)$$

where k is the von Karman constant (=0.41), z_0 is the roughness length for momentum (m), z_t is the roughness length for temperature and water vapour (m), z is the measurement height (m), and Θ is the stability correction (Webb 1970; Hock 1998). Stability is estimated using the bulk Richardson number R_b (Moore 1983, Hock 1998, Sicart et al. 2005):

$$R_b = \frac{gz(T_g - T_s)}{u^2(T_g + 273.15)} \qquad (5.20)$$

where g is the gravitational acceleration (9.8 m s^{-2}). Θ is determined following work by Braun (1985), which was also applied successfully for GMB modelling in the eastern Nepalese Himalaya (e.g., Kayastha et al. 1999):

$$\Theta = (1+10R_b) \qquad (5.21)$$

The magnitude of Θ depends on the sign of R_b, with positive R_b for stable conditions, and negative R_b for unstable conditions.

Previously, surface energy balance calculation on Place Glacier used z_0 values of 1 mm and 2 mm over snow and ice surfaces, respectively (Shea 2010). These values are adopted from a similar study on Haut Glacier D'Arolla, a temperate glacier in the Swiss Alps (Pellicciotti et al. 2005). Additionally, Shea (2010) scaled z_t to z_0, with $z_t = z_0 / 300$, following work by Hock (1998). For the present study, these roughness length values are directly adopted from Shea (2010)

The Prandtl model for estimating profiles of wind speed and temperature in pure katabatic flows has been used previously over Place Glacier (Shea 2010). The present study followed this work for simulating katabatic wind on the glacier surface. The Prandtl model is based on the assumption that buoyancy forcing (from the temperature deficit) and friction are the only terms that determine the downslope momentum budget. Analysis of RAMS air temperature and observed air temperature for Place Glacier yielded a critical ambient air temperature (T_c) of approximately 5°C required to initiate the development of a KBL. For ambient air temperature greater than or equal to T_c, katabatic winds (u) are simulated using the Prandtl model formulation proposed by Oerlemans and Grisogono (2002):

$$u(z) = -C\mu e^{-z\lambda} \sin(z\lambda) \tag{5.22}$$

where length scale (λ) and momentum scale (μ) are given by:

$$\lambda = \left[\frac{4T_s K_M K_H}{\gamma g \sin^2(\theta)}\right]^{1/4} \tag{5.23}$$

$$\mu = [\frac{gK_H}{T_s \gamma K_M}]^{1\ 2} \quad (5.24)$$

The surface temperature deficit $C = T_a - T_s$, where T_a is the ambient air temperature, which is assumed the same as T_g. K_M and K_H are eddy diffusivities of momentum and heat respectively. Values of $K_H = K_M$ 0 2 m^2 s^{-1} are adopted from a previous study on Place Glacier (Shea 2010). γ is the background potential temperature lapse rate, which is kept constant at -0.006 K m^{1} following Shea (2010) θ is the glacier surface slope. For situations when ambient air temperature is less than T_s, surface wind speeds will simply take the value equal to the RAMS wind speed. An average katabatic wind is estimated for the whole glacier and the same value is replicated for each grid cell. There may be a situation when the RAMS winds are strong enough not to allow the katabatic winds to develop. However, this situation is not considered here to avoid the computational complexity.

Heat supplied by rain (Q_R) is calculated assuming that falling rain has the same temperature as the near surface glacier air temperature:

$$Q_R = C_w P_r T_g \quad (5.25)$$

where C_w is the heat capacity of water (4.18×10^6 J m^{-3} K^{-1}), P_r is the depth of rainfall (in m), and T_g is near surface air temperature.

5.2.3 Subsurface Heat Flux and Surface Temperature

Various studies have suggested including sub-freezing surface temperature and the heat flux into the glacier for SEB modelling on cold (polar) glaciers (Greuell and Oerlemans 1986;

Konzelmann and Braithwaite 1995; Klok et al. 2005). A group of studies even suggested incorporating these components for SEB modelling on temperate glaciers as the changes in temperature of the glacier surface layer have been found to be linked with the storage and release of substantial amounts of energy (Hock 2005, Pellicciotti et al. 2008). Several subsurface models have been applied to simulate englacial temperatures and the conductive heat flux into a glacier (Klok and Oerlemans 2002, Corripio 2003; Brun et al. 1989; Andreas et al. 2004). In the present study, glacier surface temperature is simulated following a scheme similar to the one used by Klok and Oerlemans (2002), which has recently been applied for SEB modelling on glaciers in the Donjek Range, St Elias Mountains, Canada (Wheler and Flowers 2011, MacDougall and Flowers 2011). The subsurface scheme calculates the temperature change, ΔT_s, by solving the glacier heat flux, Q_G, as the residual of the SEB equation when the surface energy flux is negative, forcing the subsurface flux of heat into a thin subsurface layer, d :

$$\Delta T_s = \frac{Q_G}{\rho_s C_s d_s} \Delta t \qquad (5.26)$$

where Δt is the time-step in seconds, ρ_s and C_s are the density and specific heat capacity of the surface layer (= 2100 J kg^{-1} K^{-1} for ice). The thickness of the subsurface layer is chosen as d_s = 0.10 m following MacDougall and Flowers (2011). ρ_s values ranged from 100 kg m^{-3} (for fresh snow) to 900 kg m^{-3} (for ice) depending on surface conditions.

5.2.4 Precipitation and Air Temperature Distribution

In the GMB model, summer precipitation is distributed across the glacier DEM as:

$$P_g = P + \Gamma_{P1}.[h - H] \tag{5.27}$$

where P is the RAMS hourly precipitation (Chapter 4), Γ_{P1} is the estimated vertical gradient of RAMS hourly summer precipitation (Chapter 4), h is the elevation of each model DEM cell, and H is the elevation of the RAMS grid cell from where meteorological variables are retrieved

For each grid cell, summer accumulation (P_s) and summer rainfall (P_r) is calculated applying a static air temperature threshold (T_s) of 1 0°C for snow and rain.

$$P_s = P_g, \qquad (T_a \leq T_s) \tag{5.28}$$

$$P_r = P_g - P_s, \tag{5.29}$$

Similarly, summer temperature is distributed across the model DEM as:

$$T_g = T_a + \Gamma_t.[h - H] \tag{5.30}$$

where T_a is the RAMS hourly air temperature (Chapter 4), Γ_t is the estimated lapse rate of RAMS hourly air temperature (Chapter 4), h and H are same as in Equation (5.27).

5.2.5 Glacier Area Estimation

Computation of the specific surface mass balance on the glacier is based on the glacier area of the most recent geodetic survey, which usually remains constant for several years up until the next geodetic survey (Zemp et al. 2013). The assumption of constant glacier area may be

valid for a shorter time period such as a year or two for which the glacier area is less likely to change significantly. However, for longer time periods, as the glacier retreats, loss of area at predominantly lower elevations will make the area-averaged mass balance less negative (Leclercq et al. 2010). Under such a situation, mass balance time series computed with constant area, also known as reference-surface mass balances, need to be recalculated with updated glacier areas for every year in order to provide conventional balances (Elsberg et al. 2001; Huss et al. 2012).

Paul (2010) studied the influence of changes in glacier extent and surface elevation on modelled mass balance in the Swiss Alps. Results from Paul (2010) suggested that mass balances calculated forward in time with constant glacier extent are more negative than actual balances due to overestimation of glacier area whereas those calculated backward in time are more positive than in reality when glaciers have larger area in the past. In a similar study, Huss et al. (2012) compared the modelled time series of conventional and reference-surface balance of 36 glaciers in Swiss Alps and showed that conventional mass balance series differ relatively little from reference-surface balances. They argued that the small differences between conventional and reference-surface balances is due to the fact that about half of the negative (stabilizing) feedback on mass balance due to glacier terminus retreat is compensated by more negative mass balances due to surface lowering.

Most of the GMB modelling work is performed for generating mass balance time series mainly for hydrological purposes and therefore require the most recent glacier extent. The assumption of constant glacier extent in GMB modelling may not be a valid one for longer time periods. This is because as the glacier retreats its mean elevation rises thus potentially affecting the turbulent heat fluxes on the glacier surface. This will eventually

affect mass balance simulated on the glacier surface. The effects of glacier extent have only been roughly considered in mass balance models that simulates past and future glacier changes (e.g., Radić and Hock 2006). Stahl et al. (2008) used a volume-area scaling relationship (Chen and Ohmura 1990; Bahr et al. 1997) to simulate the glacier area change over time for one of the glaciers in BC, Canada. They calculated glacier area change and removed (added) equivalent number of glacier cells to account for the glacier area loss (gain). They then calculated glacier mass balances based on the new glacier area. In the present study, this approach is intentionally avoided to make the model less complex. In one study estimating future streamflow in the Columbia River Basin, BC, Bürger et al. (2011) rearranged the volume-area scaling relationship to estimate the glacier area by its mass. The area is then used to estimate glacier melt runoff as it is roughly proportional to the glacierized area. The current study uses a similar approach of glacier area estimation. Since there is a general consensus that glacier-wide mass balance will become less negative as a result of glacier retreat (e.g., Leclercq et al. 2010; Paul 2010), it is believed that the ratio between the glacier area calculated at the end of the balance year and the reference-glacier area can be used as a scaling factor to adjust glacier mass balances for changing glacier area. To implement this approach in the GMB model, the glacier area is first simulated using the volume-area scaling relationship (Chen and Ohmura 1990; Bahr et al. 1997):

$$v = ca^{y} \tag{5.31}$$

where v and a are the volume and surface area of the glacier, while c and y are scaling parameters. Owing to its simplicity, the volume-area scaling approach has been widely used for considering area changes in volume predictions (Radić and Hock 2006; van de Wal and Wild 2001). Based on theoretical considerations, for mountain glaciers Bahr (1997) derived

$\gamma = 1.375$, while an analysis on 144 measured glaciers yielded $\gamma = 1.36$ (Bahr et al. 1997). Using the same dataset, Bahr (1997) derived $c = 0.191 m^{1-\gamma}$, while Chen and Ohmura (1990) found $c = 0.2055 m^{3-2\gamma}$ for 63 mountain glaciers using $\gamma = 1.36$. To implement Equation (5.31) within the GMB model for area estimation, knowledge of c and γ is required. Unfortunately, these values are not available for Place Glacier. Therefore, for the present study, $\gamma = 1.375$ is adopted from Radić and Hock (2006) and the coefficient c is determined through calibration by running the GMB model from 1980 to 1985. The coefficient is fitted with the observations to obtain a minimum error in the estimated summer balance. These coefficients are used within the GMB model for estimating initial glacier volume (V_{int}) of Place Glacier using Equation (5.31). After each mass balance year a new glacier volume (V_{new}) is computed.

$$V_{new} = V_{int} + \frac{B_a}{\rho_i}.a \qquad (5.32)$$

where B_a is glacier-wide annual net mass balance and ρ_i is the density of ice. V_{new} is then used to derive new glacier area (a_{new}) following Equation (5.31). The ratio $\frac{a_{new}}{a}$ at the end of the mass balance year is used to scale the modelled glacier-wide mass balances to account for the change in glacier area every year. Over time, as the glacier retreats, this ratio will become less than unity, eventually approaching zero as the glacier disappears.

5.2.6 Model Calibration and Parameters

Most of the previous SEB melt modelling work has determined key model parameters by calibrating the model using observed mass balance records (e.g., Anslow et al. 2008; MacDougall and Flowers 2011). Such parameters include vertical gradients of precipitation, surface roughness lengths for momentum for snow and ice, the albedo decay parameter, atmospheric transmissivity and albedo of surrounding terrain However, MacDougall and Flowers (2011) found no significant improvement in model performance when roughness length parameters are tuned through model calibration thus raising a serious question about the usefulness of such calibration of SEB-based GMB model In contrast, the parameters used in the model presented here are not determined through model calibration, rather they are adopted directly from similar studies on Place Glacier (e g., Munro and Marosz-Wantuch 2009; Shea 2010). Some of the parameters are also adopted from similar studies on glaciers in the same region (e.g., Anslow et al. 2008) and elsewhere in the world (e.g., Oerlemans and Knap 1998; Cuffey and Paterson 2010; MacDougall and Flowers 2011). Albedo values for new snow, old snow, firn, and dirty ice used in this study are averages of the values reported in different studies. Parameters used in the model along with the representative ranges from the literature are given in Table 5.1.

Table 5.1 Model parameters for the GMB model together with corresponding representative literature ranges

Symbol (unit)	Description	Values	Literature Range
Γ_{P1} (mm m^{-1})	Vertical gradient of RAMS hourly summer precipitation	Variable[a]	
Γ_{P2} (mm m^{-1})	Vertical gradient of RAMS total winter precipitation	Variable[a]	
Γ_t (°C.m^{-1})	Lapse rate of RAMS summer air temperature	Variable[a]	
H (m)	Elevation of the RAMS grid cell from where input variables are retrieved	998[a]	
ψ	Clear sky atmospheric transmissivity	0 75[b]	0 69-0 76[c]
α_t	Albedo of surrounding terrain	0 21[d]	
α_{ns}	Albedo of new snow	0 88[e]	0 80-0 97[e]
α_{os}	Albedo of old snow	0 65[e]	0.63-0 67[b]
α_i	Albedo of slightly dirty ice	0 29[e]	0 26-0 33[e]
α_f	Albedo of firn	0 53[e]	0 43-0 69[e]
t (days)	Time elapsed since the last snowfall event	31[f]	
t^* (days)	Time scale for albedo decay modelling	21 9[g]	
d^* (mm w.e.)	Characteristic snow depth scale	25[i]	16-32[g,h]
T_x (°C)	Threshold air temperature for determining snow and rain	1 0[i]	0-2[f,i,j,k]
T_c (°C)	Critical ambient air temperature for the development of katabatic winds	5.0[a]	
ρ_{ns} (kg m^{-3})	New snow density	150[e]	100-200[f]
ρ_{os} (kg m^{-3})	Snow density at the end of melt season	552[b]	
ρ_f (kg m^{-3})	Density of firn	615[e]	400-830[f]
ρ_i (kg m^{-3})	Density of ice	877[e]	830-923[f]
z (m)	Reference measurement height	2	
z_{0s} (mm)	Surface roughness length for momentum for snow	1[b]	0.2-30
z_{0i} (mm)	Surface roughness length for momentum for ice	2[b]	0.1-80 [m]
ELA (m)	Equilibrium Line Altitude at the beginning of the model run	2200[n]	
A (km^2)	Area at the beginning of the model run	3.809[o]	
ε_i	Emissivity of glacier ice	0.98[i]	
ε_t	Emissivity of surrounding terrain	0.95[i]	
d_s (m)	Thickness of subsurface layer for surface temperature simulation	0.10[d]	

[a]Denotes that parameter is estimated in this study
[b]Shea (2010); [c]Greuell et al. (1997); [d](MacDougall and Flowers 2011); [e]averages across the literature values; [f]Cuffey and Paterson (2010); [g]Munro and Marosz-Wantuch (2009); [h]Oerlemans and Knap (1998); [i]Denby et al. (2002); [j]Anslow et al. (2008); [k](Arnold et al. 2006); [l]Loth et al. (1993); [m]Brock et al. (2006); [n]Pellicciotti et al. (2005); [o]Braithwaite and Muller (1980); [p]WGMS (2011)

5.2.7 Model Setup and Implementation

A control GMB model run is performed using the parameters given in Table 5.1. The model run for simulating b_s begins in the summer (1 June) of 1980 initialized with modelled winter snowpack (b_w) and glacier surface temperature (T_s), which is assumed to be 0°C initially. Two types of surfaces are considered beneath the winter snowpack: firn on the accumulation area and ice on the ablation area At the end of the summer melt season, these two zones are separated by the annual Equilibrium Line Altitude (ELA) where snow/firn transitions to bare glacier ice. After the disappearance of the winter snowpack, if the model grid cell is below this transition elevation, the model will consider the glacier surface as ice otherwise it will consider the surface as firn. The surface property values are assigned depending on whether the surface is firn or ice. To initialize the model, ELA at the end of the summer in 1979 (=2200 m a.s.l.) (Braithwaite and Muller 1980) is considered as the firn line that separates the accumulation and ablation areas. Also, an initial glacier area of 3.809 km^2 is used (WGMS 2011). The model is run in hourly time-steps during the summer melt season (1 June-30 September) until 2008. For each time-step, if the SEB flux residual is negative, this value is substituted for Q_G and ΔT_s is calculated for a 10 cm thick surface layer according to Equation (5.26). At the end of each time-step, the initial surface temperature is updated using ΔT_s and the new T_s is used to calculate the SEB for the next time-step. During the period of extended subfreezing temperatures, a positive SEB flux is first used to warm the subsurface layer and surface melting is not produced until the snow layer is warmed to 0°C by the subsurface heat flux. Surface density values ranged from 100 kg m^{-3} (for fresh snow) to 900 kg m^{-3} (for ice) depending on surface conditions. At the end

of the summer melt season every year, the model calculates b_s at each grid cell using Equation (5.2), which is then applied to Equation (5.1) to calculate b_n. ELA, glacier elevation and glacier area is updated at the end of the summer melt season and the updated values are used for melt simulation next year At the end of the model run every year, the ELA is determined as the elevation of zero net balance whereas area is estimated using volume-area scaling (Bahr et al 1997) (Equations 5 31 and 5 32). The effect of changes in glacier area on glacier-wide mass balances is included by adjusting it with the new area estimated at the end of the summer melt season At the end of the summer melt season, average glacier-wide surface lowering is estimated, which is then used to update the glacier DEM elevation for the following year. The model is developed using MATLAB script (MathWorks 2013).

5.2.8 Model Sensitivity Test and Experiment

Model sensitivity to parameter values and input meteorological variables is assessed by individually perturbing key model parameters and input variables while keeping other quantities at their respective control values. The model sensitivity test to parameter values will help understand how well the model is constrained and thus giving some idea of model uncertainty. On the other hand, sensitivity test to input meteorological variables can help understand how the GMB model will respond to the future changes in climatic conditions. For each sensitivity test, individual model parameters and input meteorological variables, except air temperature, are perturbed by 10% interval spanning ±20% (i.e. -20%, -10%, 0%, +10%, and +20%). Summer and winter temperatures are varied at the interval of 1 standard deviation (SD) spanning ±2SD in which SD is determined using long-term (1980-2008)

summer or winter air temperature. SD values of daily air temperature during summer and winter season averaged over 1980-2008 are nearly identical at 0.9°C. Model sensitivity tests are performed for Place Glacier relative to control runs in 1980 Model parameters and input variables for sensitivity tests are chosen following similar studies in the past (e.g., Kayastha et al., 1999, Anslow et al. 2008; MacDougall and Flowers 2011). Parameters selected for model sensitivity tests are α_{os}, $z_{}$, and Γ_{P2} whereas meteorological variables for sensitivity tests include summer and winter air temperature, incoming shortwave radiation, incoming longwave radiation, winter precipitation, vapour pressure and wind speed.

Additionally, model experiments are performed by fixing the surface temperature to assess the benefit of using complex processes over simpler processes. For the first set of experiments, processes governing the effects of summer snow are ignored (referred to as Setup 1), while for the second set of experiments the sub-model simulating glacier surface temperature is switched off assigning a fixed 0°C glacier surface temperature throughout the summer season (referred to as Setup 2). The results from model experiments are compared with corresponding observations to evaluate the model's predictive skill.

5.3 Empirical Melt Models

5.3.1 TI Melt Model

TI melt models are based on empirical relations between air temperature (T_a) and ablation (Braithwaite 1977). Melt M (in mm w.e. d^{-1}) is calculated as:

$$M = \begin{cases} k_s(T_a - T_0), & (T_a > T_0, \text{for snow}) \\ k_i(T_a - T_0), & (T_a > T_0, \text{for ice}) \\ 0, & (T_a \le T_0) \end{cases} \qquad (5.33)$$

where k_s is melt factor for snow (mm $K^{-1}d^{-1}$), k_i is melt factor for ice (mm $K^{-1}d^{-1}$), T_a is daily mean air temperature, T_0 is the threshold temperature (0°C) beyond which melt is assumed to occur. k_s is typically less than k_i because ice surfaces absorb more solar radiation than snow surfaces owing to their lower albedos. As a result, for an equivalent temperature, the TI melt model generates greater melt from ice surfaces than from snow surfaces. In a survey of melt factors, a wide range of values have been reported (Hock 2003). In western Canada, glaciers have been found to exhibit low spatial and temporal variability in melt factors of snow and ice obtained from historical mass balance data (Shea et al. 2009). For this study, snow and ice melt factors are adopted directly from Shea et al. (2009), which is determined by fitting the model to Place Glacier mass balance data from 1965 to 1995 using interpolated climate station air temperature (Stahl et al. 2006). Their estimated melt factors for snow (k_s=2.59 mm K^{-1} d^{-1}) and ice (k_i = 4.51 mm K^{-1} d^{-1}) were

used in this study. Previously, this model has been used on Place Glacier for melt model inter-comparison (Shea 2010).

5.3.2 Enhanced TI Melt Model

The Enhanced TI melt model includes both air temperature (T_a) and potential direct solar radiation (K_{pot}) for melt simulation (Hock 1999). Melt (in mm w e d^{-1}) is calculated as:

$$M = \begin{cases} T_a(F_m + r_s K_{pot}), & (T_a \le T_0 \text{ for snow}) \\ T_a(F_m + r_i K_{pot}), & (T_a \le T_0 \text{ for ice}) \\ 0, & (T_a \le T_0) \end{cases} \quad (5.34)$$

where F_m is a modified melt factor (mm K^{-1} d^{-1}), r_s and r_i are radiation melt factors for snow and ice, respectively (mm m^2 W^{-1} d^{-1} K^{-1}), and K_{pot} is potential solar radiation at the surface. K_{pot} is calculated using Equation (5.5) corrected for the angle of incidence on a sloped surface using Equation (5.10). Similar to the TI melt model, this model has also been applied on Place Glacier for melt model inter-comparison using F_m, r_s, and r_i values of 0.85 mm K^{-1} d^{-1}, 8.23×10^{-3} mm m^2 W^{-1} d^{-1} K^{-1}. and 1.53×10^{-2} mm m^2 W^{-1} d^{-1} K^{-1}, respectively (Shea 2010). For this study, F_m, r_s, and r_i are adopted directly from Shea (2010).

Both of these models are run for the same time period as the SEB melt model and using the same RAMS air temperature and winter snowpack amount. In contrast to the SEB-based model, which uses hourly RAMS variables, the empirical models use daily data.

5.4 Model Validation

The GMB model results from a control run are validated using historic mass balance records from Place Glacier (Chapter 3). The relative skill of the GMB model in simulating observed summer balance/melt is evaluated against the skill in TI and enhanced TI melt models. Error in the model results relative to the observations is quantified using absolute root mean squared error ($RMSE$ expressed in m w e) and relative root mean squared error ($RMSE_p$ expressed in %):

$$RMSE = \sqrt{\frac{1}{n}\Sigma\left(M^* - M\right)^2} \tag{5.35}$$

$$RMSE_p = \frac{RMSE}{\sqrt{M_m}} \times 100\% \tag{5.36}$$

where M^* is the modelled mass balance values, M is the observed mass balance values, n is the number of observations and M_m is the mean of the squared observed values.

5.5 Results and Discussion

5.5.1 Mass Balance Validation

A comparison between simulated and measured glacier-wide summer balance (B_s) over the period of 1980-2008 using the SEB-based GMB model yields an RMSE = 0.43 m w. e. ($RMSE_p$ = 15%) (Figure 5.1a). This is consistent with RMSE results obtained on the same

glacier using a full SEB model forced with in-situ meteorological data (0.49 m w. e) (Shea 2010). The small discrepancy in error is perhaps due to difference in model set up between the studies. In contrast to the model used in this study, Shea (2010) does not consider summer accumulation while simulating summer balance Also, the time period for running the model during summer months in the present study (1 June-30 September) is different from the time period used in Shea (2010) A similar study of the South Cascade Glacier (Anslow et al. 2008), which is influenced by the same modes of climate as Place Glacier, reported an average RMSE in simulated summer ablation of 0 24 m w. e. This is nearly half the RMSE in simulated B_s in the present study However, it should be noted here that the comparison is being made between two slightly dissimilar model results: glacier-wide summer ablation on South Cascade Glacier (no summer accumulation considered) against B_s on Place Glacier.

The comparison of simulated glacier-wide winter balance (B_w) with the historic glacier-wide winter balance data yields RMSE = 0.27 m w.e. ($RMSE_p$ = 21%), which is slightly larger than the percentage error in simulated B_s (Figure 5.1b). Based on this result, it can be argued that the RAMS winter precipitation gradient used in the model is performing fairly well in simulating B_w on the glacier surface. Similarly, the comparison of simulated glacier-wide annual net balance (B_a) with the observations gives an RMSE = 0.64 m w. e. ($RMSE_p$ = 50%) (Figure 5.1c). This error is relatively large compared to errors in simulated B_s and B_w. This is obvious because in both modelled and observed mass balance data, B_a is calculated as an algebraic sum of B_s and B_w where error in both the

mass balance components are cumulatively propagated to B_a resulting in a larger error result. The model reproduced 29% of the variability in the measured B_s. However, the simulated B_w could explain only 15% of the variance in the measured winter balance. The explained variance for simulated B_a is relatively better at 33%. The discrepancies between simulated and observed glacier mass balances may have been caused by several factors. The glacier mass balance data used here for model validation are glacier-wide mass balances, which are obtained by extrapolating individual stake data. As a result, these mass balance data may not represent actual mass balance on the glacier surface. The mass balance data used here for model validation therefore suffer from some amount of uncertainty. Likewise, observational error and sampling error adds further uncertainty in measured mass balance data. However, it is not possible to quantify the uncertainty in historic mass balance records due to the lack of error information in measured mass balance data. Also, it is often difficult to follow a fixed date for mass balance measurement on the glacier due to logistical reasons. As a result, the simulation period for summer (1 June-30 September) and winter balance (1 October-31 May) balance used in the GMB model may not be the same as the time period used in mass balance measurement on Place Glacier. This may have caused part of the discrepancies between modelled and measured mass balance results. Additionally, it is assumed that the glacier melt is negligible from 1 October- 31 May and any melt during this period is not considered. As a result, the GMB model may be overestimating the winter balance on the glacier surface thus affecting the estimation of net mass balance. In the GMB model, turbulent heat fluxes are calculated using surface roughness length values for snow and ice measured on glaciers elsewhere in the world. This has added further uncertainty in

GMB results on Place Glacier. Also, for a stable boundary layer, the turbulent transfer coefficients are corrected using formula in terms of the bulk Richardson number. However, this approach of stability correction tends to underestimate turbulent fluxes over the sloping glacier surface (e.g., Hock and Holmgren 2005). This is yet another source of uncertainty in modelled mass balance results.

The present GMB model also includes a volume-area scaling scheme for simulating glacier area at the end of the melt season (Figure 5.2). The fitted volume-area coefficient used in the model (=0.09) is comparable with 0.063, a coefficient determined on Storglaciären (Radić and Hock 2006), which is similar in size with Place Glacier. The derived coefficient seems to be working well in simulating the area of Place Glacier yielding an RMSE = 0.07 km^2. At the end of the model run every year, a ratio is formed between the simulated new glacier area and the reference glacier model (DEM) area ($Area_{new} / Area_{ref}$), which is then applied to B_s and B_w to adjust them for the changing glacier area. This ratio is usually less than unity because the glacier usually loses area over time whereas the glacier area remains constant in the GMB model. As a result of this adjustment, modelled B_s and B_w are slightly smaller than their un-scaled counterpart. This is justified because glacier-wide mass balance, in particular B_s, will become less negative as a result of glacier retreat (Leclercq et al. 2010; Paul 2010). However, this approach of mass balance adjustment for area change has not been studied in detail before and therefore should not be considered as complete. It is possible that this adjustment has contributed to discrepancies between modelled and measured mass balance results. The current approach of mass balance adjustment to glacier area change is used here mainly to avoid model complexity. However,

it is emphasized here that the best approach to account for glacier area change in a GMB model that should be done in future work is to update the glacier area at the end of the balance year.

Furthermore, RAMS variables contain errors due to uncertainties in NARR fields used in dynamical downscaling, as well as errors inherent in RAMS. RAMS biases in temperature and precipitation were adjusted, but possible biases in other variables could not be determined. Determination of the range of errors in GMB model results is not possible due to the lack of information on errors in RAMS variables. This could be yet another cause of disagreement seen between the modelled and observed mass balance results.

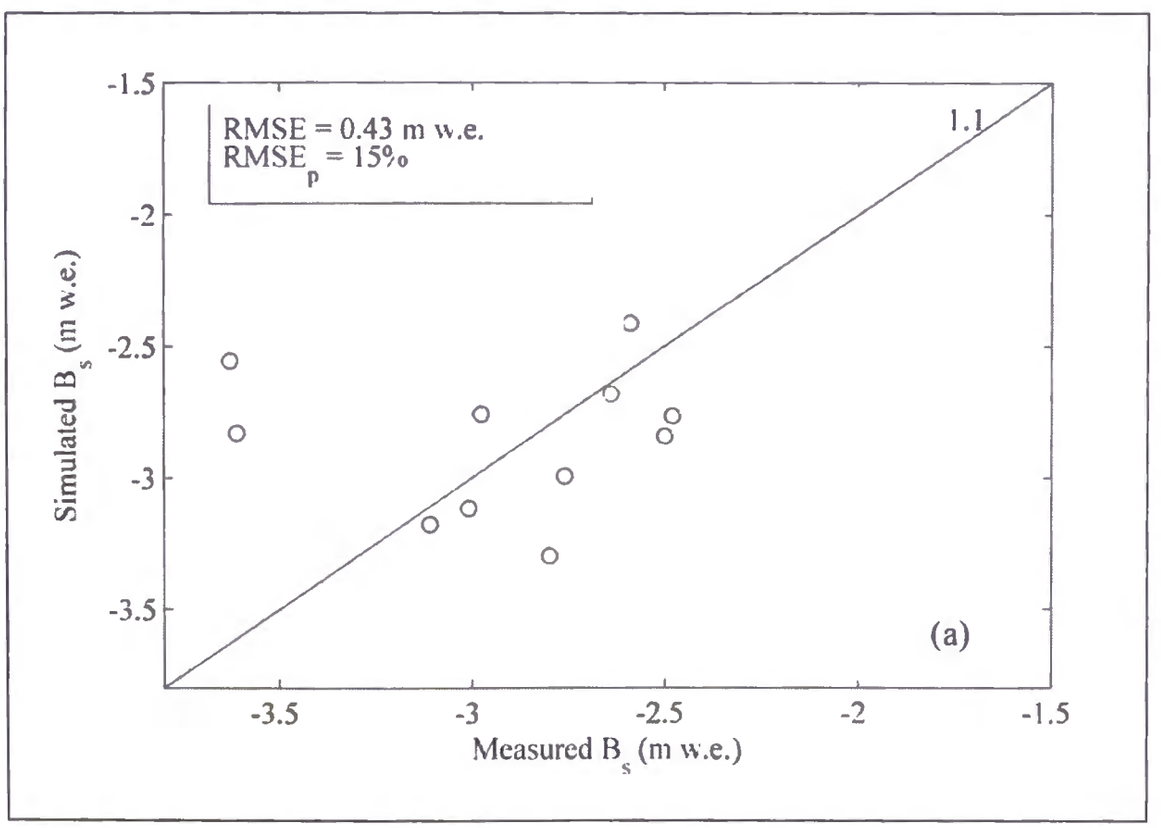

Figure 5.1 (continued on next page)

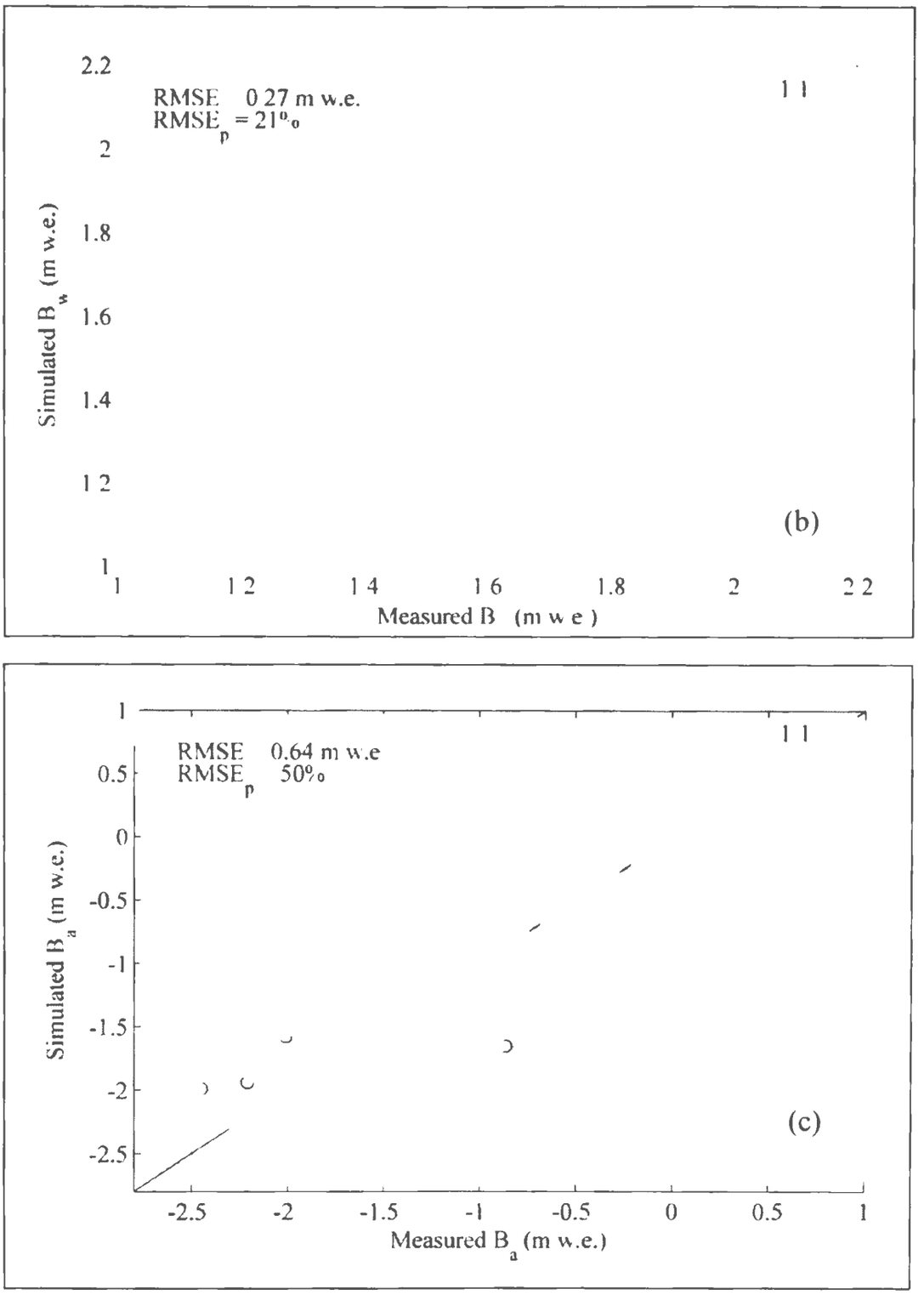

Figure 5.1 Comparison between simulated and measured glacier-wide (a) summer balance B_s, (b) winter balance B_w, and (c) annual net balance B_a from 1980-2008, Place Glacier.

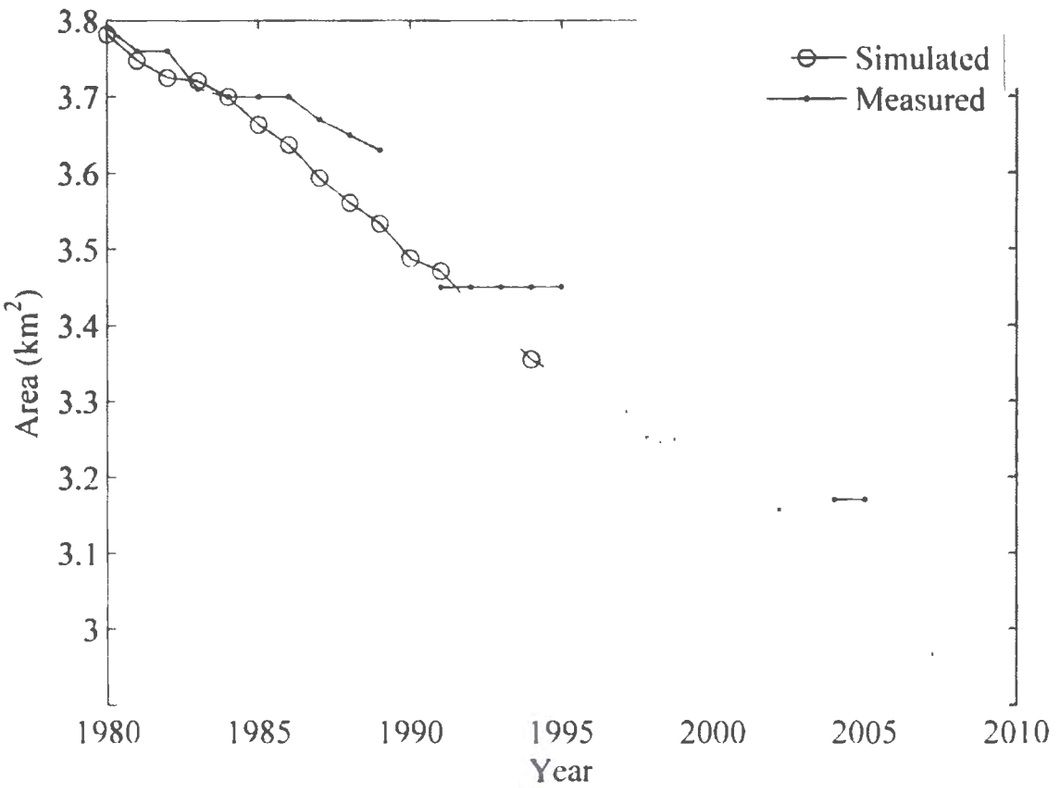

Figure 5.2 Place Glacier area simulated by the GMB model from 1980-2008.

Although the error in estimated B_a is relatively large, its cumulative value over the 29 years agrees well with corresponding measured values (Figure 5.3a). At the end of the model year in 2008, the simulated cumulative B_a = -33.72 m w.e., which is close to the measured cumulative B_a = -29.65 m w. e. However, from 2000 onwards, there is a distinct disagreement between simulated and observed cumulative B_a. This discrepancy is due to the model consistently simulating a large negative B_a from 2000 until 2003 (Figure 5.3b). Since the observed B_s and B_w are missing for these years, it is difficult to determine whether the large negative B_a is due to the model simulating large B_s or small B_w.

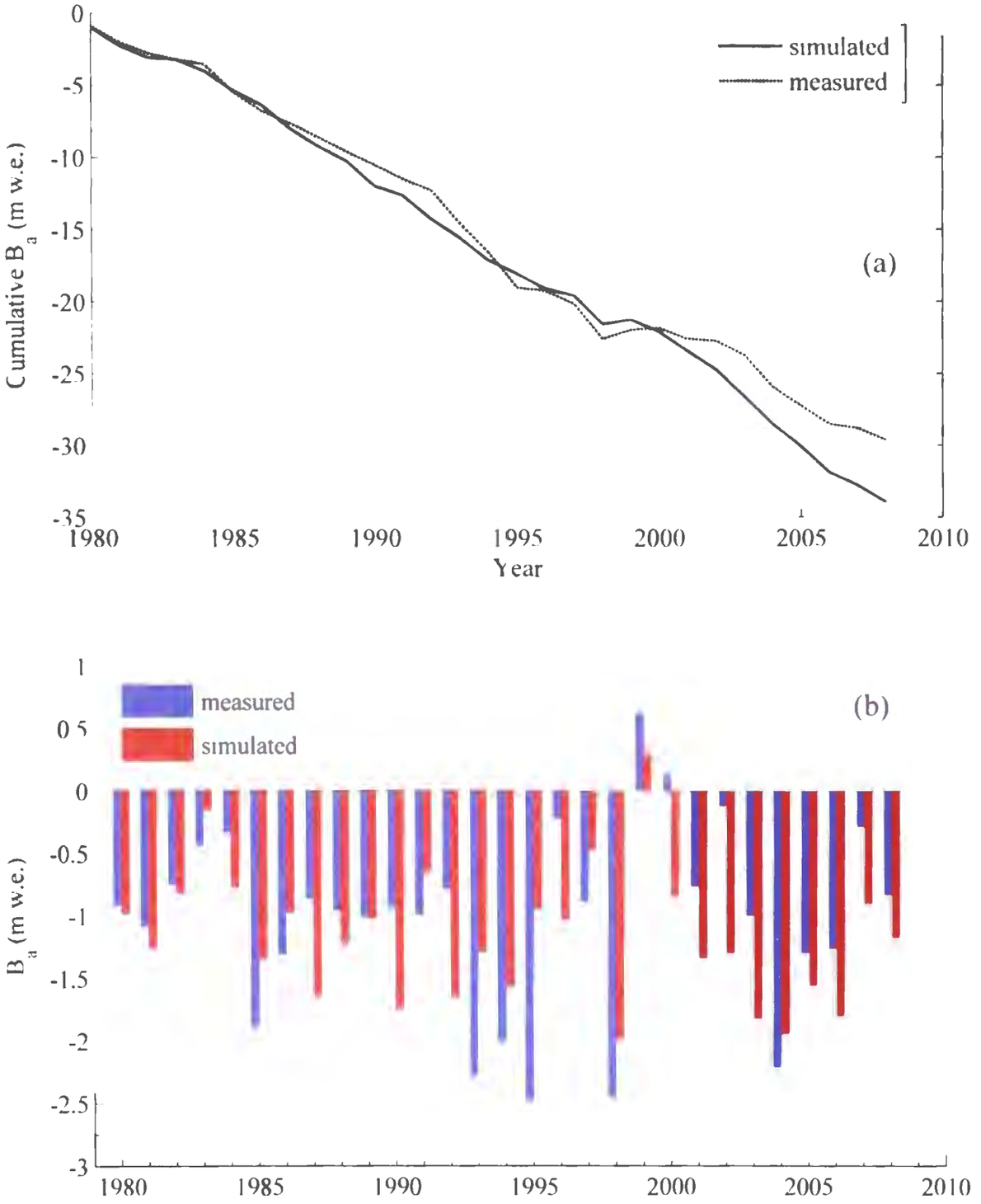

Figure 5.3 Comparison between simulated and measured glacier-wide (a) cumulative annual net mass balance, and (b) annual net mass balance time series for Place Glacier over the period from 1980-2008.

For most of the years, the simulated ELAs lie above the maximum elevation of the glacier (Figure 5.4). This suggests that for all these years the entire glacier experienced a negative B_a. From 2001-2008 all years except 2007, the model consistently simulated the ELA above the maximum glacier elevation. This perhaps suggests that the glacier is experiencing an accelerated mass loss in recent years. The spatial patterns in simulated b_n for 1980, 1990, 2000, and 2008 are shown in Figure 5.5. For the year 1980, a few grid cells in the highest part of the accumulation area show positive b_n values. The remainder of the glacier area has negative b_n with the glacier terminus area having a b_n value of -1600 mm w. e. Simulated b_n in 1990 suggests an increased negative b_n for the entire glacier. The glacier terminus area experienced a large negative b_n this year (-2500 mm w. e.) as compared to 1980. Even the accumulation area has experienced a negative b_n this year. The pattern in 2000 appears similar to that in 1980 but b_n is slightly more positive in the higher areas of the glacier this year. A cooler climatic condition may have contributed to small negative b_n this year. The pattern in 2008 again shows a large negative b_n for most of the glacier area, including the accumulation area. Based on the spatial pattern in simulated b_n for these four years, it can be argued that both accumulation and ablation area of the glacier are experiencing an increased negative net balance over time.

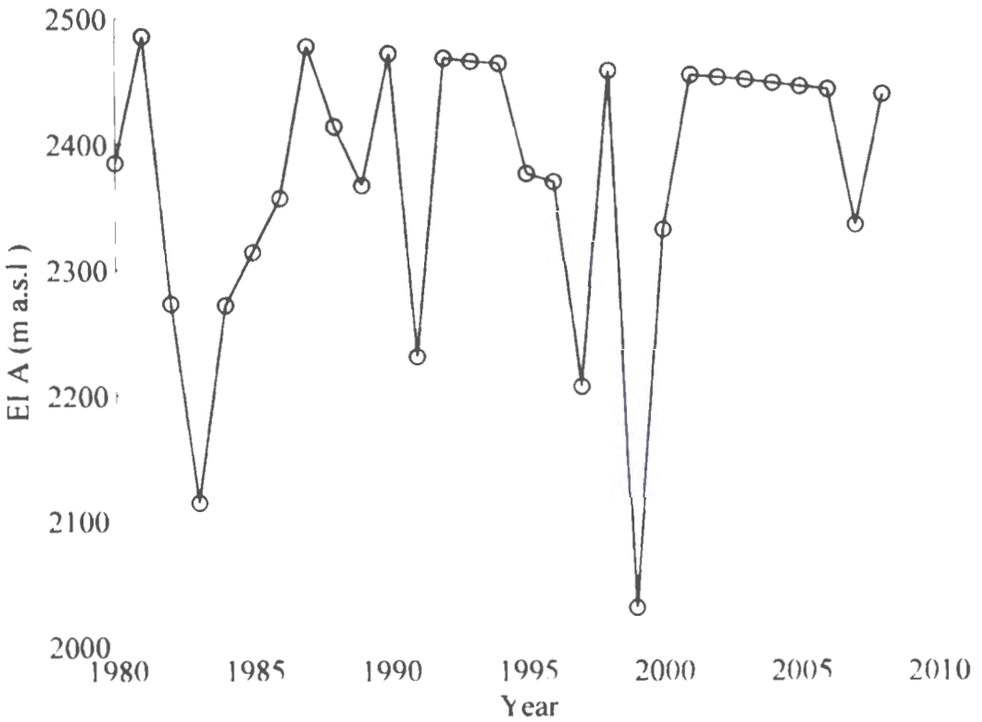

Figure 5.4 Simulated ELA for Place Glacier. The downward trend in maximum ELA is due to change in glacier elevation (downwasting) every year.

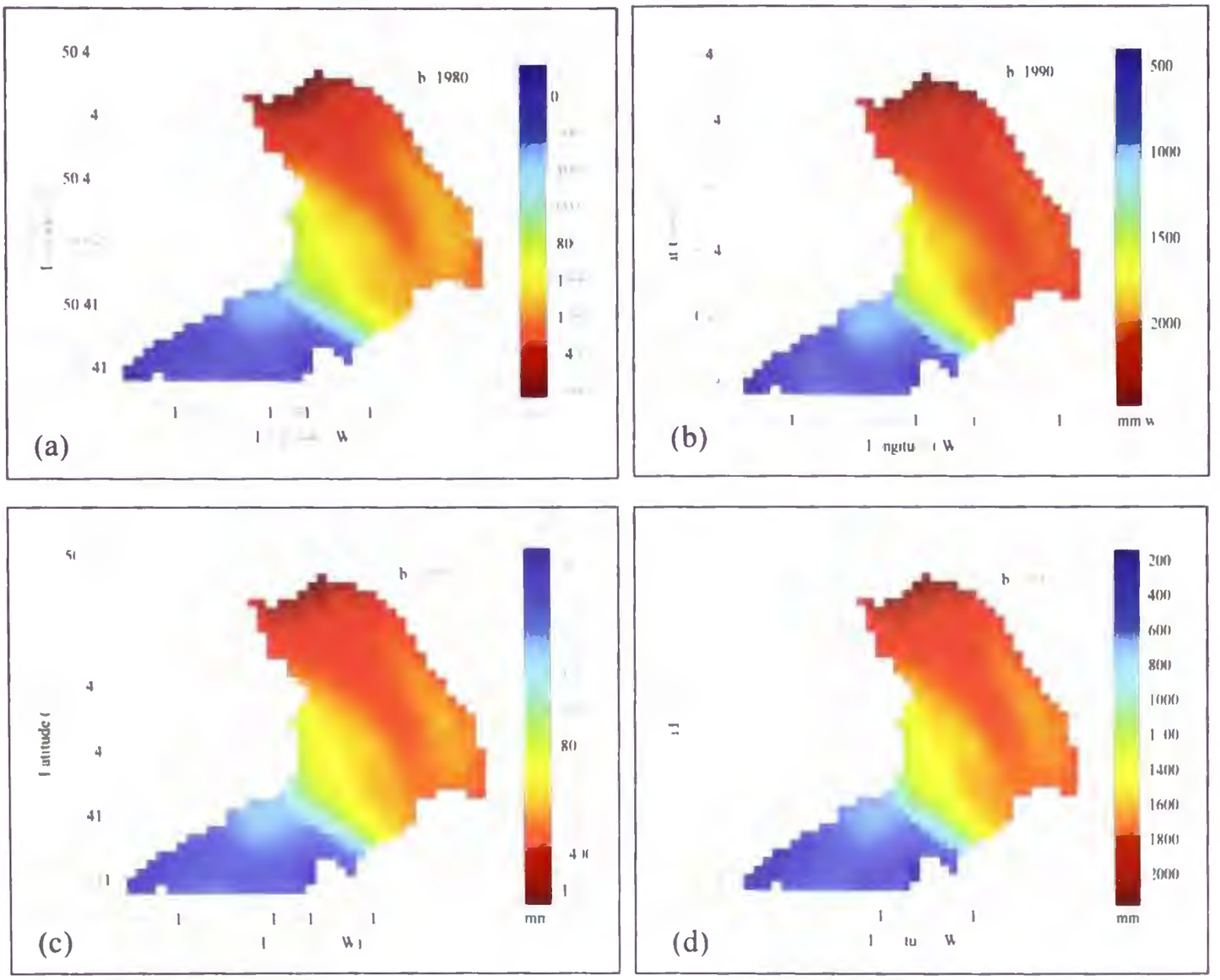

Figure 5.5 Spatially-distributed net mass balance on Place Glacier modelled for (a) 1980, (b) 1990, (c) 2000, and (d) 2008.

The model is not able to reproduce the exceptionally high negative B_s measured in 1994 (-3.61 m w. e.) and 1995 (-3.63 m w. e.). The high negative B_a measured in 1994 (-2.0 m w. e.) and 1995 (-2.48 m w. e.) are not consistent with B_a data observed on nearby Helm glacier (-1.46 m w. e.). This raises questions about the reliability of the observed mass balance data for these two years. Except for this, the model seems to be performing well in simulating glacier-wide mass balance for most of the remaining model years. However,

caution should be exercised while interpreting the results as there are several factors affecting them. One of the main factors is the number of samples used for comparison. Although the model results are available for 29 years (1980-2008), B_s and B_w results can only be validated with a limited number of observations (15 years) as they are missing from 1990-1993 and again from 1996-2005. It is possible that the error statistic and correlation results for simulated mass balance components could have been improved if the respective measured data were available for all model years. Furthermore, it should be noted here that the meteorological data used for the GMB model are dynamically downscaled NARR data, which are less likely to represent the actual conditions on the glacier than direct measurements. This is due partly to the inability of mesoscale model to resolve processes at the spatial scale of the glacier and partly due to errors in the reanalysis data. It is not possible to fully quantify the range of errors in simulated mass balance components as it is not known how much error is contained in all the RAMS downscaled meteorological variables.

Although the model performed well in simulating glacier-wide B_s and B_w, it did not perform as well in simulating altitude-wise b and b_w on the glacier surface. Simulated and observed elevation-wise b_s and b_w for the year 1981 and 1989 are shown in Figure 5.6. The model's inability to simulate altitude-wise b_w is expected because the snow depth on the glacier during winter months is highly variable in space and time due to redistribution of snow by wind and transport from valley walls to the glacier. Although a snow redistribution model has been used in glacier studies (Dadić et al. 2010), the GMB model used in the present study does not include processes governing snow redistribution on the glacier surface. In contrast to altitude-wise b_w, the model performed relatively better in

reproducing altitude-wise observed b. However, the model consistently underestimated b_s at the terminus of the glacier and overestimated it at the upper glacier site. This is possibly because the actual wind speed on higher and lower reaches of the glacier may be significantly different from what is prescribed in the model. The present model simulates glacier wind at the middle of the glacier using the Prandtl model and replicates the same wind to all model grid points (discussed in section 5.2.2). This may not be consistent with actual wind speed on the glacier where glacier terminus usually experiences higher wind speed due to downslope acceleration of the glacier wind while the upper glacier site experiences less wind. The lower (higher) than actual wind speed simulated at the terminus (upper part) of the glacier leads to decreased (increased) turbulent heat fluxes through changes in wind speed and turbulent transfer coefficient. It should be noted that historic mass balance data (both b and b_w) are missing for higher elevation areas for most of the years. Missing mass balance data for higher elevations are linearly interpolated using the vertical gradient derived from the available data. As a result, these interpolated data may not represent the true mass balance for these elevation bands thus potentially making comparison results unreliable. Also, the measurements of b on the glacier terminus are usually not accurate due to continuously changing surface. As a result, it may not represent the actual b_s on the glacier terminus. However, as mentioned before, the historic mass balance record does not contain information about errors in observations. There may be other reasons for the disagreement between simulated and measured b_s on the glacier, which need to be investigated further.

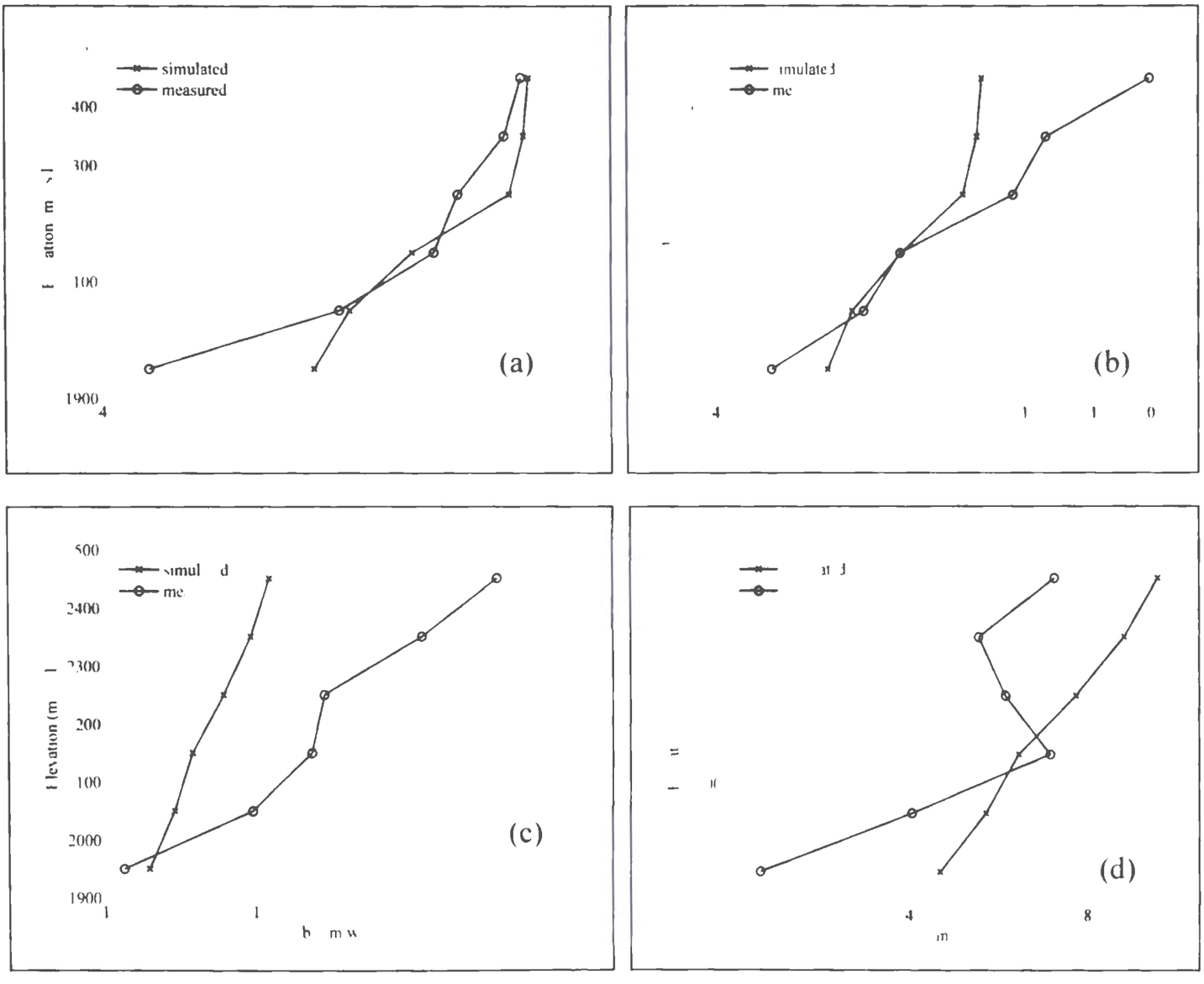

Figure 5.6 Comparison between measured and simulated elevation-wise b on Place Glacier for (a) 1981 and (b) 1989; and b_w for (c) 1981 and (d) 1989.

5.5.2 Surface Temperature and Energy Balance

Some of the important model results on the middle of the glacier for the summer of 1980 are examined. Glacier surface temperature simulated by the model is given in Figure 5.7a. Most of the subzero surface temperatures occurred during the second half of the summer melt season (August-September) with highest hourly temperature minima (= -17°C) occurring

during the middle of September. The frequency of subzero temperature between 1 August to 30 September is nearly 32%, while it is nearly 26% between 1 June to 31 August. For the entire summer season, the frequency of subzero temperature is relatively small (=29%) compared to the frequency of 0°C surface temperature (70%). The frequency of subzero surface temperature increased (=38%) for the upper glacier site, while it decreased (=24%) for a location near the terminus of the glacier (not shown). Similar results are found when simulated mid-glacier zero and subzero surface temperature is examined for other model years (Figure 5.7b). These results are consistent with the results from a similar study in southwestern Yukon, Canada, which examined energy balance on glacier surfaces applying different treatments of surface temperature and heat flux within the subsurface model (Wheler and Flowers 2011). With a one layer subsurface model (similar to the one used here), their results suggest that most of the subzero surface temperatures occur between August to September with lowest surface temperature minima below -20°C. Furthermore, their comparison of simulated surface temperature between different subsurface models suggests that the one-layer subsurface model usually estimates lower surface temperature minima than a multilayer subsurface model. Although both subsurface models account for thermal inertia of snow or ice layers, hence limiting the magnitude of surface temperature variability, the lower surface temperature minima reported by the former is mainly due to the lack of penetration of shortwave radiation below the surface. Despite the lower accuracy of the one-layer subsurface model compared to multilayer subsurface scheme, it is still a better choice over an iterative temperature scheme (ITS), which consistently simulates lower surface temperature minima during the night (period with negative energy flux) at the surface (e.g., Braun and Hock 2004; Wheler and Flowers 2011). Although results obtained

here compared fairly well with the results from Wheler and Flowers (2011), they could not be validated independently due to the lack of in-situ surface temperature measurements. The model simulating 0°C surface temperature for most of the summer melt season justifies the assumption of constant surface temperature of 0°C in a traditional GMB model. Since there would be no melting when surface temperature is less than 0°C, the assumption of constant surface temperature of 0°C may lead to an overestimation of melt rate. However, simulation of the energy fluxes during times when surface temperature is less than the freezing point does have an impact on the timing of the melt onset the following day. Nevertheless, an accurate estimation of glacier surface temperature is important, because it affects the calculation of outgoing longwave radiation and turbulent heat fluxes, which in turn affect glacier melt rate.

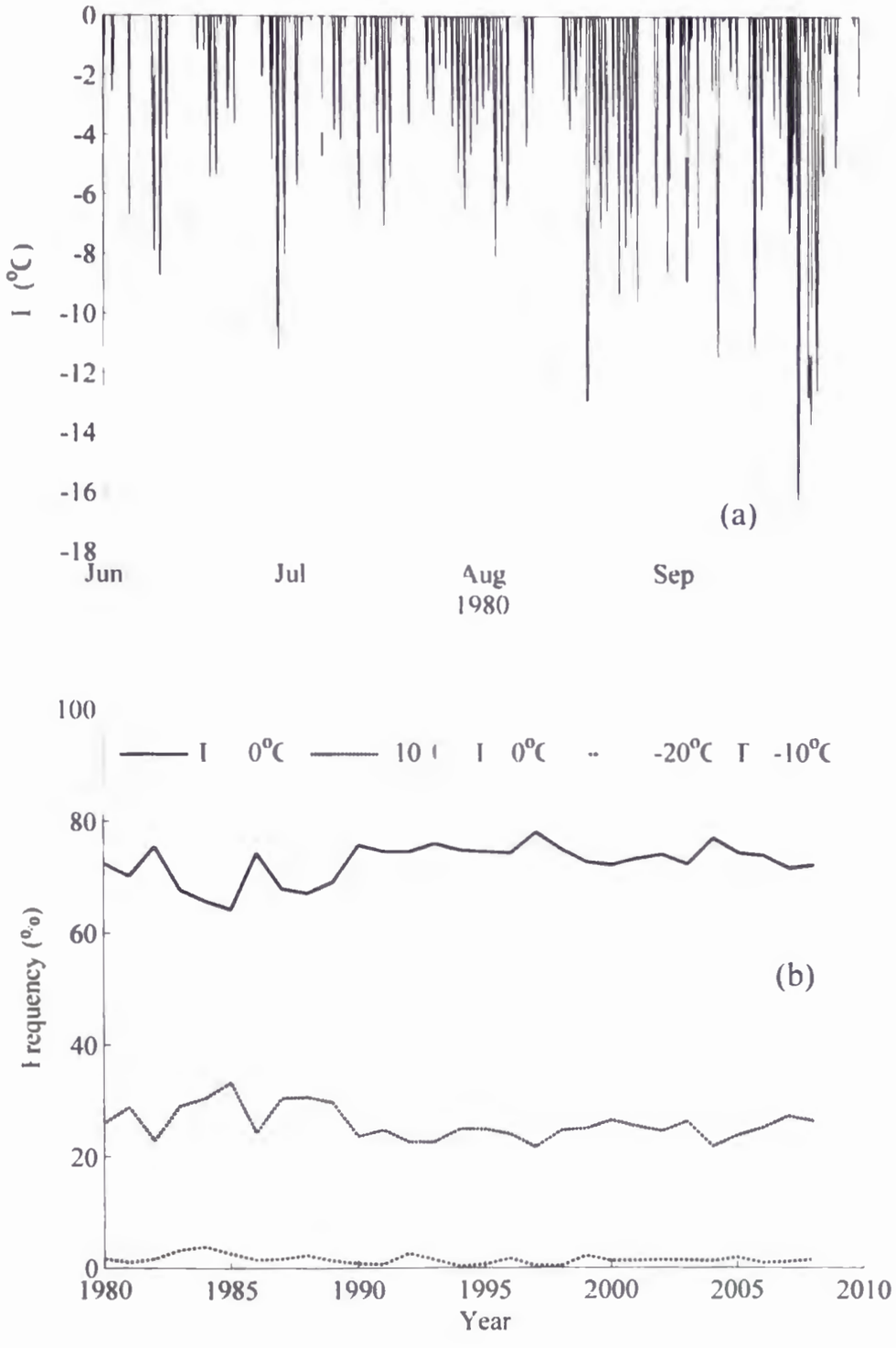

Figure 5.7 (a) Simulated mid-glacier hourly surface temperature (T_s) for the summer of 1980; (b) frequencies of simulated mid-glacier surface temperature (T_s) during the summer season from 1980-2008.

The average of the simulated glacier-wide hourly energy fluxes for the entire summer season and for each model year is presented in Figure 5.8. For all years, net shortwave radiation (K_{net}) is the dominant energy source, contributing 68% of the net energy on average. This is consistent with the SEB results from glaciers in other parts of the world that have reported net shortwave radiation as the dominant energy source for glacier melt (Anslow et al. 2008; Munro and Marosz-Wantuch 2009; Kayastha et al. 1999). Higher average shortwave values are evidence of longer periods of clear weather, less snowfall, and a longer period with low albedo firn and ice surface exposed. The turbulent heat fluxes are highly variable between years. The sensible heat flux (Q_H) represents 24% of the total energy budget, while Q_E accounts for a smaller share of 3%. These turbulent heat flux values are consistent with the values reported by similar studies on Place Glacier (Shea 2010) and elsewhere in the world (Anslow et al. 2008; Kayastha et al. 1999). The small Q_E value is a result of lower atmospheric humidity, which is expected for glaciers with less coastal influence. Also, except for the first few years, Q_E is consistently positive (downward flux) indicating condensation conditions on the glacier thus justifying the validity of neglecting sublimation on the glacier surface. The net longwave radiation (L_{net}) is the third largest magnitude component of the net energy budget, representing nearly 4% of the total energy. It is seen that the outgoing longwave loss is normally less than the incoming longwave gain resulting in a small net longwave gain. Since the model simulated 0°C surface temperature for most of the time, the calculated outgoing longwave radiation is nearly fixed at 309 W m^{-2} (Equation 5.16). For most of the time, this outgoing longwave radiation is less than RAMS incoming longwave radiation considered here for SEB

calculation. This resulted in a positive L_{net} for most of the time. This is realistic because in the summer air temperature is mostly higher than the glacier surface temperature, which is fixed at 0°C or even less, and the air is usually humid. This will result in a higher incoming longwave radiation on the glacier compared to the longwave radiation emitted from the glacier surface. Heat flux from rain (Q_R) accounts for a negligible 2% of the total energy. The large positive net energy balance on the glacier is primarily due to the temperate climate of the glacier where summer is characterized by a warm and long cloud-free period. The inter-annual variation in energy balance fluxes is the direct result of variation in RAMS meteorological variables, particularly air temperature, incoming shortwave radiation and humidity.

Time series of calculated glacier-wide daily energy balance components during the summer months are compared for 1980, 1995, and 2008 (Figure 5.9). For all years, K_{net} remains the largest contributor (70-77%) to net energy balance on the glacier surface whereas Q_H is the second larger contributor (17-24%) to net energy balance. The contribution of other energy balance components to net energy balance is much less. The temporal variability of different energy balance components is highly variable between years. However, for most of the year the contribution of K_{net} and Q_H to energy balance is maximum from July to September. L_{net} is generally negative during summer months for most of the years. Time series of glacier-wide net energy balance from 1980-2008 suggests an increasing trend in energy balance on Place glacier (Figure 5.10). This is consistent with the large negative summer balance observed on the glacier in the last few decades.

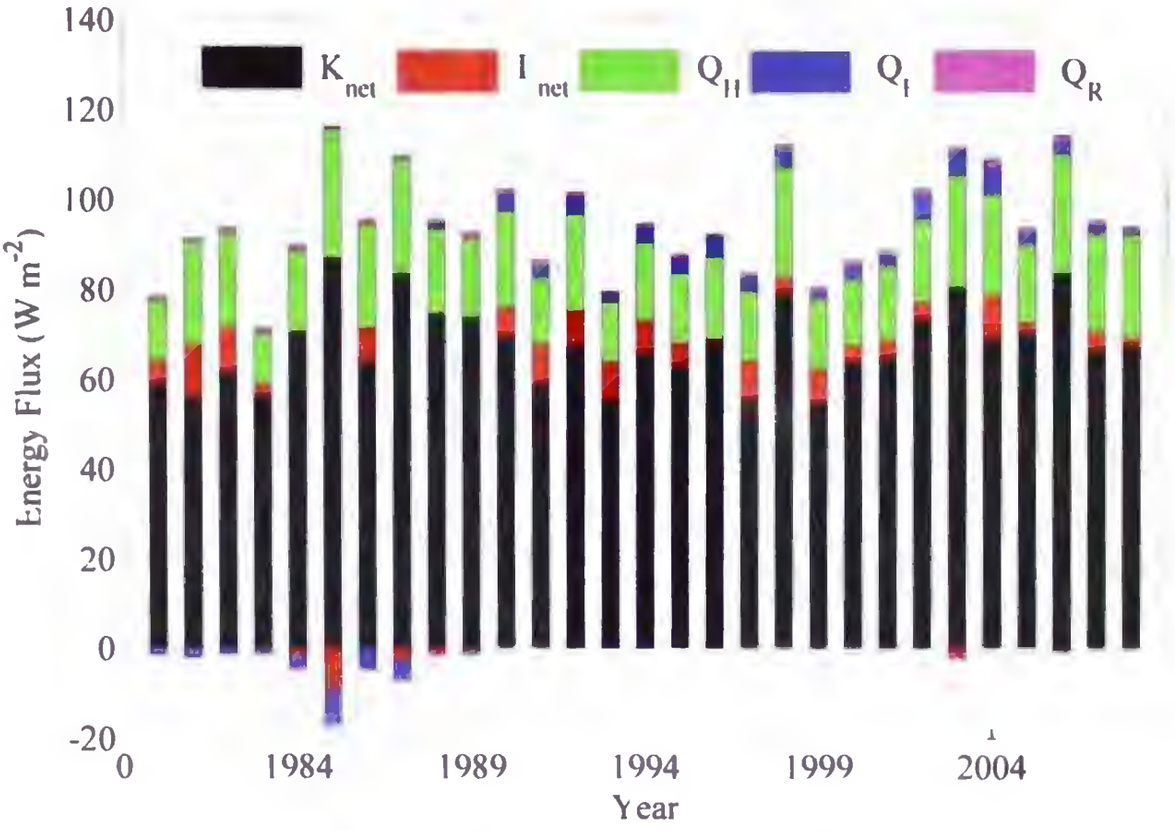

Figure 5.8 Glacier-wide averages of simulated hourly energy fluxes for the entire summer for Place Glacier: net shortwave radiation (K_{net}), net longwave radiation (L_{net}), sensible heat flux (Q_H), latent heat flux (Q_E), and heat supplied by rain (Q_R). The total length of individual bars represents the net energy balance on the glacier surface.

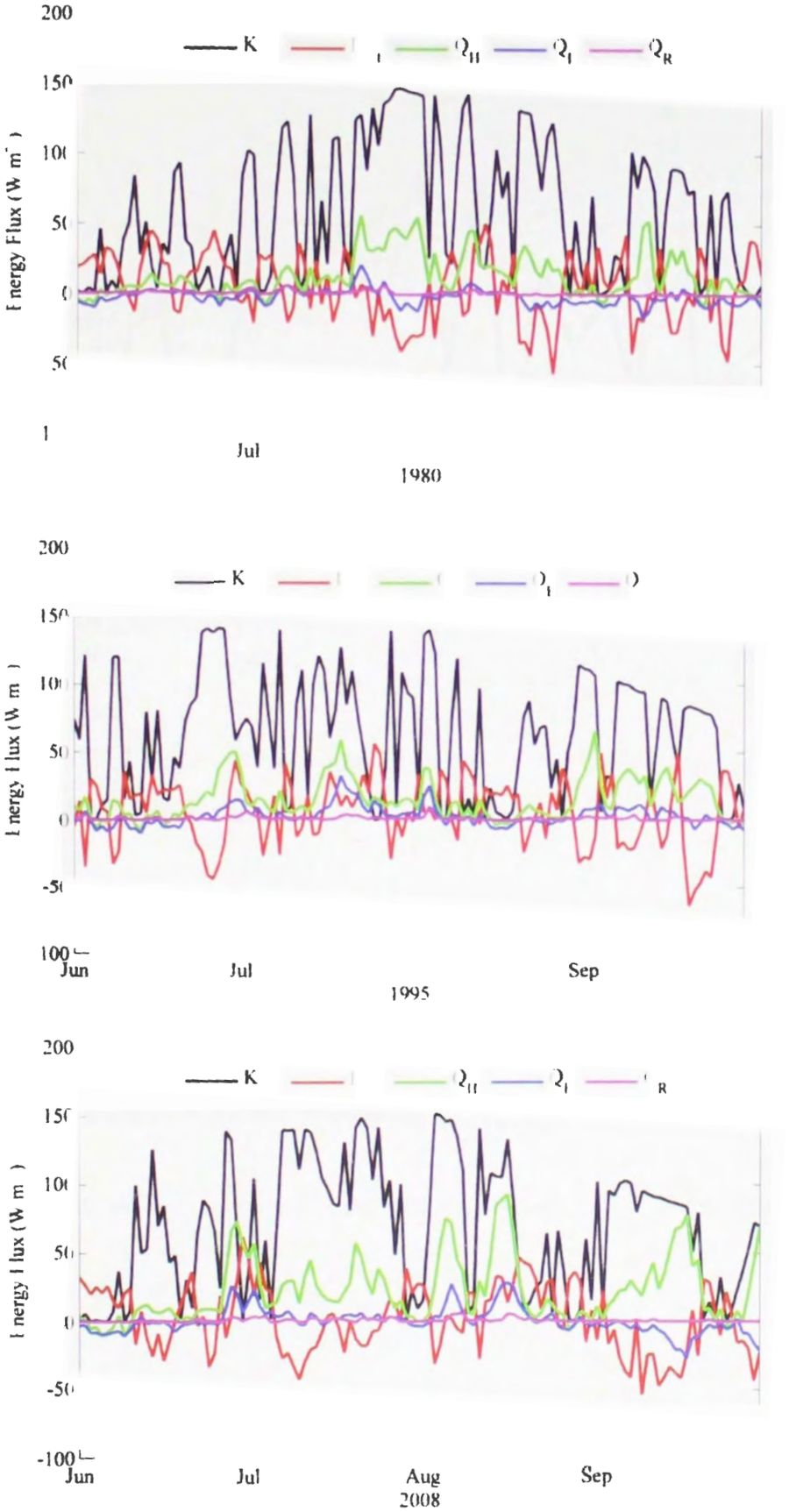

Figure 5.9 Time series of glacier-wide simulated daily energy fluxes during summer of 1980, 1995, and 2008 for Place Glacier: net shortwave radiation (K_{net}), net longwave radiation (L_{net}), sensible heat flux (Q_H), latent heat flux (Q_E), and heat supplied by rain (Q_R).

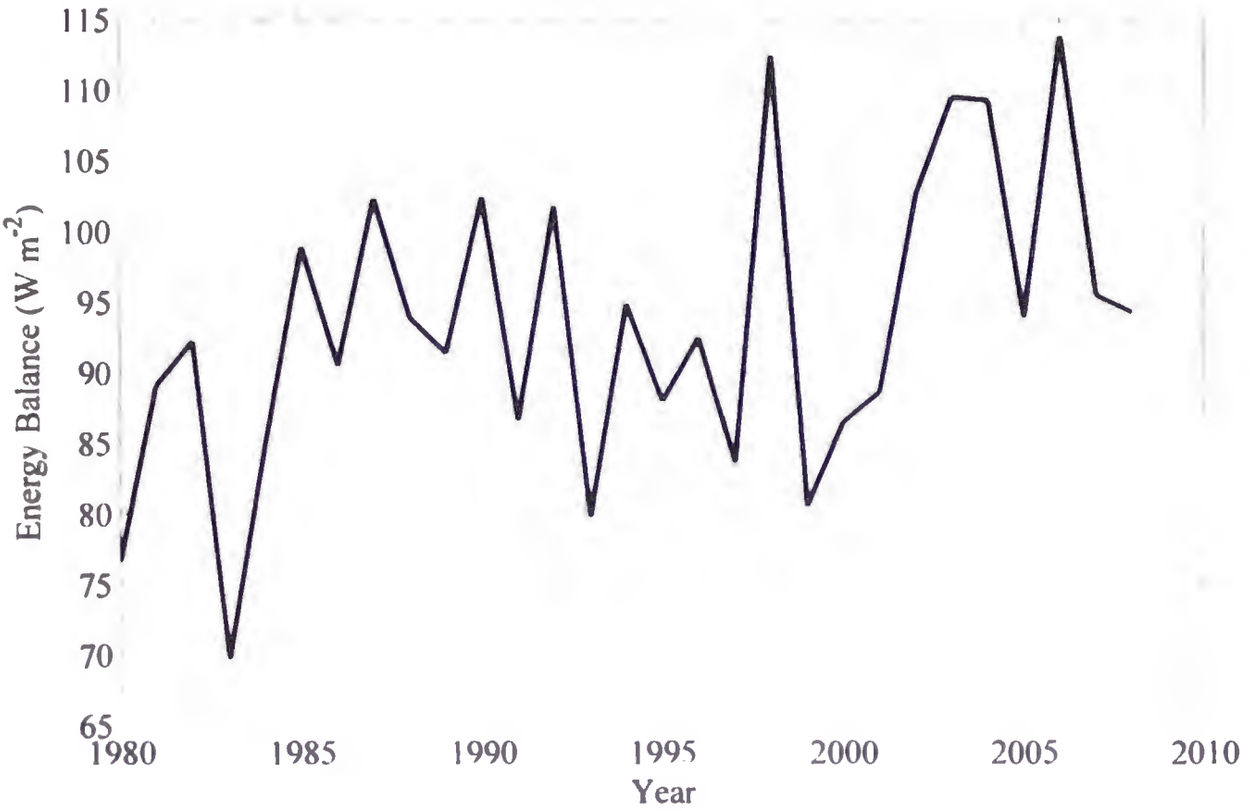

Figure 5.10 Time series of glacier-wide net energy balance averaged over the summer months from 1980-2008, Place Glacier. Result shows an increasing trend in energy balance on the glacier surface.

Simulated mid-glacier albedo for the year 1980 is shown in Figure 5.11a. Looking at the mid-glacier simulated albedo for all model years, the frequency of simulated albedo taking a value for that of new snow (=0.84) ranged between 8% and 30% (Figure 5.11b). As a result, the influence of summer snowfall on b_s via changes in glacier surface albedo is expected to be minimal.

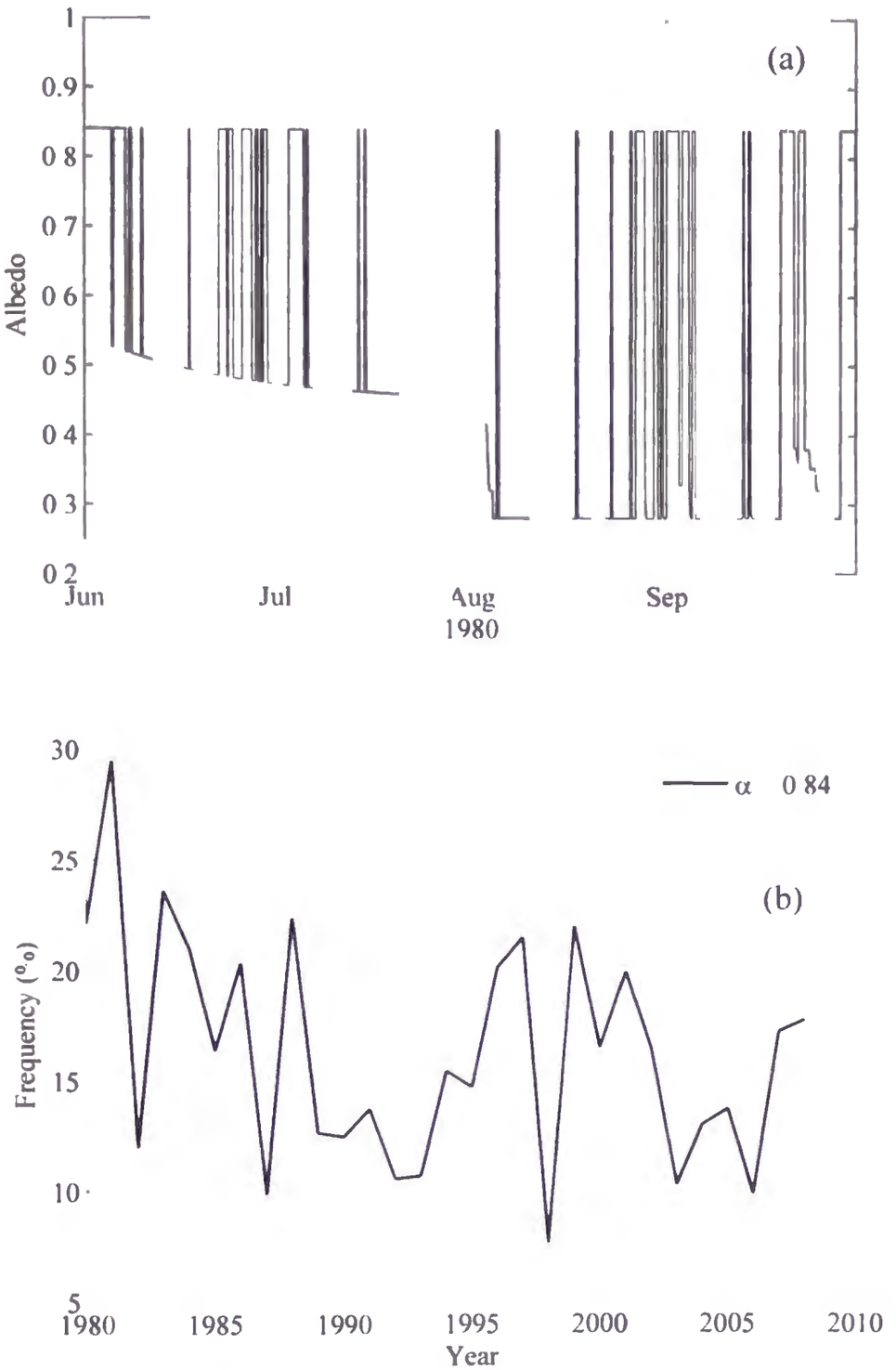

Figure 5.11 (a) Simulated mid-glacier albedo during the summer of 1980; (b) frequency of simulated mid-glacier albedo taking a value for that of new snow (=0.84), Place Glacier.

5.5.3 Model Sensitivity and Experiment

The sensitivity of simulated B_a to changes in climate variables on the glacier surface relative to conditions in 1980 is shown in Table 5.2. The sensitivity for air temperature is expressed in m w. e. per degree whereas the sensitivity for the remainder of the climate variables is expressed in m w. e. per %. In all of these sensitivity tests, the results are reasonable and no unusual model behaviour was detected. Test results suggest that the simulated B_a is more sensitive to incoming longwave radiation than the incoming shortwave radiation. This characteristic can be useful in applying the model for assessing glacier response to climate warming as most of the warming in the atmosphere is associated with changes in incoming longwave radiation. However, unlike other meteorological variables, the plausible range of variation of incoming longwave radiation over time is small. Simulated B_a showed higher sensitivity to summer temperature as compared to winter temperature. This is mainly because summer temperature has a strong influence on glacier melting through exchange of sensible heat fluxes. Additionally, air temperature determines the phases of precipitation on the glacier surface during summer months, which partly controls the glacier melt via changes in surface albedo. The higher sensitivity of glacier mass balance to summer air temperature suggests the importance of summer air temperature variation to glacier mass balance. The sensitivity to changes in winter temperature is due to the fact that the model determines winter accumulation using a threshold air temperature for discriminating the form of precipitation (snow or rain) on the glacier surface. The model is also sensitive to changes in the amount of winter accumulation. A thick (thin) snowpack at the beginning of the summer melt season delays

(expedites) the exposition of low albedo glacier ice into the summer months resulting in a decreased (increased) glacier melt and consequently affecting the overall glacier mass balance. Snowpack depth is also a direct contributor to net mass balance. The model is also moderately sensitive to changes in vapour pressure and wind speed. This sensitivity is mainly due to the influence of these variables on turbulent heat fluxes.

Table 5.2 GMB model sensitivity to changes in different climate variables relative to the condition during the summer of 1980. In the test of model sensitivity, all climate variables, except air temperature, are perturbed by 10% intervals spanning ±20%. Summer and winter temperatures are perturbed at the interval of 1 standard deviation (SD) spanning ±2SD

Variables	Climate Sensitivity
Summer temperature	-0.44 m w. e. $^{o}C^{-1}$
Winter temperature	-0.17 m w. e. $^{o}C^{-1}$
Incoming shortwave	-0.01 m w. e. $\%^{-1}$
Incoming longwave	-0.10 m w. e. $\%^{-1}$
Winter snowpack depth	+0.02 m w. e. $\%^{-1}$
Summer precipitation	+0.002 m w. e. $\%^{-1}$
Vapour pressure	-0.04 m w. e. $\%^{-1}$
Wind speed	-0.01 m w. e. $\%^{-1}$

With regard to model parameters, B_a is more sensitive to changes in albedo of old snow than other model parameters (Table 5.3). This suggests that the processes governing the decay of winter snowpack play an important role in determining mass balance on the glacier surface. The parameter governing the vertical gradient of winter precipitation has

significant control over the simulated B_a. Albedo of new snow and ice are less important in simulating B_a on the glacier surface. Although the sensitivity to changes in surface roughness length seems insignificant, it can still have appreciable effect on glacier mass balance as the surface roughness length for snow and ice can vary over many orders of magnitude. However, sensitivity of GMB model to this degree of variation of surface roughness length is not tested here. Also, it should be noted here that the arbitrary percentage changes in model parameters used in the sensitivity test are not realistic for all parameters as there natural range of variation is not meaningfully expressed as a fixed ±20%.

Table 5.3 GMB model sensitivity to changes in model parameters relative to the control run in 1980. In the test of model sensitivity, key model parameters are perturbed by 10% intervals spanning ±20%.

Model Parameters	Parameter Sensitivity
Old snow albedo	+0.02 m w. e. $\%^{-1}$
Ice albedo	+0.003 m w. e. $\%^{-1}$
New snow albedo	+0.002 m w. e. $\%^{-1}$
Surface roughness length for momentum	-0.002 m w. e. $\%^{-1}$
Vertical gradient of winter total snow	+0.01 m w. e. $\%^{-1}$

The first set of modelling experiments in which the effect of summer snow is ignored (Setup 1) yielded a $RMSE_p$ = 18% in simulated B_s which is not much different from the corresponding $RMSE_p$ = 15%, obtained in the control run. There is no significant

improvement in model skill by including summer snowfall. This is expected because summer months in the interior of the Coast Mountains are usually dry and warm with fewer chances of snowfall events.

In the second set of model experiments the impacts of assuming a constant 0°C surface temperature on simulated B_s is investigated. With this simplification, the simulated B_s yielded a $RMSE_p$ 17%, which is similar to the $RMSE_p$ 15% in the control run. Similar to summer snowfall, the inclusion of a subsurface temperature scheme does not improve the model skill in simulating B_s. This result perhaps justifies the assumption of constant surface temperature of 0°C during summer months in a traditional GMB model. However, it should be noted here that the errors in both the model experiments and control run are obtained based on observed annual B_s records. It is believed that results will be somewhat different if the errors are obtained using B_s records of shorter time scales. Previously, SEB-based models including a subsurface temperature scheme have been shown to perform better in simulating melt measured at a shorter time scale using an ultrasonic range sensor (Wheler and Flowers 2011). However, this could not be verified due to the unavailability of observed melt records at shorter time scales.

5.5.4 Empirical Melt Models

SEB melt model skill in simulated B_s is evaluated against the similar skill in an empirical TI melt model and a relatively more complex enhanced TI melt model. Results from these model runs together with results from the SEB-based melt model as compared to measurements are given in Table 5.4.

For all years, the SEB-based melt model out performed both TI and enhanced TI models in reproducing B_s. The RMSE in estimated B_s for the SEB-based GMB model is 0.43 m w.e.. while it is 1.14 and 0.79 m w.e. for the TI and enhanced TI model. The enhanced TI model performed significantly better than the TI model in reproducing the observed B_s, but its performance is still no better than the SEB-based melt model. Shea (2010) estimated melt from Place Glacier using a SEB-based melt model and the same empirical TI and enhanced TI models using the same melt factors from 2006-2008. This study reported RMSEs of 0.49, 0.53 and 0.57 m w. e. in estimated melt from these three models, respectively. For the same period (2006-2008), the SEB-based melt model, the TI model and enhanced TI model used in the present study yielded RMSEs of 0.18, 0 72 and 0.37 m w. e., respectively. In contrast to the results reported by Shea (2010), the RMSE values presented here suggest that the SEB-based melt model has highest skill in reproducing the observed melt on the glacier surface followed by enhanced TI melt model and TI melt model, which has the lowest skill. In fact, the SEB-based model used in the present study simulated B_s a little better than the SEB model used by Shea (2010), but the TI model used in the present study consistently underestimated B_s as compared to B_s simulated by Shea (2010) employing the same empirical models. Decreased melt for the TI model is due to the delay in the transition of the glacier surface from snow to ice. From 2006-2008, summer melt simulated using SEB-based melt model with RAMS variables yielded an RMSE of 0.18 m w. e. This RMSE is significantly smaller than the RMSEs in simulated melt on Place Glacier using TI (RMSE = 0.53 m w. e.) and enhanced TI (0.57 m w. e.) melt model forced with station data. This possibly suggests that the SEB-based melt

model used in this study is a better choice compared to empirical melt models when used with RAMS variables for melt modelling. For a mid-glacier location in 2007, the winter snowpack seems to last until the end of summer months thus preventing ice underneath from being exposed to the surface (Figure 5.12). As a result, these models used a melt factor for snow most of the time leading to smaller surface melts than it would otherwise generate using the melt factor for ice. The discrepancy between results from this study and the results reported by Shea (2010) is probably due to different meteorological data used in these two studies. Shea (2010) used in-situ meteorological data, while the present study used RAMS downscaled meteorological fields for the same purpose. Melt models using in-situ meteorological data are expected to perform better compared to the model runs with downscaled meteorological fields such as RAMS variables used in the present study. This is mainly because in-situ observations better resolve the processes occurring at the glacier scale than the RAMS model due to its coarse spatial resolution and the fact that it is a model. Also, the lapse rates used for distributing air temperature in TI and enhanced TI models are estimated using RAMS temperature sounding data. These lapse rates are larger in magnitude (= -7.2°C km^{-1} on average) compared to lapse rates observed on the glacier during summer months (-5.0°C km^{-1} on average) (Shea 2010). This may have contributed to underestimation of melt using the TI model. Nevertheless, it is interesting to note that the results produced by the SEB-based model compared significantly better than the results produced by empirical models even though they are all forced with the same RAMS variables using same method of air temperature distribution. For 2007, the SEB-based melt model used in the present study simulated the date of disappearance of winter snowpack in the middle of August. This

is consistent with the date of observed snowline retreat on Place Glacier reported by Shea (2010) (indicated by the arrow in Figure 5.12).

However, the results from empirical melt models presented here do have some shortcomings. The melt factors for snow and ice used in this study are adopted directly from Shea et al. (2009) and (Shea 2010), which used interpolated daily station air temperature data to calibrate the melt factors. In the present study, these melt factors are used directly in the empirical melt models using RAMS air temperature, which is usually not warranted because these parameters are not only specific to models but also to the type of input data used in the calibration. Melt factors derived through model calibration using station air temperature data may not work well when used in the same model with RAMS air temperature data.

Table 5.4 Inter-comparison of different melt models' skill in reproducing glacier-wide measured summer balance (B_s) on Place Glacier. All values are in m w. e.

	Measured	SEB model	TI model	Enhanced TI model
1980	-2.42	-2.32	-1.10	-1.46
1981	-2.64	-2.68	-1.65	-2.22
1982	-2.76	-2.99	-1.76	-2.21
1983	-2.18	-2.01	-0.84	-1.09
1984	-2.06	-2.59	-1.26	-1.60
1985	-3.11	-3.18	-1.95	-2.72
1986	-2.98	-2.76	-1.82	-2.33
1987	-2.80	-3.30	-2.32	-2.88
1988	-2.50	-2.84	-1.45	-1.80
1989	-2.48	-2.76	-1.62	-2.06
1990	NA	-3.21	-2.12	-2.64
1991	NA	-2.57	-1.42	-1.71
1992	NA	-3.13	-1.92	-2.56
1993	NA	-2.33	-1.53	-1.86
1994	-3.61	-2.83	-1.97	-2.29
1995	-3.63	-2 55	-1.47	-1.86
1996	NA	-2.64	-1.40	-1.71
1997	NA	-2.25	-1.28	-1.59
1998	NA	-3.40	-2.25	-2.76
1999	NA	-2.08	-1.33	-1.57
2000	NA	-2.38	-1.33	-1.57
2001	NA	-2.40	-1.34	-1.78
2002	NA	-2.83	-1.70	-2.14
2003	NA	-3.11	-2.23	-2.84
2004	NA	-2.99	-2.13	-2.64
2005	NA	-2.54	-1.65	-2.07
2006	-3.01	-3.11	-2.43	-2.78
2007	-2.20	-2.44	-1.61	-2.08
2008	-2.59	-2.41	-1.66	-2.01
Mean	**-2.73**	**-2.71**	**-1.68**	**-2.09**
RMSE		**0.43**	**1.14**	**0.79**

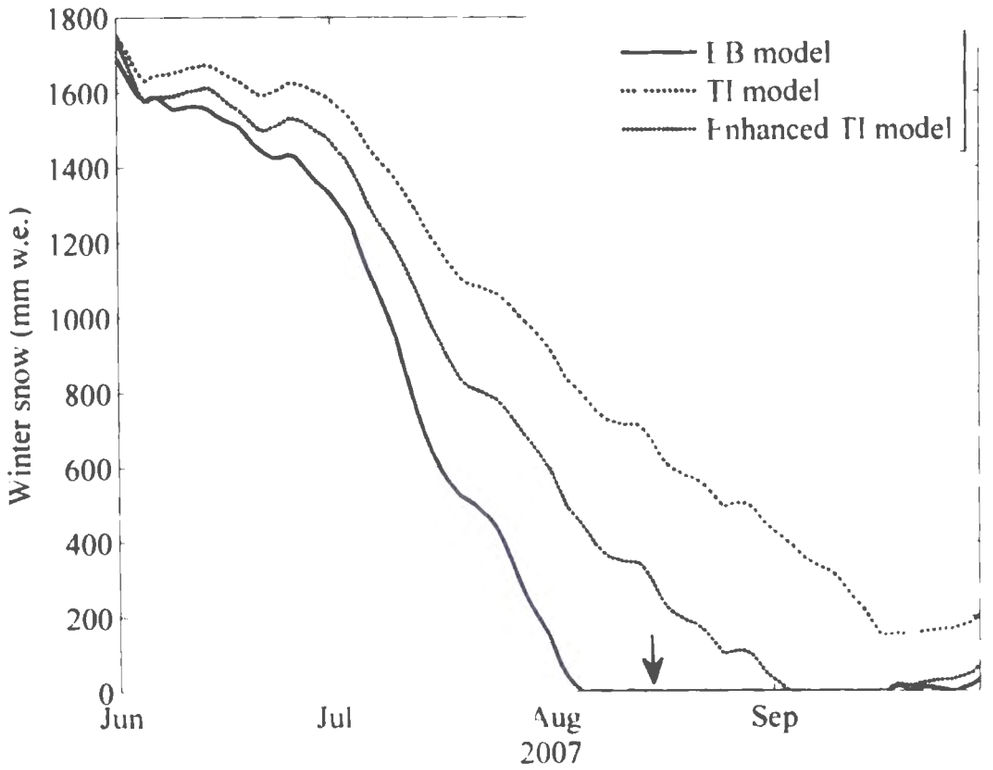

Figure 5.12 Comparison of simulations of winter snow snowpack at the middle of Place Glacier using the SEB-based melt model and empirical models for the year 2007. All models are forced with relevant RAMS variables. The arrow indicates the observed date of retreat of the snowline on Place Glacier for the same year.

5.6 Conclusion

A distributed GMB model based on surface energy balance approach has been developed and applied to Place Glacier over the 1980-2008 summer seasons using RAMS mesoscale model output. The 8 km resolution RAMS model output is obtained through dynamical downscaling of 32 km resolution NARR data. The model utilizes physical parameterizations of the most important energy transfer processes to compute ablation and includes detailed temperature and radiation distribution across the glacier. The model computes winter accumulation by distributing winter precipitation using the vertical gradient of RAMS winter precipitation. From 1980-2008, the percentage RMSE in simulated glacier-wide annual summer and winter balances are 15% and 21%, respectively. Despite some

discrepancies in simulated and measured summer and winter balance for individual years, the model performed remarkably well in simulating cumulative net mass balance over a 29-year period. By the end of the model run in 2008, the model simulated a cumulative net mass balance of -33.72 m w.e., which is close to the measured cumulative net mass balance of -29.65 m w.e. Also, the empirical volume-area scaling scheme used for estimating glacier area seems to be performing well. The model outperformed empirical TI and enhanced TI melt models in simulating the summer balance on the glacier surface. For the plausible range of variation in meteorological variables at glacier locations, the model showed a sensitivity of -0.44 m w. e. $^{o}C^{-1}$ and -0.17 m w. e. $^{o}C^{-1}$ to changes in summer and winter temperatures respectively. Among variables other than temperature, changes in incoming longwave radiation has the greatest weight in simulated net balance (-0.10 m w. e. $\%^{-1}$). With respect to physical parameters the GMB model presented here exhibits the greatest sensitivity to the parameters governing the distribution of winter precipitation and the snow aging parameters used in the simulation of winter snowpack albedo. Among parameters considered for sensitivity tests, surface roughness length for snow and ice can vary over many orders of magnitude and can have appreciable effect on simulated mass balance. However, mass balance sensitivity is not tested for this range of variation of surface roughness length. This needs to be investigated further.

Overall, the GMB model performed well in simulating summer and winter balance on Place Glacier when forced with downscaled RAMS variables. Empirical melt models did not perform as well in simulating summer balance when forced with the same meteorological data. Results from this study suggest that the accuracy of simulated mass balance results depends both on the choice of GMB model and meteorological data (e.g., observed,

reanalysis or downscaled) used for running the model. Because the model is physically-based with little site specific calibration, it is believed that the model can be applied to other glacier locations in the southern Coast Mountains for developing mass balance hindcasts. However, further study is required to determine its transferability to other glacier locations in the region. Also, the increased model skill in simulating cumulative net mass balance at longer time scale suggests the possibility of its application for future mass balance projections. Further work is also recommended to determine whether it can be included within a hydrologic model for operational purposes.

Chapter 6

Climate Downscaling

6.1 Introduction

Previous research has used numerical models of varying complexities for climate change impact studies on glaciers in different parts of the world (e.g., Radić and Hock 2006; Radić et al. 2013; Huss et al. 2014; Clarke et al. 2015). These models are run using future climate projections from a suite of GCM models As the GCMs are unable to resolve the subgrid-scale features at the local glacier scale, climate projections are usually downscaled before they are used for GMB modelling. The majority of the studies have employed simple TI melt models for resolving ablation within a GMB model and therefore required only air temperature and precipitation as input variables. Although more sophisticated statistical approaches of climate downscaling have been tested before (e.g., Bürger 1996; Zorita and von Storch 1999; Huth 1999; Widmann et al. 2003), most of the previous GMB projection work has used simple statistical methods of downscaling temperature and precipitation (e.g.,Radić and Hock 2006; Radić et al. 2013). The use of SEB-based model for climate change impact studies on glacier in the southern Coast Mountains of British Columbia appears virtually non-existent. As a result, information about downscaling of GCM projections other than air temperature and precipitation for GMB modelling is lacking in the region.

Widmann et al. (2003) successfully used a Singular Value Decomposition (SVD) based regression method for downscaling large-scale precipitation in the Pacific Northwest of North America. However, this method of climate downscaling has not been tested for

other large-scale climate variables. Furthermore, the SVD method of climate downscaling has not been applied in the context of GMB modeling in the Pacific Northwest of North America. Therefore, this study will follow the work by Widmann et al. (2003) and use the SVD technique for statistical downscaling of large-scale climate variables to be used for future GMB modelling in the southern Coast Mountains of British Columbia. The major goals of this study are (1) develop and validate SVD models for downscaling large-scale climate fields relevant for SEB-based GMB modelling (2) downscale relevant future GCM projections using the SVD model on Place Glacier in the southern Coast Mountains, BC.

6.2 Methods

6.2.1 SVD Downscaling Model

Application of the SVD technique for climate studies first appeared in a study by Bretherton et al. (1992), which used the method for detecting coupled patterns between different components of the climate system. Its application for statistical downscaling of climate is relatively new (e.g., Huth 1999) and has also been used in the context of other climatological studies (Lau and Nath 1994; Ward and Navarra 1997). SVD is mainly used for examining coupled variability of two climate fields in space and time. In the context of climate downscaling, these two climate fields are referred to as predictors and predictands and SVD seeks pairs of coupled patterns, one from predictors (large-scale variables) and one from predictands (regional or local variables), with each pair explaining a fraction of the covariance between the two fields. The first pair of patterns (modes) explains the largest fraction of the covariance followed by the second, third, etc. modes that maximize covariance not captured by the preceding pairs. SVD methods can also be applied to a single

field for understanding their spatial variability thereby identifying the dominant spatial pattern.

Next, the SVD method of climate downscaling is explained in detail following Bretherton et al. (1992). In the first step, a cross-covariance matrix, C, is formed from the two matrices,

$$C = A' \times B \tag{6.1}$$

where, A and B are anomaly matrices (mean removed from each data point) of gridded predictor and predictand fields respectively. These data matrices have the same time period but different locations. The *prime* symbol with the matrix A represents its transpose. When SVD is applied to the cross-covariance matrix (C) between two fields, it identifies the pairs of spatial patterns, which explain most of the temporal covariance between the two fields. SVD is performed using an *svd* function available in MATLAB Statistics Toolbox (MathWorks 2012):

$$[U, S, V] = svd(C) \tag{6.2}$$

The singular vectors for A are the columns of the matrix U, and the singular vectors for B are the columns of matrix V. The diagonal of matrix S contains the singular values. Columns of both U and V matrices are mutually orthogonal to each other. Each pair of singular vectors is a mode of co-variability between the fields A and B, also known as Empirical Orthogonal Function (EOFs). In the next step, PCs (Principal Components) are calculated (also known as expansion coefficients). This is essentially a time series describing how each mode of the variability oscillates in time. PCs are calculated by performing an orthogonal projection of A and B onto singular vectors U and V:

$$X = A \times U \tag{6.3}$$

$$Y = B \times V \tag{6.4}$$

The columns of matrices X and Y contain the expansion coefficients of each mode. The sum of the squared diagonal values of S gives the total squared covariance in C. This property in S provides a convenient way for assessing the relative importance of the singular modes, through the squared covariance fraction (SCF) explained by each mode. If D is the diagonal of the matrix S and D_{um} is the sum of the diagonal, SCF is calculated as:

$$SCF = \frac{D}{D_{sum}} \tag{6.5}$$

Based on SCF, a number of significant modes (n) are identified in X and Y. Given that there is a reasonable correlation between the i^{th} mode X and Y time-series values, corresponding X and Y values are linearly regressed to find the best fit model:

$$m_i = \frac{N\sum X_i Y_i - (\sum X_i \sum Y_i)}{N\sum X_i^2 - (\sum X_i)^2} \tag{6.6}$$

$$b_i = \frac{\sum Y - m_i \sum X}{N} \tag{6.7}$$

where N is the number of data points and m_i and b are coefficients of best fit for the i^{th} mode.

To reconstruct a small-scale variable from a large-scale variable (i.e. to perform the downscaling), first the anomalies of the large-scale variable are orthogonally projected at each time step onto U:

$$W = \frac{1}{U} \times K' \tag{6.8}$$

where K is the anomalies of the large-scale field and the *prime* symbol has the same meaning (i.e. it indicates the transpose of the matrix) as in Equation (6.1). Now, the reconstructed field corresponding to the i^{th} mode is:

$$W_R = m_i . W_i + b_i \tag{6.9}$$

The reconstructed small-scale (downscaled large-scale) field based on n modes is:

$$K_{DS} = \sum_{i=1}^{n} W'_R(i) \qquad (6.10)$$

When performing cross validation, m_t, b_t, variance, covariance, and correlations, are obtained from the fitting period, whereas the time series, W' and W refer to the validation period. It should be noted here that the downscaled fields given by Equation (6.10) are in terms of anomalies. To get the absolute field back, the climatological mean is added back to the SVD results.

For downscaling the precipitation, some additional procedures need to be implemented as the small time steps imply numerous observations with zero precipitation. In this case, the following steps were implemented before detrending the data:

- 0.1 was added to each precipitation values
- The base-10 logarithms were applied to the values
- 1 was added to the result of the logarithms. The purpose of doing this is to assign a minimum of 0 for detrended precipitation.

Once the precipitation is downscaled, the above process is repeated in reverse order. Further, the negative precipitation values generated by the model were considered zero. Similarly, any negative wind speed and incoming shortwave radiation values were considered zero.

6.2.2 Predictors and Predictands

The selection of a suitable predictor is important for downscaling large-scale climate variables. In this study, predictor variables are obtained from NCEP reanalysis (Chapter 3). The spatial resolution of the NCEP product (2.5 °Lat 2.5 °Lon) is similar to that of GCM

products. However, these large-scale variables do not necessarily compare well with each other due to different modelling techniques used for their development. A majority of previous statistical downscaling works are mainly limited to air temperature and precipitation and therefore there is a lack of information regarding the choice of predictors for downscaling other climate variables. NCEP reanalysis precipitation as a predictor has been shown to perform well in downscaling large-scale precipitation (Widmann et al. 2003). Huth (1999) tested different statistical techniques and predictor fields for downscaling air temperature in central Europe. This study showed that among the predictors, temperature fields result in a more accurate specification than circulation variables. The present study followed these two works and used NCEP precipitation and air temperature as predictor variables for downscaling respective variables. As the information regarding the choice of predictors for downscaling other large-scale climate variables is very limited, it is assumed that the corresponding NCEP variables will work equally well for downscaling other variables as well. In the absence of long-term high-resolution gridded observed datasets in the region (except temperature and precipitation), the present study used RAMS gridded model output over the southern Coast Mountains for the small-scale predictand variables. NCEP and RAMS data used in this study are discussed in Chapter 3. Daily NCEP and RAMS datasets are used over the period of 1979-2008. Prior to model development, RAMS air temperature and precipitation are bias-corrected using all available observations (Chapter 4). Except these two variables, no other RAMS variables are bias-corrected due to lack of corresponding observations. The first half of the dataset (1979-1993) is used for model calibration while the remainder (1994-2008) is used for model validation. Downscaling models are developed for the variables required to drive the glacier mass balance model: air

temperature, humidity, precipitation, sea level pressure, wind speed, incoming shortwave radiation and incoming longwave radiation.

6.2.3 GCM Climate Downscaling

Climate projections from a suite of GCM models considered for downscaling are discussed in Chapter 3. GCM outputs likely contain some amount of bias mainly due to improper parameterizations of physical, biological and chemical components of the climate system. Determining biases in GCM projections is difficult as information about corresponding observed fields in the future is unknown. Usually, biases in GCM results are determined by comparing historical simulations with the observations. The bias (positive or negative) is then applied to the future GCM fields to get bias-corrected future climates. This is a simple approach for removing bias in future GCM fields, which is also considered a form of downscaling. However, this approach of bias correction does not work well with the SVD methods used in the present study. Essentially, the SVD method works with anomalies (mean subtracted) of the climate variables. As a result, any bias applied to the GCM future fields will be removed while getting the anomalies of those fields. Therefore, no bias correction is applied to GCM future projection prior to their downscaling instead they are re-gridded to the NCEP domain using linear interpolation. The re-gridded GCM fields are then downscaled to the RAMS domain using the SVD model given by Equation (6.10). It should be noted here that the term anomaly used here refers to the detrending of data by subtracting the mean and should not be confused with the anomaly determined as the difference between the reference value and the value that is actually occurring.

Once the SVD model is validated, the entire dataset (1979-2008) is used for developing the SVD model for GCM downscaling. The model is then applied to downscale GCM projections from 2008 onward. As mentioned before, GCM fields downscaled to the RAMS domain will be in terms of anomalies and are not the absolute values. Absolute values are obtained by adding climatological means to them over the RAMS domain. However, it is unknown what the future climatological means will be over the RAMS domain. To resolve this problem, a 'Δ approach' is used. First, GCM future (2006-2100) and historic (1961-2005) climates are interpolated to the RAMS domain and the difference (Δ values) of their long term mean is calculated. The calculated Δ values are then added to the mean of the RAMS historical (1979-2008) fields. This gives the future climatological means over the RAMS domain, which is then added to the downscaled anomalies [Equation (6.10)] to obtain the absolute downscaled GCM fields over the RAMS domain. The downscaling method used in the present study is schematically shown in Figure 6.1.

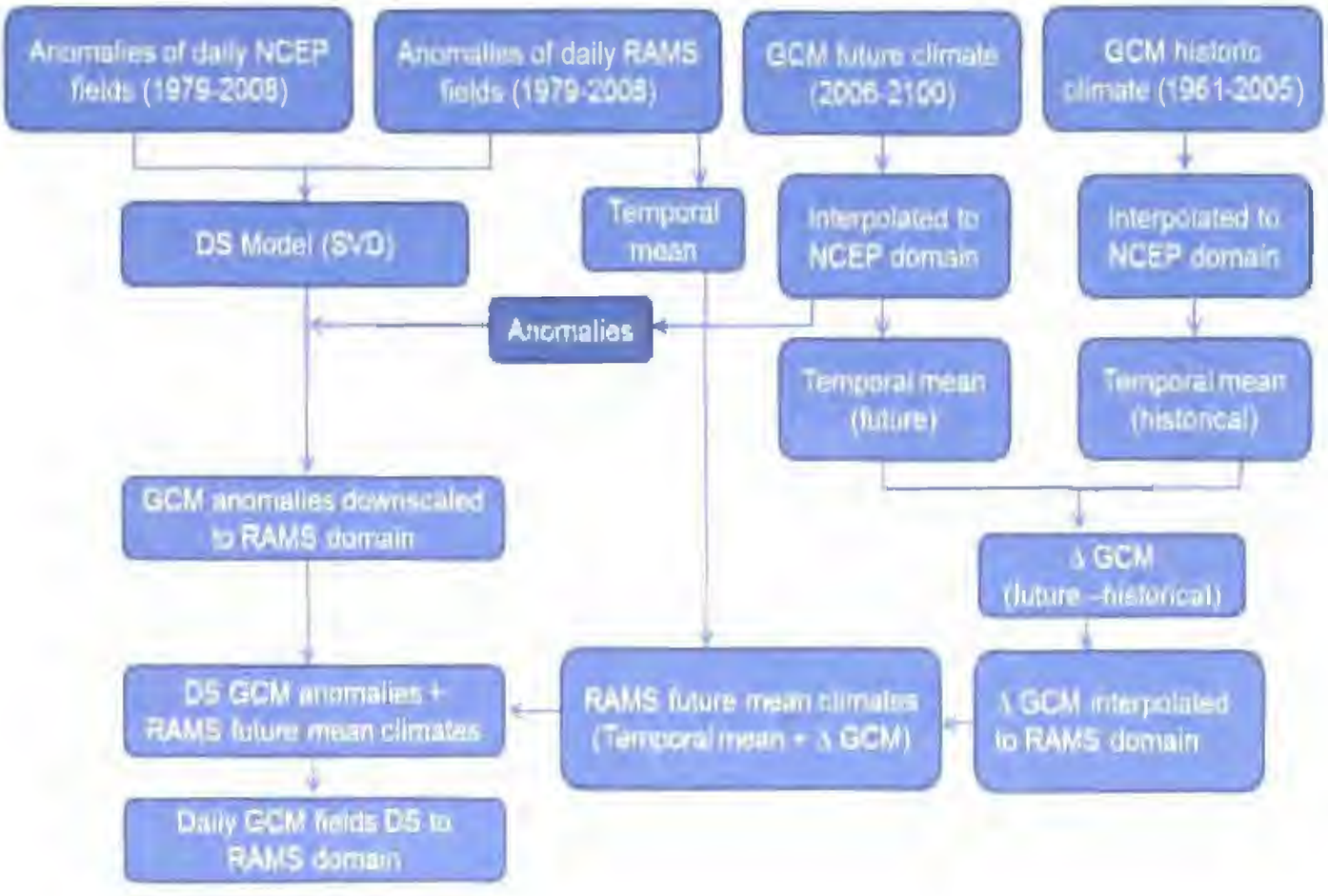

Figure 6.1 Schematic diagram showing the SVD method for GCM climate downscaling. Anomalies refer to the detrending of data by subtracting the mean.

6.3 Results and Discussion

6.3.1 Spatio-temporal Organization

Long-term averages of different variables within the RAMS domain are shown in Figure 6.2. These variables are not corrected for the potential biases. Long-term averages of RAMS air temperature, precipitation and humidity show a distinct spatial variation within the domain. Air temperature is higher along the coastal region and decreases eastward away from the coast. A similar pattern is seen for humidity. The RAMS model seems to be resolving the coastal and inland effect on temperature and humidity relatively well. Precipitation is highest along the coastal side of the mountains and decreases eastward due to the orographic influence of the Coast Mountains. Although there is no distinct spatial pattern in wind speed, isolated areas of high wind speed can be seen at many locations in the Coast Mountains. These pockets of high wind speed can be winds through valleys generated by the complex topography in the region. Similarly, as compared to the coastal region, mean incoming shortwave radiation is considerably lower over the mountainous areas, which is likely due to the influence of mountain topography on cloudiness. For incoming longwave radiation, no distinct spatial variation can be seen except that it is relatively higher over the coastal region. This is attributed to higher air temperature coupled with a higher amount of low cloud cover and humidity over the coastal region. Overall, at the given RAMS resolution and for longer time periods, the model seems to resolve the influence of topography for certain variables. However, this can change significantly when the same analysis is performed with variables averaged for shorter time duration, such as daily or hourly.

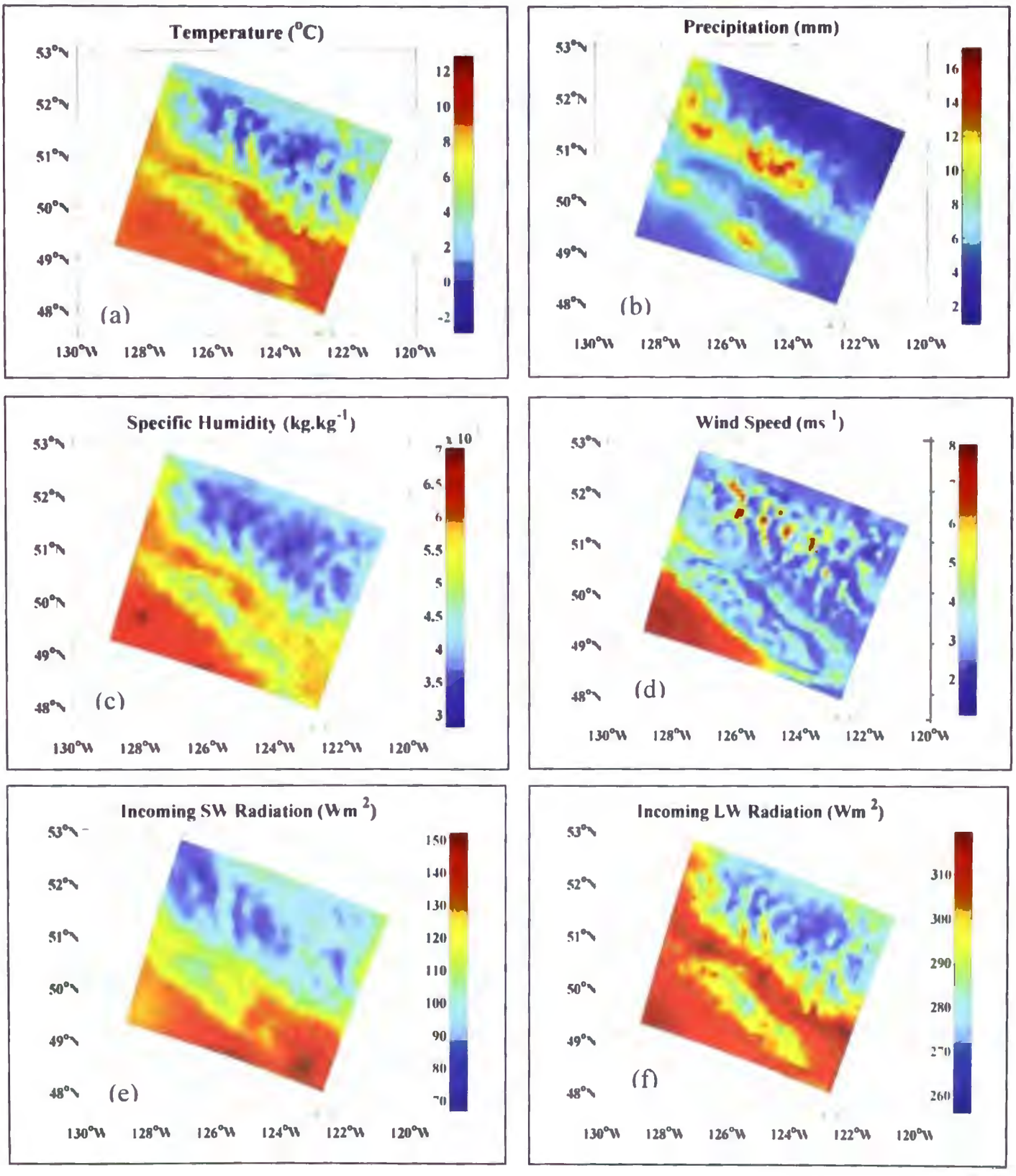

Figure 6.2 RAMS daily (a) air temperature, (b) precipitation, (c) specific humidity, (d) wind speed, (e) incoming shortwave radiation, and (f) incoming longwave radiation averaged over 1979-2008 for the RAMS domain over southwest BC.

Unlike the RAMS fields, the spatial variation in NCEP fields is relatively less distinct (Figure 6.3). Similar to RAMS variables, the corresponding NCEP variables also exhibit east-west gradients but they are less distinct compared to variations seen in the former. This is mainly due to the coarse spatial resolution used in the NCEP model for generating these fields. At the NCEP spatial resolution it is difficult to detect the spatial patterns of these variables within the southern Coast Mountains.

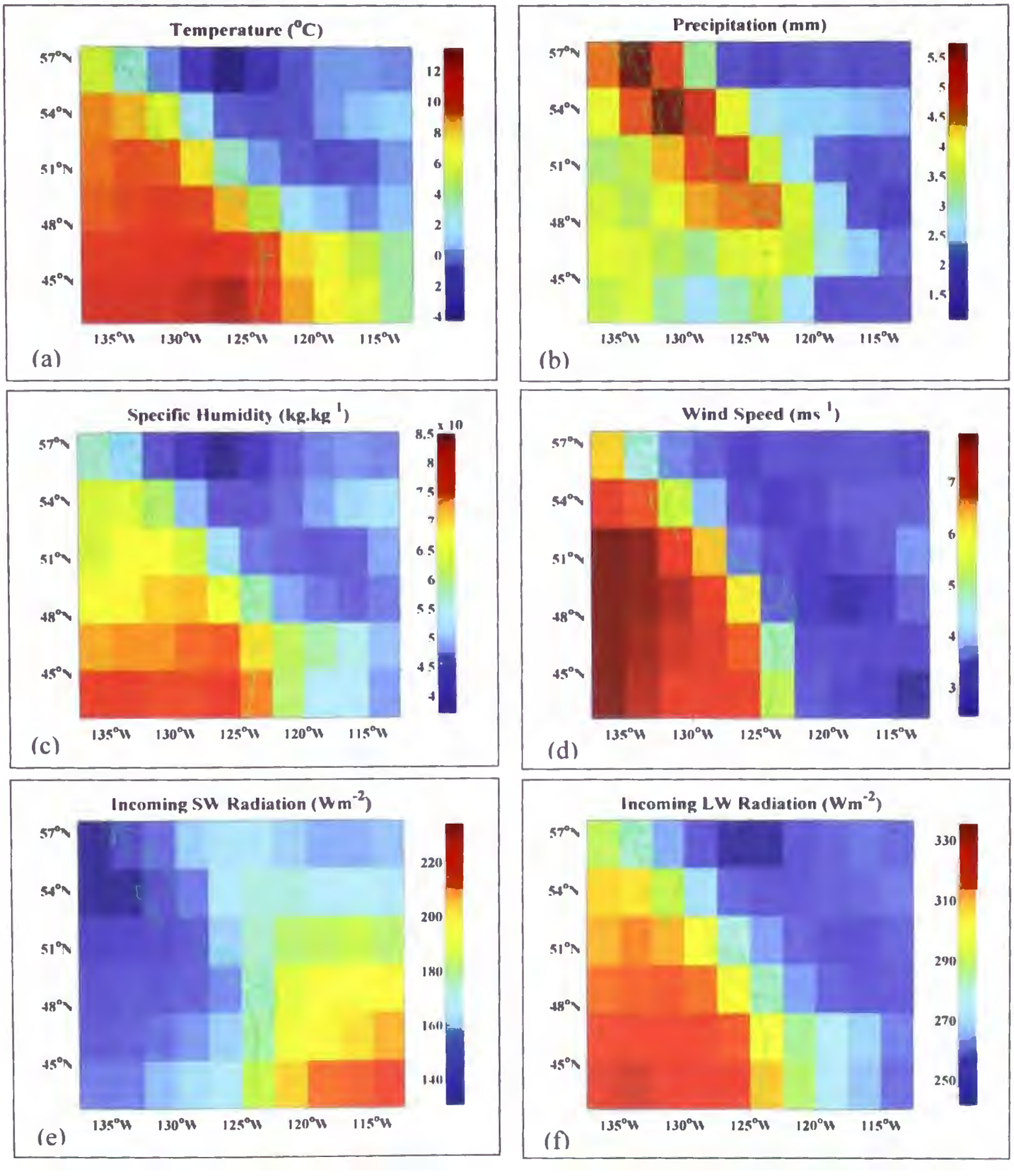

Figure 6.3 NCEP daily (a) air temperature, (b) precipitation, (c) specific humidity, (d) wind speed, (e) incoming shortwave radiation, and (f) incoming longwave radiation averaged over 1979-2008 for a section of the Pacific Northwest.

To better understand the spatial organization of RAMS fields, their modes of variability is identified using Empirical Orthogonal Function (EOF) analysis. The analysis is performed for all variables using both daily and monthly averaged datasets. However, only plots from the results of the EOF analysis using monthly RAMS temperature, precipitation and humidity are shown. Results of the analysis using daily data for both NCEP and RAMS variables are presented in Table 6.1.

Table 6.1 Percentage of total variance explained by the first three EOF modes for different NCEP and RAMS variables. Calculation is based on daily data from 1979-2008.

Variable	NCEP			RAMS		
	Mode-1	Mode-2	Mode-3	Mode-1	Mode-2	Mode-3
Temperature	85	6	3	95	1	1
Precipitation	30	17	10	71	9	6
Sp. Humidity	75	10	4	90	4	3
Wind Speed	40	13	11	60	14	7
Sea Level Pressure	58	20	13	95	2	2
Shortwave Rad.	88	3	2	78	5	5
Longwave Rad.	64	11	7	78	7	5

It should be noted here that the EOF results obtained from monthly datasets (Figures 6.4. 6.5 and 6.6) are similar to the results obtained using the daily dataset (Table 6.1). EOF plots presented below are essentially a correlation map between the grid values in the RAMS fields and the i^{th} mode of the singular vectors of the same field, also known as a homogeneous correlation map. The homogeneous correlation map is an indicator of the geographic localization of covarying parts of the field. For temperature, the EOF-1 alone explains approximately 93% of the total variance in the data (Figure 6.4). This pattern

exhibits a factor of one positive value throughout the domain that is increasing from the coast to the interior. The pattern associated with EOF-2 (3% explained variance) shows two areas of positive and negative values separated by the Coast Mountains. The lower panels in Figure 6.4 show time series of principal components (PCs) associated with the first two EOFs where the PCs are standardized. PC-1 shows some significant month to month variation in temperature data. The oscillating PC-1 time-series frequently cross the arbitrarily chosen ±1 horizontal line representing particularly high amplitude or extreme events. For PC-2, variability is negative during the first few years followed by positive variability and again negative variability during the last few years. Both the temperature PCs suggest significant temporal variation in the dataset. There is a significant annual variation in PC-2 (not shown), which perhaps suggests that the lower correlation values for EOF-2 seen in the interior could be due to cooling of the interior land mass during the winter months. For precipitation, the EOF-1 and EOF-2 explain about 71% and 9% of the total variance in the data, respectively (Figure 6.5). The dominant EOF-1 must be a result of orographic enhancement of precipitation associated with mid-latitude cyclones during winter months since it shows high values on the windward side of mountains and low values on the leeward side. Similar to temperature, EOF-1 for precipitation exhibits positive values throughout the domain. The pattern shows a decrease in values from the coast towards the interior. The actual mean precipitation in the region is characterized by a distinct east-west gradient due to the influence of the Coast Mountains. The pattern shown in EOF-1 appears consistent with the actual precipitation in the region. This result is similar to that obtained from a similar study in nearby Oregon and Washington, which reported nearly 70% and 15% of the variance in the first two EOFs, respectively (Widmann et al. 2003). Their study

used gridded area-averaged observed precipitation during winter months (50 km × 50 km lat-lon). The relatively less significant pattern associated with EOF-2 exhibits both positive and negative values in the domain. This pattern possibly represents the summertime precipitation pattern, which is mainly convective in the region. The EOF-2 dipole in the southern Coast Mountains appears to be dividing the northern and southern parts of the domain. Widmann et al. (2003) obtained similar results for the northwestern United States. They argued that the main effect of the mountain ranges is only a strong scaling of the precipitation rather than dividing two regions with a very different temporal variability. Thus, the influence of complex topography of this region is to complicate the mean pattern of precipitation and has much less impacts on its temporal variability. PC-1 for precipitation shows significant temporal variation, which often crosses the ±1 horizontal line. Temporal variability is found to be high for PC-2 as well.

The dominant pattern in specific humidity associated with EOF-1 explains nearly 90% of the total variance (Figure 6.6). Similar to precipitation, this pattern exhibits positive values throughout the domain. The values are high along the coast and decrease gradually towards the interior. However, the east-west gradient is not as strong as for precipitation and temperature. Similar to precipitation, EOF-2 divides the northern and southern parts of the domain. This probably represents the summertime moisture pattern, which appears to be influenced by an anticyclone usually situated over the domain during the summer months. For RAMS incoming shortwave radiation, incoming longwave radiation and sea level pressure (SLP) (figures not shown), only the first EOF mode is significant, which has explained variances of 78%, 78% and 95%, respectively. The variance in wind speed is

distributed in more than one EOF mode and the first EOF explains only 60% of the total variance.

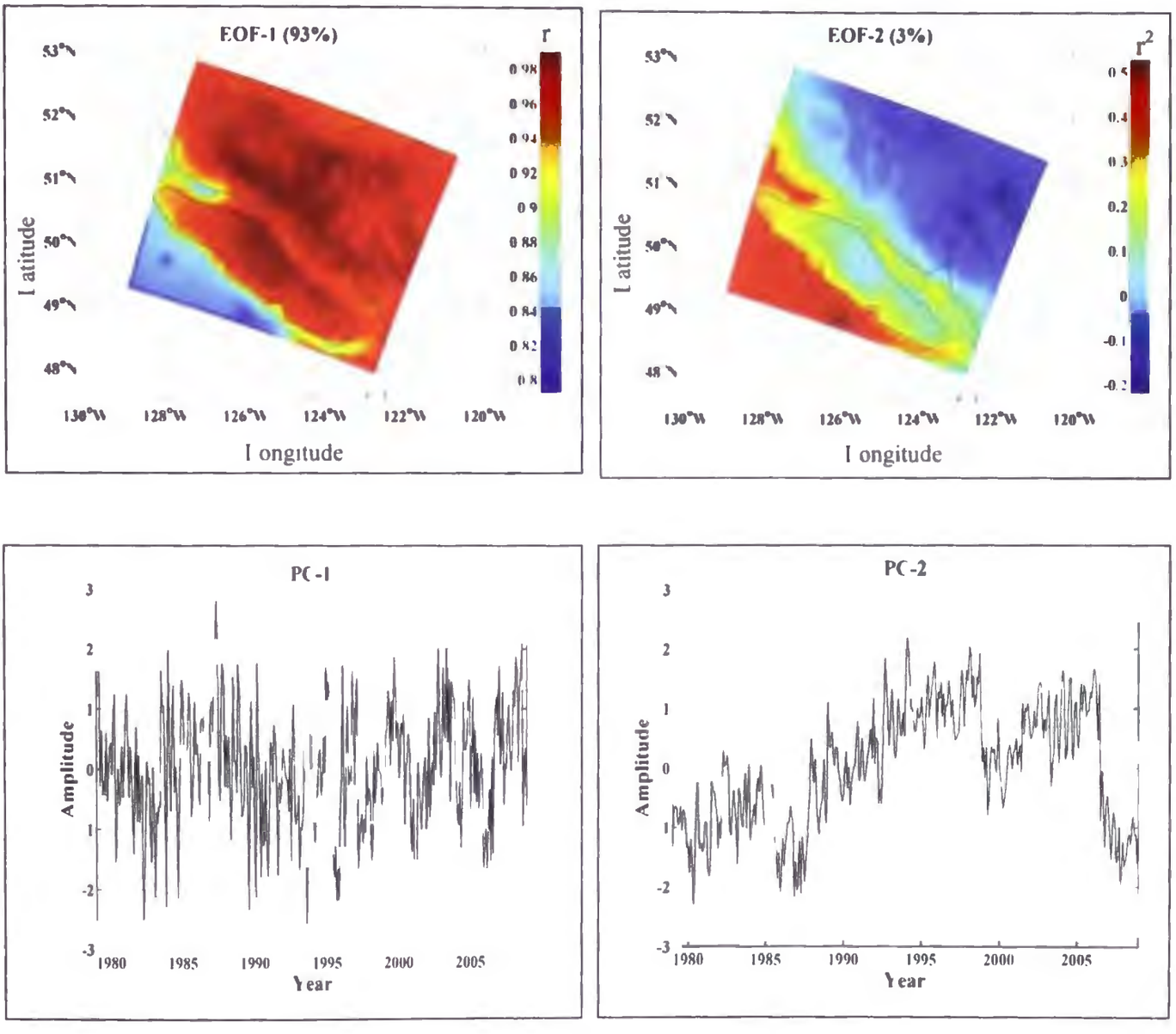

Figure 6.4 Correlation (r^2) maps of first two EOF modes (top) and Principal Components (PCs) (bottom) of monthly mean RAMS temperature for 1979-2008. EOF1 explains 93% of the total variance in the dataset. All PCs are standardized.

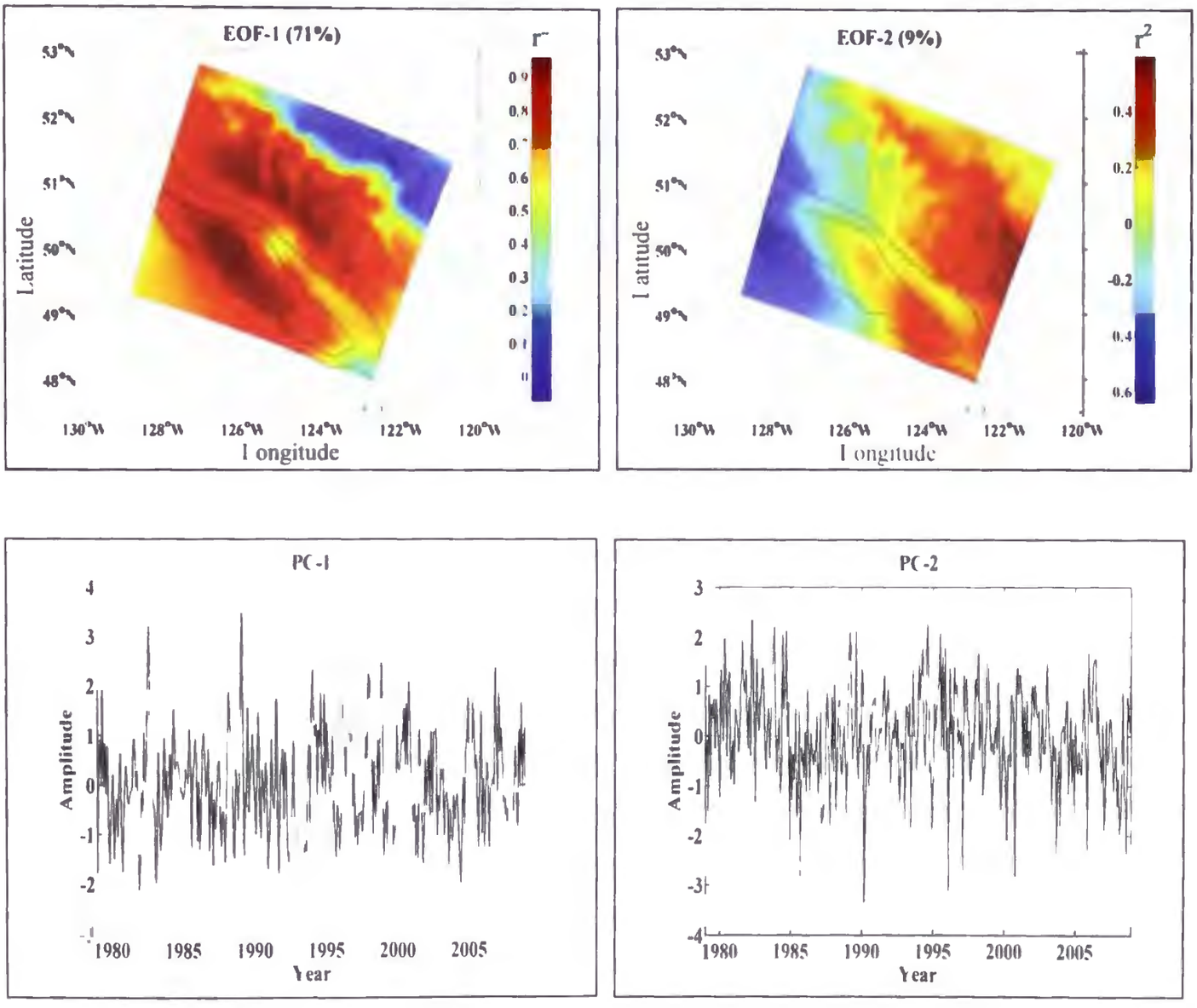

Figure 6.5 Correlation (r^2) maps of first two EOF modes (top) and Principal Components (PCs) (bottom) of monthly mean RAMS precipitation for 1979-2008. EOF-1 explains 71% of the total variance in the dataset. All PCs are standardized.

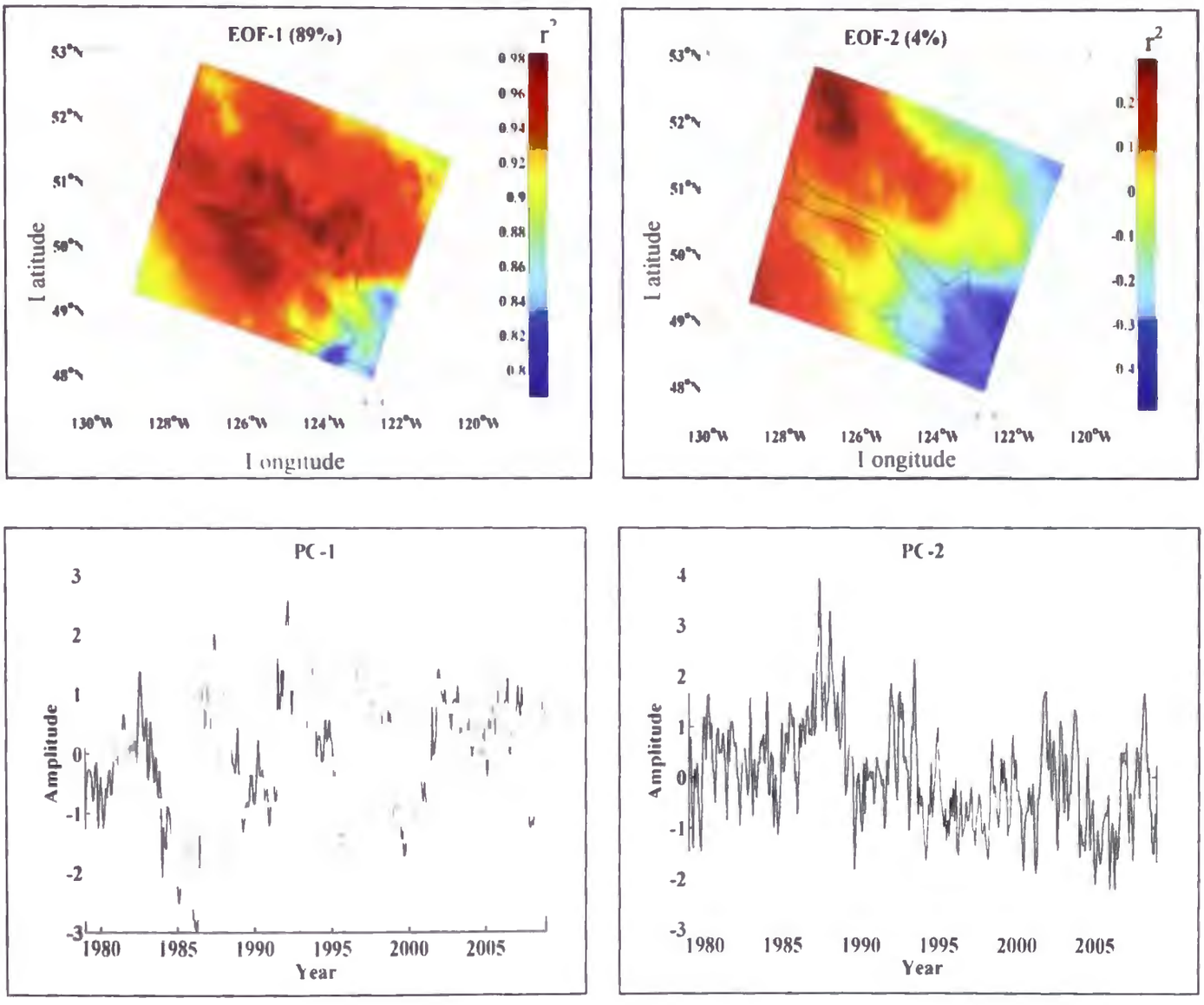

Figure 6.6 Correlation (r^2) maps of first two EOF modes (top) and Principal Components (PCs) (bottom) of monthly mean RAMS specific humidity for 1979-2008. EOF-1 explains 89% of the total variance in the dataset. All PCs are standardized.

6.3.2 SVD Downscaling Model

The SVD model calibration results for the various fields are compared in Table 6.2. Model calibration is based on daily values for 1979-1993. Results are presented for the leading three SVD modes only because these modes together explain most of variance in the predictand fields. The first column (r^2) for the i^{th} mode is the squared correlation coefficients (coefficient of determination) obtained from the correlation between the PCs of the predictor (NCEP) field and corresponding PCs for predictand (RAMS) field for that particular mode. The second column (EVF) is the percentage of overall variance of the predictand fields explained by the i^{th} mode of the reconstructed field. Sum of the EVFs for all the modes gives the total variance explained by the reconstructed field. The third column (SCF) for the i^{th} mode is the squared covariance fraction between predictor and predictand fields for that mode. Among all the variables considered, the SVD model for air temperature shows the strongest predictor-predictand relationship. With EVF of 83%, the SVD first mode for air temperature explains most of the variance in the predictand field. The strong predictor-predictand relationship is also apparent in large SCF value for Mode-1. However, this result cannot be independently verified as there have not been other studies in the region using the SVD technique for air temperature downscaling. Although the SVD method of temperature downscaling performed poorly compared to other statistical methods in central Europe (Huth 1999), the model appears to be performing well in the Coast Mountains. One more thing to note here is that the Huth (1999) study used station observations as the predictand whereas the predictand field used in the present study comes from the RAMS mesoscale model. This may also have caused the discrepancies in the results.

Table 6.2 Characterization of the leading three SVD modes for the calibration period. Rows refer to the daily NCEP and RAMS fields considered. The three columns per mode show the coefficient of determination (r^2), explained variance fraction (EVF), and squared covariance fraction (SCF). All values are in percentages. For all the variables, the correlations are statistically-significant at 95%.

Variable	Mode-1			Mode-2			Mode-3		
	r^2	EVF	SCF	r^2	EVF	SCF	r^2	EVF	SCF
Temperature	87	81	96	57	2	2	34	0.5	1
Precipitation	78	51	69	47	6	13	39	3	9
Sp. Humidity	87	78	90	59	2	6	34	3	2
Wind Speed	59	36	64	35	4	13	31	3	8
Sea Level Pressure	33	32	86	54	10	8	46	12	5
Shortwave Rad.	62	49	93	27	4	3	29	4	2
Longwave Rad.	44	34	80	25	5	8	24	3	6

For precipitation, however, the predictor-predictant relationship appeared to be less strong. The first three modes combined explained 60% of the variance and 90% of the covariance in the predictand field. The remaining variance is distributed across the other modes. By considering the first 6 modes (not shown here), the total explained variance increased to 64%, which is an improvement of only 4%. The small explained variance in modes other than the first three modes suggests that these modes are less significant for developing the SVD model for precipitation downscaling. The less significant modes detected could be due to some kind of noise or other small-scale variability in the precipitation dataset, which is not investigated in the present study. This result clearly demonstrates the complex nature of precipitation in the region. This result appears to be consistent with similar work in the Pacific Northwest that reported a Mode-1 and Mode-2

combined explained variance of 50% using the same NCEP precipitation dataset as predictor but station observations as predictands (Widmann et al. 2003). They reported a combined covariance of 98%, while the present study found a combined covariance of 90%. However, it should be noted here that the results reported by Widmann et al. (2003) are based on precipitation data for winter months whereas the data used in the present study are for the entire year. The same study argued that on a large-scale, reanalyzed precipitation is a better predictor field than any other circulation or moisture based fields.

The model for specific humidity showed relatively better skill in downscaling reanalysis humidity fields to the RAMS domain. The first three SVD modes displayed r^2 of 87, 59, and 34% indicating a strong relationship between predictor and predictand. When all three modes are combined, the model explained 83% of the total variance. The SVD model for SLP exhibits very complex results. Unlike for the other fields, the correlation in Mode-1 is lower than in Mode-2. The first three modes combined explained 54% of the total variance. The Mode-1, Mode-2, and Mode-3 combined explained variance of the SVD model for wind speed and shortwave radiation is 43 and 57%, respectively whereas it is only 42% for longwave radiation. In spite of the relatively small explained variance seen for most of the variables, the SVD models for most of the variables exhibited a higher covariance fraction. Also, similar to the modes for temperature, precipitation and humidity, a large fraction of the explained variance for all other downscaled variables is contained in the first mode. This shows the relative importance of Mode-1 in developing the SVD model. SVD results for these variables cannot be verified independently due to the lack of similar studies not only in the study domain but also in other parts of the world.

The results from the SVD analysis of different fields for the first mode are also displayed in the form of a heterogeneous correlation map (Figure 6.7). For the i^{th} mode, this is a correlation map between the grid values of the predictand field (i.e. the RAMS field) and the i^{th} principal component of the predictor field (i.e. the NCEP field). The heterogeneous correlation map indicates how well the grid values of one field can be predicted with the knowledge of the i^{th} principal component of the other. For most of the southern Coast Mountains, the SVD Mode-1 for air temperature (Figure 6.7a) exhibits higher correlation except for a few isolated locations where the correlation coefficient is relatively small. As the smaller correlation coefficients seen are mainly located over the mountains, the model will likely yield less accurate results when used for air temperature downscaling over the complex mountain terrain. The spatial variation of correlation coefficient is more distinct for Mode-1 of precipitation (Figure 6.7b). Relatively large correlation coefficients seen along the coast compared to the interior might suggest a better model skill in downscaling precipitation at the coast than in the interior. Within the southern Coast Mountains, there are isolated areas displaying small correlation coefficients. This is possibly due to the SVD model's inability to resolve orographic precipitation in those areas. Unlike the SVD model for air temperature and precipitation, the Mode-1 for humidity (Figure 6.7c) shows a uniformly distributed correlation coefficient for much of the domain except for locations near the south-eastern corner. For wind speed, the SVD Mode-1 explains 32% of the variance on average (Figure 6.7d). The variance is highly variable in space. Similar to the model for wind speed, the Mode-1 of the SVD model for SLP, incoming shortwave radiation and incoming longwave radiation show highly variable correlation coefficients, suggesting that the model skill will be different for different

locations. The model is expected to perform relatively better in downscaling this field in the northern part of the domain compared to the southern part. Mode-1 of the SVD model for incoming shortwave radiation (Figure 6.7f) has higher explained variance than its longwave counterpart. At 47% of explained variance on average, Mode-1 of the SVD model for incoming shortwave radiation shows a distinct east-west gradient in correlation coefficient. A similar spatial pattern is seen for Mode-1 of the SVD model for incoming longwave radiation (Figure 6.7g) but with less explained variance on average (32%) than its shortwave counterpart. The lower explained variance seen in Mode-1 of the SVD model for wind speed, SLP, incoming shortwave and longwave radiation suggests the need for considering other modes for developing a better model for downscaling these variables. However, the small explained variance for the other modes (not shown here) suggests that the overall variance is not going to improve significantly even by considering three or more modes. Unlike for these variables, Mode-1 of the SVD model for air temperature, precipitation and humidity alone explains more than 50% of the variance in corresponding predictand (i.e. RAMS) fields. Among these three variables, precipitation has the smallest explained variance, which is 59% of the variance if both Mode-1 and Mode-2 are combined. SVD models for air temperature, precipitation and humidity explain 84%, 63%, and 83% of the variance, respectively if the first three modes are considered. Overall, it appears that the SVD model developed for air temperature, precipitation and humidity will perform better compared to the model developed for the other variables.

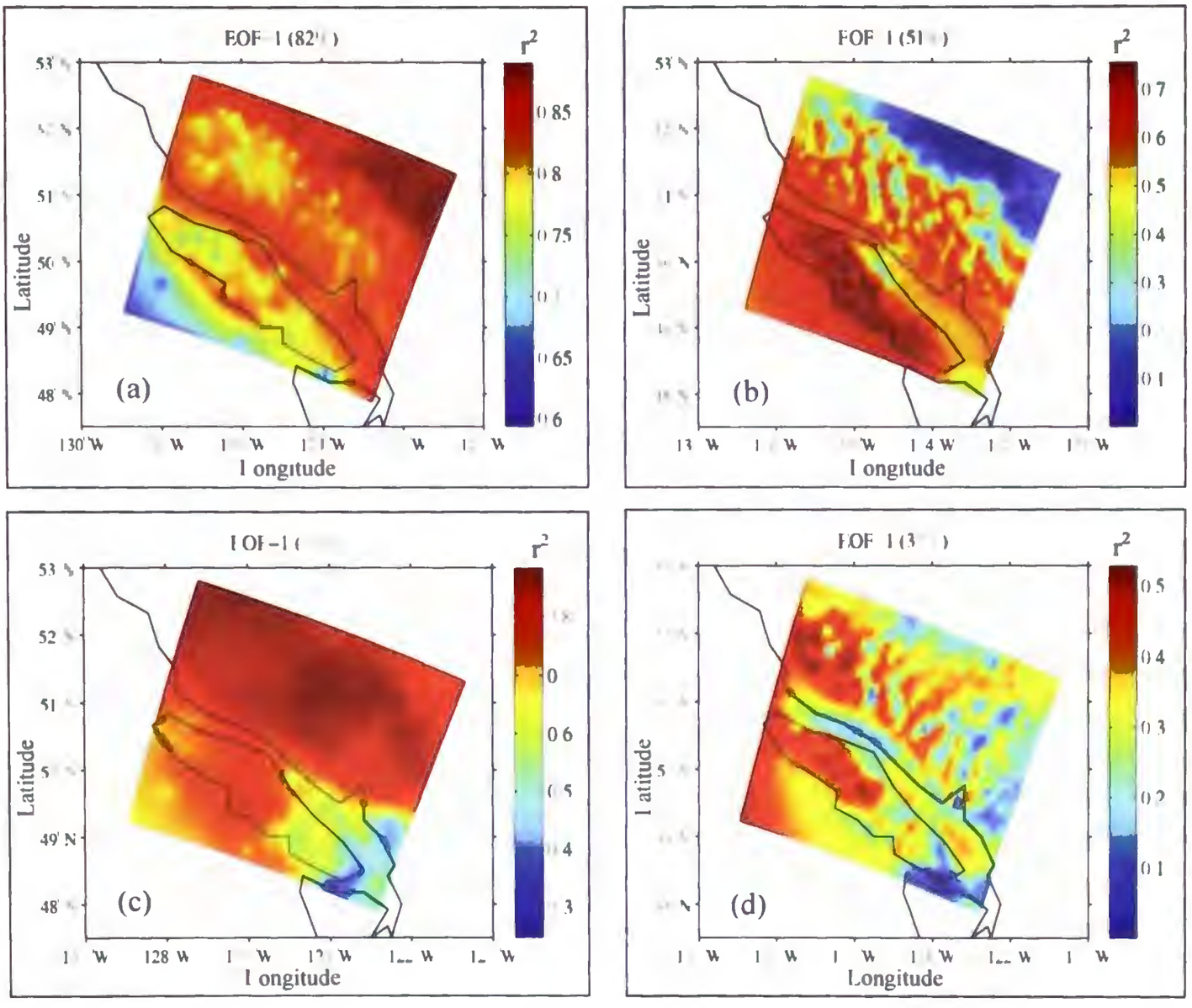

Figure 6.7 (continued on next page)

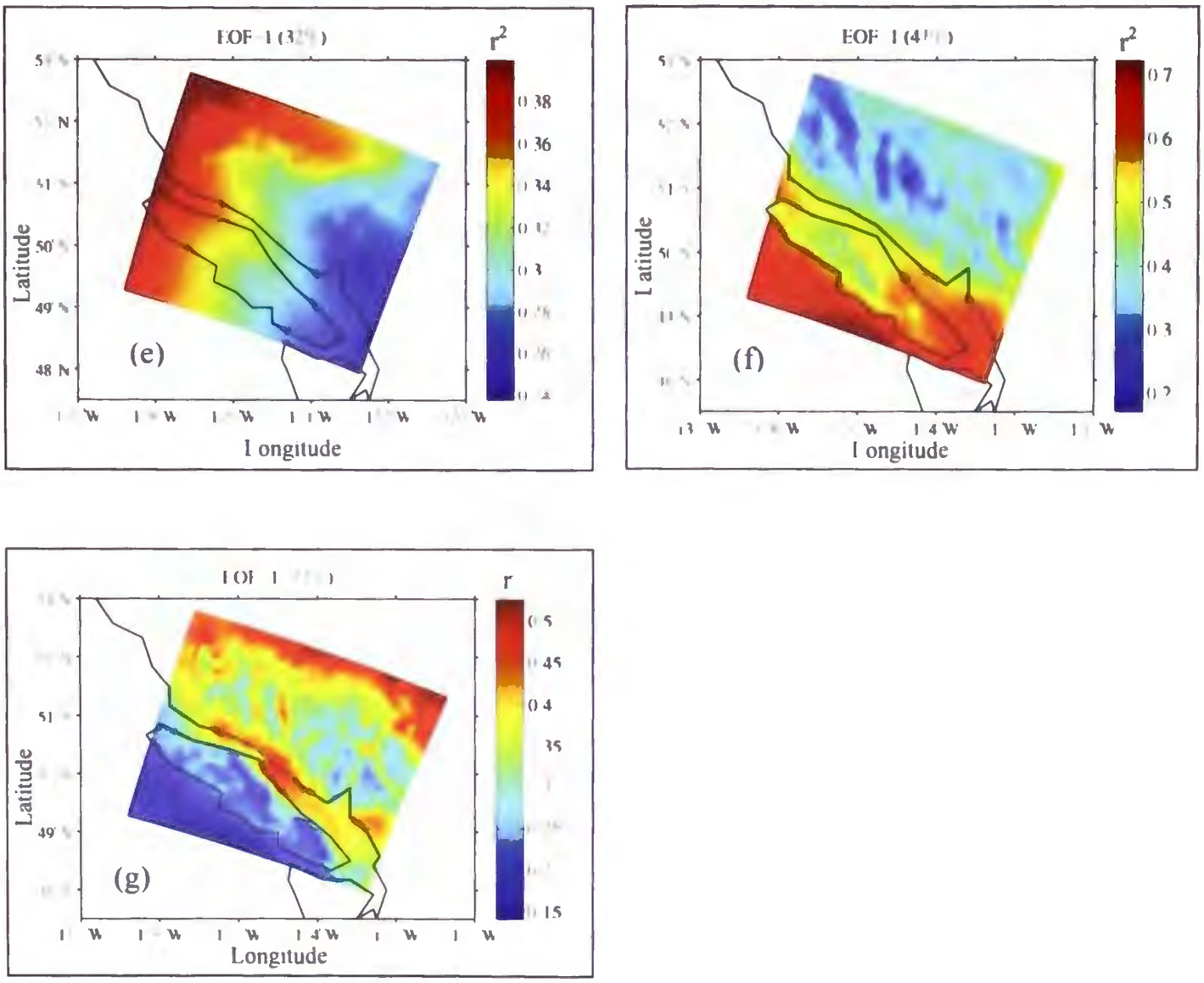

Figure 6.7 Heterogeneous correlation (r^2) maps displaying the correlation between grid values of predictand and the Mode-1 of the singular vectors of the predictor fields. Correlation map is displayed for (a) air temperature, (b) precipitation, (c) specific humidity, (d) wind speed, (e) sea level pressure (f) incoming shortwave radiation, and (g) incoming longwave radiation. Values in parentheses above each figure refer to the total variance in the predictand field explained by Mode-1 of the predictor fields.

The SVD model developed here using daily data is compared with the model developed using monthly data for the same period (1979-1993). The results from the monthly model are nearly identical to the results from their daily counterparts (not shown here). Similar results were reported by Widmann et al. (2003) for downscaling precipitation

in the Pacific Northwest. To maximize the explained variance in the downscaled fields, the final SVD model is developed using the first three leading modes. Optimized SVD model coefficients for the leading three modes are given in Table 6.3.

Table 6.3 Optimized SVD model parameters (m : slope, and b : intercept) and coefficient of determination (r^2) for the first three modes in percent. For all the variables, the correlations are statistically significant at 95% . Model calibration is performed for the listed variables using daily datasets from 1979-1993.

Variable	Mode-1			Mode-2			Mode-3		
	r^2	m	b	r^2	m	b	r^2	m	b
Temperature	87	5.29	-0.12×10^{-12}	57	2.67	0.14×10^{-12}	34	1.27	1.45×10^{-14}
Precipitation	78	10.27	$0.49\cdot10^{1}$	47	3.77	$-0.10\cdot10^{1}$	39	3.16	2.94×10^{-14}
Sp. Humidity	87	5.11	$-0.46\cdot10^{1}$	59	2.29	0.10×10^{-16}	34	2.67	-4.61×10^{-17}
Wind Speed	59	5.12	$0.01\cdot10^{1}$	35	3.17	$0.84\cdot10^{-1}$	31	3.31	1.30×10^{-14}
Sea Level Pressure	33	7.29	$-0.35\cdot10^{-09}$	54	2.01	$0.03\cdot10^{-09}$	46	1.81	-5.84×10^{-12}
Shortwave Rad.	62	5.52	$-0.08\cdot10^{-11}$	27	5.42	$0.10\cdot10^{-11}$	29	7.82	4.91×10^{-17}
Longwave Rad.	44	5.37	$-0.09\cdot10^{-11}$	25	3.56	0.17×10^{-11}	24	2.52	4.52×10^{-13}

6.3.3 SVD Model Validation

Cross validation statistics are calculated for the daily and monthly models using the remaining (1994-2008) NCEP and RAMS data. The model is evaluated using root mean squared error (RMSE) and mean absolute error (MAE). Variance in the evaluation data explained by the respective downscaled result is determined using Pearson correlation coefficient. Correlation is considered statistically significant if the p-value is less than 0.05. The MAE shows the average error in the prediction without the disproportionate weighting the RMSE gives to occasional large errors. Table 6.4 summarizes these results for daily (monthly) models. These error statistics are presented as spatially averaged values. The r^2

values indicate that the daily precipitation and wind speed are least accurately downscaled. Both daily and monthly models for air temperature and humidity appear to be performing relatively better in downscaling. The error statistics improved for the monthly model, which is more significant for precipitation. Similarly, for other variables, the error statistics show a marked improvement for the monthly model. For example, for incoming shortwave radiation, the RMSE and MAE are 75 W m^{-2} and 59 W m^{-2} when the daily model is used. The errors decreased to 14 W m^{-2} and 11 W m^{-2} when the monthly model is used. Also, error statistics improved significantly for wind speed and SLP for the monthly model as compared to the daily model. In general, the skill of the daily and monthly model to downscale air temperature, humidity and longwave radiation is better than downscaling any other variables. For all variables the downscaled result is statistically-significant at 95%.

Table 6.4 Cross-validation of the SVD model using the 1994-2008 dataset. Rows refer to downscaled NCEP variables. The last three columns refer to spatially-averaged explained variance, RMSE and MAE. Values in parentheses refer to the monthly model, whereas other values are for the daily model.

		Spatial Average	
Variable (Units)	r^2 (%)	RMSE	MAE
Temperature (°C)	85 (62)	2.4 (0.58)	1.9 (0.47)
Precipitation (mm day^{-1})	38 (57)	7.5 (0.29)	3.5 (0.23)
Sp. Humidity (kg.kg^{-1})	82 (78)	6.9 (1.4) $\times 10^{-4}$	5.3 (1.1) $\times 10^{-4}$
Wind Speed (m s^{-1})	38 (12)	1.5 (0.34)	1.2 (0.27)
Sea Level Pressure (hPa)	71 (65)	4.7 (0.9)	3.6 (0.7)
Shortwave Rad. (W m^{-2})	48 (17)	75 (14)	59 (11)
Longwave Rad. (W m^{-2})	42 (48)	32 (6)	27 (5)

Next, the performance of the daily SVD model is examined spatially (Figure 6.8). Air temperature downscaled using the leading three SVD modes are highly correlated with the validation dataset in most of the domain. The highest and lowest r^2 values for temperature in the domain are nearly 0.9 and 0.7, respectively. RMSE in downscaled air temperature shows a distinct spatial variation in the domain. RMSE is smallest over the coast and increases towards the interior with values reaching as high as 3.2°C over the Coast Mountains. On average, RMSE is nearly 3°C in the interior. The model appears to be less skillful in downscaling precipitation. The r^2 map shows a weaker correlation between the downscaled and validation dataset over the mountains and in the interior. They are practically uncorrelated in areas further east of the coastal ranges. Moderate r^2 values (0.4-0.6) over the mountain ranges suggest that the SVD model is satisfactorily downscaling precipitation over the mountains. However, RMSE in downscaled precipitation shows a different result. The RMSE in downscaled precipitation is very large in most of the domain. The value ranges between 2 mm day^{-1} and 27 mm day^{-1} in some locations. The downscaled humidity values show a better correlation with the validation dataset. For the whole domain, the correlation ranges from 0.7 to 0.85. The RMSE in downscaled humidity is also small and uniformly distributed over most of the domain (RMSE = 4.9 $x10^{-4}$ $kg.kg^{-1}$). The model seems to be performing well in downscaling the humidity. Similar to precipitation, the downscaled wind speed also shows only a moderate correlation with the validation dataset. There is no distinct pattern in correlation values in the domain. On average, the SVD model for wind speed appears to be working relatively better in the coastal region and in some areas of the interior. RMSE in downscaled wind speed shows a slight improvement in the coastal region compared to the interior. The SVD downscaling model for shortwave

radiation appears to be performing more satisfactorily in the coastal region than in the interior. The r^2 value ranges from 0.4 in the interior to 0.6 on the coast. Similarly, RMSE is also relatively high in the interior compared to the coast. Unlike shortwave radiation, the SVD model for longwave radiation shows relatively high correlation along the coast compared to the interior. The RMSE in downscaled longwave radiation is significantly smaller than the error in its shortwave counterpart. The RMSE ranges from 27 to 39 W m^{-2} in the domain.

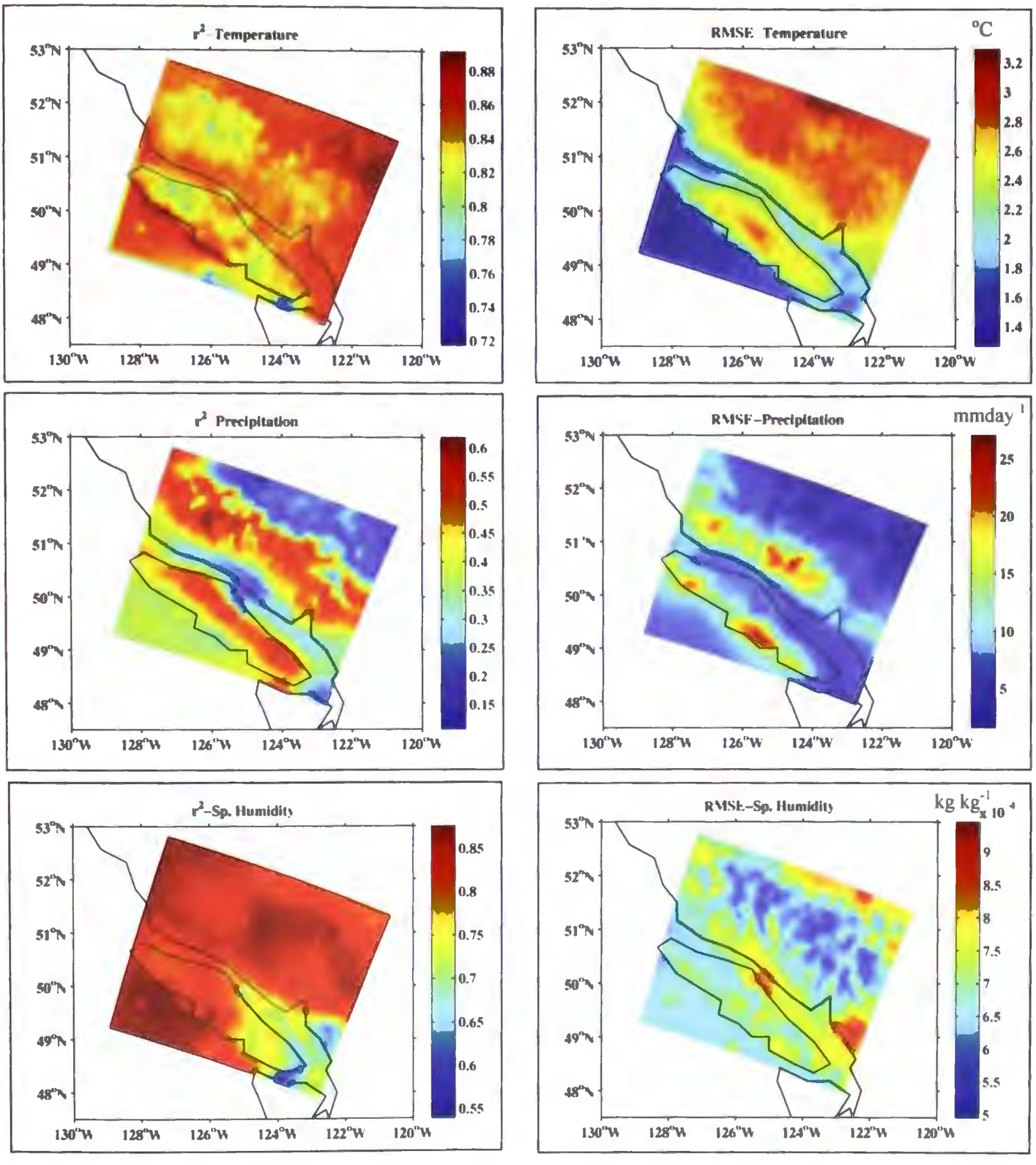

Figure 6.8 (continued on next page)

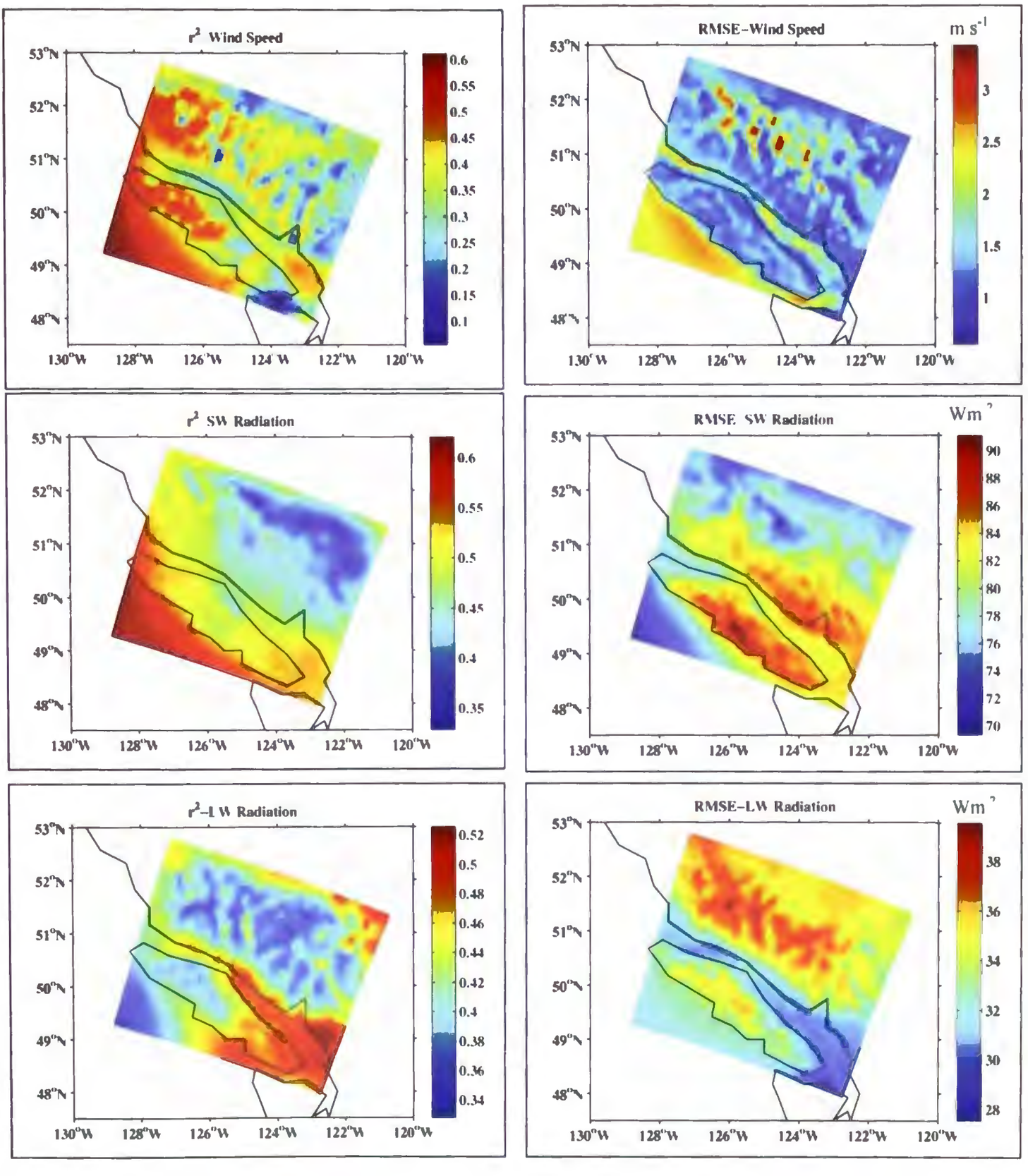

Figure 6.8 Correlation (r^2) between downscaled and validation dataset (column 1) and RMSE in downscaled values (column 2) for different variables on the RAMS domain. Results are based on the daily SVD model.

As seen in Table 6.4, the downscaling results improved significantly when a monthly downscaling model is used. Next, the performance of the monthly model is further examined for individual grid cells (Figure 6.9). The results clearly show the monthly model outperforming its daily counterpart over the domain. The monthly SVD model performed significantly better than the daily model in downscaling temperature, precipitation and humidity. For most of the coastal region, the downscaled temperature and the validation dataset has a correlation of 0.6 to 0.7. For most of the domain, RMSE values are small (0.4 to 0.8°C). Errors in downscaled temperature are relatively high over the mountain range (0.7 to 0.8°C) as compared to errors over the coastal region (0.4 to 0.6°C). The SVD model for downscaling monthly precipitation appears to be performing significantly better compared to its daily counterpart. The monthly SVD model yielded a higher correlation coefficient (0.5-0.7) for areas on the coast and in the mountains. However, the correlation is weak in the interior. RMSE in downscaled precipitation (=0.29 mm day^{-1}) also improved in the monthly SVD model. Downscaled humidity values showed a strong correlation with the validation dataset over the entire domain. Except for a few isolated locations with small correlations, most of the locations showed high correlation values ranging from 0.7 to 0.8. Also, the RMSE in downscaled humidity is small. The model for wind does not show any improvement in correlation values compared to the daily model. However, the model yielded smaller RMSE values for most of the grid cells in the domain. RMSE in downscaled shortwave radiation from the monthly model shows some improvement over the result from the daily model but there is no visible improvement in correlation values. r^2 values improved slightly for longwave radiation using the monthly model. Also, the RMSE in downscaled

longwave radiation improved significantly for the monthly model compared to the results from the daily model.

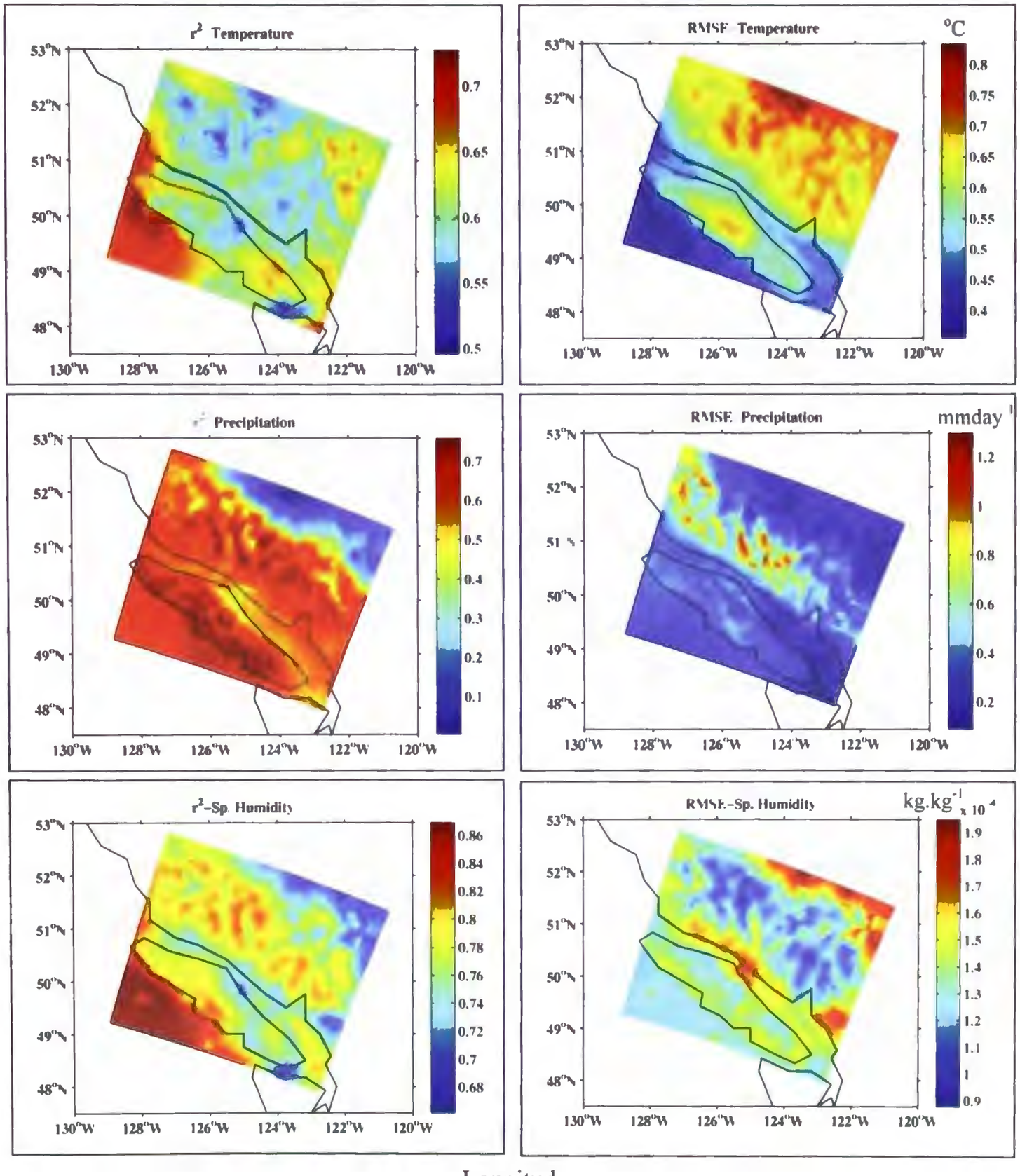

Figure 6.9 (continued on next page)

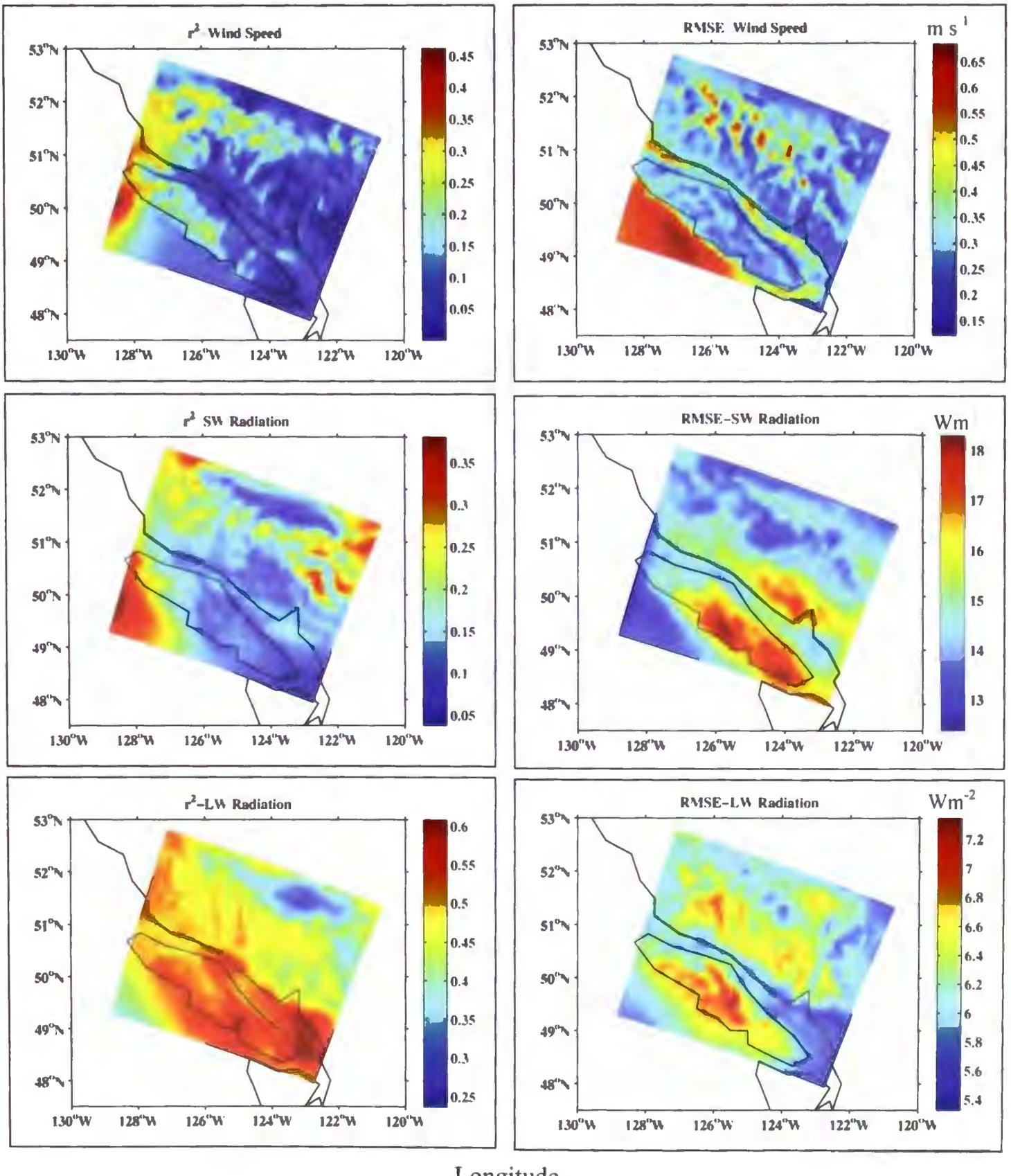

Figure 6.9 Correlation (r^2) between downscaled and validation dataset (column 1) and RMSE in downscaled values (column 2) for different variables on the RAMS domain. Results are based on the monthly SVD model.

6.3.4 GCM Climate Downscaling

Before discussing downscaling results for future GCM fields, GCM fields are examined for possible biases. Biases in GCM fields are estimated as a difference between the long-term (1961-2005) averages of GCM and NCEP fields. Here, long-term averages are used for determining bias instead of daily values because in the historic period GCMs are not initialized with actual conditions and therefore the daily fields have no meaning when compared with NCEP, which is initialized with observations. Bias estimation results are presented in Figure 6.10 through Figure 6.13 Spatially averaged biases in different variables for each GCM are given in Table 6.5. MAE error in a particular field varied between the GCMs. Also, for a particular GCM, errors varied between different fields. As an example, MAE in air temperature from different GCMs ranged between 0.55°C (CanESM2) and 2°C (MIROC-ESM). The inter-model MAE in precipitation ranged between 0.15 mm day^{-1} (CanESM2) and 0.65 mm day^{-1} (MIROC-ESM). Although the MAE and RMSE in all fields and for all models based on monthly values showed a significant improvement, these estimated bias values may not be applicable for bias correcting GCM fields with temporal resolution shorter than this.

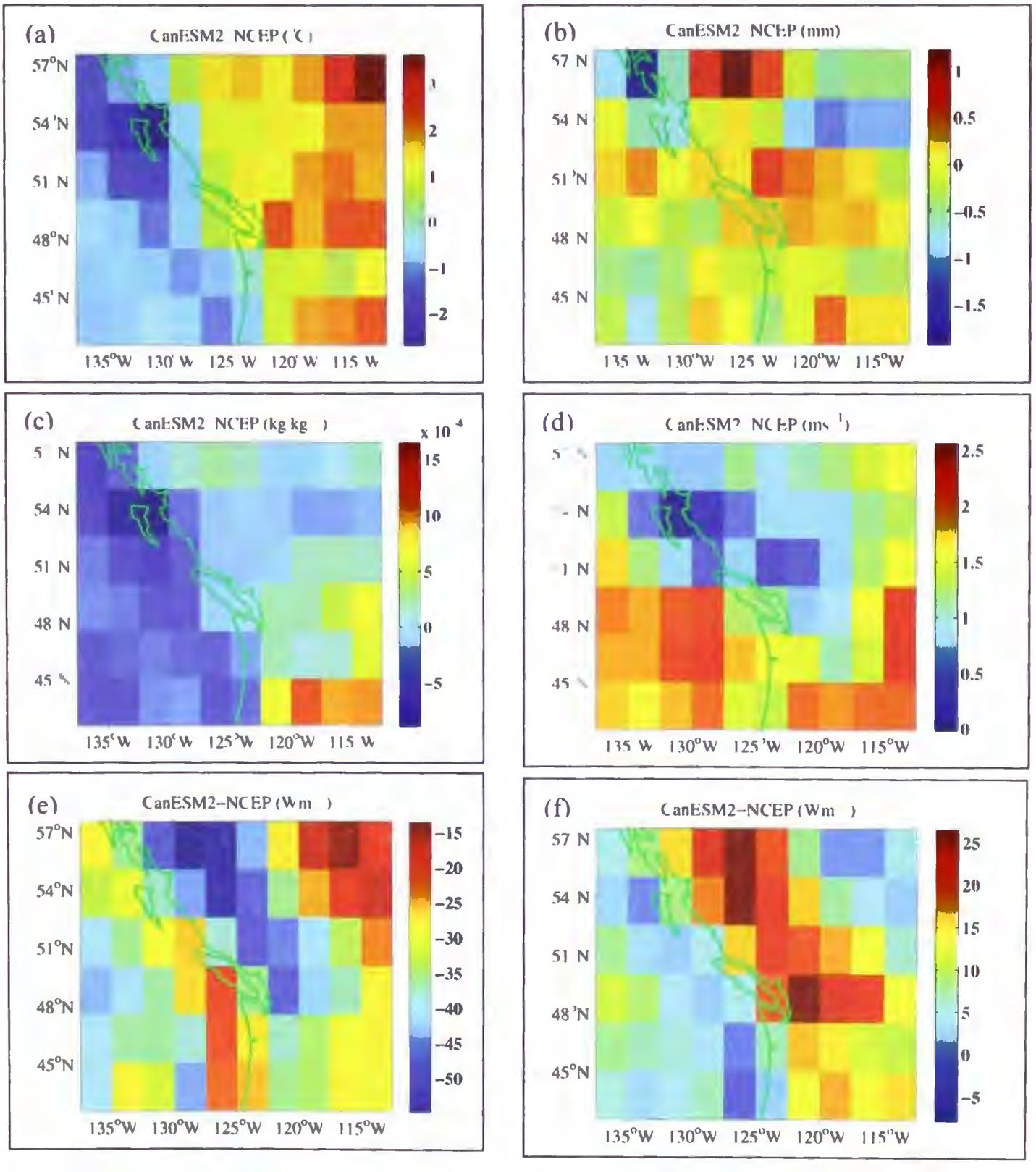

Figure 6.10 Biases in long-term (1961-2005) average CanESM2 as compared to NCEP averaged over the same period. (a) temperature, (b) precipitation, (c) specific humidity, (d) wind speed, (e) incoming shortwave radiation, and (f) incoming longwave radiation.

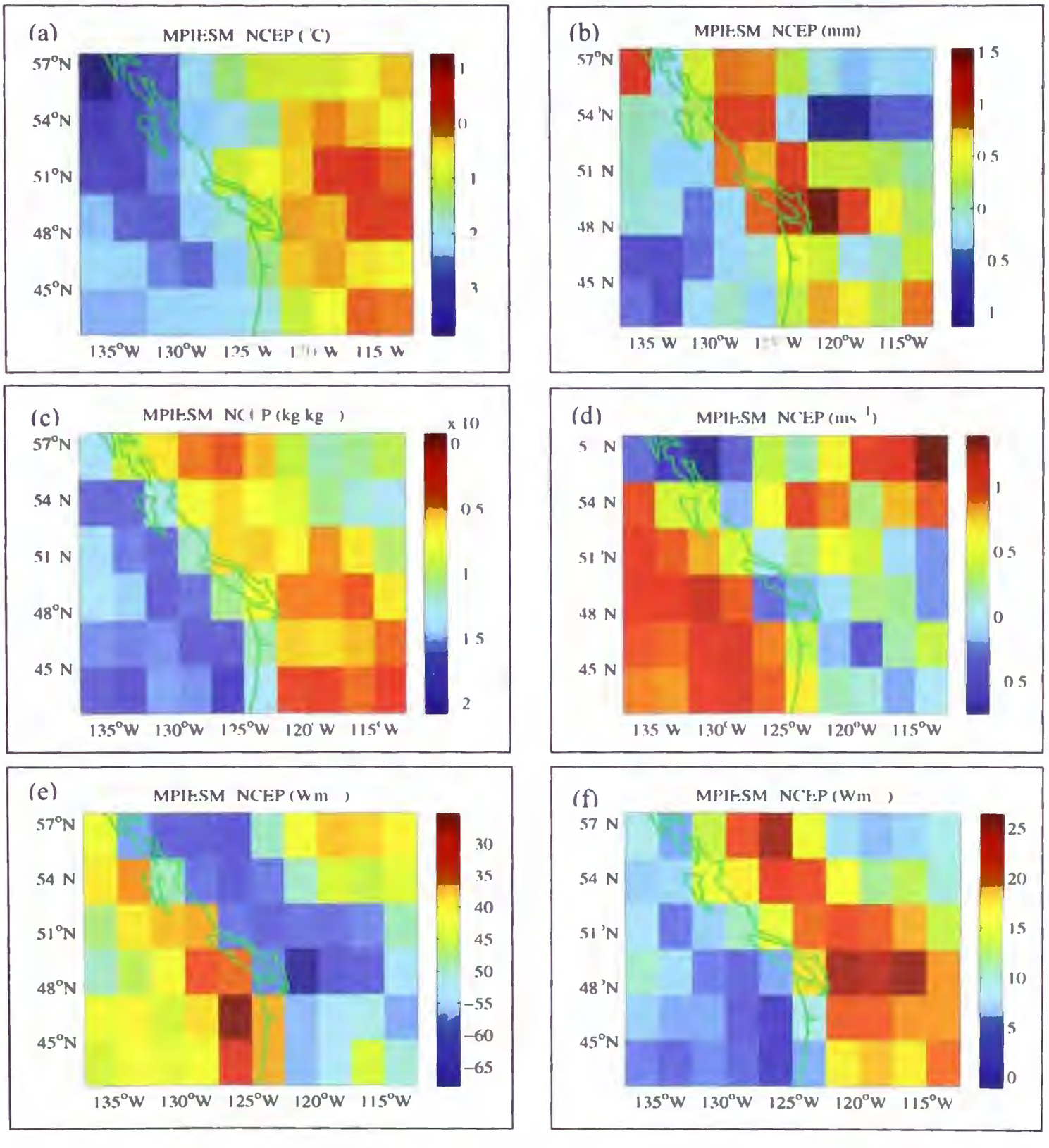

Figure 6.11 Biases in long-term (1961-2005) average MPI-ESM as compared to NCEP averaged over the same period. (a) temperature, (b) precipitation, (c) specific humidity, (d) wind speed, (e) incoming shortwave radiation, and (f) incoming longwave radiation.

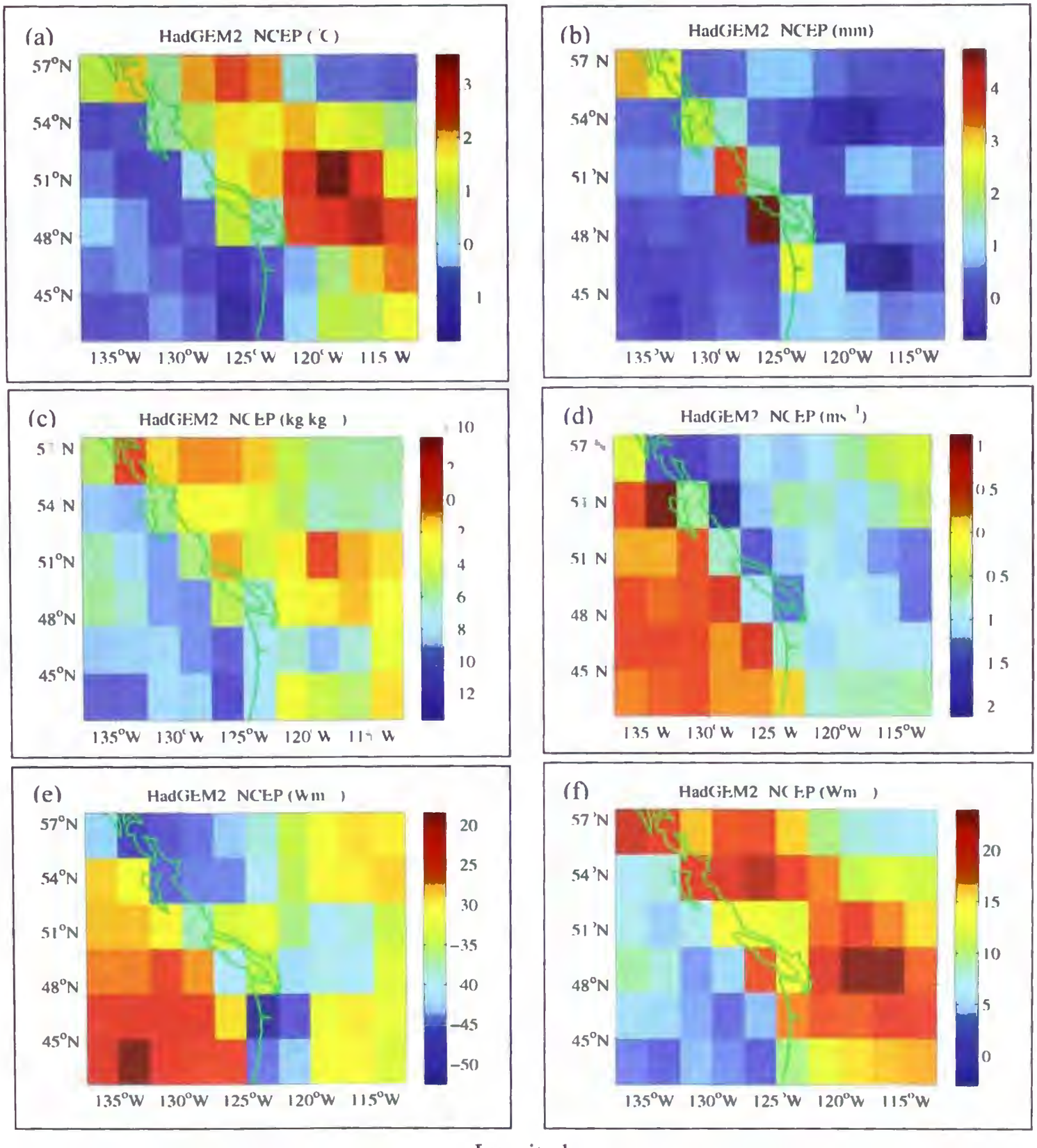

Figure 6.12 Biases in long-term (1961-2005) average HadGEM2 as compared to NCEP averaged over the same period. (a) temperature, (b) precipitation, (c) specific humidity, (d) wind speed, (e) incoming shortwave radiation, and (f) incoming longwave radiation.

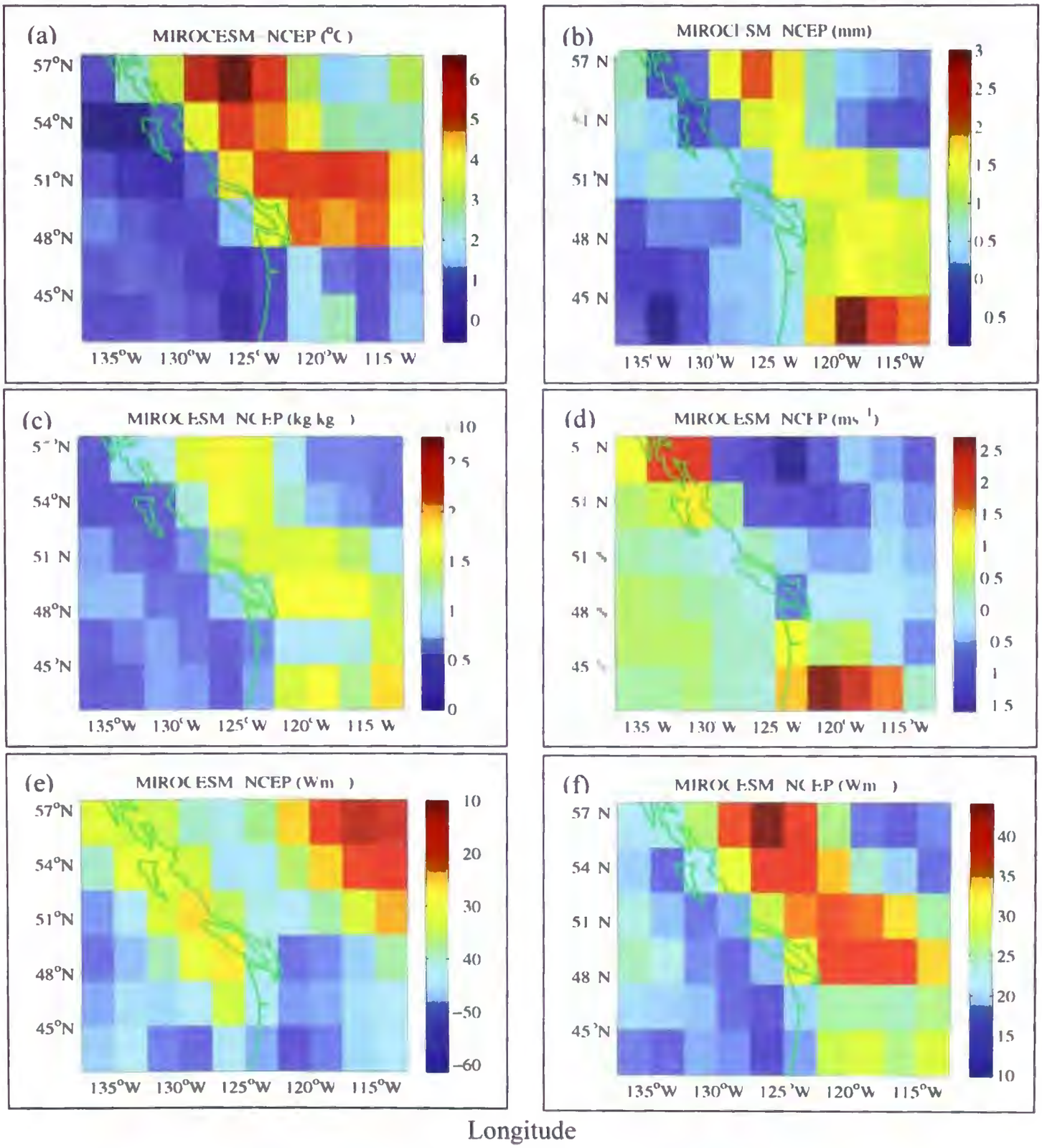

Figure 6.13 Biases in long-term (1961-2005) average MIROC-ESM as compared to NCEP averaged over the same period. (a) temperature, (b) precipitation, (c) specific humidity, (d) wind speed, (e) incoming shortwave radiation, and (f) incoming longwave radiation.

Table 6.5 Spatially averaged MAE errors in different fields from a suite of GCMs. Errors are estimated as a difference between GCM and NCEP fields (GCM-NCEP) averaged over the period 1961-2005. T_a: air temperature (°C); P: precipitation (mm day^{-1}); q: specific humidity (kg.kg^{-1}) ; u: wind speed (m s^{-1}), K_{in}: incoming shortwave radiation (W m^{-2}); and L_{in}: incoming longwave radiation (Wm^{-2}). RMSE has the same unit as the quantity being estimated.

GCM	T_a	P	q	u	K_{in}	L_{in}
CanESM2	0.55	0.15	6 6 10^{-6}	1.4	33	9
MPI-ESM-LR	1.3	0.12	0.0	0 48	46	12
MIROC-ESM	2	0.65	9.9 10	0.26	39	24
HadGEM2-ES	0.56	0.42	5.4 10^{4}	0.49	30	12

Spatially averaged annual GCM fields are compared with corresponding NCEP fields and presented as box plots in Figure 6.14. On each box, the central mark is the median, the edges of the box are the 25th and 75th percentiles, the whiskers extend to the most extreme data points not considered outliers, and outliers are plotted individually. The whisker's length corresponds to approximately ± 2.7σ and 99.3% coverage if the data are normally distributed.

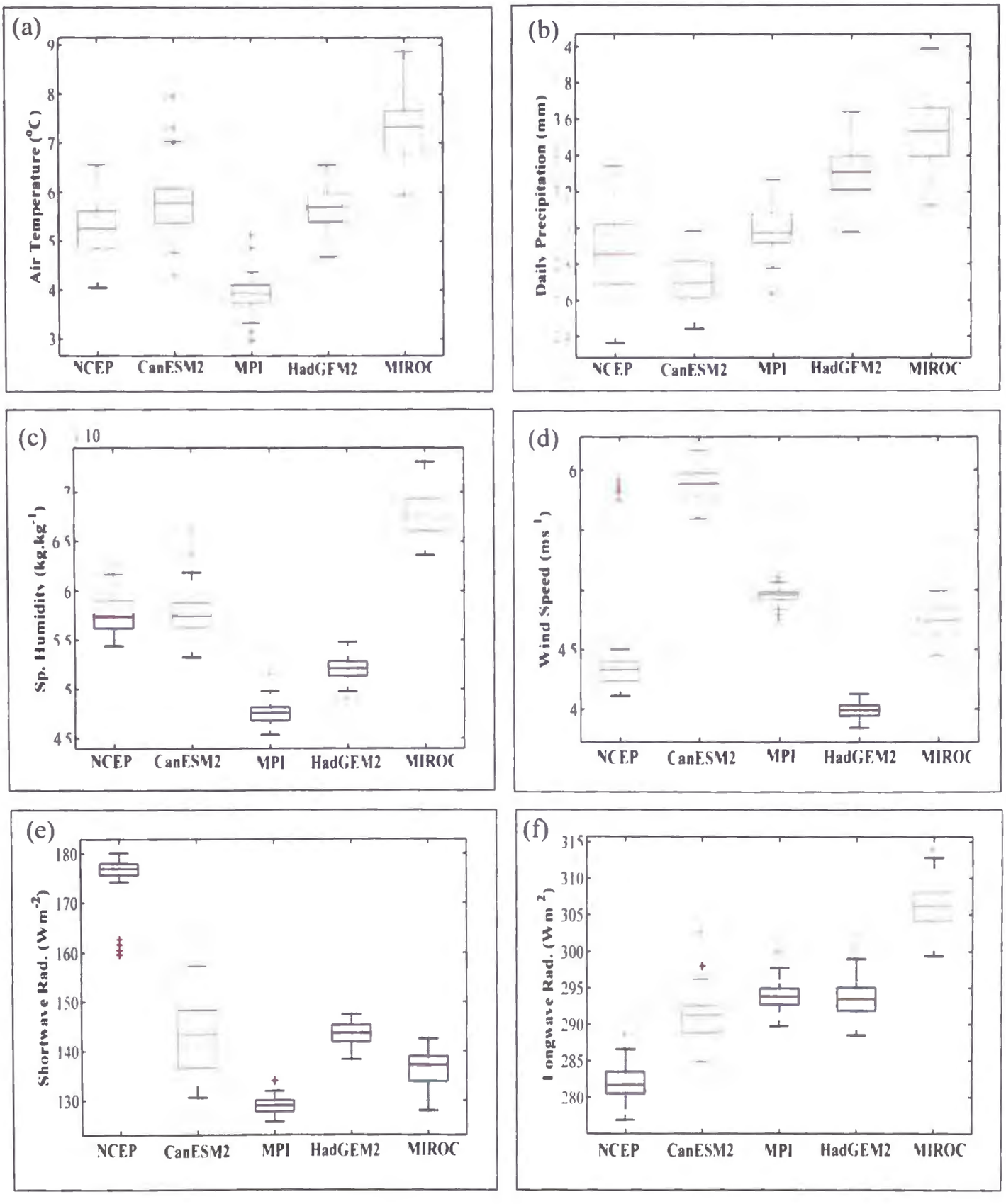

Figure 6.14 Boxplot of long-term (1961-2005) domain-averaged annual values from NCEP and different GCMs. (a) temperature, (b) precipitation, (c) specific humidity, (d) wind speed, (e) incoming shortwave radiation, and (f) incoming longwave radiation.

Next, results from downscaling of GCM projections are presented. As mentioned in the previous section, NCEP and RAMS datasets for the entire period (1979-2008) are utilized for developing the SVD model for downscaling future GCM fields. Optimized SVD model coefficients and correlation values are given in Table 6.6. These values are nearly identical to the ones obtained using the first half (1979-1993) of the dataset (see Table 6.3).

Table 6.6 Optimized SVD model parameters (m : slope, and b : intercept) and coefficient of determination (r^2) for the first three modes. Model calibration is performed for the listed variables using daily datasets from 1979-2008. For all the variables, the correlations are statistically significant at 95% o.

Variable	Mode-1			Mode-2			Mode-3		
	r^2	m	b	r^2	m	b	r^2	m	b
Temperature (°C)	88	5.34	$0\ 10\times10^{-12}$	56	2.64	$0\ 17\sim10^{-12}$	35	1.30	0.03×10^{-12}
Precipitation (mm)	78	10.24	$-0.21\cdot10^{-11}$	48	3.81	$-0.02\cdot10^{-11}$	38	3.09	0.02×10^{-11}
Sp. Humidity ($kg.kg^{-1}$) $\times10^{-}$	88	5.17	$-0.23\cdot10^{-15}$	58	2.29	$-0.16\cdot10^{-15}$	34	2.66	-0.03×10^{-15}
Wind Speed ($m\ s^{-1}$)	59	5.07	$-0.92\cdot10^{-13}$	35	3 21	0.26×10^{-1}	30	3.27	0.25×10^{-13}
SLP (hPa)	45	7.27	-0.55×10^{-09}	64	2.02	0.03×10^{-09}	55	1.85	-0.01×10^{-09}
Shortwave Rad. ($W\ m^{-2}$)	60	5.39	-0.24×10^{-11}	27	5.42	-0.27×10^{-11}	26	7.25	-0.37×10^{-11}
Longwave Rad. ($W\ m^{-2}$)	46	5.60	-0.86×10^{-11}	25	3.46	-0.65×10^{-11}	24	2.63	0.27×10^{-11}

To illustrate the effect of the SVD downscaling, the downscaled GCM variables are compared with the original GCM variables for grid cells nearest to Mt. Waddington in the southern Coast Mountains. Results from this comparison are plotted in a boxplot that is

presented in Figure 6.15. For the boxplots, the top and the bottom of the box mark the 75th and the 25th percentile of the dataset respectively. The height of the box represents the interquartile range (IQR) of the dataset and the ends of the whiskers mark the highest and lowest values of the dataset that are within 1.5 times the interquartile range of the box edges. The horizontal lines within the boxes are the medians. The plus signs mark individual values outside the range of the whiskers (outliers). At this location, for temperature, the downscaled values from all the GCMs have nearly identical median values and are always larger than the median values in the original GCM dataset. A moderate number of extreme negative temperatures were detected in the original MPI and MIROC GCM. However, they are not found in both the original and downscaled values from other GCMs. Also, MPI and MIROC have more extreme values in the original dataset than in the downscaled counterparts. Downscaled values for all GCMs have fewer extreme values. For precipitation, both original and downscaled values have a large number of extreme values. Downscaled MPI and MIROC precipitation shows a relatively large number of extreme values. Downscaled precipitation shows comparatively small median values for all GCMs but the difference is not very significant. The median values in downscaled specific humidity seem to be slightly larger than the median values in the original GCM output. Also, there were not a large number of extreme values detected in the original or downscaled specific humidity from the GCMs. Downscaled wind speed showed mixed results for different models. Downscaled wind speed from CanESM2 and MPI has smaller median values than the original GCM wind speeds. Wind speed is relatively large in the downscaled HadGEM2 output than in its original counterpart. Median value in downscaled wind speed from MIROC is nearly identical to the median value in the original GCM dataset. Both original and downscaled

GCMs have a number of extreme values, but the numbers are relatively less for HadGEM2. Except for a few extreme values in the MPI original shortwave radiation, no extreme values were detected in original or downscaled shortwave radiation for the remaining GCMs. For all GCMs, the downscaled shortwave radiation showed slightly higher median values as compared to the original datasets. Similar to shortwave radiation, the median values in downscaled longwave radiation are higher than in the original GCM data. These extreme values are mostly found below the median values. A time-series plot of downscaled GCM variables is shown in Figure 6.16. The data for each plot are obtained by first taking a spatial average of daily GCM variables over the entire domain from 2006 to 2100. The time-series of daily data thus obtained is averaged over a year to get one data point per year totaling 95 data points from 2006-2100. The time-series of downscaled GCMs seems to be preserving the positive trend in future temperature given by the original GCMs. However, this trend seems to be weakening and diverging for all the GCMs 2060 onwards. Time-series of downscaled precipitation from all the GCMs show a slight positive trend in future precipitation. However, the precipitation values show large inter-annual variability. Similar to temperature, downscaled humidity values show a strong positive trend until 2060, which is followed by a weak or no trend until 2100. Unlike temperature, there is no agreement in downscaled humidity between different GCMs. Once again, this is due to the SVD model preserving the basic characteristics in the original GCM datasets. Both wind speed and shortwave radiation do not show any significant future trend. Wind speed from MIROC-ESM not only diverges significantly from the rest of the GCMs, it has large inter-annual variability too. Shortwave radiation from GCMs except MPI-ESM appears to have good inter-model agreement. The future trend in longwave radiation shows many similarities with

the trend seen in temperature. For all the GCMs, there is a strong positive trend until 2060. This could be due to the known relationship between atmospheric temperature and the longwave radiation emitted from the sky.

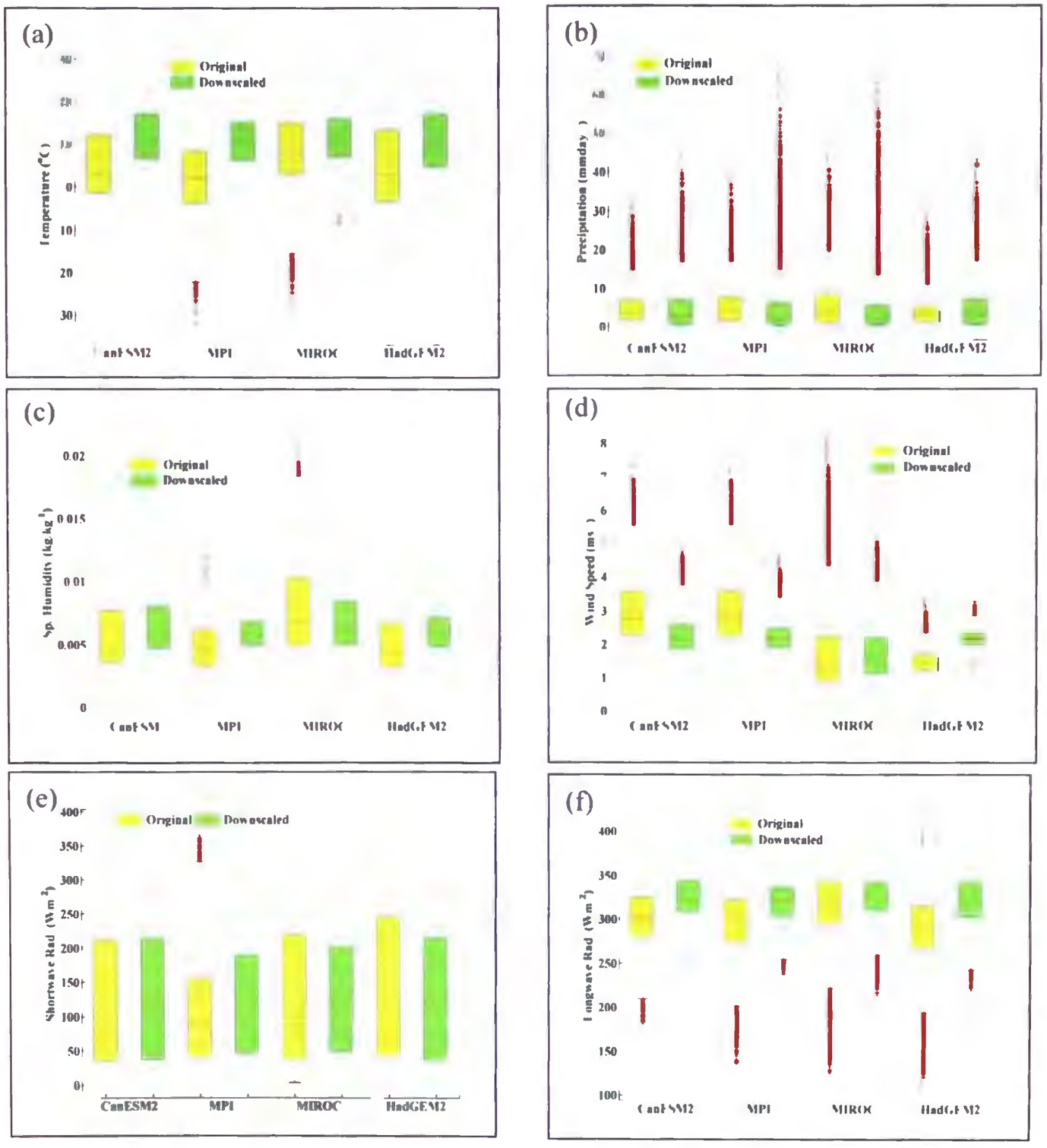

Figure 6.15 Boxplot of original and downscaled daily GCMs (2006-2100) from a grid cell nearest to Mt. Waddington in the southern Coast Mountains for (a) temperature, (b) precipitation, (c) specific humidity, (d) wind speed, (e) incoming shortwave radiation, and (f) incoming longwave radiation

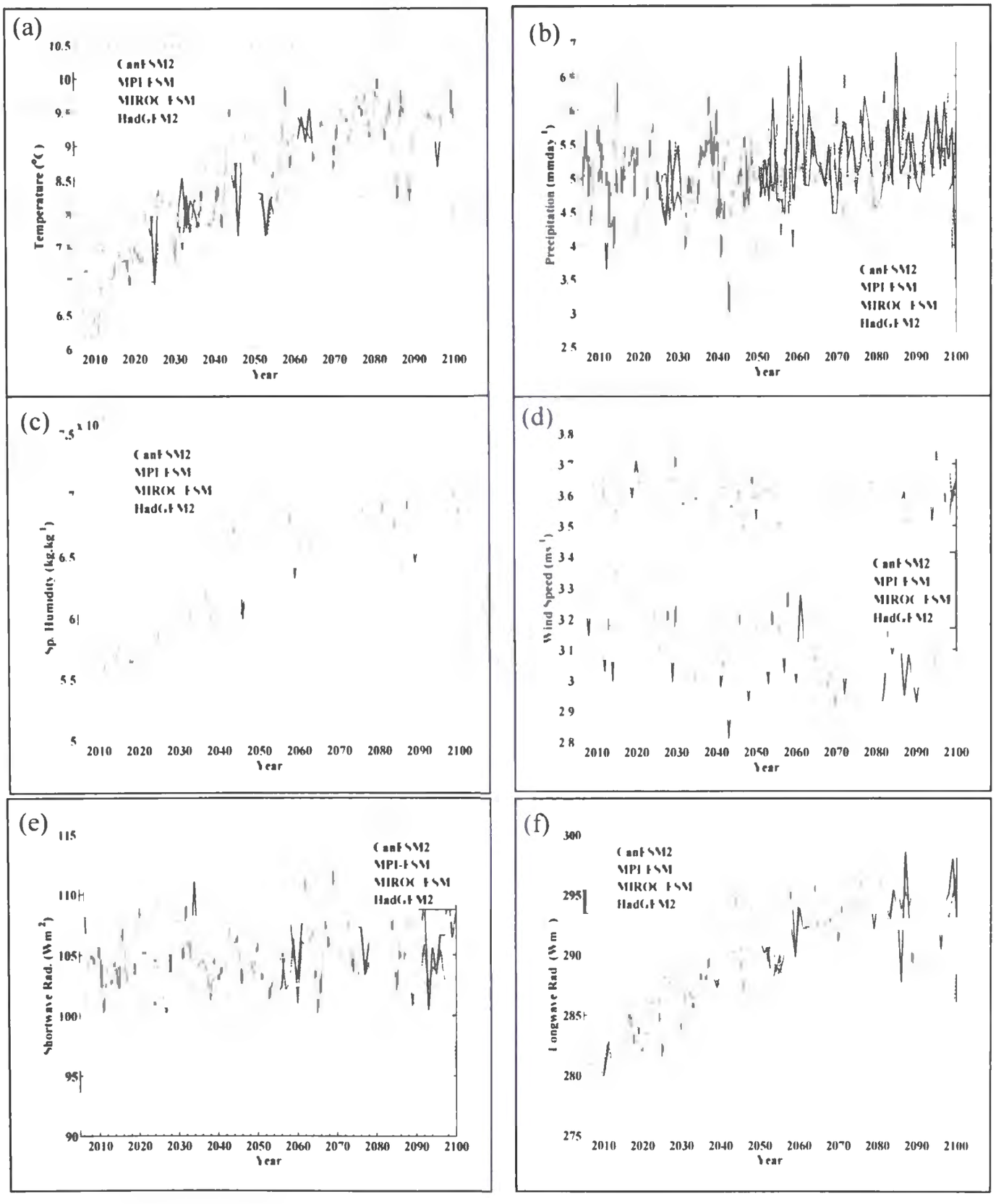

Figure 6.16 Time series of domain-averaged downscaled daily GCM variables averaged over a year. For each plot, values are given for four different GCMs for (a) temperature, (b) precipitation, (c) specific humidity, (d) wind speed, (e) incoming shortwave radiation, and (f) incoming longwave radiation

6.4 Conclusion

In this work, linear regression models based on the SVD technique are used to reconstruct several meteorological fields at the spatial resolution of RAMS (8 km × 8 km). Corresponding meteorological fields from the large-scale NCEP dataset are used as predictor variables. The SVD model for downscaling daily air temperature showed the strongest predictor-predictand relationship than for any other variables. The cross-validation of downscaled air temperature showed a strong correlation with the validation dataset. The r^2 values within the domain are more or less uniformly distributed, but the RMSE values are somewhat smaller over the coast compared to over the interior. The error statistics in the downscaled fields improved slightly with a monthly model, but there is no improvement in the correlation value. Similar to the SVD model for air temperature, the model for specific humidity also showed a strong predictor-predictand relationship. As a result, the model validation yielded a strong correlation between the downscaled and validation datasets. The use of a monthly SVD model for humidity does not improve the r^2 values, but there is a significant improvement in the error statistics. The SVD model for downscaling precipitation did not perform as well. The model calibration results do not show a strong relationship between the large-scale precipitation and small-scale RAMS precipitation fields. The correlation between downscaled and validation precipitation dataset is less strong in the interior than in the coastal area. The spatially average correlation and RMSE in downscaled daily (monthly) precipitation are 0.38 (0.57) and 7.5 mm day^{-1} (0.29 mm day^{-1}), respectively. This suggests that the daily SVD model is performing less satisfactorily in downscaling large-scale precipitation. This is probably due to the fact that the small-scale precipitation is not only conditioned by large-scale precipitation but possibly influenced by

other variables such as sea-level pressure and large-scale humidity fields, and is also influenced strongly by local topography and small-scale convective precipitation. Also, part of the discrepancies in downscaled precipitation must be due the model's inability to resolve the influence of topography on precipitation. The monthly SVD model performed relatively better in downscaling large-scale precipitation than its daily counterpart. For wind speed, no strong correlation was found between downscaled wind speed and the validation dataset. Also, the correlation values are highly variable in space. The use of a monthly SVD model improved the error statistics but decreased r^2 values. For sea level pressure, results show a strong correlation between the downscaled and validation dataset. However, the RSME and MAE results show a relatively large error in the downscaled results. The error statistics improved considerably with the monthly model, while the r^2 values were similar. The downscaled incoming shortwave radiation showed a moderate correlation with the validation dataset, but the errors in downscaled results were large. The strength of the correlation appears to be relatively better in the coastal area as compared to locations in the interior. Downscaling of incoming shortwave radiation using a monthly model did improve the error statistics but at the expenses of weaker r^2 values. Similar to the results for shortwave radiation, downscaled incoming longwave radiation also showed a moderate correlation with the validation dataset. Errors in downscaled incoming longwave radiation were also minimal. Downscaled incoming longwave radiation showed weaker correlation with the validation dataset over the mountain range compared to correlations over the coastal region. As seen with other variables, the use of a monthly SVD model improved the error in downscaled incoming longwave radiation. However, no significant improvement is seen in r^2 values with the monthly SVD model.

SVD models developed for downscaling different large-scale variables have been used for downscaling climate projections from a suite of GCMs. For a particular climate field, the performance of the downscaling model varied among GCMs. The downscaled climate projections from four different GCMs are compared with the original projections from a location near Mt. Waddington in the southern Coast Mountains. For all GCMs considered, the downscaled air temperature showed higher median values as compared to the median values in the original GCMs. However, the range in downscaled future temperature is smaller than in the original GCMs. Also, the downscaled air temperature result appears to be preserving the long-term positive trend present in the original GCM dataset. There appears to be no difference between downscaled and original precipitation from all the GCMs. Both original and downscaled precipitation values show a larger number of positive extreme values. Furthermore, the downscaled precipitation values do not show any long-term trend. The model for downscaling precipitation performed less satisfactorily compared to the model for downscaling other GCM fields. The downscaled future specific humidity generally has higher median values than their original counterparts. The downscaling process appears to be increasing the minimum values and decreasing the maximum values. The SVD model for specific humidity appears to be preserving the long-term positive trend seen in the original dataset. Downscaled wind speed from CanESM2 and MPI show a slight decrease in the median values as compared to the original values. For the remaining two GCMs, the median values appear to be slightly larger than the original values. For both incoming shortwave and longwave radiation and for all GCMs, the downscaling process appears to have increased the median value. The maximum values in downscaled incoming shortwave radiation are always smaller than in the original dataset.

There is no significant difference in the maximum values between the original and downscaled incoming longwave radiation. However, the downscaling process has decreased the minimum values in downscaled incoming longwave radiation. Also, the SVD model appears to be preserving the long-term positive trend in future incoming longwave radiation. Downscaled GCM projections may still be prone to a large amount of error and therefore cannot be considered as a true representation of future climate. Uncertainties associated with RCP scenarios, internal variability of the climate system, GCMs and statistical downscaling models all contribute to the uncertainty of downscaled climate scenarios. As the mesoscale climate data cannot truly represent the observed climate data, it has added more uncertainty in the downscaled results.

Finally, the following conclusions have been drawn from this study:

1. The SVD model worked satisfactorily for downscaling large-scale daily air temperature, relative humidity and incoming longwave radiation. Inclusion of additional large-scale predictor fields, such as 850 hPa temperature and 1000-500 hPa thickness will probably improve the downscaling results for air temperature. Similarly, the SVD model for downscaling humidity can be further improved by including circulation and humidity based predictor variables at different pressure levels.
2. The SVD model performed less well in downscaling daily precipitation. The use of large-scale precipitation alone as a predictor variable appears to be inadequate. Inclusion of more large-scale circulation and humidity based predictor variables from different pressure levels may improve the downscaling results.

3. As the errors in downscaled variables are generally large with the daily SVD model, the use of a monthly SVD model can be a better choice unless a particular study requires daily downscaled field specifically.
4. Great caution needs to be exercised when using statistical models for climate downscaling.

Chapter 7

Future GMB Projection

7.1 Introduction

Knowledge about the response of glaciers to future climate change is important for the effective management of water resources and for developing adaptation policies in response to declining water supply in the future. Downscaled GCM climate projections have been used with Glacier Mass Balance (GMB) models to understand the future changes in glaciers (Radić and Hock 2006; Radić et al. 2013, Clarke et al. 2015). Most of these studies have used either a temperature index (TI) or an enhanced TI model for estimating glacier melt where the input variables were spatially downscaled to the glacier location using simple statistical techniques.

The application of physically-based surface energy balance GMB models for future GMB projections has been limited perhaps due to their large data requirements. Physically-based GMB models are considered superior to empirical GMB models and have been shown to perform well in simulating observed mass balance on mountain glaciers around the world (Kayasta et al. 1999; Dadic et al. 2008; Anslow et al. 2008; Shea 2010; Mölg and Kaser 2011). Glacier mass loss in future glacier predictions may be under-predicted when TI or highly simplified energy-balance models are used instead of detailed energy-balance models that account for the feedback of temperature changes on each individual energy balance components separately (Hock et al. 2007). A physically-based GMB model developed for Place Glacier, southern Coast Mountains, Canada, has been shown to perform well in simulating the historic mass balance on the glacier when forced with historic RAMS fields

(this study, Chapter 5). The model clearly outperformed an empirical TI model in simulating the historic mass balance when both models were forced with the same RAMS meteorological fields. The present study will follow the work by Hock et al. (2007) with the aim to develop mass balance projections for Place Glacier using the physically-based GMB model developed and validated on the same glacier. Input meteorological variables for running the GMB model are obtained by downscaling future climate projections from a suite of GCMs (Chapter 6). However, it should be noted here that the projections provided by this study should only be considered as one of several possible real changes to be expected for Place Glacier given the uncertainties in GCM projections and their subsequent additional uncertainties due to downscaling.

7.2 Methods

The development and validation of a physically-based distributed surface energy balance GMB model was discussed in Chapter 5. With some minor changes, the same model is run in the future for developing mass balance projections for Place Glacier. The future model run used a historic (1980-2008) average of the hourly lapse rate derived from the RAMS vertical temperature sounding data (= -0.0075°C m^{-1}) for distributing air temperature on the glacier surface. This lapse rate is slightly higher than the standard environmental lapse rate of -0.0065°C m^{-1}. The total precipitation over the winter months usually has a positive vertical gradient leading to substantial variation in snow depth along the glacier length. To distribute the total winter precipitation on the glacier surface, future model runs used vertical gradient of RAMS total winter precipitation averaged over the historic period (0.97 mm m^{-1}). The model assumed that the same amount of precipitation falls over all the grid cells

during summer months. To simplify the model, it is assumed that all precipitation fall as rain during summer. As a result, effect of summer snow on glacier albedo is ignored. This assumption is reasonable because warmer temperature in the future will likely decrease the amount of precipitation falling as snow. Winter accumulation is determined using a static air temperature threshold of 1.0°C. The future model run begins in 2009 and ends in 2040. Similar to the historical run, the future model run includes the change in glacier area in the GMB model. The glacier area, glacier elevation and the ELA at the beginning of the model run is prescribed from the historical model run from the preceding year (i.e. 2008) and updated at the end of the summer every year The same volume-area scaling relationship used in the historic model run is used here for calculating glacier area at the end of summer every year. Except for these few changes explained above, the other model setup and parameters remains the same as in the original model (refer Chapter 5 for details).

The GMB model developed and validated for Place Glacier is run in the future using relevant input variables from a suite of GCMs that are downscaled to the glacier location using the SVD method (Chapter 6). These variables include air temperature, precipitation, specific humidity, sea level pressure, wind speed, incoming shortwave radiation and incoming longwave radiation from four different GCMs, which is already discussed in Chapter 3. The future model run is performed in hourly time-steps mainly because the model produced reasonable results in the past using this time-step. However, the GMB model can also be run in daily time-steps. To run the GMB model in the future, the daily downscaled GCM fields need to be converted to hourly values. This is achieved by adding diurnal variability to each downscaled field where the diurnal cycle is taken from the corresponding hourly RAMS fields from 1979 to 2008. To determine the diurnal cycle, first a daily mean is

calculated from the RAMS hourly values for each year. Each daily value is then averaged over the entire 30-year historical period. This provides 365 daily values for each grid cell in the domain. Finally, the RAMS diurnal cycle is calculated by subtracting the daily mean values from the RAMS hourly values averaged over the entire 30-years historical period. To convert downscaled GCM fields, other than precipitation and incoming shortwave radiation, from daily to hourly time-steps, first the daily values are replicated over all hours of a day. The diurnal cycle from the respective RAMS variable is then added to the replicated values, which convert daily downscaled GCM fields into hourly values. Determining the diurnal cycle in precipitation and incoming shortwave radiation is particularly difficult as they contain a number of zero values. A simple approach is used to convert daily downscaled values into hourly values. Daily downscaled precipitation values are first scaled by dividing by 24 and the result is replicated over all hours of a day. As a result of this treatment, the hourly data have the same precipitation value for all hours of a particular day. Daily downscaled incoming shortwave radiation is converted into hourly values (K_{DS}^{h}) as:

$$K_{DS}^{h} = 24 \times \left(\frac{K_{DS}^{d}}{K_{in}^{t}}\right) \times K_{in}, \qquad (7.1)$$

where K_{DS}^{d} is the downscaled daily incoming shortwave radiation, K_{in} is the hourly RAMS shortwave radiation averaged over the historical period, and K_{in}^{t} is the daily total of K_{in}. 24 refers to the number of hours in a day.

It should be noted here that due to the averaging, the resulting hourly downscaled fields show less hourly variability than the modeled hourly fields do (not shown here).

Future downscaled GCM fields used for running the GMB model on Place Glacier are shown in Figure 7.1. The time-series plots are shown for five meteorological variables (air temperature, precipitation, humidity, shortwave and longwave radiation) that are

considered important in determining SEB over the glacier surface. Except precipitation, all four variables are plotted as the mean over summer months (June-September). For precipitation, total values over the winter months (October-May) are shown. This period usually coincides with the period of maximum precipitation in the region. Although downscaled meteorological variables are shown until 2100, the GMB simulation is performed only until 2040. This is mainly to minimize the uncertainty in GMB projections due to the increased uncertainty in GCM projections longer into the future.

7.3 Bias Estimation

Biases in modelled energy balance and mass balance on the glacier surface are determined relative to observations. To determine bias in modelled energy balance components, the GMB model is run during summer months (June-September) from 1979-2005 using downscaled historical GCM fields. The modelled SEB results on the glacier are then compared with the results obtained by using RAMS fields for the same period to estimate the bias. The bias is determined relative to the results obtained from RAMS climate fields because no other long-term energy balance results are available for Place Glacier for comparison. Similarly, to determine the bias in modelled mass balance components, the GMB model is run in the historic period (1961-2005) using climate fields from different GCMs. The estimated mass balance components are then compared with the observations (1965-2005) to determine the bias. Although the mass balance data for Place Glacier are available from 1965, they are missing for a number of years during the simulation period. Therefore, only the years without missing data are used for bias estimation. The estimated future mass balance components from different GCMs are corrected for the bias.

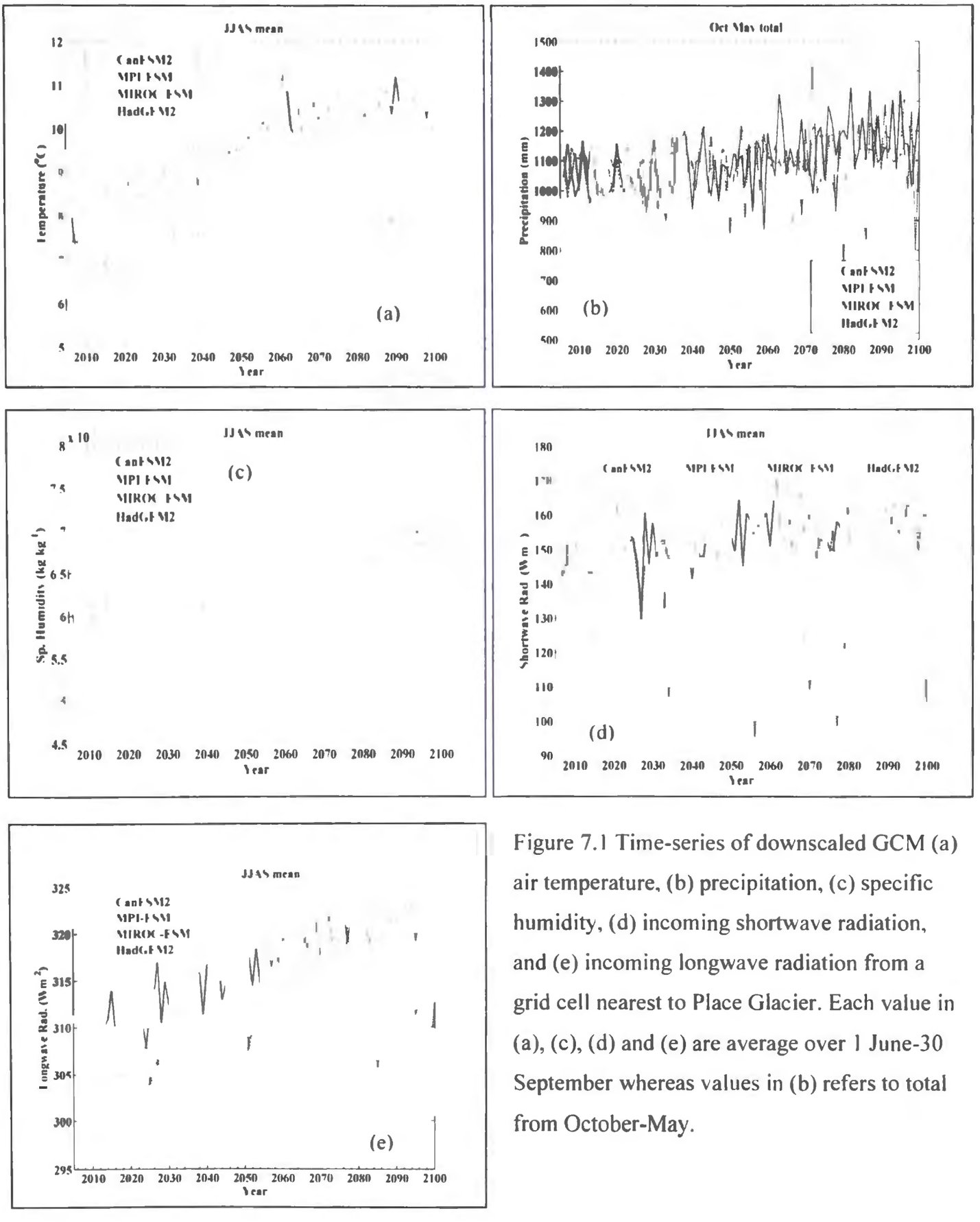

Figure 7.1 Time-series of downscaled GCM (a) air temperature, (b) precipitation, (c) specific humidity, (d) incoming shortwave radiation, and (e) incoming longwave radiation from a grid cell nearest to Place Glacier. Each value in (a), (c), (d) and (e) are average over 1 June-30 September whereas values in (b) refers to total from October-May.

7.4 Results and Discussion

7.4.1 Input Data

The model input variables, especially air temperature, humidity and longwave radiation during summer months, from all four GCMs are expected to increase in the future (Figure 7.1). CanESM2 and HadGEM2 show a distinct positive trend in future temperature. MIROC and MPI both project increasing temperature in the future but with a smaller trend. There is good agreement between CanESM2 and HadGEM2 future temperature projections. They also have less inter-annual variability than the other two GCMs. The total precipitation for winter months shows a small increasing trend for all GCMs, but the trend is not as strong as seen in air temperature (Figure 7.1b). Also, the precipitation time series show a large inter-annual variation. For humidity, all four GCMs project a positive trend but the magnitude is much larger for MIROC and CanESM2 (Figure 7.1c). Projected incoming shortwave radiation shows a small positive trend for all the GCMs. This trend is particularly small for MPI-ESM. The rest of the GCMs appear to be simulating more or less the same magnitude of positive trend in shortwave radiation flux. All GCMs show a significant increase in incoming longwave radiation in the future. The trend in incoming longwave radiation appears to be consistent with the trend in air temperature. This is expected because an important portion of the longwave radiation comes from the near surface layer of the atmosphere, which is influenced by surface air temperature. The increasing trend seen in future incoming longwave radiation may have important implications for glacier mass balance as the longwave flux is an important source of energy on the glacier surface (Ohmura 2001). However, caution should be exercised while interpreting these downscaled GCM results because the results from these models in historical period have been found to

contain some amount of bias relative to the corresponding NCEP fields (Chapter 6). As a result, future projections from these models may differ from the actual values on the glacier. As discussed in Chapter 6, MAE error in a particular field varied between the GCMs. Also, for a particular GCM, error varied between different fields. For air temperature, MAE between different GCMs ranged between 0.55°C and 1.3°C. HadGEM2 and MPI-ESM appear to have relatively small amount of errors in modelled air temperature. For all models, MAE errors in precipitation ranged between 0.12 and 0.65 mm day^{-1}. Similarly, errors in specific humidity ranged between 0 to $9.9 \cdot 10^{-4}$ $kg.kg^{-1}$.

7.4.2 Energy Balance

Before presenting energy balance results from different GCMs, the potential bias in different SEB components from different GCMs is discussed. To determine bias, the GMB model is run during summer months (June-September) from 1979-2005 using downscaled historical GCM fields. The modelled SEB results are then compared with the results obtained by using RAMS fields for the same period to estimate the bias. The bias is determined relative to the results obtained from RAMS climate fields because no other long-term energy balance results are available for Place Glacier for comparison. The biases in different SEB components and from different GCMs are presented in Table 7.1. Biases are estimated from SEB components averaged over the entire glacier and over the entire historical period during the summer months.

Table 7.1 Biases (GCM-RAMS) in different SEB components from different GCMs (downscaled) relative to the values estimated using RAMS climate fields. Each SEB component is averaged over the entire glacier and over the entire historic period (1979-2005) during summer months (June-September) before determining bias. Q_N: Net energy (melt energy), K_{net}: net shortwave radiation, L_{net}: net longwave radiation, Q_E: latent heat flux, and Q_H: sensible heat flux. Values in parentheses refer to corresponding SEB values estimated from RAMS climate fields. All values are in W m^{-2}.

GCMs	K_{net} (67)	L_{net} (4)	Q_E (1)	Q_H (19)	Q_N (91)
CanESM2	-21	-19	-10	-14	-64
MIROC	2	-10	2	-8	-14
MPI	-5	-10	-9	0	-24
HadGEM2	3	-11	-4	-1	-13

The mean net shortwave radiation flux predicted from downscaled historical CanESM2 (=46 W m^{-2}) is substantially smaller than the value estimated from RAMS climate fields (=67 W m^{-2}) for the same period. Similarly, the mean sensible heat flux value of 5 W m^{-2} is too small compared with the sensible heat flux estimated from RAMS climate fields. Both mean net longwave and latent heat flux predicted from CanESM2 are smaller than the corresponding values estimated from RAMS fields. As a result of this, the net energy balance on the glacier surface predicted from CanESM2 (= 27 W m^{-2}) is substantially smaller than the net energy estimated from RAMS fields (=91 W m^{-2}). The mean net shortwave radiation flux predicted from MIROC (=69 W m^{-2}) and MPI (=62 W m^{-2}) are comparable to the value determined from RAMS climate fields. MPI predicted mean sensible heat flux (=19 W m^{-2}) is identical to the sensible heat flux estimated from RAMS climate fields. Similarly, mean sensible heat flux from MIROC (=11 W m^{-2}) appears slightly

smaller than the value estimated from RAMS climate fields. HadGEM2 predicted mean net shortwave radiation flux (=70 W m^{-2}), latent heat flux (= -3 W m^{-2}) and sensible heat flux (= 18 W m^{-2}) appear consistent with the values determined from RAMS climate fields. Net longwave radiations from all GCMs are smaller than the values obtained from RAMS climate fields. The bias in net energy balance on the glacier surface between different GCMs ranged from -13 W m^{-2} (HadGEM2) to -64 W m^{-2} (CanESM2). On average, bias in CGM predicted energy balance components is largest for CanESM2. The fact that all historical GCMs are predicting smaller SEB components compared to SEB components calculated from RAMS climate data for the same period possibly suggests that the projected future SEB on the glacier surface would be generally smaller than the actual value on the glacier surface. However, since the GMB model does not take into account the effect of glacier retreat on the SEB calculation, it is possible that SEB calculated here is higher than the actual value on the glacier surface would be. It should be noted here that these biases in energy balance components from different downscaled GCMs presented here may not represent a true bias as they are determined relative to the values from RAMS climate fields, which is different from observed climate data.

The energy balance calculated on Place Glacier using downscaled climate projections from a suite of GCMs is illustrated in Figure 7.2. Values plotted for each year are the averages for the summer melt season (1 June- 30 September) and refer to the location at the middle of the glacier.

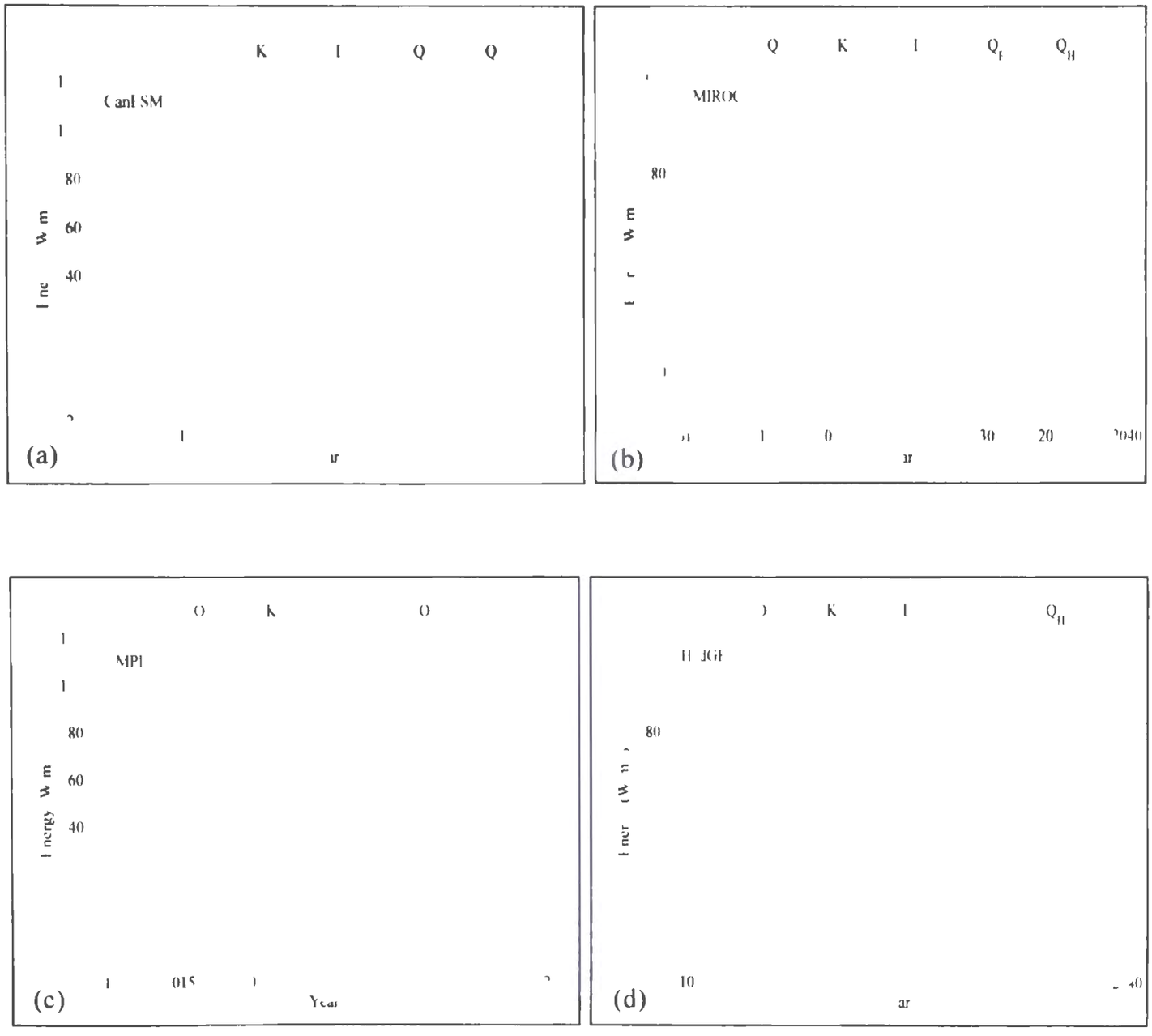

Figure 7.2 Time-series of surface energy balance fluxes at the middle of Place Glacier calculated using downscaled future climate projection from (a) CanESM2, (b) MIROC-ESM, (c) MPI-ESM, and (d) HadGEM2. Values for each year refer to the average over the summer melt season (1 June-30 September). Q_N: Net energy (melt energy), K_{net}: net shortwave radiation, L_{net}: net longwave radiation, Q_E: latent heat flux, and Q_H: sensible heat flux.

Calculated values of energy balance components for different GCMs at the glacier terminus are given in Table 7.2.

Table 7.2 Calculated averaged values (W m^{-2}) of energy balance components at the terminus along the mid-line of Place Glacier over the summer season (1 June-30 September) from 2009-2040. Values in parentheses refer to percentage contribution by each energy balance component to the net energy. Q_N: Net energy (melt energy), K_{net}: net shortwave radiation, L_{net}: net longwave radiation, Q_L . latent heat flux, and Q_H: sensible heat flux

GCMs	K_{net}	L_{net}	Q_L	Q_H	Q_N
CanESM2	80 (79%)	4 (4%)	2 (2%)	15 (15%)	101
MIROC-ESM	75 (83%)	1 (1%)	6 (6%)	9 (10%)	91
MPI-ESM	60 (94%)	0 (0%)	-10 (-16%)	14 (22%)	64
HadGEM2	74 (85%)	0 (0%)	-6 (-7%)	19 (22%)	87

For all GCMs, net shortwave radiation is the main source of net energy on the glacier surface. Sensible heat flux is the second largest contributor to the net energy followed by net longwave radiation and the latent heat flux. The negative latent heat flux for most of the GCMs is indicative of sublimation on the glacier surface. The summer net energy balance on the glacier surface showed a slight positive trend over the period 2009-2040. However, none of the energy balance components show any significant trend in their long-term values. These results cannot be independently verified due to the lack of similar work elsewhere in the world. However, there are a number of energy balance studies on the glacier surface that used observed climate data (e.g., Anslow et al. 2008; Shea 2010; Kayastha et al. 1999). These studies have suggested net shortwave radiation flux as the dominant energy source for glacier ablation during the summer months. The contribution of net shortwave radiation to

the net energy on the glacier surface ranged from 60% to 80% depending upon factors such as number of clear weather days, amount of snowfall and duration of exposition of low-albedo firn and ice. Similarly, the contribution of sensible heat flux ranged from 10% to 30%. The contribution of latent heat flux and net longwave radiation is usually negative. Energy balance results from different GCMs presented in Table 7.2 appear generally consistent with these results.

Anslow et al. (2008) calculated the energy balance on south Cascade Glacier in the northwestern United States using observed data for the summer of 2004 and 2005. The monthly averaged (June-September) net shortwave radiation near the terminus of the glacier averaged over 2004 and 2005 were 110 W m^{-2}. Similarly, for the same period estimated net longwave radiation flux was -6 W m^{-2}. They reported an average sensible heat flux and latent heat flux of 45 W m^{-2} and 22 W m^{-2}, respectively. The average net radiation flux was 100 W m^{-2}. All of these values are higher than the values calculated in the present study from different downscaled GCMs. Shea (2010) calculated the energy balance on glaciers in the southern Coast Mountains, which also included Place Glacier. Average monthly energy balance for all glaciers during the period April-September from 2006-2008 is presented in Figure 7.3. This result suggests that from June-September, net shortwave radiation flux is the dominant energy source on the glacier surface. Sensible heat flux is the second largest sources of energy while the latent heat flux has a small positive contribution. Net longwave radiation is the smallest magnitude component of the net energy budget and is mainly negative. The estimated net shortwave radiation ranged from 40 W m^{-2} to 95 W m^{-2} (average = 67 W m^{-2}). This value compares fairly well with the modelled net shortwave radiation from all GCMs. Based on observations on Place Glacier during the summer of 2007, the

same study reported an average daily net radiation of about 60 W m^{-2}. The net radiation flux from CanESM2 (= 84 W m^{-2}), MIROC (=76 W m^{-2}), and HadGEM2 (=74 W m^{-2}) are slightly higher than the value observed on Place Glacier. However, the net radiation from MPI (=60 W m^{-2}) equals the value observed on Place Glacier. Similarly, the sensible heat flux reported by Shea (2010) ranged from 5 W m^{-2} to 20 W m^{-2}, which is smaller than the values calculated from all GCMs (Table 7.2). The latent heat fluxes estimated from different GCMs ranged from -10 W m^{-2} to 6 W m^{-2}. The latent heat flux calculated from CanESM2 (–2 W m^{-2}) and MIROC (=6 W m^{-2}) appear consistent with the values reported in Figure 7.3. However, the latent heat fluxes calculated from MPI (-10 W m^{-2}) and HadGEM2 (= -6 W m^{-2}) are too small compared to values reported in Figure 7.3. Also, simulated net longwave fluxes from most of the GCMs ranged from 0 W m^{-2} to 4 W m^{-2} whereas the values reported in Figure 7.3 ranged from -10 W m^{-2} to 15 W m^{-2}. However, it should be noted here that the results reported by Shea (2010) refer to spatially-averaged values from four different glaciers in the southern Coast Mountains whereas the results presented in Table 7.2 refer to the values from a location at the terminus of Place Glacier.

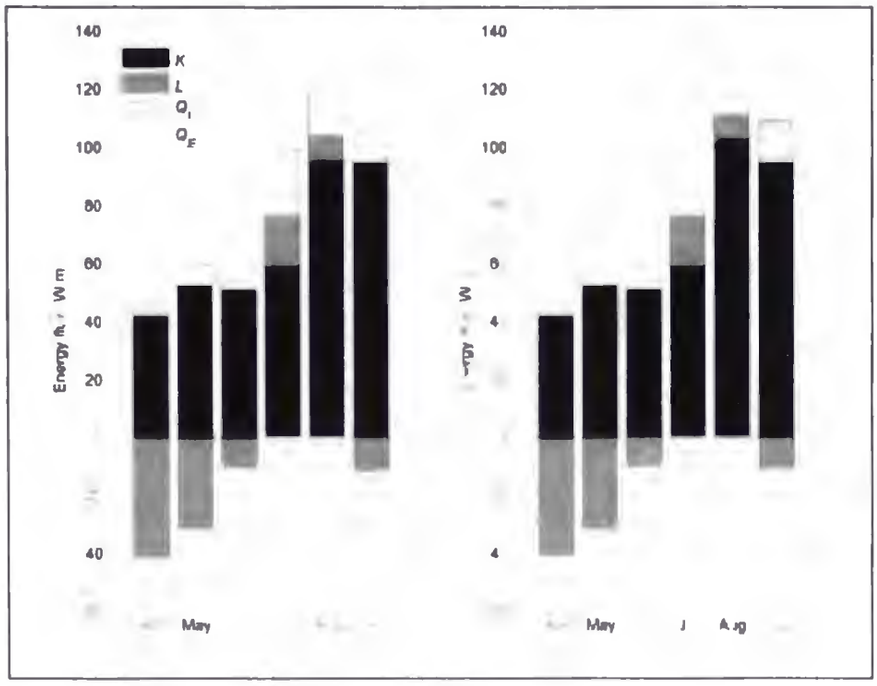

Figure 7.3 Mean monthly energy fluxes for full energy balance models with (left) and without (right) KBL corrections. K : net shortwave radiation, L^*: net longwave radiation, Q_E: latent heat flux, and Q_H: sensible heat flux (Shea 2010).

It is seen that the energy balance results from future GCMs are within the range reported by a number of glacier energy balance studies in the past (e.g., Anslow et al. 2008; Shea 2010; Kayastha et al. 1999). However, SEB estimated from historic GCMs have been found to contain some amount of negative bias (Table 7.1). As a result, summer ablation (summer balance) simulated from downscaled future GCMs will possibly have some amount of bias that needs to be corrected before determining net mass balance on the glacier.

7.4.3 Mass Balance

Summer and winter mass balance on Place Glacier from 2009-2040 (32 years) are modelled using statistically downscaled climate projections from four different GCMs. The estimated future mass balance components from different GCMs are corrected for the bias. To

determine the bias, the GMB model is run in historic period (1961-2005) using climate fields from different GCMs. The estimated mass balance components are then compared with the observations (1965-2005) to determine the bias. Although the mass balance data for Place Glacier are available from 1965, they are missing for a number of years during the simulation period. Therefore, only the years without missing data are used for bias estimation. Before discussing the mass balance results, estimated biases in modelled summer and winter balances are discussed. The estimated biases in summer and winter balance from different GCMs are given in Table 7.3.

Table 7.3 Biases in glacier-wide summer (B_s) and winter (B_w) balance modelled from different GCMs for the historical period (1965-2005). Bias is determined as a difference between the values from downscaled historical GCM and observations (GCM-Observation) averaged over the entire historic period. Glacier-wide values estimated from RAMS fields refer to the average for the period 1980-2008.

GCM/RAMS	B_s (m w.e.)			B_w (m w.e.)		
	Historic	Observed	Bias	Historic	Observed	Bias
CanESM2	-1.05	-2.76	1.71	1.53	1.59	-0.06
MIROC	-2.52	-2.76	0.24	1.88	1.59	0.29
MPI	-2.19	-2.76	0.58	1.78	1.59	0.19
HadGEM2	-2.55	-2.76	0.21	1.87	1.59	0.28
RAMS	-2.71	-2.73	0.02	1.54	1.63	-0.09

As seen in Table 7.3, CanESM2 predicted historical summer balance is substantially smaller than the observed value for the same period. This has resulted in a large bias in summer balance for CanESM2 (=1.71 m w.e.). As presented in Table 7.1, the net energy predicted from historical CanESM2 during summer season (=27 W m^{-2}) is too small

compared to the value estimated from RAMS climate fields for the same period (=91 W m^{-2}). The smaller summer balance predicted from historical CanESM2 is a direct result of small net energy estimated from this GCM in the historical period. The bias in summer balance is relatively small for the remaining three GCMs. The estimated bias in HadGEM2 predicted summer balance is smallest at 0.21 m w.e. while the bias in MPI predicted summer balance is 0.58 m w.e. The estimated bias in MIROC predicted summer balance is 0.24 m w.e. Unlike summer balance, winter balance predicted from different GCMs in the historic period does not contain a large amount of bias. The average winter balance predicted from different GCMs in the historic period ranged between 1.53 m w.e. to 1.88 m w.e. These values are comparable to the observed average winter balance of 1.59 m w.e. for the same period. Modelled future summer and winter balances from different GCMs with and without bias correction are plotted in a boxplot that is shown in Figure 7.4.

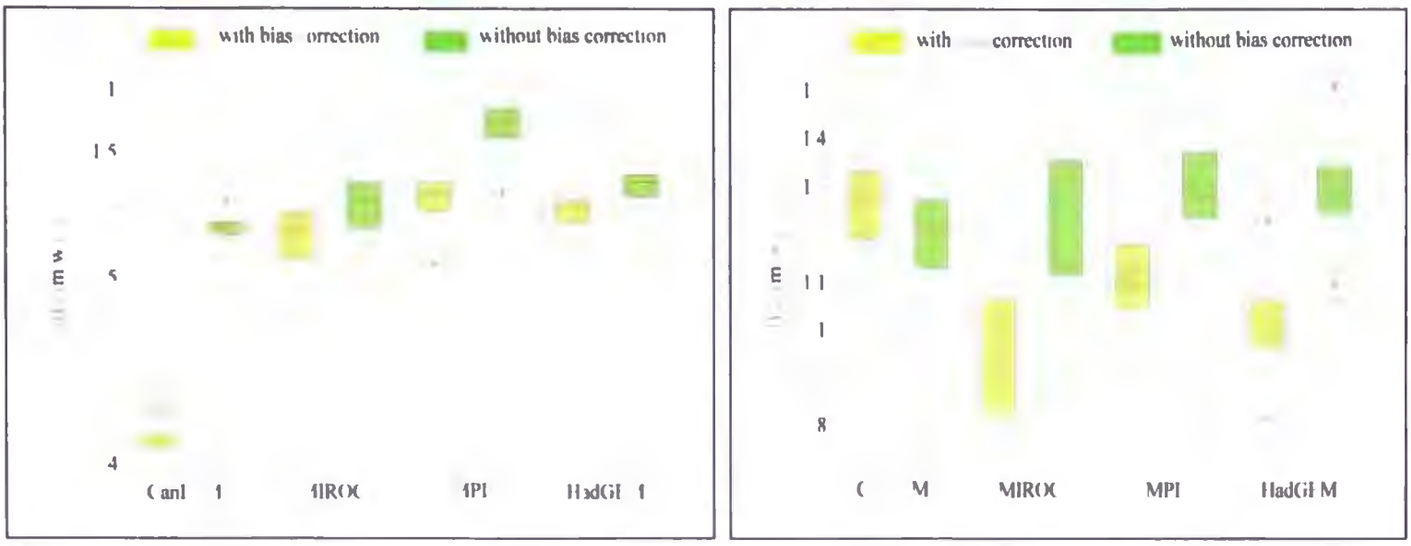

Figure 7.4 Boxplot of glacier-wide (a) summer balance (B_s) and (b) winter balance (B_w) predicted from four different GCMs averaged over the period 2009-2040 Results are shown for with and without bias correction The top and the bottom of the box mark the 75th and the 25th percentile of the dataset, respectively. The height of the box represents the interquartile range (IQR) of the dataset and the ends of the whiskers mark the highest and lowest values of the dataset that are within 1.5 times the interquartile range of the box edges. The horizontal lines within the boxes are the median. The plus signs mark individual values outside the range of the whiskers (outliers).

The bias corrected modelled summer balance from CanESM2 averaged over the entire period is -3.80 m w.e. This value is substantially higher than the values from MIROC (= -2.16 m w.e.), MPI (= -1.86 m w.e.) and HadGEM2 (= -1.96 m w.e.). The large negative summer balance from CanESM2 is the direct consequence of bias correction. Even without bias correction, the estimated summer balance from CanESM2 (= -2.10 m w.e.) is the largest of all the GCMs. This is mainly due to the positive trend in air temperature, humidity and incoming longwave radiation for this GCM. As seen in Figure 7.1, although all of these variables have a positive trend, the magnitude is particularly large for CanESM2 and MIROC. The large negative summer balance estimated here from CanESM2 appears unrealistic. Although the modelled future values cannot be independently verified, the estimated summer balance from MIROC, MPI and HadGEM2 are smaller compared with

the average long-term (1965-2005) summer balance observed on Place Glacier, which is -2.50 m w.e. The mean summer balance from MPI (– -1.86 m w.e) is smallest of all the GCMs. The small summer balance from MPI is mainly due to small net energy balance simulated on the glacier surface (see Table 7.2). On average, the modelled winter balance from all the GCMs ranges between 1.00 m w.e and 1.30 m w.e. These values are smaller than the average long-term winter balance observed on Place Glacier, which is 1.7 m w.e. This is possibly because even if there is an increase in the amount of precipitation in the future (Figure 7 1a), it is less likely that it will contribute to glacier accumulation as the warmer temperature will decrease the proportion of precipitation that falls as snow.

Average glacier-wide net mass balance on Place Glacier predicted from different downscaled GCMs in the future period is shown in Figure 7.5. The modelled net mass balance result shows large negative values for CanESM2. CanESM2 predicts a future mass loss ranging between -2.22 m w.e and -2.76 m w.e with an average value of nearly -2.50 m w.e. These values are substantially higher than the observed long-term average value (– -0.84 m w.e.) on Place Glacier. MIROC predicts an average mass loss of -1.20 m w.e., which is larger than the observed long-term average value. The MPI predicts an average mass loss of -0.75 m w.e., which is comparable to the observed value. Similarly, HadGEM2 predicts an average net mass balance of -0.94 m w.e., which is slightly larger than the observed long-term average value but is equally plausible. The net mass balance from bias-corrected CanESM2 is nearly three times as large as observed long-term average value. Without bias correction, CanESM2 predicted a summer and winter balance of -2.10 m w.e and 1.21 m w.e., respectively, yielding a net mass balance of -0.89 m w.e. These values appear reasonable compared to the ones obtained from bias-corrected CanESM2. Therefore,

the large negative net mass balance from CanESM2 is the direct result of bias correction. Excluding the large negative net mass balance predicted from CanESM2, the negative net mass balance predicted from the remaining three GCMs is believed to be due to accelerated melt in the future. Part of it can be attributed to a diminishing amount of winter accumulation in the future due to warmer temperatures. This is also evident in modelled future winter accumulation from all GCMs that are smaller than the long-term average value.

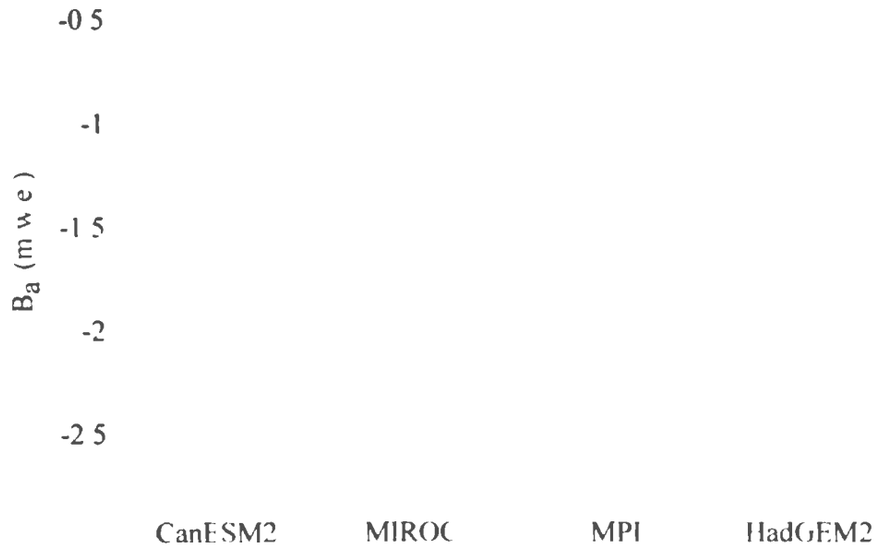

Figure 7.5 Boxplot of glacier-wide average future (2009-2040) net mass balance on Place glacier predicted from four different GCMs. The net mass balance is based on bias corrected summer and winter balance. The top and the bottom of the box mark the 75th and the 25th percentile of the dataset respectively. The height of the box represents the interquartile range (IQR) of the dataset and the ends of the whiskers mark the highest and lowest values of the dataset that are within 1.5 times the interquartile range of the box edges. The horizontal lines within the boxes are the median. The plus signs mark individual values outside the range of the whiskers (outliers).

Time series plots of modelled glacier mass balance components from 2009-2040 (32 years) from four different GCMs are shown in Figure 7.6. Modelled summer and winter balances are corrected for biases. None of the GCMs show any significant trend in summer balance in the future (Figure 7.6a). For all GCMs, there is a small negative trend in modelled winter accumulation (winter balance) in the future (Figure 7.6b). Winter balance from CanESM2, MIROC and HadGEM2 showed a small negative trend of -10 mm a^{-1}, -8 mm a^{-1} and -5.2 mm a^{-1} respectively. Winter balance from MPI has the smallest negative trend of -1.1 mm a^{-1}. However, these trend values are so small that they are not significant for the purpose of mass balance modelling. Inter-annual variability in modelled winter balance is large for all the GCMs considered, which is consistent with the winter precipitation data. Similar to the modelled future summer balance, no significant trend is detected in future net mass balance from any of the GCMs (Figure 7.6c). CanESM2 predicts consistently large negative net mass balances in the future period owing to large negative summer balances predicted by this GCM. As discussed before, the large negative net balances predicted from this GCM is a direct consequence of bias correction.

The bias-corrected cumulative net mass balance from different GCMs is shown in Figure 7.6d. For CanESM2, the cumulative net mass loss from 2009-2040 is nearly -81 m w.e. Without bias correction, CanESM2 predicted a cumulative mass loss of -30 m w.e. by the end of 2040. Compared to observed cumulative net mass balance from 1965-2005 (41 years) of -34 m w.e, the bias corrected cumulative net mass balance from CanESM2 appears too large whereas the cumulative net mass loss without bias correction appears reasonable. MIROC predicted a cumulative mass loss of -39 m w.e over the same period, which is slightly larger than historical trends but is equally plausible. HadGEM2 predicted a net mass

loss -30 m. w.e. from 2009-2040. In contrast to this, MPI predicted a much smaller net mass loss of -24 m w.e. during his period. This is mainly due to MPI generating small summer ablation on the glacier surface owing to a small net SEB on the glacier surface.

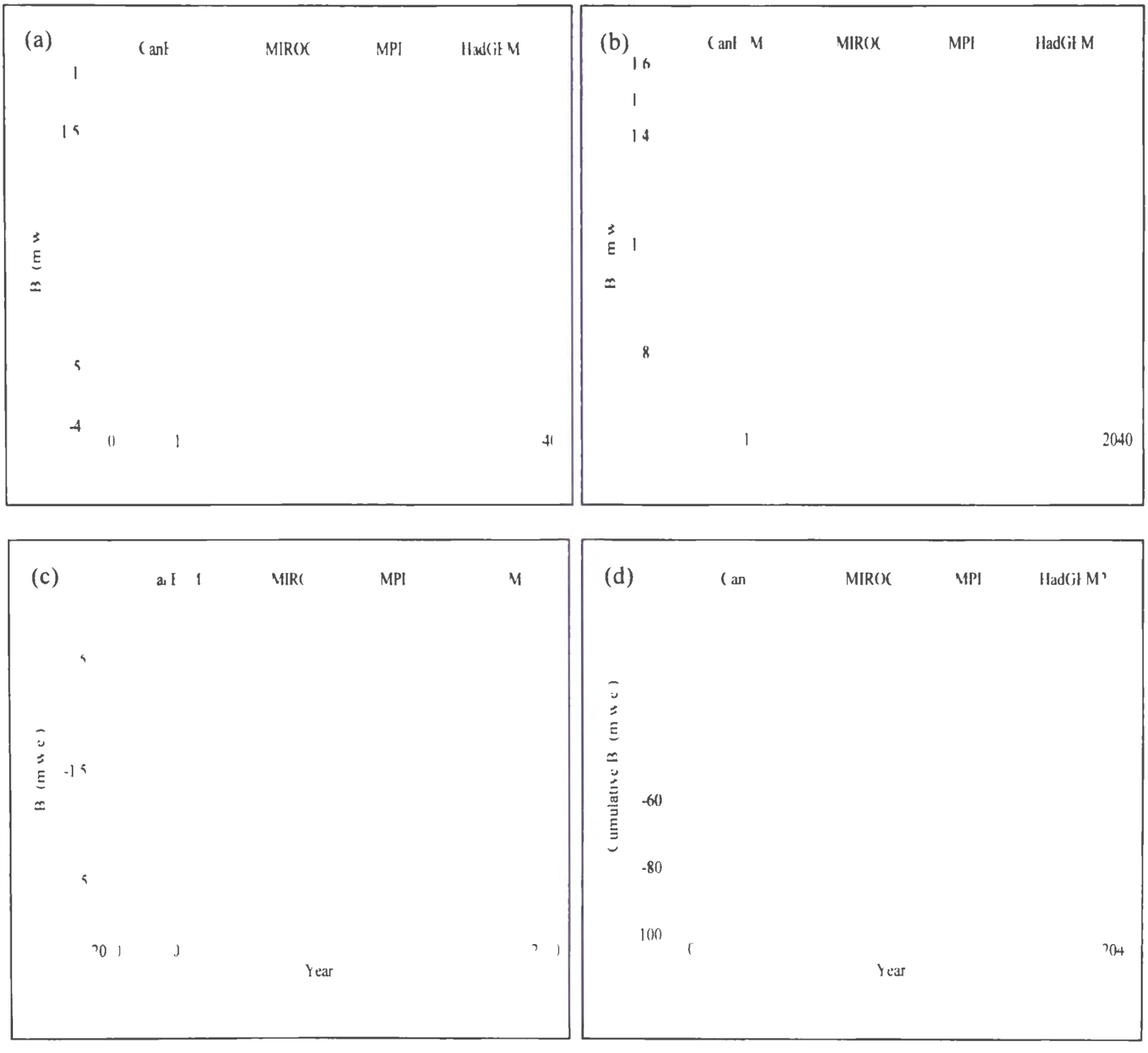

Figure 7.6 Mass balance projections for Place Glacier for the mass balance years 2008/09-2039/40 based on downscaled climate projections from four different GCMs. (a) glacier-wide summer balance, (b) glacier-wide winter balance, (c) glacier-wide net balance, and (d) cumulative glacier-wide net balance. Results are based on bias-corrected summer and winter balances.

The modelled cumulative net mass balance result is converted to volume of ice loss/gain where the area required for the estimation is obtained from the volume-area scaling relationship (see Chapter 3 for details) implemented within the GMB model (Figure 7.7a). Over a period from 2009-2040, CanESM2 predicted an average loss of -7.77×10^6 m^3 of ice volume with a cumulative loss of -0.25 km^3. For the same period, MIROC predicted an average loss of $-4.44\cdot10^6$ m^3 of ice volume with cumulative loss of -0.14 km^3. Similarly, during this period, MPI and CanESM2 predicted an average (cumulative) ice volume loss of $-2.94\cdot10^6$ m^3 (-0.09 km^3) and $-3.59\cdot10^6$ m^3 (-0.11 km^3) respectively. The cumulative volume loss from CanESM2 in the future is particularly large because it has predicted a large negative net balance in the future. With downscaled CanESM2 future projections, the GMB model predicted a glacier area of nearly 1.4 km^2 by the end of 2040 (Figure 7.7b). Since the glacier area at the beginning of the model run in 2009 was 2.94 km^2, this accounts for an area loss of 52% over a period from 2009-2040. Glacier mass balance record for Place Glacier suggest that the glacier has lost nearly 0.8 km^2 (20%) of area during the period from 1965-2005. Glacier area loss predicted by CanESM2 in the future appears too high compared to glacier area loss in the historical period. With downscaled MIROC and HadGEM2 projections, the GMB model predicted a glacier area of 2.12 km^2 and 2.29 km^2, respectively, by the end of 2040. This accounts for an area loss of 28% and 22% from these GCMs over a period from 2009-2040. Area loss predicted from MIROC and HadGEM2 are comparable to area loss observed in the historical period. For MPI, the GMB model predicted an area of 2.41 km^2 by the end of 2040 that accounts for an area loss of 18% over the future period. In terms of magnitude, the area loss predicted from MIROC, HadGEM2 and MPI are all comparable to the area loss observed in the historical period. Again, the

smaller area loss predicted by MPI is a direct consequence of small negative net mass balance predicted from this GCM. On average, compared to the observed historic glacier area, the area predicted by the GMB model from MIROC, MPI and HadGEM2 seems plausible.

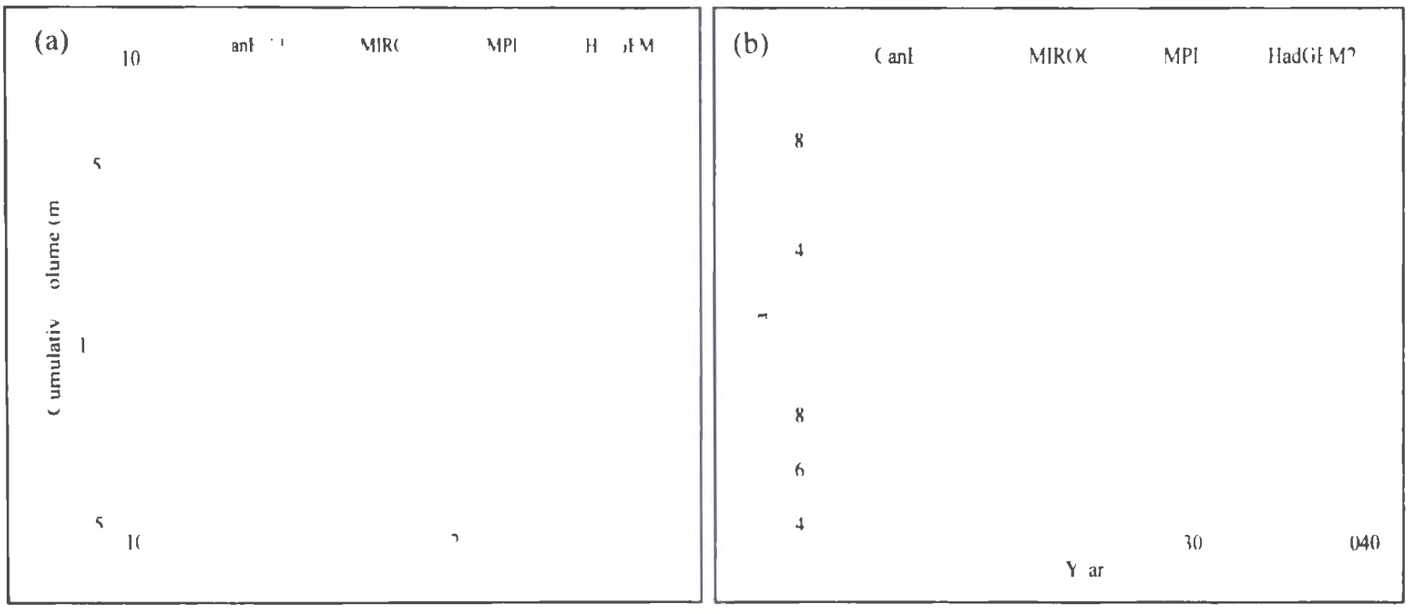

Figure 7.7 (a) Cumulative volume loss/gain for Place Glacier for the mass balance years 2008/09-2039/40, (b) estimated glacier area. Volume loss/gain is calculated using the ice density of 900 kg m^{-3}.

7.5 Conclusion

A physically-based distributed glacier mass balance model developed and validated for Place Glacier has been used to develop projections of future mass balance for the same glacier from 2009-2040. Mass balance is modelled using downscaled projections from four different GCMs: CanESM2, MIROC, MPI and HadGEM2. GCM experimental results are considered for RCP4.5, a midrange mitigation emission scenario and for multiple runs (realizations) with different but equally realistic initial conditions (e.g., Taylor et al. 2012).

A number of ensemble projections are averaged to get a single value. Historic (1961-2005) and future (2009-2040) projections from different GCMs are downscaled to the RAMS spatial resolution (8 km × 8 km) using the SVD method. Surface energy balance modelled using historical GCMs are found to contain some amount of bias relative to energy balance calculated using RAMS climate fields. The estimated glacier-wide bias (GCM-Observation) in surface energy balance is the largest for CanESM2 (= -64 W m^2) and smallest for HadGEM2 (= -13 W m^2). As a result, glacier-wide summer balance (summer ablation) predicted from CanESM2 shows a substantially smaller negative value compared to the observed summer balance on Place Glacier. Although the glacier-wide summer balance predicted from all GCMs in the historic period show smaller negative values compared to the observations, the bias (GCM-Observation) is particularly large for CanESM2 (= -1.71 m w.e.). The bias in historical glacier-wide summer balance predicted from the remaining three GCMs ranged from -0.21 m w.e. (HadGEM2) to -0.58 m w.e (MPI). Unlike summer balance, biases in historical glacier-wide winter balance predicted from all GCMs are relatively small. Bias in glacier-wide winter balance is largest for MPI (= 0.3 m w.e.) whereas it is negligible for CanESM2. The future glacier-wide summer and winter balance from all GCMs are corrected for the bias. The bias corrected future glacier-wide summer balance from CanESM2 (= -3.80 m w.e.) is substantially larger than the summer balance observed in the historic period (=-2.50 m w.e.). Bias corrected future glacier-wide summer balances from the remaining GCMs are comparable to the summer balance observed in the historic period. The future glacier-wide summer balance results from CanESM2 appear more reasonable without bias correction. The bias corrected modelled future glacier-wide winter balance from all the GCMs are smaller than the winter balance observed in the

historic period. This is expected because the warmer temperature in the future will decrease the proportion of precipitation that falls as snow. On average, modelled glacier-wide net mass balance from CanESM2 showed a large negative value of -2.50 m w.e. in the future. This is a direct consequence of bias correction applied to the glacier-wide summer balance predicted from this GCM. Compared to glacier-wide net mass balance observed in the historic period, the net mass balance predicted by CanESM2 in the future appears less likely. The unrealistically small energy balance predicted from the historical CanESM2, which led to a smaller negative summer balance (smaller ablation) compared to the observations possibly suggests that the historical CanESM2 is not performing well in reconstructing the observed climate in the past MIROC and HadGEM2 predicted an average net mass balance of -1.20 m w.e. and -0.94 m w.e., respectively, which appears more realistic based on comparison with observed historical data. MPI predicted a slightly smaller net mass balance of -0.75 m w.e. in the future period but is equally plausible. The average of the net mass balance projections between MIROC, MPI and HadGEM2 is -0.96 m w.e. By including the results from CanESM2, the average net mass balance value increased to -1.35 m w.e. Although the average of the net mass balance projections between MIROC, MPI and HadGEM2 appears reasonable, it is possible that this value is still underpredicted. This is because the GMB model neglects any melt on the glacier surface during the period 1 October-31 May assuming that it is too small to be considered. However, this assumption may not be valid in the future because the ongoing climate change is expected to prolong the summer melt season into autumn thus making summer balance more negative.

The exceptionally large cumulative glacier-wide net mass balance predicted from CanESM2 over a period 2009-2040 (= -81 m w.e.) appears unlikely. The cumulative glacier-

wide net mass balance from the remaining three GCMs for the same period ranged from -24 m w.e. to -39 m w.e. with an average of -31 m w.e. This value is comparable to the observed cumulative glacier-wide net mass balance from 1965-2005 (41 years) (= -34 m w.e). An independent verification of mass balance projections developed here for Place Glacier is difficult because there are only a few similar studies in the region (e.g., Radić et al. 2013; Clarke et al. 2015). Moreover, most of these studies are conducted at the regional scale and therefore do not provide much information about the mass balance at the scale of an individual glacier. Radić et al. (2013) used twenty-first-century ensemble projections from 14 different GCMs and estimated a multi-model average cumulative mass loss of -125 m w.e. for glaciers in western Canada and US for the period 2006-2100 (95 years). Compared to this result, the multi-model average mass loss from 2009-2040 (32 years) estimated for Place Glacier (= -31 m w.e.) appears reasonable. Recently, Clarke et al. (2015) used twenty-first-century climate scenarios from an ensemble of GCMs to develop projections of glacier area and volume changes in western Canada. Their results indicate that by 2100, the area and volume of glaciers in western Canada will decrease by 75±10% and 70±10% relative to 2005, respectively. With a reference glacier area of 26,700 km^2 and volume of 2,980 km^3 in 2005, this volume loss equates to a cumulative mass loss of -94 m w.e (assuming ice density of 900 kg m^{-3}) over the period 2009-2100 (92 year). This value is comparable to the cumulative mass loss of -31 m w.e. estimated for Place Glacier from 2009-2040 (32 year). The glacier area loss predicted from CanESM2 over 2009-2040 period (=52%) is too large compared to observed glacier area loss during the period 1965-2005 (= 20%). For the remaining GCMs, the simulated glacier area loss ranged between 18% and 28% with an average of 23%. The area loss predicted from MIROC, MPI and HadGEM2 appear more

realistic than the area estimate from CanESM2. Again, for the relatively shorter period of 2009-2040, this area loss appears reasonable compared to the area loss estimated by Clarke et al. (2015) for the period 2009-2100 (=75±10% km^2). Overall, downscaled MIROC, MPI and HadGEM2 perform better than the CanESM2 in predicting future net mass balance and area loss on Place Glacier. Since an independent validation of future mass balance is not possible, the above judgments are made entirely based on historic mass balance trends and with the assumption that the glacier will continue to lose mass in a more accelerated rate in the future following the climate warming (IPCC 2013).

However, it is emphasized here that these projections may be different from the actual change to be expected for Place Glacier due to the following consideration. First, the GCM projections suffer from many uncertainties due to factors such as coarse model resolution, parameterization of several physical processes in the atmosphere, improper or inadequate characterization of various feedback mechanisms, etc. It is possible that the SVD downscaling applied to these projections in this study has further amplified existing uncertainties in GCM projections. This may be particularly true for variables other than air temperature, which has received far less attention in the past in terms of their downscaling. Second, the glacier will lose area and move to higher elevations where the environment is usually cooler. This means less negative mass balance as the glacier approaches a new steady state. Third, the mass balance modelled here is a 'static mass balance' where the influence of other factors such glacier geometry, dynamics and other non-linear effects have been neglected. In other words, the present GMB model does not include the transport of glacier ice from higher to lower reaches of the glacier, which usually helps a glacier maintain its mass. Nevertheless, the mass balance projection obtained here can help

understand an overall state of Place Glacier in the future while keeping in mind the uncertainties in projected values between the different GCMs used.

Chapter 8

Conclusion

This research developed and applied methods for modelling the past and future mass balance on Place Glacier in the southern Coast Mountains of British Columbia. It focused on developing a physically-based distributed GMB model that is forced with climate data from the RAMS mesoscale model and the result is validated using observed mass balance data. The performance of the physically-based model is compared with two empirical GMB models: Temperature Index Model and Enhanced Temperature Index Model. The research also addressed the challenges associated with distribution of different meteorological variables from the RAMS mesoscale model on the glacier surface for running the GMB model. The GMB model developed and validated for Place Glacier is run using future climate projections to develop a future projection of GMB where the input variables are derived from the GCM projection, which is downscaled to the glacier location using a Singular Value Decomposition (SVD) technique. This concluding chapter provides a summary of the key findings of this research, its shortcomings, and suggestions for future research.

8.1 Summary of Key Findings

8.1.1 RAMS Variables

In Chapter 4, different RAMS variables used for running the GMB model are analysed and the biases are determined for precipitation and air temperature. The 8 km resolution RAMS model output is obtained through dynamical downscaling of 32 km resolution NARR data.

The bias correction factor (observed/modelled) for RAMS daily precipitation within the domain ranges from 0.2-1.6. The RAMS model underestimates precipitation in the Coast Mountains and overestimates it in the interior. Comparison of bias-corrected RAMS precipitation with the PRISM precipitation yielded a spatially averaged daily RMSE value of 4.6 mm day^{-1}. However, the bias corrected RAMS precipitation compared relatively better with the PRISM data in the interior than in the Coast Mountains. The bias correction offset (observed-modelled) for RAMS air temperature shows a more or less uniform distribution within the domain. Bias correction offset for most of the locations within the domain lie between 0 and -1°C. The RAMS air temperature showed cold (less than observed value) bias for most of the locations in the domain. When compared with daily PRISM air temperature, the spatially averaged RMSE in bias-corrected daily RAMS air temperature is 1.44°C. Generally, the bias corrected RAMS air temperature showed relatively good agreement with its PRISM counterpart in the interior as compared to other locations. Biases in other RAMS variables could not be determined due to the lack of relevant observations in the region.

The lapse rate of air temperature calculated for a number of high elevation sites using the RAMS vertical temperature sounding data ranged between 6.9 and 7.7°C km^{-1}, which is comparable to the standard air temperature lapse rate of 6.5°C km^{-1} used previously in GMB modelling. The estimated vertical gradient of hourly precipitation averaged over the summer months showed distinct year to year variation. These values are on the order of 10^{-3} mm m^{-1}. Similarly, the estimated gradient of winter total precipitation averaged over a period from 1980-2008 is 0.97 mm m^{-1}. This value is nearly twice as large as the long-term (1965-2005) averaged gradient of observed winter accumulation, which is only 0.5 mm m^{-1}.

The RAMS topography has been found to differ from the actual topography due to horizontal averaging in the 8 km resolution RAMS grid. At Place Glacier, the RAMS topography is 251 m higher than the actual elevation. The RAMS temperature and precipitation are corrected for this difference in elevation.

The comparison of bias corrected RAMS air temperature and glacier temperature on Place Glacier showed the influence of cooling within the katabatic boundary layer on air temperature. The onset of katabatic boundary layer development corresponds to a critical ambient temperature (T_c), which is estimated at nearly 5°C. For values less than T_c, bias-corrected RAMS air temperature generally agreed well with the observed glacier temperature. Above this value, there is relatively less agreement between bias-corrected RAMS air temperature and observed glacier air temperature. The value for T_c estimated here is comparable to the one estimated previously on Place Glacier, which ranged between 4.29 and 8.37°C (Shea 2010).

8.1.2 GMB Model Development and Validation

In Chapter 5, GMB model development and its application on Place Glacier is discussed. A distributed GMB model based on the surface energy balance approach has been developed and applied to Place Glacier over the 1980-2008 summer seasons using RAMS mesoscale model output. The model utilized physical parameterizations of the most important energy transfer processes to compute ablation and includes detailed temperature and radiation distribution across the glacier. The model computed winter accumulation by distributing winter precipitation using the vertical gradient of RAMS winter total precipitation. Similarly, precipitation during the summer months is distributed using the vertical gradient

of RAMS hourly precipitation. The model takes into account changes in glacier area over time when calculating specific ablation and accumulation on the glacier surface. Glacier area change is determined using a volume-area scaling relationship that is implemented within the GMB model. The model simulates surface temperature using a one layer subsurface scheme. The model is initialized with the total winter snow amount and a glacier surface temperature of 0°C. A comparison between simulated and measured glacier-wide summer balance over 1980-2008 yielded an annual RMSE = 0.43 m w. e. This is comparable with RMSE results obtained on the same glacier using a full energy balance model forced with in situ meteorological data from 2006-2008 (= 0.49 m w. e.) (Shea 2010). The comparison of simulated glacier-wide winter balance with the available observations yielded an annual RMSE = 0.27 m w.e., which is smaller than the RMSE in simulated summer balance. The RAMS bias-corrected simulated precipitation and its gradient used in the model appear to be performing well in simulating glacier-wide winter accumulation on the glacier surface. The model performed well in simulating cumulative net mass balance over a 29-year period. By the end of the model run in 2008, the simulated cumulative net mass balance of -33.72 m w.e. compared well with the measured cumulative net mass balance of -29.65 m w. e. The SEB-based GMB model outperformed both the empirical TI melt model and enhanced TI melt model in simulating the summer balance when all models were run with RAMS data. The average RMSE in estimated summer melt from the SEB based GMB model is 0.43 m w.e. while it is 1.14 m w.e. and 0.79 m w.e. for TI and enhanced TI melt model, respectively. For the plausible range of variation in temperature in glacier areas, the simulated mass balance showed highest sensitivity to changes in summer temperature. Winter temperature is second in importance in terms of its influence on simulated net

balance. Mass balance sensitivity to changes in summer and winter temperatures were -0.44 m w. e. $^{\circ}C^{-1}$ and -0.17 m w. e. $^{\circ}C^{-1}$, respectively. Among variables other than temperature, changes in incoming longwave radiation yielded a sensitivity of -0.10 m w. e. $\%^{-1}$ in simulated net balance. Net mass balance showed a sensitivity of 0.02, 0.002, and 0.003 m w. e. $\%^{-1}$ to changes in albedo of old snow, new snow, and ice, respectively. Although the mass balance sensitivity to changes in surface roughness length is insignificant, it should be noted here that the chosen range of perturbation (±20%) of surface roughness length is too small compared to the actual range of variation over glacier surfaces that can vary over many orders of magnitude. As a result, surface roughness length can still have appreciable effect on glacier mass balance. Also, in the case of other model parameters and variables, the chosen range of perturbation may not be sufficient to account for the actual changes occurring on the glacier. For about 70% of the time during the summer months, the model simulated glacier surface temperature of 0°C. The frequency of sub-zero surface temperature is about 30%, which mainly occurred during August-September. The model simulated hourly temperature minima of -16°C during this period. This result perhaps justifies the assumption of constant glacier surface temperature of 0°C in a traditional GMB model.

Although the model performed well in simulating glacier-wide summer and winter balances, it did not perform as well in reproducing altitude-wise summer and winter balances. The model consistently underestimated summer melt at the terminus of the glacier and overestimated it at the upper glacier site. This is possibly because the actual wind speed on higher (lower) reaches of the glacier may be larger (smaller) than what is prescribed in the model thus affecting the calculation of turbulent heat fluxes. The model's inability to reproduce altitude-wise winter balance is expected because the model does not take into

account the redistribution of snow by wind and transport from valley walls to the glacier. However, it should be noted here that of the entire simulation period (1980-2008), altitude-wise observed summer and winter balance data are available only from 1980-1989. Additionally, for most of these years, observations are missing for higher elevation areas. Missing mass balance data for higher elevations are linearly interpolated using the vertical gradient derived from the available data. As a result, these interpolated data may not represent the true mass balance for these elevation bands thus potentially making comparison results unreliable. The simulated snowpack decay at one of the locations on the glacier surface is compared with the observed snowline retreat data from a nearby location. For the summer of 2007, the model reported a complete disappearance of winter snowpack at a location by the middle of August. This is nearly the same as the observed date of disappearance of snowpack from that location.

The downscaled RAMS variables performed well in developing the summer and winter balance hindcast for Place Glacier using the physically-based distributed GMB model. Results from this study suggest that the accuracy of simulated mass balance results depends both on choice of the GMB model and meteorological data (e.g., observed, reanalysis or downscaled) used for running the model. Because the model is physically based with little site specific calibration, it can be applied to other glacier locations in the southern Coast Mountains for developing mass balance hindcasts. The model's inability to simulate the altitude-wise mass balance for Place Glacier suggests that it needs to be tested further in other glacier locations using reliable mass balance data. The model's skill in simulating cumulative net mass balance at longer time scale suggests that the model can be potentially used for future mass balance projections.

8.1.3 Climate Downscaling

The focus of Chapter 6 was to downscale several future climate projections from a suite of GCMs to be used as input for a GMB model for developing projections of future mass balance on Place Glacier. A linear regression model based on an SVD technique was used for downscaling large-scale climate variables. The SVD downscaling model was developed using daily RAMS (8 km × 8 km) variables as predictand and the corresponding daily NCEP ($2.5^{o} \times 2.5^{o}$) variables as predictor from the period 1979-1993. RAMS and NCEP datasets from the period 1994-2008 are used for cross-validation. The large-scale variables considered for downscaling were air temperature, humidity, precipitation, sea level pressure, wind speed, incoming shortwave and longwave radiation. Among all variables, daily air temperature showed the strongest predictor-predictand relationship. The cross-validation of downscaled daily air temperature showed a strong correlation with the validation dataset. Averaged over the entire domain, the downscaled daily air temperature explained 85% of the variance in the validation dataset with an RMSE value of $2.4^{o}C$. The model for daily specific humidity also showed a strong predictor-predictand relationship yielding a strong correlation between the downscaled and validation datasets. Unlike for air temperature and specific humidity, the SVD model for daily precipitation did not show a strong relationship between the large-scale precipitation and small-scale RAMS precipitation field. With spatially-averaged correlation of 0.38 and RMSE of 7.5 mm, the model for daily precipitation appears to be performing less satisfactorily in downscaling large-scale precipitation. This perhaps suggests that the use of large-scale precipitation alone as a predictor variable is not adequate for downscaling precipitation. A combination of large-scale predictor variables that include circulation-based variables and humidity may improve

the downscaling result. As the topography is known to have a strong influence on precipitation, using it as one of the predictor variables may further improve the results. For wind speed, the correlation between downscaled values and the validation dataset is weak and spatially variable. For sea level pressure, the correlation between the downscaled values and the validation dataset is relatively strong. The downscaled incoming shortwave radiation showed a moderate correlation with the validation dataset, but the errors in downscaled results were large. Similar to the results for shortwave radiation, downscaled incoming longwave radiation also showed a moderate correlation with the validation dataset. Errors in downscaled incoming longwave radiation were also minimal. For all variables, the error statistics improved with the monthly model, but there was no significant improvement in the correlation values. As the errors in downscaled variables are generally large with the daily SVD model, the use of a monthly SVD model can be a better choice unless a particular study requires daily downscaled field specifically.

Future daily climates from four different GCMs (CanESM2, MIROC-ESM, MPI-ESM-LR, and HadGEM2-ES) are downscaled using the SVD models developed and validated in the historic period. Since it is not possible to validate the downscaled GCM fields in the future, they are simply compared with the original GCMs (without downscaling) with their original counterpart to understand the effect of downscaling. For a particular climate field, the performance of the downscaling model varied between GCMs. For all GCMs considered, the downscaled air temperature showed higher median values as compared to the median values in the original GCMs. The downscaled air temperature result appears to be preserving the long-term positive trend present in the original GCM dataset. For all GCMs, both original and downscaled precipitation values show a large number of

positive extreme values. No long-term trend was detected in the downscaled precipitation values. The downscaled specific humidity from different GCMs has higher median values than their original counterpart. The downscaled specific humidity appears to be preserving the long-term positive trend seen in the original GCM dataset. There was a slight decrease in median values in downscaled wind speed from CanESM2 and MPI. Downscaled wind speed from MIROC and HadGEM2 showed a slight increase in the median values as compared to the original values. For both incoming shortwave and longwave radiation and for all GCMs, the downscaling process appears to have increased the median value. The downscaled incoming longwave radiation appears to be preserving the long-term positive trend seen in the original GCM data. As discussed before, since the SVD model for downscaling daily air temperature, humidity and longwave radiation performed better compared to the models for downscaling other large-scale fields, these models are expected to perform well in downscaling corresponding climate fields from different GCMs in the future.

8.1.4 Future GMB projection

In Chapter 7, a SEB-based GMB model developed and validated for Place Glacier was used to develop projections of future mass balance for the same glacier from 2009-2040. The GMB model is driven by statistically downscaled climate projections from a suite of GCMs: CanESM2, MIROC-ESM, MPI-ESM-LR and HadGEM2-ES. To determine the bias (GCM-Observation) in energy and mass balance predicted from different GCMs, the GMB model is also run in the historic period (1961-2005) using statistically downscaled GCM climate fields. Bias in energy balance is determined relative to the energy balance modelled using RAMS variables. All GCMs show some amount of bias in modelled energy balance on the

glacier surface. However, the average energy balance modelled from CanESM2 showed the largest amount of bias (= -64 W m^{-2}). For the remaining GCMs, the average bias ranged from -13 W m^{-2} to -24 W m^{-2}. As a result of this, summer ablation (balance) predicted from historic CanESM2 is substantially smaller compared to the summer balance observed on Place Glacier. Bias in modelled summer and winter balance values in the historic period is also determined relative to summer and winter balance records available for Place Glacier from 1965-2005. However, there are a number of years with missing mass balance records, which are not considered for bias estimation. For CanESM2, the estimated average bias in modelled glacier-wide summer balance over a period 1965-2005 is very large (= -1.71 m w.e.). Average bias in modelled glacier-wide summer balance from remaining GCMs for the same period ranged from -0.21 m w.e. to -0.58 m w.e. However, the modelled glacier-wide winter balance from all the GCMs showed a small bias, which ranged from -0.1 m w.e. to 0.30 m w.e. The modelled future glacier-wide summer and winter balance values from different GCMs are corrected for these biases additively. With the bias correction, CanESM2 predicted a glacier-wide summer balance of -3.80 m w.e., which is substantially larger than the glacier-wide summer balance observed in the historic period (= -2.50 m w.e.). Bias corrected future glacier-wide summer balances from the remaining GCMs are comparable to the glacier-wide summer balance observed in the historic period. The future glacier-wide summer balance results from CanESM2 appear more reasonable without bias correction (= -2.10 m w.e). The bias corrected modelled future winter balance from all the GCMs are smaller than the winter balance observed in the historic period. As a result of bias correction in the summer balance, CanESM2 predicted a large negative net mass balance of -2.50 m w.e. in the future that appears unrealistic. The unrealistically small energy balance

predicted from the historic CanESM2 that led to a smaller summer ablation (balance) compared to the observations possibly suggests that the historic CanESM2 is not performing well in reconstructing the observed climate in the past. MIROC, MPI and HadGEM2 predicted an average net mass balance of -1.20 m w.e., -0.75 m w.e. and -0.94 m w.e., respectively. These values are comparable to the average observed net mass balance in the historic period (= -0.84 m w.e.). Without correcting the bias in summer balance, CanESM2 predicted a net mass balance of -0.89 m w.e., which is very close to the observed historic net mass balance. The average of the net mass balance projections between MIROC, MPI and HadGEM2 is -0.96 m w.e. By including the results from CanESM2, the average net mass balance value between the GCMs increased to -1.35 m w.e. As a result of the large negative net mass balance predicted from CanESM2, the cumulative net mass balance from this GCM over the future period (2009-2040) was exceptionally large at -81 m w.e. This value is more than two times as large as the observed cumulative mass balance in the historic period and therefore seems unlikely. The cumulative net mass balance from the remaining three GCMs ranged from -24 m w.e. to -39 m w.e. with an average of -31 m w.e. This value is comparable to the observed cumulative net mass balance in the historic period. The glacier area loss predicted from GCMs other than CanESM2 ranged from 18% to 28% with an average of 23%. This value is comparable to the observed area loss from 1965-2005, which is 20%. The CanESM2 predicted area loss is significantly larger than the area loss observed in the historic period. Overall, downscaled MIROC, MPI and HadGEM2 perform better than the CanESM2 in predicting future net mass balance and area loss for Place Glacier. The average mass balance predicted from these GCMs compared well with the results from similar other studies in the region. However, due to uncertainties in GCM projections and

the uncertainties in NCEP and RAMS variables used in SVD downscaling, these predictions of mass balance for Place Glacier may be different from the actual mass balance in the future period.

Overall, this research has demonstrated the usefulness of mesoscale climate model data for physically-based distributed GMB modelling in the southern Coast Mountains of British Columbia, Canada. For the first time, a time series of mass balance hindcast has been developed for Place Glacier, southern Coast Mountains. The success of the physically-based GMB model at Place Glacier suggests the possibility of its use for GMB modelling in other glaciers in the region. The fact that the model produced results comparable to the observations when forced with mesoscale climate model data suggests that this approach of mass balance modelling can potentially be used as an alternative to in situ glacier mass balance measurements in the region, which is generally void of mass balance data. This approach of mass balance modelling has not been tested before in the southern Coast Mountains. Additionally, for the first time, a physically-based GMB model has been used to develop projections of future mass balance on Place Glacier. The input variables for future GMB modelling were obtained by statistical downscaling of GCM projections using a more advance SVD technique. SVD technique of climate downscaling has never been applied in the past for physically-based GMB modelling in the region. Although, GMB projections in western Canada have been developed at the regional scale using empirical GMB models forced with downscaled GCM projections (e.g., Clarke et al. 2015), this is the first time mass balance projections were developed at the scale of an individual glacier using a physically-based model in the southern Coast Mountains. The past and future mass balance simulations developed here for Place Glacier can be useful for understanding the response of

glacier to climate change in the region. This information may be important for developing future water management policies in response to dwindling water supply in the region.

8.2 Shortcomings and Suggestions for Future Research

While the present research has demonstrated the usefulness of mesoscale and large-scale climate fields in distributed GMB modelling in the southern Coast Mountains of British Columbia, it has certain limitations arising from a number of knowledge gaps in areas that require further research. Additionally, there are a number of shortcomings in this research that need to be addressed in future work. These limitations and shortcoming are discussed in the following section.

Input Variables and Distribution

Due to the lack of long-term observed data for variables other than air temperature and precipitation, only these two RAMS variables are corrected for bias before they are used in the GMB model. However, other variables may potentially contain some bias. Further research is recommended to estimate the bias in other RAMS variables. The GMB model distributes air temperature on the glacier surface using the lapse rate estimated from the RAMS model values. However, the KBL usually present over the melting glacier provides a cooling effect on the glacier surface. As a result, the actual air temperature lapse rate on the glacier may differ from the lapse rate estimated using RAMS values, which cannot resolve the processes occurring at the glacier scale. Similarly, precipitation is distributed on the glacier surface using the vertical gradient estimated from the RAMS data. This may not be accurate as the mountain topography is known to have strong influence on precipitation,

which the RAMS model is unable to resolve in detail. Therefore, further research is recommended to understand the vertical distribution of air temperature and precipitation on the glaciers in the southern Coast Mountains.

GMB Model

- The SEB-based GMB model presented in this study assumes that there is no melt during the winter months (1 October-31 May) and therefore calculates glacier melt during the summer months (1 June-30 September) only. This may not be a valid assumption in the future because summer is expected to be prolonged as a result of climate change. In future research, the model setup needs to be changed to simulate the melt for the entire hydrologic year (1 October-30 September).
- The effect of topographic shadow on direct solar radiation is neglected in the model. This may have caused some amount of uncertainty in the model results because the surface does not receive direct solar radiation when it is in shadow. Therefore, the radiation parameterization scheme requires further improvement by including the shadow effect from the surrounding terrain.
- The model simulates the mass balances on a fixed glacier area ($Area_{ref}$) and adjusts them for the glacier area change simply by applying an area ratio ($Area_{new} / Area_{ref}$). The glacier area at the end of the model run ($Area_{new}$) is calculated using volume-area scaling relationship, which is not calibrated for Place Glacier. This empirical approach of adjusting glacier mass balances for the area change has not been tested yet and therefore requires further research. The best approach to account for glacier area change in a GMB model that should be done in future work is to calculate the area evolution by updating the glacier area at the end of the balance year.

- The model sensitivity to input variables (except air temperature) and parameters are tested by perturbing them at 10% interval spanning ±20%. However, this arbitrary percent changes are not realistic for all variables and parameters as their natural range of variability is not meaningfully expressed as a fixed ±20%. This issue needs to be addressed in future work.
- Empirical TI and enhanced TI melt model calculate melt using RAMS air temperature with melt coefficients calibrated on Place Glacier using interpolated daily station air temperature. This is usually not warranted because these parameters are not only specific to models but also to the type of input data used in the calibration. In future work, it is recommended that these melt parameters be determined through calibration using RAMS air temperature.
- The GMB model results are validated using historical glacier-wide mass balance records. However, glacier-wide mass balances are obtained by extrapolating individual stake data and therefore suffer from some amount of uncertainty. As a result, glacier-wide mass balances are usually considered less suitable for validating GMB results. Therefore, in the future research, GMB models results should be validated with the actual stake data.
- The GMB model presented in the present study can be improved by including a physically-based approach for precipitation distribution in complex terrain (e.g., Jarosch et al. 2010). Although an empirical approach for distributing air temperature within a KBL has been presented before (e.g., Shea 2010), a physically-based method would be beneficial.

- The estimation of turbulent heat flux suffers from uncertainty in estimated turbulent transfer coefficients owing to the uncertainty related to estimated surface roughness length. Future research should focus on measuring the profiles of wind speed and temperature at multiple locations to help refine estimates of surface roughness length. Also, the bulk Richardson number approach used for stability correction may be underestimating turbulent heat fluxes. It is suggested that this approach of stability correction be replaced with an approach based on Monin-Obhukov similarity theory.
- Since the model neglects sublimation, it is possible that it is underestimating glacier ablation, especially when latent heat fluxes are negative. This issue should be addressed in future work.
- Some of the parameters used in the albedo sub-model have been adopted from studies elsewhere in the world. It is recommended that the albedo sub-model be calibrated for selected glaciers in the southern Coast Mountains.
- Further study is recommended to determine the transferability of the GMB model to other glacier locations in the region.
- Further work is also recommended to determine whether the GMB model can be included with a hydrologic model for operational purposes.

Climate Downscaling

- The statistical SVD model developed for downscaling different large-scale variables produced mixed results. The present study has used RAMS variables as predictands and the corresponding NCEP fields as predictor variables. Further work is recommended to test the different methods of statistical downscaling using a

combination of predictor variables. Future research should consider statistical downscaling of future projections from a number of GCMs to determine the range of uncertainty in downscaled values.

Future GMB Projection

- Although the physically-based GMB model outperformed both empirical TI and enhanced TI model in simulation of glacier ablation, these models have not been compared using downscaled future GCM projections. This can be another avenue for future research. Also, to determine the uncertainty in future GMB projection, it is recommended that the model be run using climate projections from a number of GCMs.

In the future, a collaborative effort at collecting and collating meteorological, glaciological, hydrological and remote sensing data from selected glaciers is recommended for better evaluation of the GMB model in the southern Coast Mountains.

References Cited

Ainslie, B., and P. L. Jackson, 2010: Downscaling and bias correcting a cold season precipitation climatology over coastal southern British Columbia using the Regional Atmospheric Modeling System (RAMS). *J. Appl. Meteorol. Climatol.*, **49**, 937–953.

Andreas, E. L., R. E. Jordan, and A. P. Makshtas, 2004: Simulations of snow, ice, and near-surface atmospheric processes on Ice Station Weddell. *J. Hydrometeor.* **5**, 611–624.

Andreassen, L. M., B. KJøllmoen, A Rasmussen, K. Melvold, and Ø. Nordli, 2012: Langfjordjøkelen, a rapidly shrinking glacier in northern Norway. *J. Glaciol.*, **58**, 581–593.

Anslow, F. S., S. Hostetler, W. R. Bidlake, and P. U. Clark, 2008: Distributed energy balance modeling of South Cascade Glacier, Washington and assessment of model uncertainty. *J. Geophys. Res.*, **113**, F02019, doi:10.1029/2007JF000850.

Arendt, A. A., K. A. Echelmeyer, W. D. Harrison, C. S. Lingle, and V. B. Valentine, 2002: Rapid wastage of Alaska glaciers and their contribution to rising sea level. *Science*, **297**, 382–386.

——, S. B. Luthcke, C. F. Larsen, W. Abdalati, W. B. Krabill, and M. J. Beedle, 2008: Validation of high-resolution GRACE mascon estimates of glacier mass changes in the St Elias Mountains, Alaska, USA, using aircraft laser altimetry. *J. Glaciol.*, **54**, 778–787.

Arnold, N. S., M. J. Wills, M. J. Sharp, K. S. Richards, and W. J. Lawson, 1996: A distributed surface energy-balance model for a small valley glacier. I. Development and testing for Haut Glacier d'Arolla, Valais, Switzerland. *J. Glaciol.*, **42**, 77–89.

——, W. G. Rees, A. J. Hodson, and J. Kohler, 2006: Topographic controls on the surface energy balance of a high Arctic valley glacier. *J. Geophys. Res.*, **111**, F02011, doi:10.1029/2005JF000426.

Arora, V. K., J. F. Scinocca, G. J. Boer, J. R. Christian, K. L. Denman, G. M. Flato, V. V. Kharin, W. G. Lee, and W. J. Merryfield, 2011: Carbon emission limits required to satisfy future representative concentration pathways of greenhouse gases. *Geophys. Res. Lett.*, **38**, L05805, doi:10.1029/2010GL046270.

Bahr, D. B., 1997: Global distribution of glacier properties: A stochastic scaling paradigm. *Water Resour. Res.*, **33**, 1669–1679.

——, M. F. Meier, and S. D. Peckham, 1997: The physical basis of glacier volume-area scaling. *J. Geophys. Res.*, **102**, 20355–20362.

Barnett, T. P., J. C. Adam, and D. P. Lettenmaier, 2005: Potential impacts of a warming climate on water availability in snow-dominated regions. *Nature*, **438**, 303–309.

Barrow, E. M., M. Hulme, and M. Semenov, 1996: Effect of using different methods in the construction of climate change scenarios: examples for Europe. *Clim. Res.*, **7**, 195–211.

BC Ministry of Water, Land and Air Protection, 2002: Indicators of Climate Change for British Columbia. Tech. Rep., Beacon Hill Communications Group Inc, Victoria, Canada.

Berthier, E., E. Schiefer, G. K. C. Clarke, B. Menounos, and F. Rémy, 2010: Contribution of Alaskan glaciers to sea-level rise derived from satellite imagery. *Nat. Geosci.*, **3**, 92–95.

Bitz, C. M., and D. S. Battisti, 1999: Interannual to decadal variability in climate and the glacier mass balance in Washington, western Canada, and Alaska. *J. Clim.*, **12**, 3181–3196.

Bolch, T., B. Menounos, and R. Wheate, 2010: Landsat-based inventory of glaciers in western Canada, 1985–2005. *Remote Sens. Environ.*, **114**, 127–137.

Bougamont, M., J. L. Bamber, and W. Greuell, 2005: A surface mass balance model for the Greenland Ice Sheet. *J. Geophys. Res.*, **110**, F04018, doi:10.1029/2005JF000348.

——, ——, J. K. Ridley, R. M. Gladstone, W. Greuell, E. Hanna, A. J. Payne, and I. Rutt, 2007: Impact of model physics on estimating the surface mass balance of the Greenland ice sheet. *Geophys. Res. Lett.*, **34**, L17501, doi:10.1029/2007GL030700.

Box, J. E., D. H. Bromwich, and L.-S. Bai, 2004: Greenland ice sheet surface mass balance 1991–2000: Application of Polar MM5 mesoscale model and in situ data. *J. Geophys. Res.*, **109**, D16105, doi:10.1029/2003JD004451.

——, and A. Rinke, 2003: Evaluation of Greenland Ice Sheet surface climate in the HIRHAM Regional Climate Model using automatic weather station data. *J. Clim.*, **16**, 1302–1319.

Braithwaite, R. J. 1995. Positive degree-day factors for ablation on the Greenland ice sheet studied by energy-balance modelling. *J. Glaciol.*, **41**, 153-160.

——, and Y. Zhang, 1999: Modelling changes in glacier mass balance that may occur as a result of climate changes. *Geogr. Ann.*, **81A**, 489–496.

——, and F. Müller, 1980: On the parameterization of glacier equilibrium line altitude. *IAHS Publication*, **126**, 263–271.

——, 1977: Air temperature and glacier ablation: a parametric approach. Ph.D. Thesis. McGill University.

Braun, L.N. and H. Escher-Vetter, 1996: Glacial discharge as affected by climate change. *International Congress- Protection of habitat against floods, debris flows and avalanches, 1996*, Germany, 65-74.

Braun, M., and R. Hock, 2004: Spatially distributed surface energy balance and ablation modelling on the ice cap of King George Island (Antarctica). *Glob. Planet. Change*, **42**, 45–58.

Bretherton, C. S., C. Smith, and J. M. Wallace, 1992. An intercomparison of methods for finding coupled patterns in climate data. *J. Clim.*, **5**, 541–560.

Brock, B. W., I. C. Willis, and M. J. Sharp, 2006: Measurement and parameterization of aerodynamic roughness length variations at Haut Glacier d'Arolla, Switzerland. *J. Glaciol.*, **52**, 281 – 297.

——, ——, and ——, 2000: Measurement and parameterization of albedo variations at Haut Glacier d'Arolla, Switzerland. *J. Glaciol.*, **46**, 675–688.

Bromwich, D. H., L. Bai, and G. G. Bjarnason, 2005: High-resolution regional climate simulations over Iceland using Polar MM5. *Mon. Weather Rev.*, **133**, 3527–3547.

Brown, L. E., D. M. Hannah, and A. M. Milner, 2005: Spatial and temporal water column and streambed temperature dynamics within an alpine catchment: implications for benthic communities. *Hydrol. Process.*, **19**, 1585–1610.

——, ——, and ——, 2007: Vulnerability of alpine stream biodiversity to shrinking glaciers and snowpacks. *Glob. Chang. Biol.*, **13**, 958–966.

Brun, E., E. Martin, V. Simon, C. Gendre, and C. Coléou, 1989: An energy and mass model of snow cover suitable for operational avalanche forecasting. *J. Glaciol.*, **35**, 333–342.

Bürger, G., 1996: Expanded downscaling for generating local weather scenarios. *Clim. Res.*, **7**, 111–128.

Bürger, G., J. Schulla, and a. T. Werner, 2011: Estimates of future flow, including extremes, of the Columbia River headwaters. *Water Resour. Res.*, **47**, 1–18.

Carenzo, M., F. Pellicciotti, S. Rimkus, and P. Burlando, 2009: Assessing the transferability and robustness of an enhanced temperature-index glacier-melt model. *J. Glaciol.*, **55**, 258–274.

Cassano, J. J., E. Box, D. H. Bromwich, L. Li, and K. Steffen, 2001: Evaluation of Polar MM5 simulations of Greenland's atmospheric circulation. *J. Geophys. Res.*, **106**, 33867–33889.

CDED, 2013: Canadian Digital Elevation Data, Natural Resources Canada, Government of Canada [Available from the web site of GeoBase at http://www.geobase.ca/geobase/en/data/cded/index.html]

Chen, J., and A. Ohmura, 1990: Estimation of Alpine glacier water resources and their change since the 1870s. *Hydrology in Mountainous Regions. I-Hydrological Measurements; the Water Cycle*, IAHS Publ. no. 193, 127–135.

Clarke, G. K. C, A. H. Jarosch, F. S. Anslow, V. Radic, and M. Menounos, 2015: Projected deglaciation of western Canada in the twenty-first century. *Nature Geoscience Letter*, **8**, 372-377.

——, and W. P. Adams, 1998: Mass balance of glaciers other than the ice sheets. *J. Glaciol.*, **44**, 315–325.

Cogley, J.G., 2005: Mass and energy balances of glaciers and ice sheets. Anderson Eds. *Encyclopaedia of hydrological sciences, Part 14 Snow and glacier hydrology*, New York, Wiley, 2555–2573.

Colle, B. A., K. J. Westrick, and C. F. Mass, 1999: Evaluation of MM5 and Eta-10 precipitation forecasts over the Pacific Northwest during the cool season. *Weather Forecast.*, **14**, 137–154.

Collins, D.N., 1987: Climatic fluctuations and runoff from glacierized Alpine basins. *The Influence of Climate Change and Climatic Change on the Hydrologic Regime and Water Resources,* IAHS Publ. no. 168, 77–89.

Conway, D., R. L. Wilby, and P. D. Jones, 1996: Precipitation and air flow indices over the British Isles. *Clim. Res.*, **7**, 169–183.

Corripio, J., 2003: Modeling the energy balance of high altitude glacierized basins in the Central Andes. Ph.D Thesis. University of Edinburgh.

Cotton, W. R., and Coauthors, 2003: RAMS 2001: Current status and future directions. *Meteorol. Atmos. Phys.*, **82**, 5–29.

Cuffey, K. M., and W. S. B. Paterson, 2010: *The Physics of Glaciers*. Fourth Edition. Elsevier Press, 693 pp.

Dadic, R., R. Mott, M. Lehning, and P. Burlando, 2010: Wind influence on snow depth distribution and accumulation over glaciers. *J. Geophys. Res.*, **115**, F01012, doi:10.1029/2009JF001261.

Dadic, R., J. G. Corripio, and P. Burlando, 2008: Mass-balance estimates for Haut Glacier d'Arolla, Switzerland, from 2000 to 2006 using DEMs and distributed mass-balance modeling. *Ann. Glaciol.*, **49**, 22–26.

Daly, C., W. Gibson, G. Taylor, G. Johnson, and P. Pasteris, 2002: A knowledge-based approach to the statistical mapping of climate. *Clim. Res.*, **22**, 99–113.

——, M. Halbleib, J. I. Smith, W. P. Gibson, M. K. Doggett, G. H. Taylor, J. Curtis, and P. P. Pasteris, 2008: Physiographically sensitive mapping of climatological temperature and precipitation across the conterminous United States. *Int. J. Climatol.*, **28**, 2031–2064.

DeBeer, C. M., and M. J. Sharp, 2007: Recent changes in glacier area and volume within the southern Canadian Cordillera. *Ann. Glaciol.*, **46,** 215–221.

Demuth, M., and A. Pietroniro, 1999: Inferring glacier mass balance using Radarsat: results from Peyto Glacier, Canada. *Geogr. Ann.*, **81A**, 521–540.

——, and R. Keller, 2006: An assessment of the mass balance of Peyto Glacier (1966–1995) and its relation to recent and past century climate variability. *Peyto Glacier: One Century of Science.* Demuth et al., Eds., Scientific Report No. 8, National Hydrology Research Institute, Saskatoon, Saskatchewan, Canada, 83–132.

Denby, B., W. Greuell, and J. Oerlemans, 2002: Simulating the Greenland atmospheric boundary layer. Part I: Model description and validation. *Tellus A*, **54,** 512-528.

Dozier, J., and J. Frew, 1990: Rapid calculation of terrain parameters for radiation modeling from digital elevation data. *IEEE Trans. Geosci. Remote Sens.*, **28**, 963–969.

Dyurgerov, M.B., 2010: Reanalysis of glacier changes: from the IGY to the IPY, 1960-2008. *Data of Glaciological Studies,* **108**, 5-116.

——, and M. F. Meier, 1997a, Year-to-year fluctuations of global mass balance of small glaciers and their contribution to sea-level changes. *Arctic, Antarct. Alp. Res.*, **29**, 392-401.

——, and M. F. Meier, 1997b, Mass balance of mountain and subpolar glaciers: a new global assessment for the period of instrumental records (1961-1990). *Arctic, Antarct. Alp. Res.*, **29**, 379-391.

——, 2002: Glacier Mass Balance and Regime : Data of measurements and analysis. Tech. Rep. Occasional Paper 55, Institute of Arctic and Alpine Research, 268 pp.

——, and M. F. Meier, 2005: Glaciers and the changing earth system: A 2004 snapshot. Tech. Rep. Occasional Paper 58, Institute of Arctic and Alpine Research, 188 pp.

Elsberg, D. H., W. D. Harrison, K. a. Echelmeyer, and R. M. Krimmel, 2001: Quantifying the effects of climate and surface change on glacier mass balance. *J. Glaciol.*, **47**, 649–658.

Escher-Vetter, H.,1985: Energy balance calculations for the ablation period 1982 at Vernagtferner, Oetztal Alps. *Ann. Glaciol.*, **6**, 158-160.

ESRI, 2011: ArcGIS Desktop; Release 10. Redlands, CA: Environmental Systems Research Institute.

Farinotti, D., S. Usselmann, M. Huss, A. Bauder, and M. Funk, 2012: Runoff evolution in the Swiss Alps: Projections for selected high-alpine catchments based on ENSEMBLES scenarios. *Hydrol. Process.*, **26**, 1909–1924.

Fettweis, X., H. Gallée, F. Lefebre, and J.-P. Ypersele, 2005: Greenland surface mass balance simulated by a regional climate model and comparison with satellite-derived data in 1990–1991. *Clim. Dyn.*, **24**, 623–640.

Fleming, S. J., and G. K. C. Clarke, 2003: Glacial control of water resource and related environmental responses to climate warming: empirical analysis using historical streamflow data from northwestern Canada. *Can. Water Resour. J.*, **28**, 69-86.

Flower, H. J., C. G. Kilsby, and P. E. O'Connell, 2000: A stochastic rainfall model for the assessment of regional water resource systems under changed climatic conditions. *Hydrol. Earth Syst. Sci.*, **4**, 261–280.

——, ——, C. G. Kilsby, P. E. O'Connell, and A. Burton, 2005: A weather-type conditioned multi-site stochastic rainfall model for generation of scenarios of climatic variability and change. *J. Hydrol.*, **308**, 50–66.

Fountain, A. G., and W. V. Tangborn, 1985: The effect of glaciers on streamflow variations. *Water Resour. Res.*, **21**, 579–586.

——, and T. Nuimura, 2011: Spatially heterogeneous wastage of Himalayan glaciers. *Proceedings of the National Acedamy of Sciences*, **108**, 14011–14014.

Gardner, A. S., and Coauthors, 2011: Sharply increased mass loss from glaciers and ice caps in the Canadian Arctic Archipelago. *Nature*, **473**, 357–360.

——, and Coauthors, 2013: A reconciled estimate of glacier contributions to sea level rise: 2003 to 2009. *Science*, **340**, 852–857.

Garnier, B., and A. Ohmura, 1968: A method of calculating the direct shortwave radiation income of slopes. *J. Appl. Meteor.*, **7**, 796–800.

Gerbaux, M., C. Genthon, P. Etchevers, C. Vincent, and J. P. Dedieu, 2005: Surface mass balance of glaciers in the French Alps : Distributed modeling and sensitivity to climate change. *J. Glaciol.*, **51**, 561–572.

Giorgetta, M. A., and Coauthors, 2013: Climate and carbon cycle changes from 1850 to 2100 in MPI-ESM simulations for the Coupled Model Intercomparison Project phase 5. *J. Adv. Model. Earth Syst.*, **5**, 572–597.

Giorgi, F., and B. Hewitson, 2001: Regional climate information-Evaluation and projection. Climate Change 2001: The Scientific Basis. Houghton et al., Eds., Cambridge University Press, Cambridge, UK, 585-638.

Greuell, W., W. H. Knap, and P. C. Smeets, 1997: Elevational changes in meteorological variables along a midlatitude glacier during summer. *J. Geophys. Res.*, **102**, 25941–25954, doi:10.1029 97JD02083.

——, and J. Oerlemans, 1986: Sensitivity studies with a mass balance model including temperature profile calculations inside the glacier. *Z. Gletscherkd. Glazialgeol.*, **22**, 101–124.

Hanssen-Bauer, I., E. J. Forland, J. E. Haugen, and O. E. Tveito, 2003: Temperature and precipitation scenarios for Norway: Comparison of results from dynamical and empirical downscaling. *Clim. Res.*, **25**, 15-27.

Hare, F. K., and J. E. Hay, 1974: The climate of Canada and Alaska.Climates of North America, R. A. Bryson and F. K. Hare, Eds.,Vol. 11, World Survey of Climatology, Elsevier, 49–192.

Hellström, C., D. Chen, C. Achberger, and J. Räisänen, 2001: Comparison of climate change scenarios for Sweden based on statistical and dynamical downscaling of monthly precipitation. *Clim. Res.*, **19**, 45–55.

Hock, R., 2003: Temperature index melt modelling in mountain areas. *J. Hydrol.*, **282**, 104–115.

——, 2005: Glacier melt: a review of processes and their modelling. *Prog. Phys. Geogr.*, **29**, 362–391.

——, 1999: A distributed temperature-index ice- and snowmelt model including potential direct radiation. *J. Glaciol.*, **45**, 101-111.

——, and B. Holmgren, 2005: A distributed surface energy-balance model for complex topography and its application to Storglaciaren, Sweden. *J. Glaciol.*, **51**, 25–36.

——, V. Radic, and M. De Woul, 2007: Climate sensitivity of Storglaciaren, Sweden: an intercomparison of mass-balance models using ERA-40 re-analysis and regional climate model data. *Ann. Glaciol.*, **46**, 342–348.

——, and C. Noetzli, 1997: Areal melt and discharge modelling of Storglaciaren, Sweden. *Ann. Glaciol.*, **24**, 211–214.

——, 1998: Modelling of glacier melt and discharge. Ph.D. Thesis. ETH Institute of Geography.

Hopkinson, C., and G. J. Young, 1998: The effect of glacier wastage on the flow of the Bow River at Banff, Alberta, 1951-1993. *Hydrol. Process.*, **12**, 1745-1763.

Huo, Z., 1991: Measurement and modelling of the radiation budget of alpine tundra, Plateau Mountain, Alberta, Canada. Master's thesis, Simon Fraser University.

Huss, M., D. Farinotti, A. Bauder, and M. Funk, 2008: Modelling runoff from highly glacierized alpine drainage basins in a changing climate, *Hydrol. Process.* **22**, 3888–3902.

Huss, M., R. Hock, A. Bauder, and M. Funk, 2012: Conventional versus reference-surface mass balance. *J. Glaciol.*, **58**.

Huss, M., M. Zemp, P. C. Joerg, and N. Salzmann, 2014: High uncertainty in 21st century runoff projections from glacierized basins. *J. Hydrol.*, **510**, 35–48.

Huth, R., 1999: Statistical downscaling in central Europe: evaluation of methods and potential predictors. *Clim. Res.*, **13**, 91–101.

——, 2002: Statistical Downscaling of daily temperature in Central Europe. *J. Clim.*, **15**, 1731–1742.

IPCC, 2013: Climate Change 2013: The Physical Science Basis. Contribution of Working Group I to the Fifth Assessment Report of the Intergovernmental Panel on Climate Change. T. F. Stocker et al., Eds., Cambridge University Press, 1535 pp.

Immerzeel, W. W., L. P. H. van Beek, and M. F. P. Bierkens, 2010: Climate change will affect the Asian water towers. *Science*, **328**, 1382–1385, doi:10.1126/science.1183188.

Iqbal, M., 1983: *An Introduction to Solar Radiation*. Academic Press, London, 390 pp.

Jacob, T., J. Wahr, W. T. Pfeffer, and S. Swenson, 2012: Recent contributions of glaciers and ice caps to sea level rise. *Nature*, **482**, 514–518.

Janowiak, J. E., A. Gruber, C. R. Kondragunta, R. E. Livezey, and G. J. Huffman, 1998: A comparison of the NCEP–NCAR Reanalysis precipitation and the GPCP rain gauge–satellite combined dataset with observational error considerations. *J. Climate*, **11**, 2960–2979.

Jarosch, A. H., F. S. Anslow, and G. K. C. Clarke, 2010: High-resolution precipitation and temperature downscaling for glacier models. *Clim. Dyn.*, **38**, 391–409.

Johannesson, T., T. Laumann, and M. Kennett, 1995: Degree-day glacier mass-balance modelling with applications to glaciers in Iceland, Norway and Greenland. *J. Glaciol.*, **41**, 345–358.

Jones, C. D., and Coauthors, 2011: The HadGEM2-ES implementation of CMIP5 centennial simulations. *Geosci. Model Dev.*, **4**, 543–570.

Kalnay, E., and Coauthors, 1996: The NCEP/NCAR 40-Years Reanalysis Project. *Bull. Am. Meteorol. Soc.*, 77, 437–471.

Kaser, G., J. G. Cogley, M. B. Dyurgerov, M. F. Meier, and a. Ohmura, 2006: Mass balance of glaciers and ice caps: Consensus estimates for 1961–2004. *Geophys. Res. Lett.*, **33**, L19501, doi:10.1029/2006GL027511.

Kaser, G., M. Grosshauser, and B. Marzeion, 2010: Contribution potential of glaciers to water availability in different climate regimes. *Proc. Natl. Acad. Sci. U. S. A.*, **107**, 20223–20227.

Kayastha, R., T. Ohata, and Y. Ageta, 1999: Application of a mass-balance model to a Himalayan glacier. *J. Glaciol.*, **45**, 559-567.

Kienzle, S. W., 2008: A new temperature based method to separate rain and snow. *Hydrol. Process.*, **22**, 5067–5085.

Klok, E. J., and J. Oerlemans, 2002: Model study of the spatial distribution of the energy and mass balance of Morteratschgletscher, Switzerland. *J. Glaciol.*, **48**, 505–518.

——, M. Nolan, and M. R. van den Broeke, 2005: Analysis of meteorological data and the surface energy balance of McCall Glacier, Alaska, USA. *J. Glaciol.*, **51**, 451–461.

——, and J. Oerlemans, 2004: Modelled climate sensitivity of the mass balance of Morteratschgletscher and its dependence on albedo parameterization. *Int. J. Climatol.*, **24**, 231–245.

Koch, J., B. Menounos, and J. J. Clague, 2009: Glacier change in Garibaldi Provincial Park, southern Coast Mountains, British Columbia, since the Little Ice Age. *Glob. Planet. Change*, **66**, 161–178.

Konzelmann, T., and R. J. Braithwaite, 1995: Variations of ablation, albedo and energy balance at the margin of the Greenland ice sheet, Kronprins Christian Land, eastern north Greenland. *J. Glaciol.*, **41**, 174–182.

Koppes, M., H. Conway, L. A. Rasmussen, and M. Chernos, 2011: Deriving mass balance and calving variations from reanalysis data and sparse observations, Glaciar San Rafael, northern Patagonia, 1950-2005. *Cryosphere*, **5**, 791–808.

Kostopoulou. E., and Coauthors, 2007: Simulating maximum and minimum temperatures over Greece: a comparison of three downscaling techniques. *Theor. Appl. Climatol.*, **90**, 65–82.

Krimmel, R. M., 1999: Analysis of difference between direct and geodetic mass balance measurements at South Cascade Glacier, Washington. *Geogr. Ann.*, **81A**, 653–658.

Lau, N. C., M. J. Nath, 1994: A modeling study of the relative roles of tropical and extratropical SST anomalies in the variability of the global atmosphere-ocean system. *J. Clim.*, 7, 1184-1207.

Leclercq, P. W., R. S. W. van de Wal, and J. Oerlemans, 2010: Comment on "100-year mass changes in the Swiss Alps linked to the Atlantic Multidecadal Oscillation" by Matthias Huss et al. (2010). *Cryosph. Discuss.*, **4**, 2475–2481.

Leith, R. M. M., and P. H. Whitfield, 1998: Evidence of climate change effects on the hydrology of streams in south-central British Columbia. *Can. Water Resour. J.*, **23**, 219-230.

Letreguilly, A., 1988: Relation between the mass balance of western Canadian mountain glaciers and meteorological data. *J. Glaciol.*, **34**, 11–18.

Loth, B., H-F. Graf, and J. M. Oberhuber, 1993: Snow cover model for global climate simulations. *J. Geophys. Res.*, **98**, 10451–10464.

Luckman, B. H., 1998: Landscape and climate change in the central Canadian Rockies during the 20th century. *Can. Geogr.*, **42**, 319–336.

MacDougall, A. H., and G. E. Flowers, 2011: Spatial and temporal transferability of a distributed energy-balance glacier melt model. *J. Clim.*, **24**, 1480–1498.

——, B. A. Wheler, and G. E. Flowers, 2011: A preliminary assessment of glacier melt-model parameter sensitivity and transferability in a dry subarctic environment. *Cryosph.*, **5**, 1011–1028.

Mantua, N. J., S. R. Hare, U. Zhang, J. M. Wallace, and R. C. Francis, 1997: A Pacific interdecadal climate oscillation with impacts on salmon production. *Bull. Amer. Meteor. Soc.*, **78**, 1069–1079.

Marshall, S. J., E. C. White, M. N. Demuth, T. Bolch, R. Wheate, B. Menounos, M. J. Beedle, and J. M. Shea, 2011: Glacier water resources on the eastern slopes of the Canadian Rocky Mountains. *Can. Water Resour. J.*, **36**, 109-134.

Marzeion, B., J. G. Cogley, K. Richter, and D. Parkes, 2014: Attribution of past glacier mass Loss to anthropogenic and natural climate forcing. *Science.*, **345**, 919–921.

Mason, S. J., 2004: Simulating climate over Western North America using stochastic weather generators. *Clim. Change*, **62**, 155–187.

MathWorks, 2012: MATLAB and Statistics Toolbox Release 2013a, The MathWorks, Inc., Natick, Massachusetts, United States.

Matulla, C., E. Watson, S. Wagner, and W. Schöner, 2008: Downscaled GCM projections of winter and summer mass balance for Peyto Glacier, Alberta, Canada (2000 – 2100) from ensemble simulations with ECHAM5-MPIOM. *Int. J. Climatol.*, doi:10.1002/joc.

Matheron, G, 1963. Principles of Geostatistics. *Econ. Geol.*, **58**, 1246-1266.

Mesinger, F., and Coauthors, 2006: North American Regional Reanalysis. *Bull. Am. Meteorol. Soc.*, **87**, 343–360.

Mo, K. C., and R. W. Higgins, 1996: Large-scale atmospheric moisture transport as evaluated in the NCEP/NCAR and the NASA/ DAO reanalyses. *J. Climate*, **9**, 1531–1545.

Mölg, T., and D. R. Hardy, 2004: Ablation and associated energy balance of a horizontal glacier surface on Kilimanjaro. *J. Geophys. Res.*, **109**, D16104, doi:10.1029/2003JD004338.

——, and G. Kaser, 2011: A new approach to resolving climate-cryosphere relations: Downscaling climate dynamics to glacier-scale mass and energy balance without statistical scale linking. *J. Geophys. Res.*, **116**, D16101, doi:10.1029/2011JD015669.

Moore, R. D., 2006: Stream temperature patterns in British Columbia, Canada, based on routine spot measurements. *Can. Water Resour. J.*, **31**, 41–56.

——, and M. N. Demuth, 2001: Mass balance and streamflow variability at Place Glacier, Canada, in relation to recent climate fluctuations. *Hydrol. Process.*, **15**, 3473–3486.

——, S. W. Fleming, B. Menounos, R. Wheate, A. Fountain, K. Stahl, K. Holm, and M. Jakob, 2009: Glacier change in western North America : influences on hydrology, geomorphic hazards and water quality. *Hydrol. Process.*, **23**, 42–61.

——, 1983: On the use of bulk aerodynamic formulae over melting snow. *Nordic Hydrol.* **14**, 193–206.

Morrison, J., M. C. Quick, and M. G. G. Foreman, 2002: Climate change in the Fraser River watershed : flow and temperature projections. *J. Hydrol.*, **263**, 230–244.

Moss, R. H., and Coauthors, 2010: The next generation of scenarios for climate change research and assessment. *Nature*, **463**, 747–756.

Munro, D. S., 1990: Comparison of melt energy computations and ablatometer measurements on melting ice and snow. *Arctic, Antarct. Alp. Res.*, **22**, 153–162.

——, and M. Marosz-Wantuch, 2009: Modeling ablation on Place Glacier, British Columbia, from glacier and off-glacier data sets. *Arctic, Antarct. Alp. Res.*, **41**, 246–256.

Murphy, J., 2000: Predictions of climate change over Europe using statistical and dynamical downscaling techniques. *Int. J. Climatol.*, **20**, 489–501.

National Centers for Environmental Prediction, 2009: NCEP/NCAR Reanalysis Data. NCEP Reanalysis data provided by the NOAA/OAR/ESRL PSD, Boulder, Colorado, USA, from their Web site at http: www.cdc.noaa.gov/

NSIDC, 2005 (updated 2012): GLIMS Glacier Database, Boulder, Colorado USA [Available online at http: /nsidc.org/data/nsidc-0272].

Oerlemans, J., 1992: Climate sensitivity of glaciers in southern Norway: application of an energy-balance model to Nigardsbreen, Hellstugubreen and Alfotbreen. *J. Glaciol.*, **38**, 223–232.

——, and B. Grisogono, 2002: Glacier winds and parameterisation of the related surface heat fluxes. *Tellus A*, **54**, 440–452.

——, and W. H. Knap, 1998. A 1 year record of global radiation and albedo in the ablation zone of Morteratschgletscher, Switzerland. *J. Glaciol.*, **44**, 231-238.

Ohmura, A., 2004: Cryosphere during the twentieth century. *The State of the Planet: Frontiers and Challenges in Geophysics.* R. S. J. Sparks and C. J. Hawkesworth, Eds, American Geophysical Union, Geophysical Monograph Series, **150**, 239– 257.

Oke, T., 1987: *Boundary Layer Climates*. Routledge, London, 435 pp.

Østrem, G., 1966: Mass balance studies on glaciers in western Canada, 1965. *Geogra. Bull.*, **8**, 81–107.

——, and M. Brugman, 1991: Glacier mass balance measurements-a manual for field and office work. Scientific Report No. 4, National Hydrology Research Institute, Saskatoon, Saskatchewan, Canada, 224 pp.

Paul, F., 2010: The influence of changes in glacier extent and surface elevation on modeled mass balance. *Cryosphere*, **4**, 569–581.

——, and S. Kotlarski, 2010: Forcing a distributed glacier mass balance model with the Regional Climate Model REMO. Part II: Downscaling strategy and results for two Swiss glaciers. *J. Clim.*, **23**, 1607–1620.

Pellicciotti, F., B. Brock, U. Strasser, P. Burlando, M. Funk, and J. Corripio, 2005: An enhanced temperature-index glacier melt model including the shortwave radiation balance: development and testing for Haut Glacier d'Arolla, Switzerland. *J. Glaciol.*, **51**, 573–587.

——, J. Helbing, A. Rivera, V. Favier, J. Corripio, J. Araos, J. E. Sicart, and M. Carenzo, 2008: A study of the energy balance and melt regime on Juncal Norte Glacier, semi-arid Andes of central Chile, using melt models of different complexity. *Hydrol. Process.*, **22**, 3980-3997.

Pelto, M. S., and J. Riedel, 2001: Spatial and temporal variations in annual balance of North Cascade glaciers, Washington 1984-2000. *Hydrol. Process.*, **15**, 3461–3472.

Press, W. H. P., S. A. Teukolsky, W. T. Vetterling, and B. P. Flannery, 1992: *Numerical Recipes in Fortran.* Cambridge University Press, New York.

Prudhomme, C., N. Reynard, and S. Crooks, 2002: Downscaling of global climate models for flood frequency analysis: where are we now? *Hydrol. Process.*, **16**, 1137–1150.

Radić, V., and R. Hock, 2006: Modeling future glacier mass balance and volume changes using ERA-40 reanalysis and climate models: A sensitivity study at Storglaciären, Sweden. *J. Geophys. Res.*, **111**, F03003, doi:10.1029/2005JF000440.

——, and ——, 2011: Regionally differentiated contribution of mountain glaciers and ice caps to future sea-level rise. *Nat. Geosci.*, **4**, 91–94.

——, and G. K. C. Clarke, 2011: Evaluation of IPCC models' performance in simulating late-Twentieth-Century climatologies and weather patterns over North America. *J. Clim.*, **24**, 5257–5274.

——, A. Bliss, A. C. Beedlow, R. Hock, E. Miles, and J. G. Cogley, 2013: Regional and global projections of twenty-first century glacier mass changes in response to climate scenarios from global climate models. *Clim. Dyn.*, **42**, 37–58.

Raper, S. C. B., and R. J. Braithwaite, 2006: Low sea level rise projections from mountain glaciers and icecaps under global warming. *Nature*, **439**, 311–313.

Rasmussen, L. A., and H. Conway, 2004: Climate and glacier variability in Western North America. *J. Clim.*, **17**, 1804–1815.

Richards, G., and R. D. Moore, 2003: Suspended sediment dynamics in a steep, glacier-fed mountain stream, Place Creek, Canada. *Hydrol. Process.*, **17**, 1733–1753.

Salathé, E. P., 2005: Downscaling simulations of future global climate with application to hydrologic modelling. *Int. J. Climatol.*, **25**, 419–436.

——, R. Steed, C. F. Mass, and P. Zahn, 2008: A high-resolution climate model for the United States Pacific Northwest: Mesoscale feedbacks and local responses to climate change. *J. Clim.*, **21**, 5708–5726.

Schiefer, E., B. Menounos, and R. Wheate, 2007: Recent volume loss of British Columbian glaciers, Canada. *Geophys. Res. Lett.*, **34**, L16503 DOI:10.1029/2007GL030780

Shea, J. M., 2010: Regional-scale distributed modelling of glacier meteorology and melt, southern Coast Mountains, Canada. Ph.D Thesis. Department of Geography, University of British Columbia.

——, and S. J. Marshall, 2007: Atmospheric flow indices, regional climate, and glacier mass balance in the Canadian Rocky Mountains. *Int. J. Climatol.*, **247**, 233–247.

Shea, J. M., R. D. Moore, and K. Stahl, 2009: Derivation of melt factors from glacier mass-balance records in western Canada. *J. Glaciol.*, **55**, 123–130.

Sicart, J. E., P. Wagnon, and P. Ribstein, 2005: Atmospheric controls of the heat balance of Zongo Glacier (16°S, Bolivia). *J. Geophys. Res.*, **110**, D12106, doi:10.1029/2004JD005732.

Singh, P., and N. Kumar, 1997: Impact assessment of climate change on the hydrological response of a snow and glacier melt runoff dominated Himalayan river. *J. Hydrol.*, **193**, 316–350.

Springer, C., C. Matulla, W. Schöner, R. Steinacker, and S. Wagner, 2012: Downscaled GCM projections of winter and summer mass balance for Central European glaciers (2000-2100) from ensemble simulations with ECHAM5-MPIOM. *Int. J. Climatol.*, **33**, 1270–1279.

Stahl, K., and R. D. Moore, 2006: Influence of watershed glacier coverage on summer streamflow in British Columbia, Canada. *Water Resour. Res.*, **42**, W06201 doi:10.1029/2006WR005022.

Stahl, K., R. D. Moore, J. A. Floyer, M. G. Asplin, and I. G. McKendry, 2006: Comparison of approaches for spatial interpolation of daily air temperature in a large region with complex topography and highly variable station density. *Agric. For. Meteorol.*, **139**, 224–236.

——, ——, J. M. Shea, D. Hutchinson, and a. J. Cannon, 2008: Coupled modelling of glacier and streamflow response to future climate scenarios. *Water Resour. Res.*, **44**, doi:10.1029/2007WR005956.

Taylor, K. E., R. J. Stouffer, and G. A. Meehl, 2012: An overview of CMIP5 and the experiment design. *Bull. Am. Meteorol. Soc.*, **93**, 485–498.

Tennant, C., B. Menounos, B. Ainslie, J. Shea, and P. Jackson, 2012: Comparison of modeled and geodetically-derived glacier mass balance for Tiedemann and Klinaklini glaciers, southern Coast Mountains, British Columbia, Canada. *Glob. Planet. Change*, **82-83**, 74–85.

USGS, 2002: Glaciers of North America — Glaciers of Canada. R.S.J. Williams and J.G. Ferrigno, Eds. Tech. Rep. Professional Paper 1386-J-1, US Geological survey, 28 pp.

Van de Wal, R. S., and M. Wild, 2001: Modelling the response of glaciers to climate change by applying volume-area scaling in combination with a high resolution GCM. *Clim. Dyn.*, **18**, 359–366.

Viviroli, D., and Coauthors, 2011: Climate change and mountain water resources: Overview and recommendations for research, management and policy. *Hydrol. Earth Syst. Sci.*, **15**, 471–504, doi:10.5194/hess-15-471-2011.

Walraven, R., 1978: Calculating the position of the sun. *Solar Energy*, **20**, 393– 397.

Wang, T., A. Hamann, D. L. Spittlehouse, and S. N. Aitken, 2006: Development of scale-free climate data for Western Canada for use in resource management. *Int. J. Climatol.*, **26**, 383–397.

Ward, M. N., and A. Navarra, 1997: Pattern analysis of SST-forced variability in ensemble GCM simulations: examples over Europe and the tropical Pacific. *J. Clim.*, **10**, 2210-2220.

Watanabe, S., and Coauthors, 2011: MIROC-ESM 2010: model description and basic results of CMIP5-20c3m experiments. *Geosci. Model Dev.*, **4**, 845–872.

Watson, E., B. H. Luckman, and B. Yu, 2006: Long-term relationships between reconstructed seasonal mass balance at Peyto Glacier, Canada, and Pacific sea surface temperatures. *The Holocene*, **16**, 783–790.

Webb, E. K., 1970: Profile relationships: The log-linear range, and extension to strong stability. *Quart. J. Roy. Meteor. Soc.*, **96**, 67–90.

WGMS/UNEP, 2008: Global Glacier Changes : facts and figures. M. Zemp, I. Roer, A. Kaab, F. Paul, and W. Haeberli, Eds. Scientific Report, World Glacier Monitoring Service, 47 pp.

WGMS, 2011: Glacier fluctuation data provided by World Glacier Monitoring Service, Univerisity of Zurich [Available online at http://www.wgms.ch/access.html]

Wheler, B. A., and G. E. Flowers, 2011: Glacier subsurface heat-flux characterizations for energy-balance modelling in the Donjek Range, southwest Yukon, Canada. *J. Glaciol.*, **57**, 121–133.

Widmann, M., and C. S. Bretherton, 2000: Validation of mesoscale precipitation in the NCEP Reanalysis using a new gridcell dataset for the Northwestern United States. *J. Clim.*, **13**, 1936–1950.

——, ——, and E. P. Salathé, 2003: Statistical precipitation downscaling over the Northwestern United States using numerically simulated precipitation as a predictor. *J. Clim.*, **16**, 799–816.

Wilby, R. L., and T. M. L. Wigley, 1997: Downscaling general circulation model output: a review of methods and limitations. *Prog. Phys. Geogr.*, **21**, 530–548.

Wilks, D. S., 1992: Adapting stochastic weather generation algorithms for climate change studies. *Climatic Change*, **22**, 67–84.

Xu, J., R. E. Grumbine, A. Shrestha, M. Eriksson, X. Yang, Y. Wang, and A. Wilkes, 2009: The melting Himalayas: Cascading effects of climate change on water, biodiversity, and livelihoods. *Conserv. Biol.*, **23**, 520–530.

Zemp, M., and Coauthors, 2013: Reanalysing glacier mass balance measurement series. *Cryosphere*, 7, 1227–1245.

Zhang, J., U. S. Bhatt, W. V. Tangborn, and C. S. Lingle, 2007a: Response of glaciers in northwestern North America to future climate change: an atmosphere/glacier hierarchical modeling approach. *Ann. Glaciol.*, **46**, 283–290.

Zhang, J., U. S. Bhatt, W. V. Tangborn, and C. S. Lingle, 2007b: Climate downscaling for estimating glacier mass balances in northwestern North America: Validation with a USGS benchmark glacier. *Geophys. Res. Lett.*, **34**, L21505, doi:10.1029/2007GL031139.

Zorita, E., and H. von Storch, 1999: The analog method as a simple statistical downscaling technique: Comparison with more complicated methods. *J. Climate*, **12**, 2474–2489.